Phase switching behaviour in lead-free $Na_{0.5}Bi_{0.5}TiO_3$-based ceramics

A thesis submitted to the University of Manchester for the degree of

Doctor of Philosophy

in the Faculty of Science & Engineering

2016

Ge Wang

School of Materials

List of Contents

List of Figures

Chapter 1

Chapter 2

Chapter 3

Chapter 4

Chapter 5

Chapter 6

Chapter 7

Chapter 8

Chapter 11

List of Tables

Chapter 2

Chapter 3

Chapter 5

Chapter 6

Chapter 7

Symbols and Abbreviations

Symbols

A	Area of electrode
a_{pc}	Lattice parameter
α_{pc}	Interaxial angle
C	Cubic structure
C_s	Capacitance of the samples
d	D-spacing
d_{200}	d-spacing for (200) peak
d_{31}	Piezoelectric coefficient measured perpendicular to the poling direction
d_{33}	Piezoelectric coefficient measured along the poling direction
D_i	Direct piezoelectric effect
d_{ijk}	Third-rank tensor of piezoelectric coefficients
$\bar{d}$	Average grain size
E	Electric field
E_b	Backward electric field
E_c	Coercive field
E_f	Forward electric field
E_{max}	Maximum electric field
$\bar{\varepsilon}$	Tensile remanent stain
ε'	Real part
ε''	Imaginary part
ε_0	Permittivity of free space
ε_{200}	Lattice strain for (200) peak
ε_r	Relative permittivity
F_p	Frequency
F_s	Resonant frequency
hkl	Set of planes
I_{charge}	Current charge
I_{loss}	Current loss
$I_{\bar{1}11}$	Intensity for $(\bar{1}11)$ peak
I_{111}	Intensity for (111) peak
J_0/J_1	Bessel function
k_{eff}	Effective electromechanical coupling coefficient
k_p	Planar coupling coefficient
m	Mass
N_A	Avogadro's constant

P	Polarisation
P_{max}	Maximum polarisation
P_{rem}	Remanent polarisation
r	Diameter
R	Rhombohedral structure
R(111)	Intensity ratio for (111) peak
R_A	Ionic radii for A-site atom
R_B	Ionic radii for B-site atom
R_O	Ionic radii for O-site atom
S_{11}	Strain component perpendicular to poling direction
S_{33}	Strain component along with poling direction
t	Tolerance factor
tanδ	Dielectric loss
T_B	Burns temperature
T_c	Curie temperature
T_d	Depolarisation temperature
T_{F-R}	Phase transition temperature from ferroelectric to relaxor ferroelectric
T_{ir}	Additional anomaly in loss-T curve
T_m	Temperature for dielectric peak
T_p	First anomaly in permittivity-T curve
T_{ST}	Structural transformation temperature
v	Unit cell volume
V_C	Measured voltage
X	Co-ordinate system
X_{jk}	Stress
Y	Modified co-ordinate system
χ	Dielectric susceptibility
λ	Wavelength
μ	Absorption coefficient
ν	Poisson's ratio
ν_{111}	Domain fraction
ρ_m	calculated density
ρ_r	Practical density
ρ_t	Theoretical density
ψ	Grain orientation
ΔQ	Pyroelectric charge

Abbreviations

AC	Alternating current
BLSF	Bismuth layered-structured ferroelectrics
BMT	Bismuth magnesate titanate $BiMg_{0.5}Ti_{0.5}O_3$
BT	Barium titanate $BaTiO_3$
DOD	Domain orientation distribution
ER	Ergodic relaxor
Ev	Electron volt
EXAFS	Extended x-ray absorption fine structure
FE	Ferroelectric
ICDD	International centre for diffraction date database
J-E	Current density-electric field
KBT	Potassium bismuth titanate $K_{0.5}Bi_{0.5}TiO_3$
KN	Potassium niobate $KNbO_3$
KNN	Potassium sodium niobate $K_{0.5}Na_{0.5}NbO_3$
LF4T	(Li, Ta)-doped $K_xNa_{1-x}NbO_3$
MPB	Morphotropic phase boundary
NBT	Sodium bismuth titanate $Na_{0.5}Bi_{0.5}TiO_3$
NCSD	National chemical service database
NN	Sodium niobate $NaNbO_3$
NR	Nonergodic relaxor
OPS	Oxide polishing suspension
PDF	Pair distribution function
PE	Paraelectric
P-E	Polarisation-electric field
PNR	Polar nano-region
PST	Lead scandate tantalite $Pb(Sc_{0.5}Nb_{0.5})O_3$
PZT	Lead zirconate titanate $Pb(Zr_xTi_{1-x})O_3$
R/T	Rhombohedral and tetragonal phase mixture
RF	Relaxor ferroelectric
S-E	Strain-electric field
SEM	Scanning electron microscopy
ST	Strontium titanate $SrTiO_3$
SXPD	Synchrotron x-ray powder diffraction
TBT	Tungsten bronze type
TEM	Transmission electron microscopy
XRD	X-ray diffraction

Publications

1. **G. Wang**, D. A. Hall, Yizhe Li, Claire A. Murray, Chiu C. Tang, "Structural characterization of the electric field-induced ferroelectric phase in $Na_{0.5}Bi_{0.5}TiO_3$-$KNbO_3$ ceramics." Journal of European Ceramic Society, 2016, **36**(16), 4015-4021. DOI: 10.1016/j.jeurceramsoc.2016.06.022

2. **G. Wang**, D. A. Hall, T. P. Comyn, L. Daniel, and A. K. Kleppe, "Structure and ferroelectric behaviour of $Na_{0.5}Bi_{0.5}TiO_3$-$KNbO_3$ ceramics." Advances in Applied Ceramics, 2016, **115** (2). 89-95. DOI:10.1080/17436753.2015.1104053

Abstract

Phase switching behaviour in lead-free $Na_{0.5}Bi_{0.5}TiO_3$-based ceramics

Ge Wang

The University of Manchester for the degree of Doctor of Philosophy in the Faculty of Engineering of Physical Sciences

2016

This PhD project is focused on three lead-free ferroelectric solid solutions, which are specifically $Na_{0.5}Bi_{0.5}TiO_3$-$KNbO_3$(NBT-KN), $Na_{0.5}Bi_{0.5}TiO_3$-$NaNbO_3$(NBT-NN) and $Na_{0.5}Bi_{0.5}TiO_3$-$BaTiO_3$(NBT-BT), to evaluate the effects of composition, electric field and temperature on structural and electrical properties. Novel observations of both reversible and irreversible electric field-induced phase switching were made in both NBT-KN and NBT-NN ceramics.

The NBT-KN solid solution is the primary focus of this thesis. All compositions were observed to be cubic in the as-sintered, unpoled state. However, a well-defined ferroelectric hysteresis P-E loop was obtained for compositions with low KN contents, indicating that an irreversible phase transition from a weak-polar relaxor ferroelectric (RF) to a long-range ordered metastable ferroelectric (FE) state had occurred during the measurement procedure. Both the unpoled and poled ceramic powders were examined using high resolution synchrotron XRD. For the poled state, a rhombohedral R3c structure was identified for compositions with low KN content, confirming the occurrence of the irreversible electric field-induced structural transformation from cubic to rhombohedral. In contrast, a cubic structure was retained for high KN contents, giving rise to reversible phase switching evidenced by constricted P-E hysteresis loops. Similar behaviour was observed for NBT-NN system.

An 'in-situ' electric field poling experiment was conducted using high energy synchrotron XRD. In certain NBT-KN compositions the structural transformation, from cubic to mixed phase cubic+rhombohedral and finally single phase rhombohedral, occurred progressively with increasing cycles of a bipolar electric field. Similar behaviour was observed for NBT-NN compositions having low NN contents. Furthermore, the distributions of domain orientation and lattice strain over a range of orientations relative to the poling direction were determined for NBT-KN, NBT-NN and NBT-BT ceramics exhibiting the rhombohedral phase.

By combining the structural information with the results of dielectric and ferroelectric measurements, a phase diagram was constructed to illustrate the influence of temperature and composition on the stability of the metastable ferroelectric and relaxor ferroelectric states for the NBT-KN system. Furthermore, the phase transition temperatures obtained from dielectric measurements were correlated with the ferroelectric and thermal depolarisation characteristics for each of the NBT-KN, NBT-NN and NBT-BT systems.

Declaration

No portion of the work referred to in the thesis has been submitted in support of an application for another degree or qualification of this or any other university or other institute of learning.

Copyright statement

Acknowledgements

First of all, I would like express my deepest gratitude to my supervisor, Dr. David Hall, who has supported and guided me throughout my studies. During my PhD, he did not only share his wisdom and broad knowledge but also gave me endless encouragement and confidence anytime I needed.

I would like to thank other colleagues who have been involved in the research project, including Prof. Chiu Tang, Dr. Claire Murray, Dr. Dominik Daisenberger, Prof. Laurent Daniel and Dr. Tim Comyn who helped the Diamond synchrotron X-ray experiments, Dr. Zhenbo Zhang and Dr. Ying Chen who helped me with sample preparation, Dr. Liang Qiao who helped me with project and thesis. And I would like to give special thanks to Yizhe Li who helped me with the dielectric, synchrotron XRD, TEM and DIC experimental work and inspired me all the time.

I would like to thank the technician staff in the school of Materials for their help on my experiments, including Mr. Kenneth Gyves, Mr. Michael Faulkner, Dr. John Warren, Mr. Gary Harrison and Dr. Christopher Wilkins.

I would like to thank all the members of the electroceramics group for your generous help during my PhD, including Li Wang, Dongting Jiang, Nuth Kulwongwit, Deepanshu Srivastava, Karim Khalf, Ilkan Calisir, Mohammand Al-Aaraji, and Jirapa Tangsritarakul.

I would like to thank all my 'Manchester family' here to give me support and love all the time, including Claire Occleston, Jules Whitehead, Sandy Yip, Kathy Xu, Livia Wu and Sissi Qu. I had a wonderful time with all of you when I am out of University.

At last, I would like to special thank my parents-Hua/Quansheng, aunt-Yan, uncle-Gang, grandma-Fengying and sister-Nan-Chun. Your support and love are always my endless power to conquer the difficulties. I am always trying my best to be better myself and make you guys to be proud of.

TO DEAR

MOM;

DAD;

GRANDPA

（献给我最爱的妈妈、爸爸及爷爷）

1 Introduction

1.1 Introduction

Piezoelectric materials have been widely used in many electric applications for over 100 years due to their unique electrical properties. Normally, they are utilised in sensor and actuator technologies because they are capable of coupling electrical and mechanical displacement, i.e., to change polarisation in response to an applied mechanical stress or strain. Compared to other electromechanical technologies, piezoelectric materials can achieve better stability when subjected to changes in temperature and pressure, and exhibit chemical and environmental resistance. This leads to applications ranging from actuators, transducers, sensors to nano-positioners, ultrasonic motors and imaging devices.[1]

As shown in Figure. 1.1(a), it is estimated that the global market for piezoelectric actuators was about 12290 million US dollars in 2014, which is double that in 2009. Specifically, the main types of piezoelectric applications did not change too much between 2009 and 2014. With largest share, piezoelectric devices are mainly utilised in ultra-small scale motion related applications and camera related applications, which combined amounted to over 40%. Only the share for fuel injectors was predicted to increase from 3.8 % to 4.9 % by 2014, which indirectly reflects the requirements for achieving both high fuel efficiency and eco-friendly to environment, such as reducing emissions of carbon dioxide. There is also related requirement to reduce lead pollution from lead zirconate titanate (PZT).

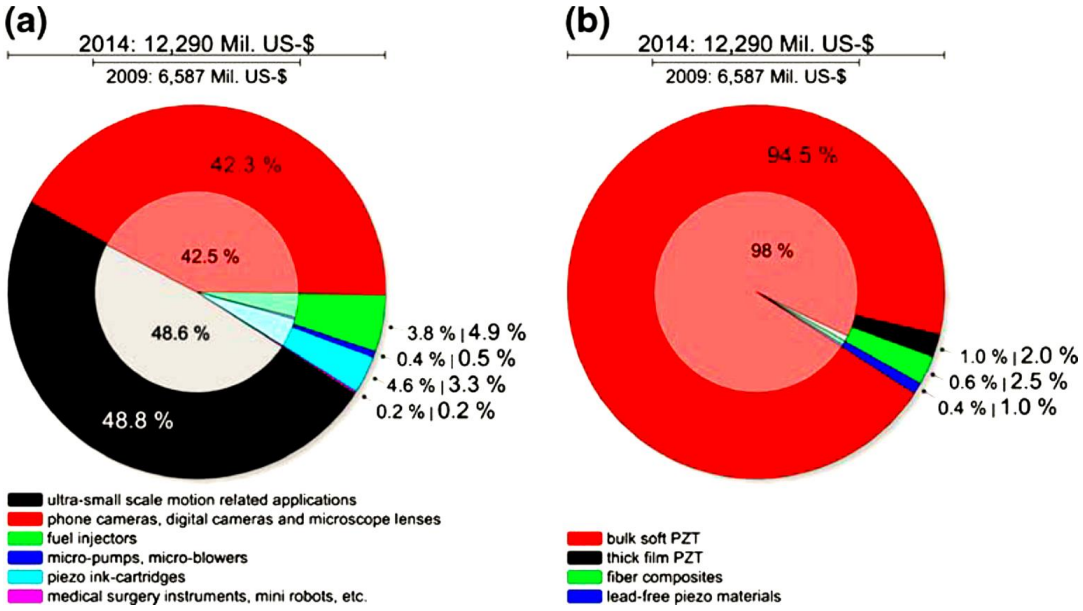

Figure 1.1 Global market shares of piezoelectric actuators with respect to (a) applications and (b) materials. The scale bars on top of each plot denotes the market size.[1]

Currently, the most popular and widely used piezoelectric ceramic is PZT, $Pb(Zr_x,Ti_{1-x})O_3$. PZT is an inorganic compound with a typical perovskite structure, which shows a marked piezoelectric effect. From the perspective of materials, PZT dominated the piezoelectric application market by over 98 % in 2009, which included 97 % of bulk ceramic and 1 % of thin film. Both lead-free piezoelectric ceramics and fibre composites were expected to grow from 0.6 % to 2.5 % and 1.0 % to 2.0 % respectively, which represents the attempt to reduce lead pollution to the environment by replacing PZT by lead-free piezoelectric ceramics gradually.

Although PZT has already dominated piezoelectric applications for decades and has the best piezoelectric properties compared to most other choices, there is one huge disadvantage of PZT in that its lead content is greater than 60 wt%. This lead component, which originates as PbO, has been found to be toxic and can cause serious problems both contaminating the environment and health abilities and even causing death. Also, new legislation introduced by the EU was designed to regulate and restrict the use of hazardous substances such as lead and mercury after July 2006.[2-6] Due to these health concerns and EU directives,

the amount of research in lead-free piezoelectric ceramics has grown exponentially since 1997, as shown by Figure 1.2.

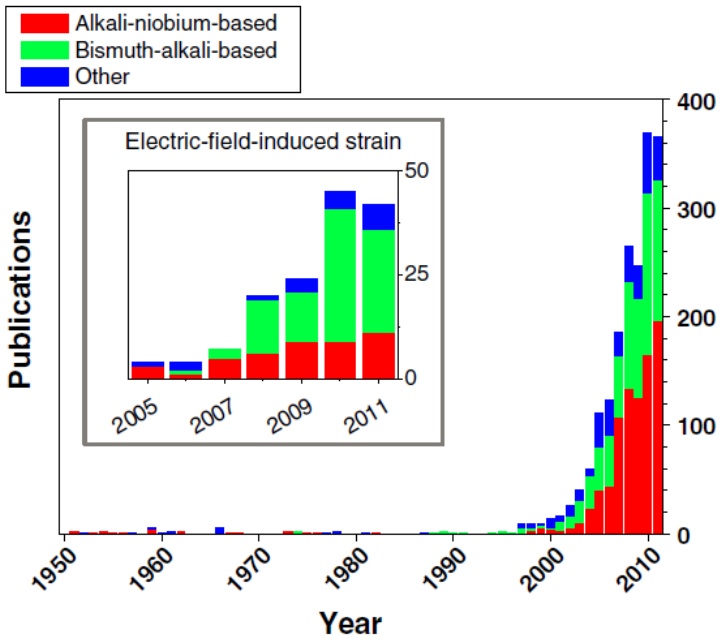

Figure 1.2 The number of publications on lead-free piezoelectric materials in total with on studying electric-field-induced strain as a function of year as an inset.[1]

The development in performance and understanding of lead-free piezoelectric ceramics is reflected by the growing number of publications each year. As we can see from the Figure 1.2, the publications grew dramatically in the last decade and can be mainly divided into three different groups of materials. These are alkali-niobium-based ceramics, represented by potassium sodium niobate (KNN), bismuth-alkali-based ceramics, represented by sodium bismuth titanate (NBT) and 'others', which may include barium titanate and bismuth ferrite-based ceramics. The explosive increase of research into lead-free piezoceramics can be traced back to the discovery of the $Na_{0.5}Bi_{0.5}TiO_3$-$BaTiO_3$ (NBT-BT) system in 1991 when Takenaka[7] first reported the existence of a morphotropic phase boundary (MPB) in this system, which was recognised as a key feature in maximizing the piezoelectric properties. Another example of a superior lead-free piezoceramic based on exploiting the MPB in a KNN-based system was reported by Saito et al in 2004.[8] These two systems have since dominated much of the research on lead-free piezoelectrics. Also, it was recognised that new mechanisms could be

exploited to induce high strain in actuators, such as the reversible electric field-induced phase transformation in NBT-BT-KNN, reported by Rodel.[9]

1.2 Aims and objectives

The main aim of this PhD project is to determine the contributions of phase switching to the behaviour of three lead-free piezoelectric ceramic solid solutions. $Na_{0.5}Bi_{0.5}TiO_3$, one of the typical lead-free relaxor-ferroelectric (RF) piezoelectric materials, was chosen as the majority component, which was then combined with $KNbO_3$, $BaTiO_3$ and $NaNbO_3$ to form binary solid solutions.

Initial research work was carried out on one of the most well-known NBT-based solid solutions, NBT-BT. Many unique structural and electrical properties in the NBT-xBT system have been reported, such as the 'phase diagram' for compositions between x=0 and 0.11, unusual temperature-dependent dielectric properties, the occurrence of constricted ferroelectric hysteresis loops and electric field-induced structural transformations between cubic, rhombohedral and tetragonal phases. [10-12] One objective of the project was to further investigate the contributions made by phase switching and domain switching mechanisms. Synchrotron XRD measurements were performed to determine the crystal structures and preferred orientation due to ferroelectric domain switching. Changes in ferroelectric and dielectric properties as a function of composition and temperature were combined with the results of thermal depolarisation measurements to provide further evidence of the phase transition between relaxor-ferroelectric and long-range ordered ferroelectric phase.

A novel concept was developed in which an irreversible electric field-induced structural transformation and phase transition was found to occur in both NBT-xKN and NBT-xNN systems, in contradiction with the previous literature. This idea was introduced to explain the observation that certain compositions in these systems, which were found by diffraction methods to possess a pseudo-cubic structure, exhibited well-saturated polarisation-electric field (P-E) ferroelectric hysteresis loops. Furthermore, constricted P-E hysteresis loops were also

observed over certain ranges of composition and temperature, indicating that a reversible phase transition occurred between weak-polar RF and long-range ordered ferroelectric (FE) states.

Hence, the main objective of this project is to determine the structures at room temperature as well as structural transformations over a certain temperature range for both NBT-xKN and NBT-xNN specimens in poled and unpoled states by means of *ex-situ* experiments using high-resolution synchrotron x-ray powder diffraction (SXPD). Additionally, further *in-situ* poling experiments were conducted using high-energy synchrotron XRD to determine the mechanism of structural transformation under a cyclic electric field for both NBT-xKN and NBT-xNN ceramics.

Another objective is to combine structural information with the electrical measurements, including temperature-dependent ferroelectric, dielectric and thermal depolarisation measurements, to illustrate the influence of temperature and composition on the stability of different states for NBT-KN, NBT-NN and NBT-BT ceramics.

2 Literature review

This chapter presents the fundamental theory and concepts of atomic structure and electroceramics. Later Sections focus on structural, electrical and mechanical properties of the lead-free piezoelectric materials, which are of most relevance to the present work.

2.1 Crystal structure

2.1.1 Crystal structure

Crystals are built up of regular arrangements of atoms in three dimensions, which are normally represented by a repeated unit called the *unit cell*. The unit cell is defined as the smallest repeating unit to show full symmetry of the crystal structure. In general, there are 7 independent crystal systems in three dimensions, which are listed in Table 2.1 below.[13]

Table 2.1 Different crystal systems with lattice parameters.[13]

Crystal system	Unit cell lattice parameters	Unit cell angles
Cubic	a=b=c	$\alpha=\beta=\gamma=90^o$
Tetragonal	a=b≠c	$\alpha=\beta=\gamma=90^o$
Orthorhombic	a≠b≠c	$\alpha=\beta=\gamma=90^o$
Hexagonal/ Rhombohedral	a=b≠c/ a=b=c	$\alpha=\beta=90^o$, $\gamma=120^o$/a=b=c≠90º
Trigonal	a=b≠c or a≠b≠c	$\alpha=\beta=90^o$,$\gamma=120^o$ or $\alpha=\beta=\gamma\neq90^o$
Monoclinic	a≠b≠c	$\alpha=\gamma=90^o$,$\beta\neq90^o$
Triclinic	a≠b≠c	$\alpha\neq\beta\neq\gamma\neq90^o$

A unit cell having only lattice points at the corner is called the primitive cell, P. Apart from P, some other useful types represent the manner of repetition of atoms, ions or molecules in a crystal. For example, the face centred lattice, F, represents additional lattice points in the centre of each face. The body cantered lattice, I, possesses an extra lattice point at the body center. Therefore, to combine crystal system and lattice type, 14 different types of possible lattices

exist, referred to as *Bravais* lattices, for example a body centred (I) tetragonal structure with a=b≠c and $\alpha=\beta=\gamma=90^{o}$.[13]

A *solid solution* is a crystalline phase that can have variable composition.[13] Normally, if the dopant concentration is above 1%, the system is denoted as a solid solution rather than a *doped* system. Simple solid solutions are divided into two types: substitution solid solutions and interstitial solid solutions. For a substitutional solid solution, the atom or ion directly replaces host atom or ion. On the other hand for an interstitial solid solution, a site that would normally be empty is occupied by an additional ion or atom. Apart from these two types, complex solid solution mechanisms are also found, which involve both substitution and interstitial site occupancy.

2.1.2 Perovskite structure

The perovskite structure, which has great significance in many types of functional ceramics, is a common natural crystalline structure named after calcium titanate, $CaTiO_3$. An ideal perovskite structure has the general formula ABX_3 within a cubic structure. The A-site is occupied by a cation, A, in the cube corner, the B-site is occupied by cation, B, which is in the centre of the cube, and X-site is occupied by anion, typically O, located in the face centre, as shown in Figure 2.1.[14]

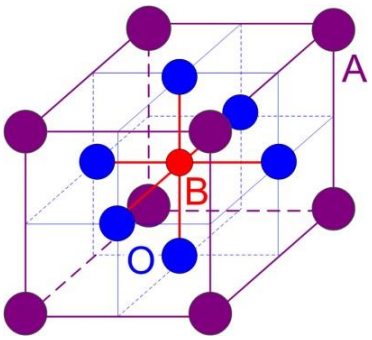

Figure 2.1 Typical perovskite structure showing A-site cation at the corner, B-site cation at the cube centre and O anion at the face centre.[14]

2.1.3 Tolerance factor

The tolerance factor was first introduced by Goldschmidt[15] in 1926 to describe the stabilities of perovskite-type compounds in which different ionic species occupy the lattice sites. The ideal perovskite is defined by the lengths of the bonds between atoms in the unit cell, which are assumed to be equal to the sum of the ionic radii, yielding the relationship shown in Equation 2.1.

$$R_A + R_O = \sqrt{2}(R_B + R_O) \quad (2.1)$$

$R_{A, B, O}$ are the ionic radii of A, B and O ions, respectively. However, not many compounds satisfy this relationship, so it is essential to use the tolerance factor, *t*, to demonstrate the deviation from the ideal cubic perovskite structure, which is given in Equation 2.2 according to Jaffe.[16]

$$t = \frac{R_A + R_O}{\sqrt{2}(R_B + R_O)} \quad (2.2)$$

It is found that those compounds with a t value of 0.80 to 1.06 are usually stable. If the t value is over 1, a tetragonal distortion is preferred while a t value below 1 favours a rhombohedral distortion. Therefore, most morphotropic phase boundaries (MPB) tend to occur for t values between 0.97 and 1.02.[17]

2.1.4 Distortion of perovskite structure

Some distorted perovskite structures are referred to as "pseudo-cubic" due to slight differences in lengths or angle orientations compared to the cubic structure. To specify different kinds of distortion, another equivalent view of the perovskite structure is presented in Figure 2.2 to illustrate the oxygen octahedra; perovskite structures have been categorised by Glazer[18] into three different types:

1. Tilting of anion octahedra
2. Displacement of the cations, two possible displacements being parallel and antiparallel
3. Distortions of the octahedra

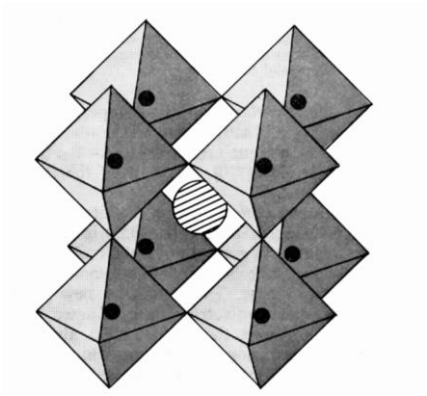

Figure 2.2 B-site cornered octahedral unit cell.[19]

2.1.5 Octahedral tilting

Octahedral tilting is the most important factor in the distortion of perovskite structures. When an octahedral tilt occurs in a perovskite structure, it will cause some octahedral tilt of the neighbouring octahedron. Glazer[18] proposed a methodology to classify different distortions according to unit-cell lengths and angle orientations. If the angle of tilt about the pseudo-cubic [100], [010] and [001] directions is denoted by α, β and γ, then the new length of the pseudo-cubic (p) unit cell will be

$$a_p = a_o \cos\beta \cos\gamma$$

$$b_p = a_o \cos\alpha \cos\gamma \qquad (2.3)$$

$$c_p = a_o \cos\alpha \cos\beta$$

In the three-dimension tilt system, equality of tilt magnitudes is identified by using the same letters. Thus, tilts along different axes are specified as $a_p=b_p\neq c_p$ for aaa, $a_p=b_p=c_p$ for aaa and $a_p\neq b_p\neq c_p$ for abc.

For the unit cell angle, there are basically two types of tilt. If tilts occur along the three axes, it is denoted as in-phase tilted with superscript "+", or anti-phase tilted with superscript "-", or no tilts with "0". For example, $a^0a^0c^+$ indicates that there are no tilts along the a and b axes but an in-phase tilt with different magnitude along the c axis. Glazer[18] has worked out 23 possible tilt systems, as illustrated in Table 2.2.

Table 2.2 Full list of simple tilt systems.[19]

Serial number	Symbol	Lattice centring	Multiple cell	Relative pseudocubic subcell parameters	Space group
Three-tilt systems					
(1)	$a^+b^+c^+$	*I*	$2a_p \times 2b_p \times 2c_p$	$a_p \neq b_p \neq c_p$	*Immm* (No. 71)
(2)	$a^+b^+b^+$	*I*		$a_p \neq b_p = c_p$	*Immm* (No. 71)
(3)	$a^+a^+a^+$	*I*		$a_p = b_p = c_p$	*Im*$\bar{3}$ (No. 204)
(4)	$a^+b^+c^-$	*P*		$a_p \neq b_p \neq c_p$	*Pmmn* (No. 59)
(5)	$a^+a^+c^-$	*P*		$a_p = b_p \neq c_p$	*Pmmn* (No. 59)
(6)	$a^+b^+b^-$	*P*		$a_p \neq b_p = c_p$	*Pmmn* (No. 59)
(7)	$a^+a^+a^-$	*P*		$a_p = b_p = c_p$	*Pmmn* (No. 59)
(8)	$a^+b^-c^-$	*A*		$a_p \neq b_p \neq c_p$ $\alpha \neq 90°$	$A2_1/m11$ (No. 11)
(9)	$a^+a^-c^-$	*A*		$a_p = b_p \neq c_p$ $\alpha \neq 90°$	$A2_1/m11$ (No. 11)
(10)	$a^+b^-b^-$	*A*		$a_p \neq b_p = c_p$ $\alpha \neq 90°$	*Pmnb* (No. 62)*†
(11)	$a^+a^-a^-$	*A*		$a_p = b_p = c_p$ $\alpha \neq 90°$	*Pmnb* (No. 62)*†
(12)	$a^-b^-c^-$	*F*		$a_p \neq b_p \neq c_p$ $\alpha \neq \beta \neq \gamma \neq 90°$	$F\bar{1}$ (No. 2)
(13)	$a^-b^-b^-$	*F*		$a_p \neq b_p = c_p$ $\alpha \neq \beta \neq \gamma \neq 90°$	$I2/a$ (No. 15)*
(14)	$a^-a^-a^-$	*F*		$a_p = b_p = c_p$ $\alpha = \beta = \gamma \neq 90°$	$R\bar{3}c$ (No. 167)
Two-tilt systems					
(15)	$a^0b^+c^+$	*I*	$2a_p \times 2b_p \times 2c_p$	$a_p < b_p \neq c_p$	*Immm* (No. 71)
(16)	$a^0b^+b^+$	*I*		$a_p < b_p = c_p$	*I*4/*mmm* (No. 139)†
(17)	$a^0b^+c^-$	*B*		$a_p < b_p \neq c_p$	*Bmmb* (No. 63)
(18)	$a^0b^+b^-$	*B*		$a_p < b_p = c_p$	*Bmmb* (No. 63)
(19)	$a^0b^-c^-$	*F*		$a_p < b_p \neq c_p$ $\alpha \neq 90°$	*F*2/*m*11 (No. 12)
(20)	$a^0b^-b^-$	*F*		$a_p < b_p = c_p$ $\alpha \neq 90°$	*Imcm* (No. 74)*
One-tilt systems					
(21)	$a^0a^0c^+$	*C*	$2a_p \times 2b_p \times c_p$	$a_p = b_p < c_p$	*C*4/*mmb* (No. 127)
(22)	$a^0a^0c^-$	*F*	$2a_p \times 2b_p \times 2c_p$	$a_p = b_p < c_p$	*F*4/*mmc* (No. 140)
Zero-tilt system					
(23)	$a^0a^0a^0$	*P*	$a_p \times b_p \times c_p$	$a_p = b_p = c_p$	*Pm*$\bar{3}$*m* (No. 221)

For example, due to its octahedral tilt and cation displacement, both the Pbcm phase and a "new" $P2_1ma$ phase were reported to coexist in the $NaNbO_3$ crystal (Figure 2.3), which was determined using synchrotron XRD at the Diamond light source.[20]

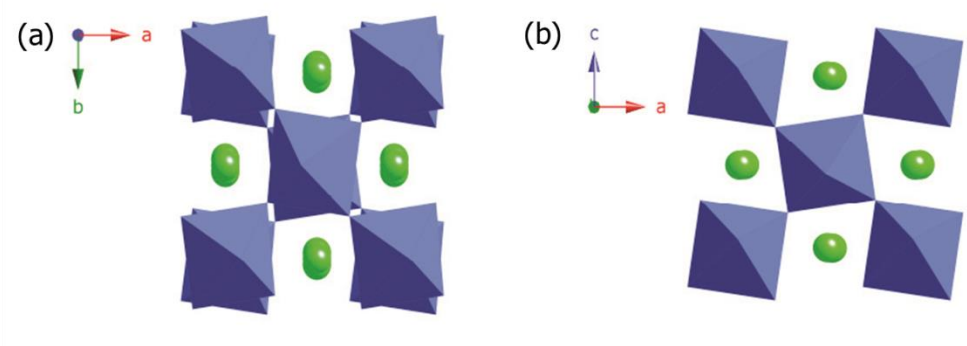

Figure 2.3 The two polymorphs of $NaNbO_3$, showing the differing 'tilt' systems, and cation displacement modes: (a) the well-known Pbcm phase (b) the 'new' $P2_1ma$ phase.[20]

2.2 Electroceramics

The evolution of ceramics took place over several centuries until the first use of ceramics in the electrical industry took advantage of their stability when exposed to extremes of weather or high electrical resistivity around the 1900s.[14] Following this, the properties of electroceramics have been exploited in a wide range of applications and are the focus of much active research.

2.2.1 Dielectrics

Ideally, a dielectric material has zero electric conductivity and is considered as an insulator. During application of an external electric field across a dielectric material, polarisation is generated due to the occurrence of dipole moments.[14] There are four different mechanism of polarisation existing in the material, including atomic, ionic, dipolar and space charge or diffusional, as presented in Figure 2.4.

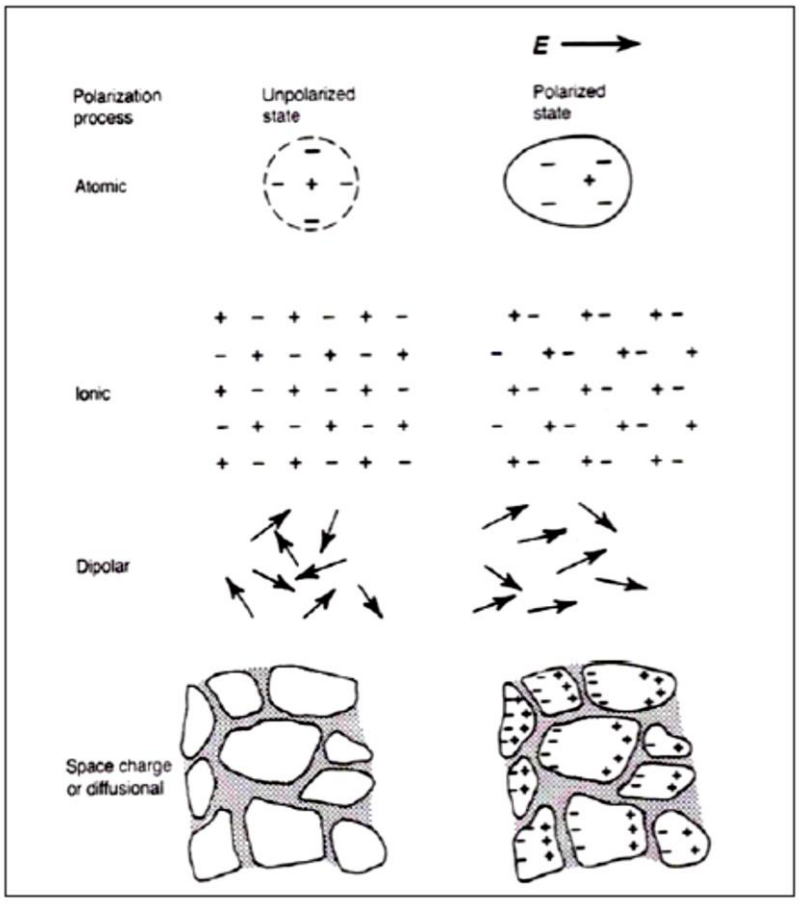

Figure 2.4 The four mechanisms of polarisation.[14]

Furthermore, the amount of polarisation, P, is defined as the dipole moment per unit volume of a material which, for a linear dielectric, is proportional to the external electric field, E, as illustrated in Equation 2.4.[14]

$$P=\chi\varepsilon_0 E \tag{2.4}$$

Where the χ is dielectric susceptibility and ε_0 is the permittivity of free space with a value of $8.854\text{x}10^{-12}$ F m^{-1}.

2.2.1.1 Relative permittivity

In dielectrics, the permittivity, ε, is used to describe a material that can support an electrostatic field and quantify the amount of induced polarisation. The relative permittivity, ε_r, is relative to the permittivity of free space, ε_0, as shown in Equation 2.5.

$$\varepsilon_r = \frac{\varepsilon}{\varepsilon_0} \tag{2.5}$$

2.2.1.2 Dielectric loss

If a sinusoidal voltage is applied to an ideal dielectric, the current (I) is 90º out of phase with the voltage (V), as illustrated in Figure 2.5(a). Specifically, the capacitor is charged by the voltage and current drops to zero during the first-half cycle. Then, the voltage decreases to zero as the charge releases as the current during second-half cycle.[14]

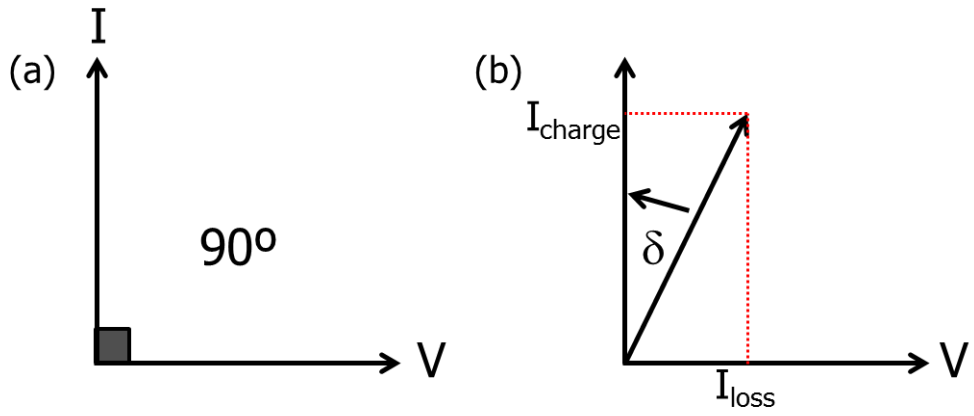

Figure 2.5 The illustration of (a) Ideal dielectrics and (b) Real dielectrics with a dielectric loss.[14]

However, the current and voltage cannot reach the maximum and minimum at the same time under application of external electric field for the real dielectrics. Hence, the angle between voltage and current is not at 90º and the relationship between V and I is exhibited in Figure 2.5(b). The current can be split into two parts, I_{charge} and I_{loss}, described as real, ε', and imaginary, ε'', parts respectively.[14] Therefore, the dielectric loss can be defined as the ratio between real and imaginary permittivity, as indicated in Equation 2.6.[14]

$$tan\delta = \frac{I_{loss}}{I_{charge}} = \frac{\varepsilon''}{\varepsilon'} \tag{2.6}$$

2.2.2 Piezoelectricity

All materials undergo small changes in dimensions in response to an electric field, with the corresponding strain being proportional to the square of the field, which is defined as the *electrostrictive effect*. In contrast, some solids exhibit a linear strain-electric field relation, which is referred to as the *converse piezoelectric effect*. Piezoelectric solids also display the *direct piezoelectric effect*, which means that the material is able to create a change in polarisation under an applied stress.[14]

As illustrated in Figure 2.6, if a piezoelectric plate, which has conductive electrodes applied to the top and bottom faces, is polarized in the direction indicated by P, a compressive stress causes a transient current to flow in the circuit, while a tensile stress causes one in opposite direction. Similarly, if an electric field is applied to the material, it will induce a compressive strain; reversal of the electric field will cause a tensile strain. This is the mechanism of the piezoelectric effect.[14]

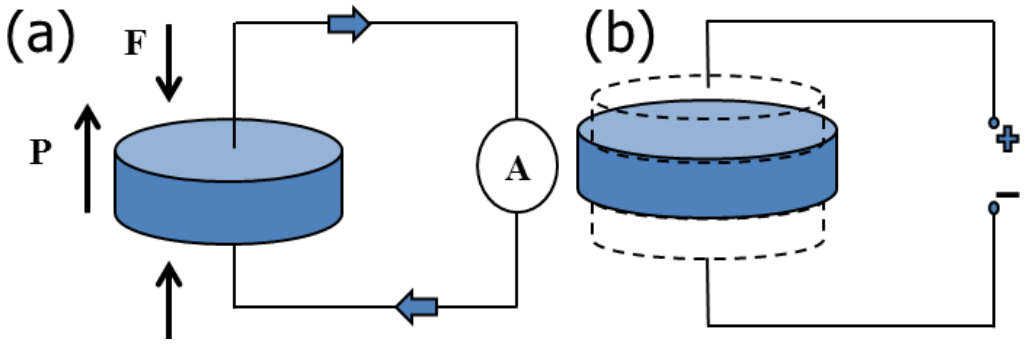

Figure 2.6 The direct piezoelectric effects and the indirect piezoelectric effects.[14]

In terms of crystal structures, 11 of the 32 crystal classes show a centre of symmetry and are denoted "non-polar", which means that they will experience a symmetric ionic displacement under an applied stress with no change in dipole moment. The other 21 crystal classes are non-centrosymmetric and are denoted "polar" structures. 20 of these show the piezoelectric effect.[14]

For piezoelectric materials, changes in polarisation can be induced by both electric field and mechanical stress. The linear relationship between stress, X_{ik}, and resulting charge density, D_i, is known as the direct piezoelectric effect and is written as[21]

$$D_i = d_{ijk} X_{jk} \tag{2.7}$$

The converse piezoelectric effect describes the strain that is developed in a piezoelectric material due to the applied electric field, which was defined as[21]

$$x_{ij} = d_{kij} E_k \tag{2.8}$$

Several different parameters are used to describe the piezoelectric properties of poled ferroelectric ceramics. Conventionally, the poling direction is defined as the 3-axis, as illustrated in Figure 2.7. For example, d_{31} is the coefficient relating the electric field applied along the polar axis to the axial strain developed perpendicular to it. d_{33} is the corresponding coefficient for both axial strain and field along the polar axis, which is the most common coefficient used for comparing the piezoelectric activity of different materials.[14]

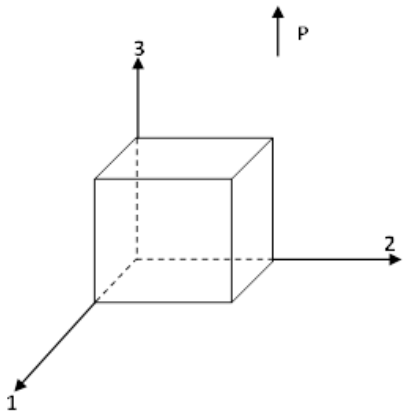

Figure 2.7 labelling of reference axes and planes for piezoceramics.[14]

2.2.3 Electro-mechanical coupling

Another important parameter of a piezoelectric material is the effective electromechanical coupling coefficient k_{eff}, which is defined as follows.[14]

$$k_{eff}^2 = \frac{\text{Mechanical energy converted to electric energy}}{\text{Input mechanical energy}} \tag{2.9}$$

$$k_{eff}^2 = \frac{\text{Electrical energy converted to mechanical energy}}{\text{Input electrical energy}} \tag{2.10}$$

k_{eff}^2 measures the conversion ratio of electrical and mechanical energies; it is a dimensionless parameter that is always less than 1. A common specimen geometry is a thin circular disk, which is electroded on both surfaces and then poled in a direction perpendicular to the surfaces. In this case, the piezoelectric effect across the thickness of the pellet and the simultaneous mechanical actions in the x- and y-axis directions is regarded as the radial coupling or radial vibration, known as the *planar coupling coefficient*, k_p. It can be determined using the following relationship.[14]

$$\frac{k_p^2}{1-k_p^2} = f(J_0, J_1, \nu \frac{f_p - f_s}{f_s}) \tag{2.11}$$

J_0 and J_1 are *Bessel* functions, ν is *Poisson's* ratio, f_s is the resonant frequency at which the series arm has zero reactance and f_p is the frequency when the resistive component is a maximum.

2.2.4 Ferroelectricity

A ferroelectric (FE) is a material that exhibits a spontaneous electric polarisation that is capable of being reversed or reoriented by an applied electric field over a certain range of temperature. Polarisation, P, is the key feature of ferroelectricity. Polarisation is related to electric displacement D through the linear expression, as displayed in Equation 2.12.[14] For materials belonging to non-polar crystal classes the polar state can be induced by an applied electric field, while poled ferroelectrics possess non-zero remanent polarisation even in the absence of an applied field.

$$D_i = P_i + \varepsilon_0 E_i \tag{2.12}$$

Note that D_i and P_i are, in general, nonlinear and hysteretic functions of E, although linear or near-linear behaviour is observed for many dielectrics.

The different possible orientations of P in a ferroelectric crystal are defined as orientation states. Normally a ferroelectric crystal has two or more orientation states under an applied electric field and also it can be switched from one to another in response to different orientations of a sufficiently high electric field. A spontaneous polarisation P is a fundamental property of all pyroelectric crystals and it is reversible or reorientable only in ferroelectric materials. The spontaneous polarisation is defined as the magnitude of the polarisation within a single ferroelectric domain in the absence of an external electric field.

2.2.5 Domain structure

Ferroelectric domains are another key feature of FE materials; a domain is a region of ferroelectric crystal that shows homogeneous and uniform spontaneous polarisation, as presented in Figure 2.8.[14] In terms of energy, a single domain is the most energetically favourable structure in a crystal due to the additional strain energy associated with the domain walls; this is counter-balanced by the energy associated with the depolarisation field. The formation of a domain wall is affected by either electric field or mechanical stresses, which could be due to

both internal and external effects.

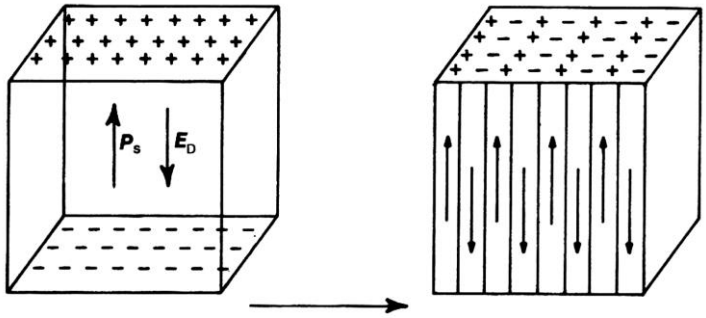

Figure 2.8 The initial surface charges in a material when spontaneously polarized (right) and how energy is preserved through 180° domains (left).[14]

For the case illustrated in Figure 2.8, the 180° domain structure exhibits two opposite directions after the application of an electric field. The boundaries between two different domain variants are called domain walls, which have a typical width of 1-10 nm. The size of the domains depends on the interaction of electric and elastic energies, which is particularly important when switching from the paraelectric to the ferroelectric state in a polycrystalline ceramic.[14]

Furthermore, in polycrystalline materials, each grain can contain many differently-oriented domains. Apart from 180º domains, there are also non-180º domains that are created as a result of mechanical stress in order to minimize elastic energy.[14] For example, in tetragonally-distorted perovskites, there are 90º domain walls, as shown in Figure 2.9. It has been reported that both 180º and non-180º domains result in local electric fields and mechanical stresses.[14]

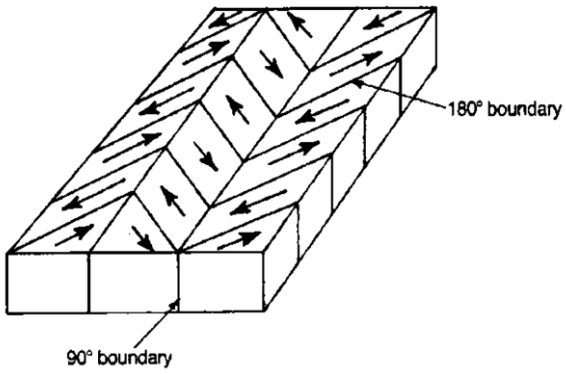

Figure 2.9 Schematic diagrams showing (a) how a polycrystalline ferroelectric material splits into 90º and 180º domains.[14]

To illustrate how an external electric field changes the domain structure, a P-E loop is shown schematically in Figure 2.10, as reported by Gauckler.[22] Beginning at the initial state (Ⅰ), the domain structures are aligned randomly with zero average polarisation. With small signal of electric field, the polarisation increases linearly after reaching the materials' threshold field.[23] This small amount of polarisation is actually partially reversible but irreversible switching occurs if the electric field is further increased, causing nonlinear behaviour (II) until reaching the maximum polarisation (III), where all domains align along the same direction as that of the electric field. This process is called the poling effect and results in a material's poled state.

When the electric field decreases to zero, the polarisation partially switches back to the original direction due to local stress and a remanent polarisation, P_{rem}, remains at zero-field (IV). As the electric field reverses, a reversal of 180º domains is created, leading to a reduction in polarisation. A further increase of negative field causes an increase in the proportion of reversed domains, which act to neutralize the positively oriented domains, yielding an average polarisation of zero on reaching the coercive field (E_c) at (V). When the electric field reaches its maximum negative value (VI), all domains experience 180º domain switching to the negative orientation. The hysteresis loop is formed when the electric field goes back to zero again, leaving a negative remanent polarisation.

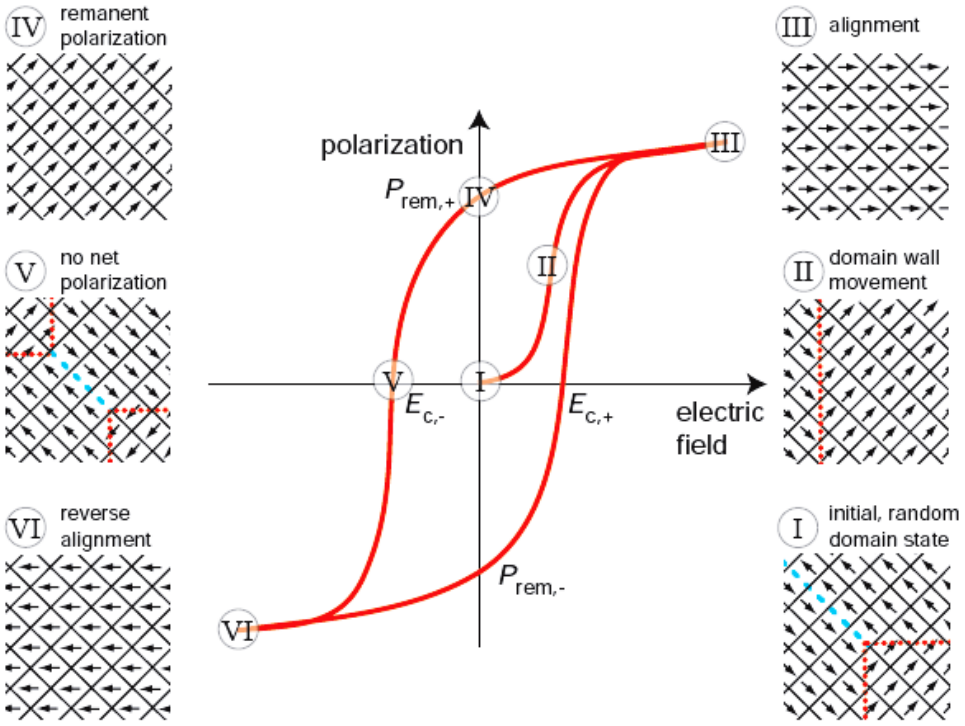

Figure 2.10 Ferroelectric polarisation-electric field hysteresis loop.[22]

2.2.6 Curie-Weiss behaviour

The ferroelectric Curie point, T_c can be understood in terms of the temperature at which a ferroelectric material undergoes a structural phase transition to a state where the spontaneous polarisation vanishes. Above T_c, the material transforms to the paraelectric phase with the permittivity exhibiting Curie-Weiss behaviour (Equation 2.13).[14]

$$\chi = C / (T - T_c) \qquad (2.13)$$

χ=dielectric susceptibility

C = Curie constant

T = Absolute temperature in K

T_c = Curie-Weiss temperature in K

A paraelectric phase always has a higher crystallographic symmetry and is obtained at high temperature from ferroelectric states. It is usually non-polar which means that a remanent polarisation is not obtained after applying an

electric field. Therefore, above T_c the material behaves as a linear dielectric and the P-E relationship takes the form a straight line instead of a hysteresis loop.[24]

2.2.7 Relaxor ferroelectrics

Relaxor ferroelectric (RF) materials are similar in many ways to conventional ferroelectric (FE) materials, but exhibit some unique structural and functional properties. There are two distinct types of crystal structure in RF, the perovskite structure and the tungsten bronze structure. In terms of perovskite structure, either the A-site or B-site is shared by more than one element such as the B-site complex perovskite, $Pb(Mg_{1/3}Nb_{2/3})O_3$.[25] In terms of lead-free perovskites, the first RF systems reported were based on $BaTiO_3$, for example $BaTiO_3$-$BaSnO_3$.[26]

Comparing RFs with conventional FEs, slim polarisation-electric field (P-E) hysteresis loops with little remanent polarisation are observed instead of a saturated P-E loop, as shown in Figure 2.11.

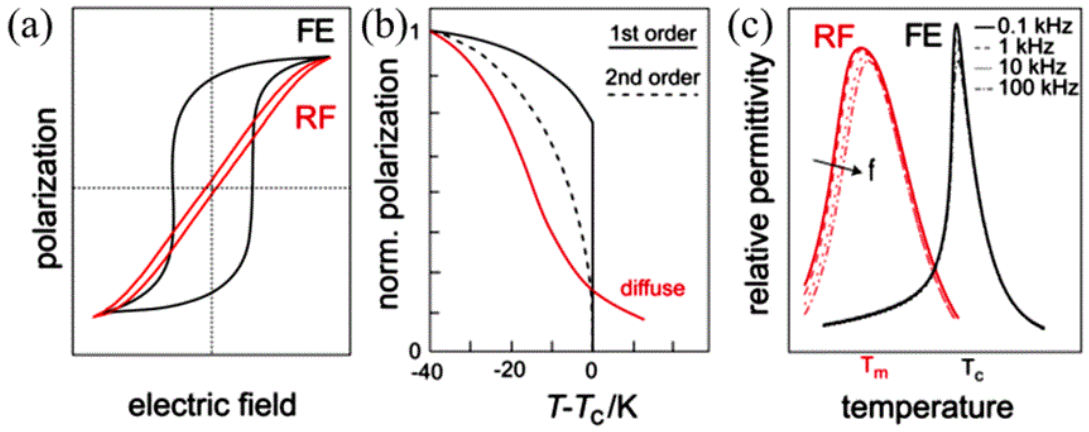

Figure 2.11 Comparison of FE and RF behaviour (a) P-E loop (b) non Curie-Weiss law (c) Temperature-dependent relative permittivity.[27]

Also, the typical characteristic features of RFs are the frequency dispersion in the ε_r-T relationship and high electric field-induced strain, often attributed to the electrostrictive effect.[28] In contrast to conventional ferroelectric behaviour, the peak in permittivity is not directly correlated with a distinct structural transition and it does not obey Curie-Weiss law for all $T>T_m$.

Moreover, the existence of order-disorder and polar nano-regions (PNRs) in RFs is another important feature to establish the mechanisms that contribute to the electrical properties. A RF can be categorised according to two states that indicate the weakness and mobility of the dipoles within PNRs; the ergodic RF state and non-ergodic RF state. In a RF, the term *ergodic* means that the polarisation state returns to its initial value after responding to an external excitation due to the mobility of the PNRs. On the other hand, a *nonergodic* RF state can retain the influence of the external excitation.[29]

The type of ergodicity in a RF depends on the external excitation, including electric field, temperature and mechanical load. For example, the electric field-induced metastable FE order can be either stable or unstable after removal of the electric field. This behaviour is dependent on the nature of the PNRs, which are lower-symmetry structural regions embedded in a higher-symmetry matrix and difficult to identify by conventional characterization techniques due to their nano-sized structures.

In recent publications, advanced techniques such as TEM, atomic pair distribution function (PDF) and extended x-ray absorption fine structure (EXAFS) analysis using synchrotron high-energy x-ray diffraction have been employed to identify the structure of PNRs on a local scale.[30-32] For example, an in-situ experiment on NBT-BT using TEM was used to directly visualise the transformation from PNRs into a ferroelectric micro-domain structure under an electric field.[33-35]

An indirect method to identify the reversible transition between PNRs and the long-range ordered FE phase was reported by Viola[36]; this involved the observation of constricted P-E loops and associated splitting of the polarisation switching peaks in the current density-electric field curves (J-E). For an ergodic RF, the net average polarisation is zero when the applied electric field is removed, which explains the formation of a constricted P-E loop. However, each individual PNR has a finite polarisation at any instant so that $P_i^2 \neq 0$; this gives rise to other functional properties such as electrostriction and quadratic electro-optic

effects.[37]

The intrinsic mechanisms in RFs are complex and still not fully understood in many cases. Many mechanisms have been reported such as the random field model,[37, 38] superparaelectric model,[39] and phase transition model.[40] However, the two most widely accepted and useful mechanisms in RFs are order-disorder and the existence of PNRs.

Normally the RF materials with a perovskite structure have chemical formula $A_{1/2}A_{1/2}BO_3$ or $AB_{1/2}B_{1/2}O_3$. Differences in both charge and ionic radii can cause disorder symmetry and RF behaviour. In some materials, like $Pb(Sc_{1/2}Nb_{1/2})O_3$ (PST)[41, 42] at 1500 K, these disordered regions are capable to be transformed into an ordered structure by thermal motion and the time to diffuse two different ions into one position is called the relaxation time.[27, 43]

2.2.8 Energy storage capacitors

Ceramic capacitors are expected to play a key role in the next generation of power generation systems and power electronics. Polymeric materials such as polypropylene are regarded as an excellent choice for capacitors due to their high breakdown fields and very low dielectric loss.[44, 45] However, in many important demanding environments such as aerospace, military and automobile, the operating temperature ranges of polymers cannot match the requirements. With higher melting temperatures and more temperature-stable properties than those of polymeric materials, ceramics can also exhibit higher dielectric permittivity and, with advanced processing methods, a high breakdown field to achieve higher energy densities.[46-52]

Normally, typical ferroelectric ceramics exhibit a square polarisation hysteresis loop under high electric fields; this gives rise to a relatively low energy storage density and low energy conversion efficiency. The energy conversion efficiency is the ratio calculated by the discharged energy density and the consumed energy density, as represented by areas 1 and 2 in Figure 2.12. Therefore, conventional

ferroelectrics are not considered to be strong candidates for energy storage capacitors.

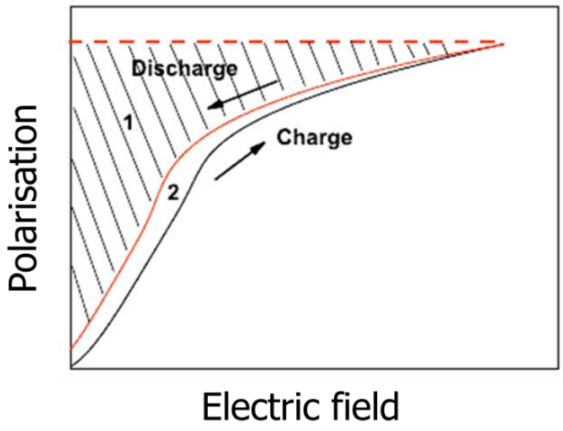

Figure 2.12 The illustration of calculation of the energy conversion efficiency by ferroelectric hysteresis P-E loop.[53]

On the other hand, relaxor ferroelectric materials tend to exhibit both high maximum polarisation and a slim hysteresis loop, leading to high energy density and efficiency. For example, it was reported recently that a constricted P-E loop was obtained by adding $SrTiO_3$ (ST) into NBT, as presented in Figure 2.13. [52]

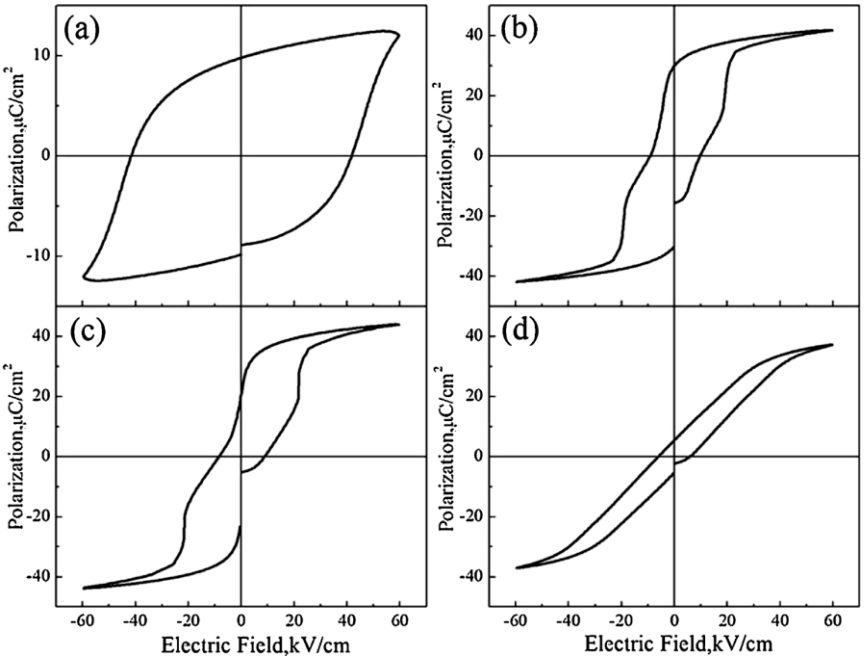

Figure 2.13 The ferroelectric hysteresis P-E loop for (1-x) NBT-xST system with (a) x=0.10 (b) x=0.25 (c) x=0.26 (d) x=0.30 at room temperature. [52]

Furthermore, it has been found that some lead-free relaxor ferroelectrics display constricted P-E hysteresis loops over a certain temperature range, which enhances the energy storage properties. For example, the temperature-dependent ferroelectric hysteresis P-E loops for NBT-0.08BT and NBT-0.08BT-0.10BiMg$_{0.5}$Ti$_{0.5}$O$_3$ (BMT) ceramics are displayed in Figure 2.14. A square-shape loop was observed for NBT-0.08BT at room temperature. However, a constricted P-E loop was obtained at elevated temperature due to the reversible transition between the polar FE state and weak-polar PNRs. On the other hand, adding BMT into the NBT-BT solid solution increased the compositional disorder, resulting in slim P-E loops for all temperatures. [53]

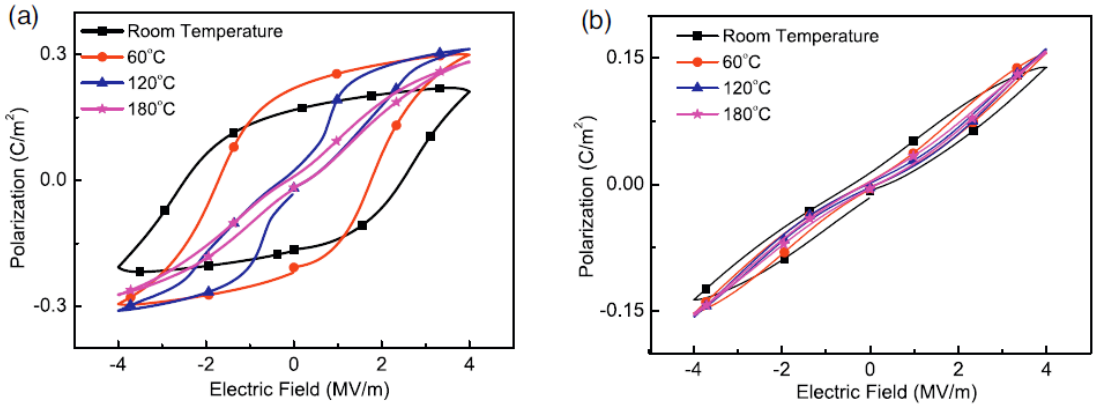

Figure 2.14 The temperature-dependent ferroelectric hysteresis P-E loop for (a) NBT-0.08BT and (b) NBT-0.08BT-0.10BMT. [53]

Several different materials have been evaluated with respect to their optimum energy density, as illustrated in Table 2.3.

Table 2.3 Comparison of energy density for different relaxor ferroelectrics.

Composition	E / kV mm^{-1}	Energy density / J cm^{-3}	Author
NBT-BT-0.05NN	6	0.524	Viola[36]
NBT-0.30ST	6.5	0.65	Cao[54]
NBT-BT-0.01KNN	5	0.598	Chandrasekhar[55]
NBT-BT-0.10KNN	5	0.424	Gao[56]
NBT-0.10KN	10.4	1.17	Luo[57]
NBT-0.08BT	13.5	0.88	Chen[53]

2.3 Morphotropic phase boundary

A morphotropic phase boundary (MPB) is defined as a specific composition in a solid solution between two different crystal structures at which a structural phase transformation occurs.[58] This term was first used to indicate the boundary between tetragonal and rhombohedral symmetry in ferroelectric lead zirconate-lead titanate (PZT) solid solutions in 1954.[59] The abrupt change in crystal structure at the MPB leads to an enhancement of polarisability between the two possible phases, giving more potential directions for domains to re-orientate during poling. The improvement of both intrinsic and extrinsic polarisation mechanisms in the vicinity of the MPB yields superior dielectric and piezoelectric properties, as illustrated in Figure 2.15. Normally the MPB is located at a specific composition ratio in a binary solid solution system, such as PZT at a Zr/Ti ratio of 52:48[60] and KNN at a K/Na ratio of 50:50.[61] However, some binary solid solutions possess a mixed-phase region that extends across a range of compositions. For example, a mixed-phase region of rhombohedral and tetragonal phases was identified within the composition ranging from x value of 0.06 to 0.11 in the (1-x)NBT-xBT system.[10, 14]

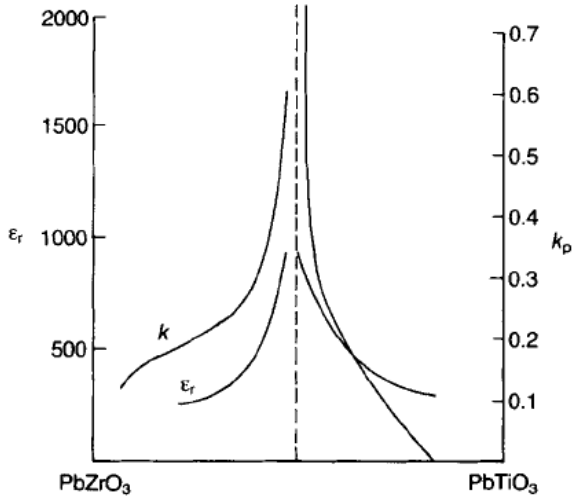

Figure 2.15 Coupling coefficient k_p and permittivity ε_r value across the PZT composition range.[62]

2.4 Structural transformations

2.4.1 Temperature-induced structural transformations

$BaTiO_3$ was the first ceramic material in which ferroelectric behaviour was observed and serves as an ideal model for demonstrating the structural transformations in perovskites. The centro-symmetric unit cell of $BaTiO_3$ is cubic and analogous to that of the perovskite ($CaTiO_3$) structure. The *Curie point*, T_c, denotes the temperature at which the non-polar paraelectric phase transforms into the polar ferroelectric phase. Above T_c, which is about 130 ºC, the unit cell is cubic with the ions arranged as shown in Figure 2.16.

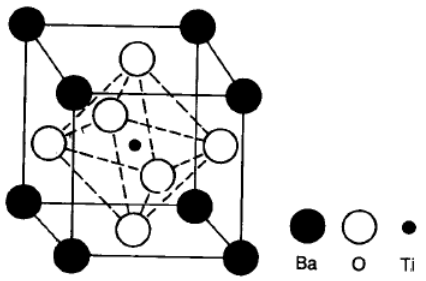

Figure 2.16 The unit cell of $BaTiO_3$.[14]

Below T_c, the structure is slightly distorted to tetragonal with elongation along the c-direction. Other transformations occur at temperatures close to 0 ºC and

-80 ºC which involves transformations firstly to orthorhombic, with the polar axis parallel to a face diagonal, and finally rhombohedral, with the polar axis along a body diagonal, respectively. The transformation is illustrated in Figure 2.17 below, which also shows the corresponding changes in lattice parameters and spontaneous polarisation.[14]

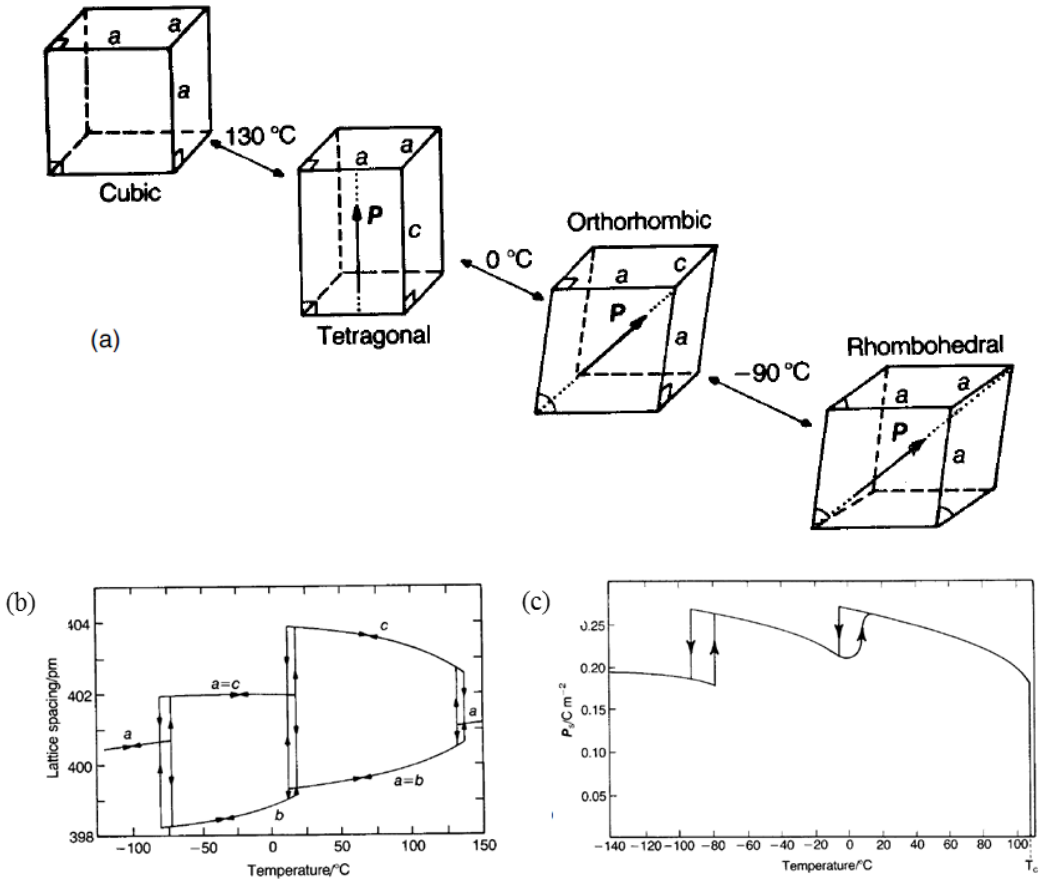

Figure 2.17 Structural transformations in single-crystal $BaTiO_3$ (a) Unit-cell distortions of the polymorphs, (b) Lattice dimensions versus temperature and (c) Spontaneous polarisation versus temperature.[14]

When the material undergoes thermally-induced changes in crystal structure from cubic to rhombohedral, it also experiences more subtle changes inside the unit cell in the form of ion displacements. Taking the transformation from cubic to tetragonal as an example, the polarisation might is coupled from one unit cell to another. By analysing XRD results, it is found that the ions are slightly displaced relative to the four central oxygen ions, as illustrated in Figure 2.18. If the central Ti^{4+} ion is closer to one of the O^{2-} ions, marked as A, the Ti^{4+} ion on the opposite side of A will prefer to be displaced further away from that O^{2-} ion due to energy

minimisation, which results in the same displacement direction for all Ti^{4+} ions in a particular column.[14]

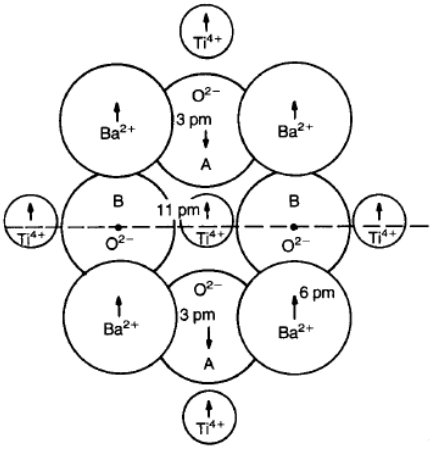

Figure 2.18 Ion displacements in the cubic-tetragonal distortion in $BaTiO_3$.[14]

2.4.2 Electric field-induced structural transformations

It has been found that most ferroelectric materials are very sensitive to external excitement, such as electric field and hydrostatic pressure. It was reported firstly by Berlincourt that the phases can be transform under electric field for modified PZT.[63, 64] This kind of behaviour provides the excellent property of electric field-induced strain, which used in application of actuators.[65]

For lead-free piezoelectrics, some of the NBT-based materials were identified as pseudo-cubic structure by x-ray diffraction, which is attributed to unstable randomly-oriented PNRs. Surprisingly, some of the PNRs are able to transform into a ferroelectric domain structure and retain the domain structure after removal of the external field, which indicates a non-ergodic RF.[29] At the same time, the pseudo-cubic structure was transformed into a different structure under external excitation. For example, an electric field-induced pseudo-cubic to tetragonal structural transformation was found in NBT-7BT under an electric field of 7 kV mm^{-1} using high-energy synchrotron x-ray diffraction.[12] The ceramic was observed to possess a strong preferred orientation of ferroelectric domains, giving rise to significant differences in the relative intensities of diffraction peaks

as a function of grain orientation, as presented in Figure 2.19. A transformation from single-phase tetragonal structure to a mixed-phase of rhombohedral and tetragonal structure was observed in 0.8NBT-0.2$K_{0.5}B_{0.5}TiO_3$ under 7 kV mm^{-1}, as reported by Royles.[66] Structural transformations of this nature, but with different character, are reported within the present work.[67]′[68]

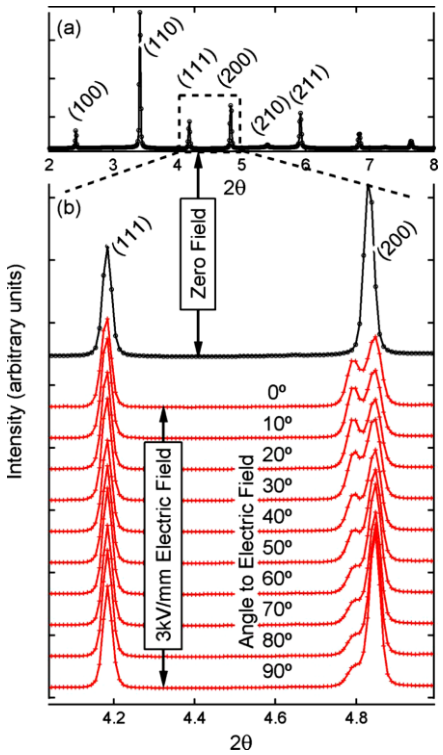

Figure 2.19 The crystallographic texture effect for poled NBT-0.07BT ceramics.[12]

Apart from x-ray diffraction, other characterisation techniques such as TEM and PFM can be used to visualise changes in the appearance of PNRs due to field-induced phase transformations *in-situ*. For example, observations on NBT-0.06BT were made using TEM to identify localised structural transformations in response to applied electric field.[34] Single grains with pure P4bm nanodomains were found to coalesce and transform into wedge-shaped and lamellar shape domains under the electric field, indicating that a structural transformation from single-phase P3bm to mixed-phase R3c/P4mm was induced. Also, it was noted that these transitions were irreversible under electric field poling.[69, 70]

2.4.3 Pressure-induced structural transformations

The idea of the pressure-induced structural transformation was firstly reported by Berlincourt in PbNb(Zr, Ti, Sn)O_3 ceramics. It was found that it took a pressure value of 2.8 x 10^7 N m^{-2} to induce the transition between ferroelectric and anti-ferroelectric states, yielding a volume difference of 0.42%.[64] Direct evidence for the ferroelectric to anti-ferroelectric transformation in PZT 95/5 ceramics under hydrostatic pressure was obtained using neutron diffraction, as reported by Hall.[71]

2.5 Phase transitions in relaxor ferroelectrics

In terms of phase transitions in NBT-based binary systems, it is not possible to define a conventional Curie temperature, T_c, due to the RF nature of the materials. Instead, a frequency-dependent maximum in the ε_r-T relationship, T_m, is used to indicate the progressive transformation from a conventional long-range ordered FE to a nano-polar RF state and finally a paraelectric (PE) state on heating. Furthermore, the loss of remanent polarisation and the associated degradation of the piezoelectric and ferroelectric properties provide an additional depolarisation temperature, T_d, which is usually found to be much lower than T_m. The latter transformation also creates an additional anomaly in the loss tangent-temperature curve of a poled specimen, which is referred to as the FE to RF transition temperature, T_{F-R}.[72, 73] Additionally, it was reported by Jo[74] that this phase transition consisted of two stages. The FE domains first lose their preferred orientation, then the randomly-oriented ferroelectric domains dissociate into PNRs with further increasing temperature.

2.6 Defects and fatigue

In real ferroelectric materials, the properties are strongly influenced by the microstructure, defect structure, external fields and domain wall displacement. These factors may not provide positive contributions to the functional properties, including spontaneous polarisation and domain switching, but also cause some

serious problems in some cases both for thin film and bulk materials. Therefore, the occurrence and influence of defects is a key factor in research on ferroelectric ceramics.

Ferroelectric fatigue is defined as the loss of the switchable remnant polarisation in a ferroelectric material as a function of the number of bipolar switching cycles.[14] The fatigue behaviour in NBT-BT-KNN under bipolar and unipolar cycling has been reported.[75] Both polarisation and strain drop dramatically after 10^4 and 10^7 bipolar cycles, resulting in a decrease of d_{33}. Both bulk and thin-film materials are susceptible to ferroelectric fatigue. Based on the experiments, two types of fatigue mechanisms were identified. The first mechanism is related to micro-cracking, which was found to result in a field-induced phase transformation. The micro-cracking accumulates during large grain deformation under electric field and it is not reversible. The second mechanism is attributed to domain-wall pinning by space charges or injected charges. This type of fatigue was affected strongly by temperature. Most of the fatigue in bulk materials depends on the electrode materials and deposition method, surface treatment, porosity and grain size.[76]

Point defects occur in a crystal lattice where an atom is missing or replaced by another atom. Normally, point detects include vacancies, self-interstitial atoms, impurities and substitutional atoms. In terms of ferroelectric perovskites, oxygen vacancies are the most common type of point defects; these oxygen vacancies can be influenced by an external electric field, stress or temperature and also contribute to ferroelectric fatigue.[76]

2.7 Lead-based piezoelectric ceramics

The first piezoelectric ceramic developed commercially was $BaTiO_3$, but the most widely commercial used and manufactured piezoelectric ceramic is now $Pb_{0.5}Zr_{0.5}TiO_3$, also known as PZT. $PbTiO_3$ has a similar tetragonal structure to that of $BaTiO_3$ but with a c-axis approximately 6% longer than its a-axis at room temperature. On the other hand, $PbZrO_3$ has an orthorhombic structure with

anti-ferroelectric state. The PZT phase diagram is illustrated in Figure 2.20, where the key feature is the MPB between two different crystal structures. It was found relatively recently that several MPBs between different crystal structures exist, for example a MPB between monoclinic and rhombohedral phase[77] and a MPB between tetragonal and monoclinic.[60]

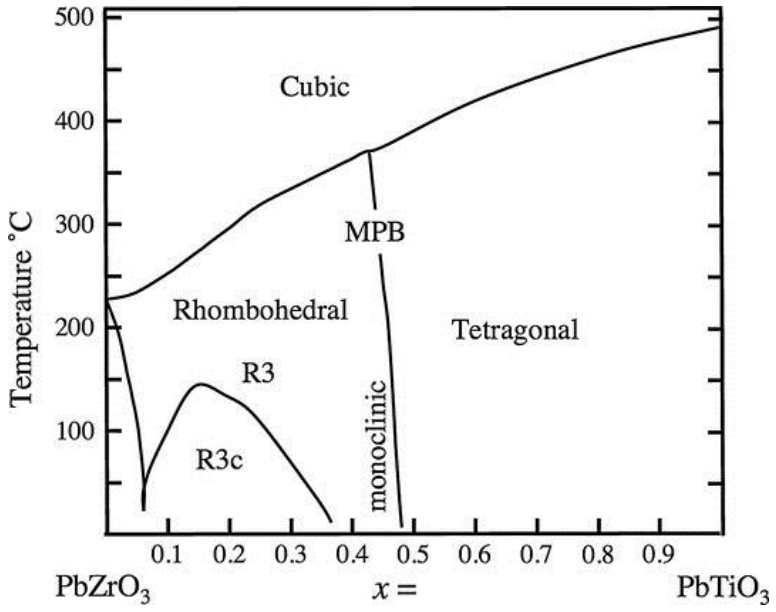

Figure 2.20 Phase stabilities in the PZT system.[14]

As a piezoceramic, a poled PZT specimen is capable of developing an electric field along its polar axis in response to an applied compressive or tensile stress. Furthermore, it can physically change shape in response to an applied electric field. Due to their excellent electromechanical properties, PZT-based materials are widely used in many areas, such as ultrasound transducers, electromechanical actuators and sensors. Commercially, it is not used in its pure form but rather when doped with acceptor or donors, denoted as *hard* PZT (acceptor doping) and *soft* PZT (donor doping). Their different electromechanical properties are listed in Table 2.4.[14] Furthermore, zirconium-rich solid solutions are of interest as a result of their anti-ferroelectric behaviour, which is desirable for applications as energy storage dielectrics.[14]

Table 2.4 *Soft* and *hard* PZT properties.

Piezo Type	*Soft* PZT	*Hard* PZT
Curie T / T_c (℃)	250-350	300-370
Permittivity / ε	1450-4200	1050-1650
Dielectric loss tanδ / (10^{-3})	20-30	3-5
Coupling factor / k_p	0.55-0.62	0.48-0.56
Piezo constant d_{33} / (10^{-12} C/N)	300-500	155-310

2.8 Lead-free piezoelectric ceramics

2.8.1 Unitary systems

2.8.1.1 $BaTiO_3$

Barium titanate (BT) was found to be the first polycrystalline oxide material which was capable of piezoelectric properties around the 1940s to 1950s.[14] It has a very high permittivity, which makes it a good choice as a material for capacitors. In terms of piezoelectricity, two disadvantages of BT are low piezoelectric coefficients and an extremely low T_c of around 120º, which restricts its use in higher temperature applications. BT undergoes several crystal structure transformations, as illustrated above in Section 2.4.1, and is often combined with other compounds to form binary lead-free piezoceramic systems.

2.8.1.2 $Na_{0.5}Bi_{0.5}TiO_3$

The complex perovskite sodium bismuth titanate (NBT) is considered to be a good lead-free candidate piezoceramic and exhibits useful dielectric, ferroelectric and piezoelectric properties. This material was first reported by Smolenskii[78] in the 1960s but did not draw much more attention until further publications in the 1990s,[79, 80] which investigated the diffuse phase transition in NBT below 280 ºC. At room temperature, NBT exhibits a rhombohedral structure with space group of R3c and transforms to tetragonal at elevated temperature.[81-84] At room temperature, NBT initially reported to exhibit a single rhombohedral structure.[26] In 2010, Gorfman[85] identified a non-rhombohedral phase in NBT due to a significant A-site distortion during refinement of neutron diffraction data. Later on, the crystal structure of NBT was examined using high-resolution x-ray

diffraction by Aksel[86] and a monoclinic structure with Cc space group was proposed. Further evidence of localised monoclinic phase in NBT was provided by Reaney[31, 87] using high-resolution TEM. It was also found that this localised monoclinic phase can be transformed to rhombohedral phase during electric field poling.[70, 88-90] In itself, NBT is a promising lead-free piezoelectric material, with a d_{33} coefficient of 73 pC N^{-1} and Curie point at 325 ºC. Both Bi and Na are located at the A-site of the perovskite structure.

Some limitations can be highlighted in the electrical properties of NBT. For example, high coercive field and high conductivity are serious issues. The high conductivity is associated with volatilisation of both Na and Bi oxides during the sintering process, which also seriously degrades the density of the sintered material. Therefore, the development of processing methods that can avoid volatilisation and improve the density of NBT has been a key research topic; one approach is by adding excess bismuth and sodium before sintering. Additionally, a low depolarisation temperature of 187 ºC was reported,[91] which limits its use at elevated temperatures. To decrease the high coercive field, some dopants may be added into NBT. Compared with the doping in PZT, which can take place on either the A- or B-sites, doping in NBT usually focuses on A-site substitution. For example, the incorporation of Li^+ and K^+ ions on the A-site are found to enhance both the piezoelectric coefficients and coupling factors.[92, 93]

2.8.1.3 $K_{0.5}Bi_{0.5}TiO_3$

Similar to NBT, $K_{0.5}B_{0.5}TiO_3$ (KBT) is another bismuth-containing lead-free piezoceramic. Compared to NBT, a tetragonal structure is observed for KBT at room temperature and its depolarisation temperature has been determined as 270 ºC.[94] In common with NBT, it was found that there are issues associated with volatilisation of bismuth and potassium oxides during sintering.[95] Furthermore, the temperature-dependent ferroelectric P-E hysteresis behaviour of KBT is illustrated in Figure. 2.21. With increasing temperature, a slight constriction in the P-E hysteresis loops was observed, indicating depolarisation

induced by the phase transition.

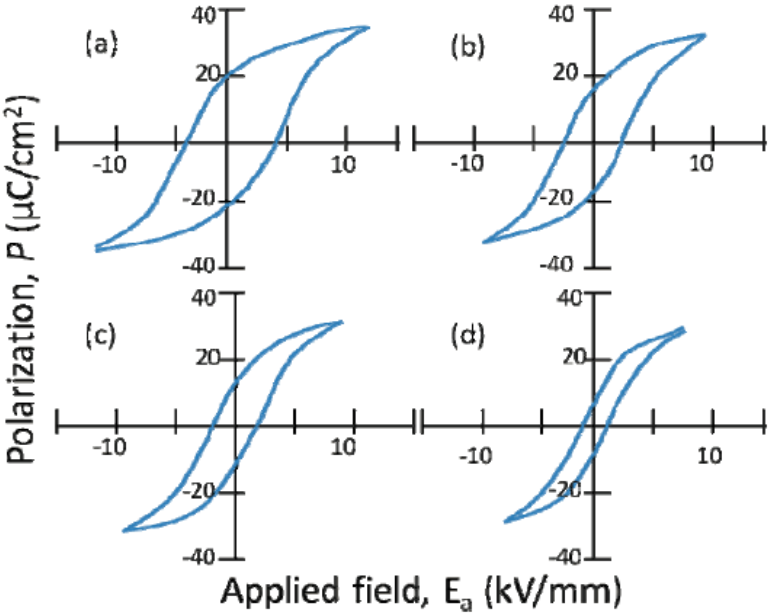

Figure 2.21 Polarisation of KBT measured at temperatures of (a) 100 °C, (b) 200 °C, (c) 240 °C, and (d) 260 °C. [94]

2.8.1.4 $K_{0.5}Na_{0.5}NbO_3$

The $K_{0.5}Na_{0.5}NbO_3$ system has been found to be one of the most promising solid solutions for lead-free piezoceramics. $KNbO_3$(KN) is a common ferroelectric compound with high T_c and large spontaneous polarisation; it undergoes a sequence of phase transformations during heating that are analogous to those of BT.[96] At room temperature, an orthorhombic structure occurs in KN.[97] By using the MPB between a ferroelectric and anti-ferroelectric phase, it can be combined with $NaNbO_3$ (NN) to form $KNbO_3$-$NaNbO_3$ (KNN). Similar to PZT, a phase diagram was reported to illustrate the different crystal structures and phase boundaries.[61] Notably, it was reported by Saito[8] that the optimum electrical properties were obtained for textured-(Li, Ta)-doped KNN, referred to as LF4T, which was capable of competing with PZT(Figure 2.22(a)). The important piezoelectric properties are illustrated in Figure 2.22(b), including the Curie temperature, coupling factor and piezoelectric constant.

(a)

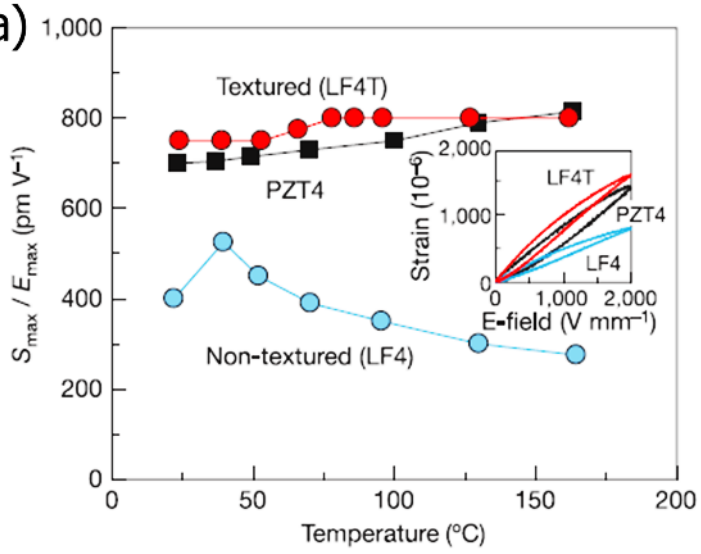

(b)

Piezoelectric property		LF4T	PZT4
Curie temperature	T_C (°C)	253	250
Piezoelectric coupling constant	K_p	0.61	0.60
Piezoelectric charge sensor constant	d_{31} (pC N^{-1})	152	170
	d_{33} (pC N^{-1})	416	410
Piezoelectric voltage constant	g_{31} (10^{-3} V m N^{-1})	11.0	8.3
	g_{33} (10^{-3} V m N^{-1})	29.9	20.2
Dielectric constant	$\varepsilon_{33}^T / \varepsilon_0$	1,570	2,300
Normalized strain	S_{max} / E_{max} (pm V^{-1})	750	700

Figure 2.22 Comparison of actuator performances between the developed KNN-based ceramic, LF4T, and the lead-based piezoelectric ceramic, PZT-4 (a) temperature-dependence of electric-field-induced longitudinal strain and (b) piezoelectric properties.[8]

2.8.2 NBT-based piezoelectric solid solutions

2.8.2.1 NBT-KBT

It was found that a MPB exists between NBT with rhombohedral structure and KBT with tetragonal structure in (1-x)NBT-xKBT with x in the range of 0.16 to 0.20 i.e. towards the NBT-rich side of the solid solution.[98, 99] The enhancement of piezoelectric constant and coupling factor were obtained for composition near the MPB, as displayed in Figure 2.23. However, the problem of volatilisation of metal oxides that occurs during processing for both unitary systems remains for the binary system. Hence an increasing number of research projects have been conducted to investigate how to enhance the grain growth,

densification and improvement of piezoelectric and ferroelectric properties.[99]

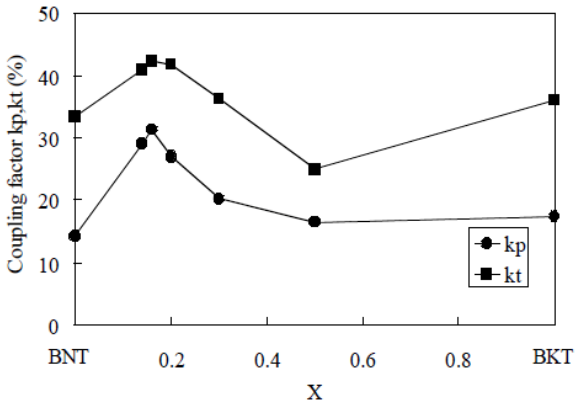

Figure 2.23 Electromechanical coupling factors for NBT-KBT system as function of concentration of KBT. [99]

It was reported by Zhang[100] that the sintering temperature played an important role in controlling the problem of volatilisation . In Figure 2.24(a), it is shown that the best density was obtained at a sintering temperature between 1150 ºC and 1160 ºC, which also yielded the highest spontaneous polarisation, as shown in Figure 2.24(b).

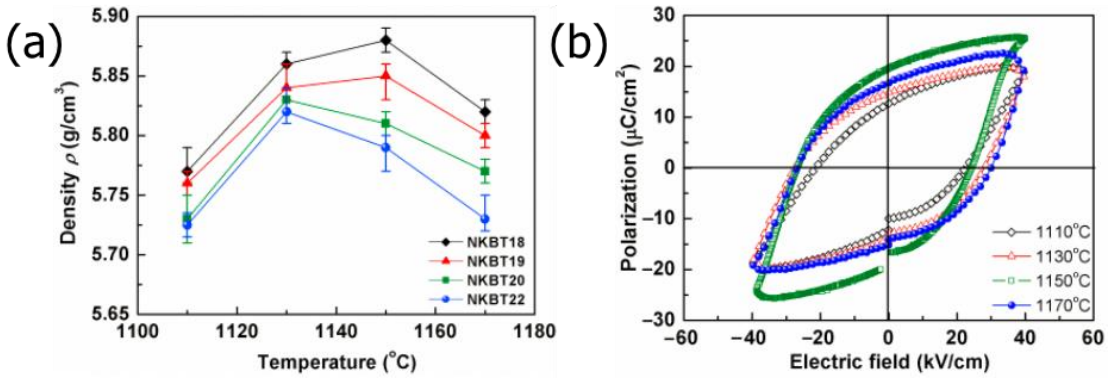

Figure 2.24 The temperature-dependent (a) densification and (b) ferroelectric P-E loops for NBT-22KBT.[100]

2.8.2.2 NBT-BT

To overcome the high coercive field of NBT, the binary system of NBT and BT was investigated its both electromechanical and structural properties. For the last 10 years, the NBT-BT system has been widely-reported to be one of the most promising candidates to replace PZT. Overall, one of the most interesting

properties reported is its "giant" electric field-induced strain, which can reach values of 0.3 % to 0.6 %,[101-104] indicating that it could provide the basis for an excellent actuator material.[105] With increasing temperature, the NBT-xBT system was found to be an excellent energy-storage dielectric for NBT-0.08BT.[106, 107] Furthermore, excellent energy storage characteristics and dielectric stability were obtained for compositions with higher BT content.[106, 108]

To further investigate its structure and the mechanisms contributing to the origin of large electric field-induced strain, many advanced techniques such as synchrotron XRD and neutron diffraction have been used to determine the crystal structure.[10, 90, 103, 109-114] A full 'phase diagram' for (1-x)NBT-xBT, with x ranging from 0 to 0.15, as illustrated in Figure 2.25, was obtained using high-energy synchrotron x-ray diffraction, as reported by Jo.[10] Specifically, in the unpoled state, NBT-xBT is considered to have a rhombohedral R3c structure for x values from 0 to 0.04, followed by a rhombohedral phase with R3m structure for x values from 0.05 to 0.11. Then, the crystal structure transforms into a tetragonal P4mm phase for x values above 0.11. On the other hand, for the poled state a mixed-phase region was identified instead of a MPB. It was found that a single rhombohedral phase was observed at an x value of 0.05. With increasing x value, the structure transforms to a mixed-phase of both rhombohedral and tetragonal for x values between 0.05 and 0.11, followed by a single tetragonal phase for x values above 0.11. Therefore, it was demonstrated that both a structural transformation and a phase transition from the RF to metastable FE state occurred under application of electric field.[115]

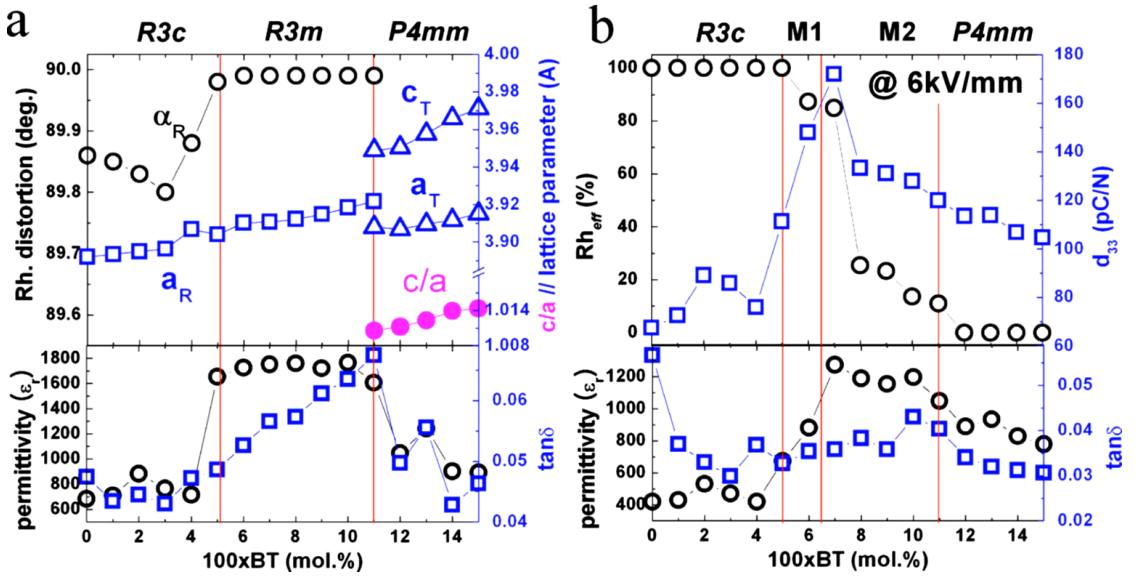

Figure 2.25 Changes in crystallographic parameters and piezoelectric properties for (a) unpoled NBT-xBT and (b) poled NBT-xBT.[10]

In addition, an electric field-induced phase transformation from pseudo-cubic to tetragonal phase was found for NBT-0.07BT, as reported by Jones.[12] After removing the electric field, the material retained the tetragonal phase with a strong domain texture and spontaneous polarisation, with an associated increase in volume of nearly 0.3%.[116]

However, NBT-xBT is not a traditional FE but a RF material. From the dielectric point of view, a frequency-dependent ε_r-T relationship was observed at lower temperatures and two anomalies were observed at different temperatures.[11] Additionally, constricted P-E loops were observed over a certain temperature range, which is in common with PLZT, indicating the reversible transition between the electric field-induced FE and the RF state, as illustrated in Figure 2.26.[11] Due to the existence of different PNR symmetries and TEM studies have been conducted to understand more about its local structure, which indicated the presence of nano-polar regions within the grains.[11, 33, 117]

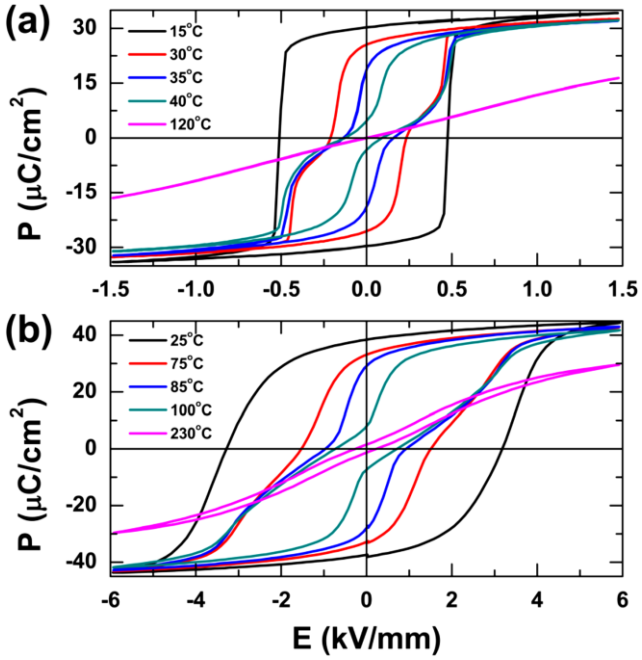

Figure 2.26 The temperature-dependent ferroelectric P-E loops for (a) PLZT and (b) NBT-6BT. [11]

2.8.2.3 NBT-KN

In order to reduce the high coercive field in pure NBT, a binary system of NBT and KN has also been investigated. With increasing KN content, a constricted P-E loop was observed with the reduction of remanent polarisation and coercive field, as illustrated in Figure 2.27.[118]

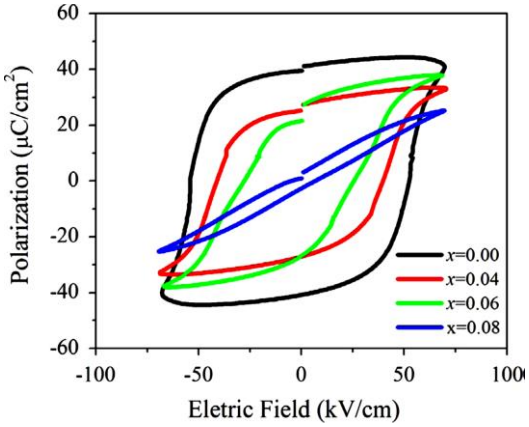

Figure 2.27 The ferroelectric P-E loop for NBT-xKN.[118]

Furthermore, the ferroelectric P-E loop became constricted over a certain of temperature range for NBT-0.06KN, as illustrated in Figure 2.28, indicating that a similar behaviour of reversible transition occurred.[119]

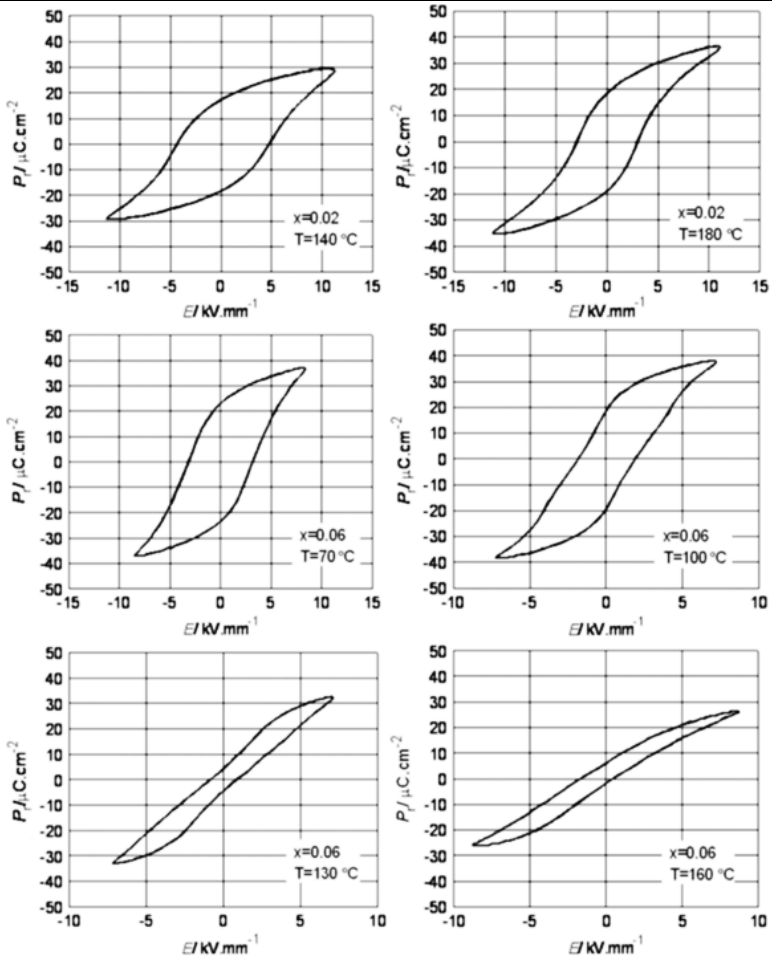

Figure 2.28 The temperature-dependent P-E loops for NBT-0.02KN and NBT-0.06KN.[119]

Furthermore, it was found that a relative high d_{33} value of 140 pC N^{-1} and k_p of 40% were obtained for NBT-xKN, as reported by Jiang.[72, 120] An electric field-induced strain value of nearly 0.3% was obtained for certain compositions and temperatures, as displayed in Figure 2.29.[121] Recently, new electrocaloric and energy density properties were reported for compositions with x greater than 0.06 in the NBT-xKN system.[53, 57, 72, 122]

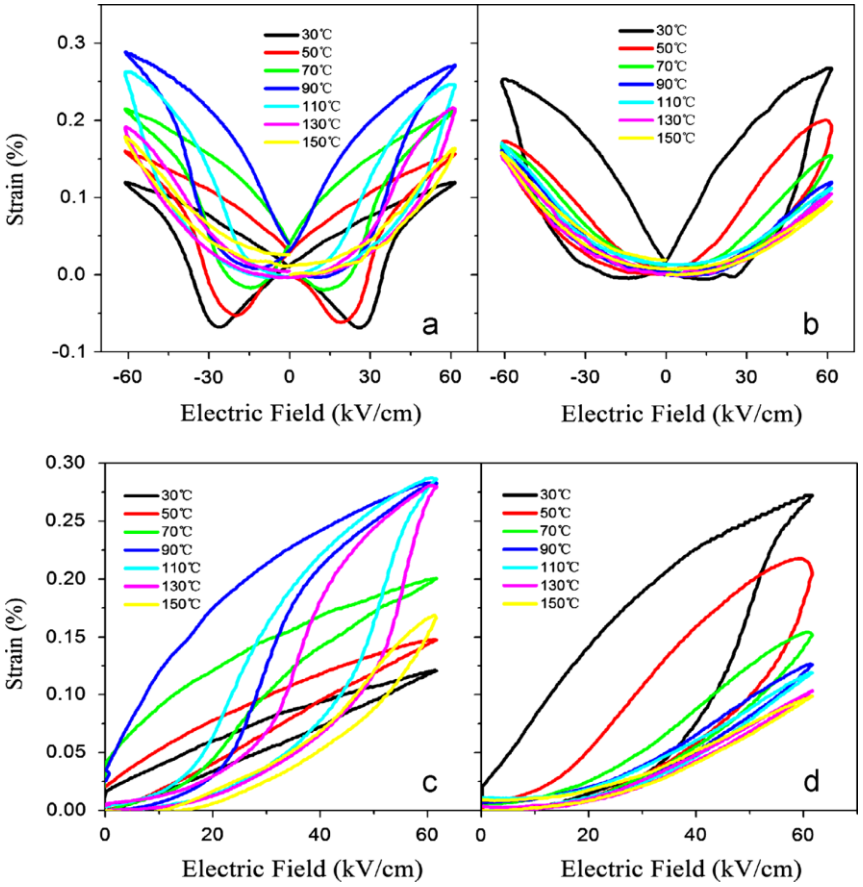

Figure 2.29 The temperature-dependent electric field-induced (a) bipolar strain for NBT-0.02KN (b) bipolar strain for NBT-0.06KN (c) unipolar strain for NBT-0.02KN and (d) unipolar strain for NBT-0.06KN.[120]

In terms of the structural properties at room temperature, it was reported by Pisitpipathsin[123] that the existence of pure rhombohedral phase at low KN contents and the presence of mixed rhombohedral and orthorhombic phases for x values between 0.05 and 0.15 was observed. The occurrence of mixed pseudo-cubic and rhombohedral phases was also reported by Fan for x in the range 0.04 to 0.06.[119] The structural transformations in NBT-KN as a function of composition, temperature and an applied electric field are examined in-depth within the present research; some aspects of this research have already been published.[67, 124]

The thermally-induced phase transformations in NBT-xKN ceramics were studied indirectly by Fan[125] by conducting temperature-dependent permittivity measurements on unpoled specimens, giving rise to the phase diagram illustrated in Figure 2.30. Both T_d and T_m were determined by identifying

anomalies on the permittivity-temperature curves. By analogy with pure NBT, it was assumed that the structure for all compositions between T_m and T_d was tetragonal, although no evidence was presented to support this assertion. A similar approach was adopted by Jiang, although in the latter case the experiments were conducted on poled specimens.[72, 120] Two anomalies in the permittivity-temperature curves were defined as T_p and T_m, while one extra peak in the loss tangent-temperature curve, T_{ir}, was attributed to the irreversible transition from long-range ordered FE to a weak-polar phase. On the other hand, Hiruma referred to the lower-temperature anomaly as the structural transformation temperature from rhombohedral to tetragonal, T_{R-T}, but without direct evidence of the crystal structure at elevated temperatures.[126]

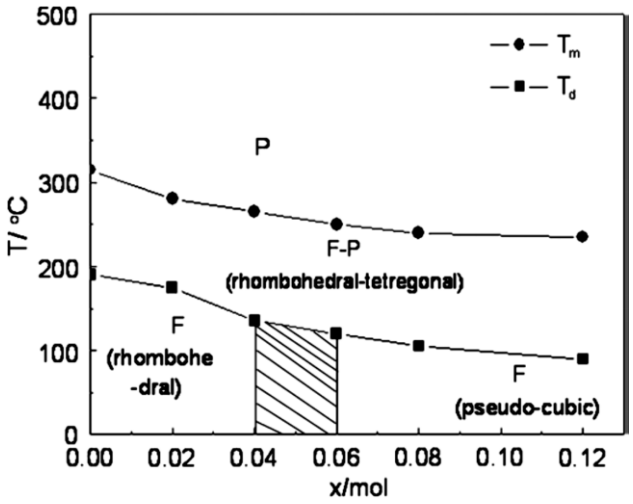

Figure 2.30 The phase diagram for NBT-xKN system.[119]

2.8.2.4 NBT-NN

In common with NBT-xKN, anti-ferroelectric $NaNbO_3$ was combined with NBT to form NBT-$NaNbO_3$ (NBT-NN) binary solid solutions. It was reported by Li[127] that the optimum piezoelectric properties of d_{33} (88 p N^{-1}) and K_p (18 %) were obtained for NBT-0.02NN due to the dominant effect of doping with the Nb^{5+} ion. In terms of crystal structure, even though $NaNbO_3$ is a typical anti-ferroelectric material, there is no MPB observed in NBT-NN solid solutions. With increasing NN content to 0.08, all single (unsplit) peaks were observed in Figure 2.31, indicating a cubic structure.[127-129]

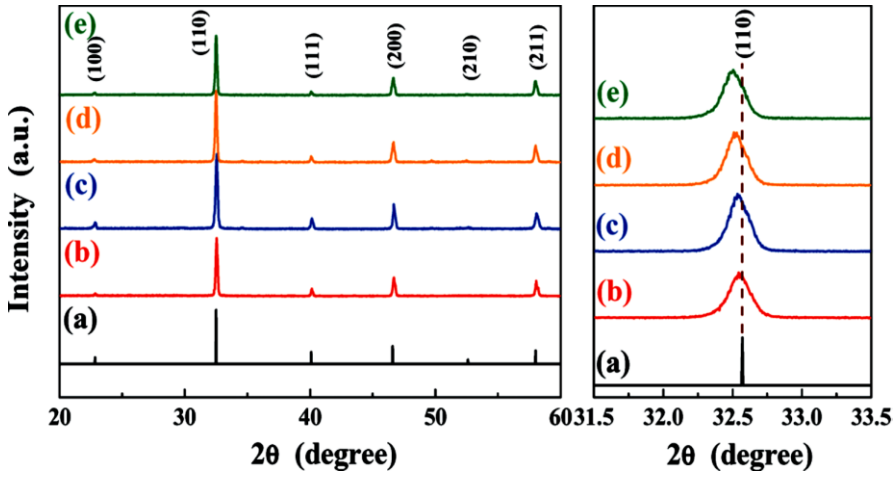

Figure 2.31 The XRD profiles for (a) NBT-0.02NN (b) NBT-0.04NN (c) NBT-0.06NN and (d) NBT-0.08NN.[129]

However, a rhombohedral phase was observed in (1-x)NBT-xNN ceramics with x values between 0 and 0.16, as reported by Yuji.[126] Specifically, the separation of the $\{111\}_p$ split peak declined significantly with increasing x value from 0 to 0.08, as illustrated in Figure 2.32, indicating a reduced rhombohedral distortion. With increasing temperature, both T_d and T_{R-T} were observed as anomalies in the ε_r-T curves via temperature-dependent dielectric measurements.[126]

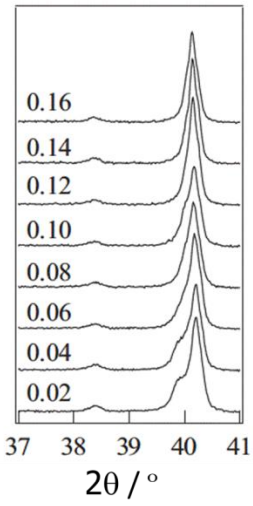

Figure 2.32 The representative peak profiles of $\{111\}_p$ over a wide range of composition in the NBT-xNN system.[126]

A detailed phase diagram was created by combining the ferroelectric P-E and piezoelectric S-E results, as illustrated in Figure 2.33.[126] It was found that 4 different phases were identified. In terms of electrical properties, the best d_{33} and

d_{33}^* values were obtained for NBT-0.07NN and NBT-0.10NN at 83 pC N^{-1} and 259 pm V^{-1} respectively. In the latest publication reported by Xu,[130, 131] the NBT-xNN system was considered to be a promising candidate for capacitor dielectrics and energy storage applications with wide temperature stability. For example, the composition with x value from 0.25 to 0.35 exhibits a relatively constant permittivity over an ultra-wide temperature range from -60 to 400 ºC.

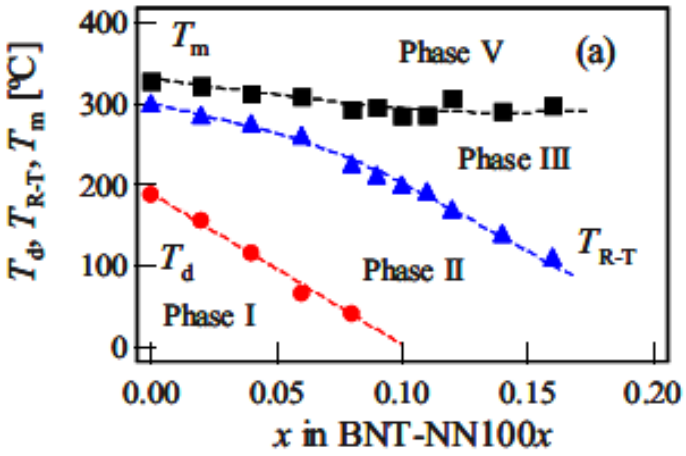

Figure 2.33 A phase diagram for NBT-xNN system.[126]

2.8.2.5 NBT-BT-KNN

To further improve the electrical properties of lead-free piezoelectric ceramics, a third component, KNN, was added into the binary system of NBT-BT to form the ternary system NBT-BT-KNN.

One of the most interesting electrical properties for the NBT-BT-KNN ternary system, is the large electric-field induced strain, yielding a value of approximately 0.45% under an electric field of 8 kV mm^{-1} for compositions close to the MPB.[132] Additionally, the temperature-dependent ferroelectric and dielectric behaviour were reported by Zhang[133] to investigate the phase transitions induced by changes in electric field and temperature. During the phase transition, the structural properties were examined by high-energy synchrotron XRD.[134] It was found that an electric field-induced structural transformation from pseudo-cubic to tetragonal occurred for certain compositions, as illustrated in Figure 2.34. After transformation, the ceramics retained the tetragonal structure

and developed a strong texture effect, contributing directly to the large field-induced macroscopic strain.[134]

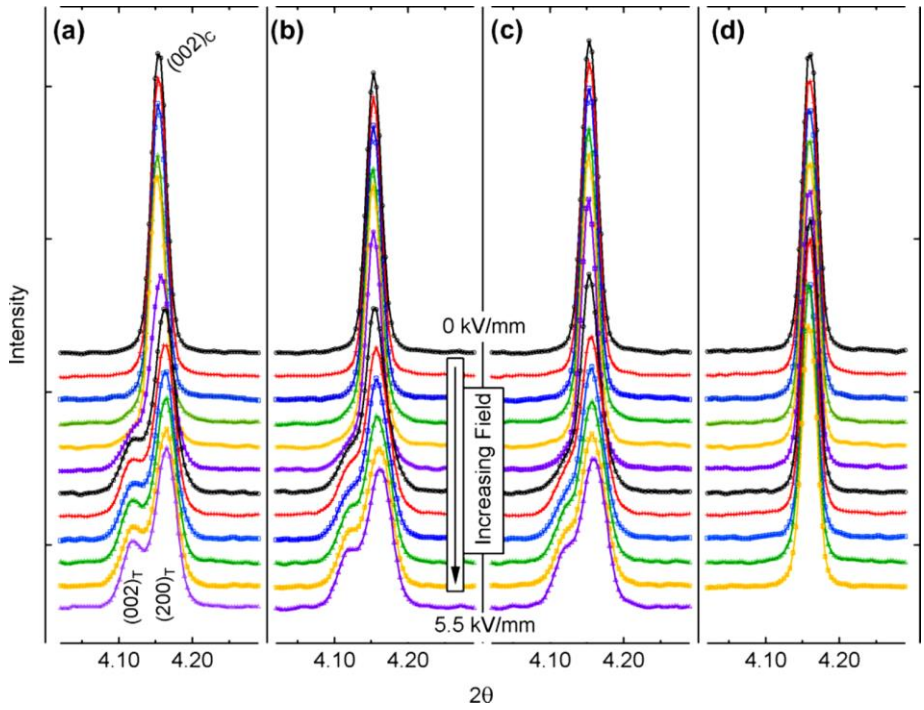

Figure 2.34 The $\{200\}_p$ diffraction reflection under in-situ electric field poling of 5.5 kV mm^{-1} for (a) NBT-0.07BT (b) NBT-0.053BT-0.09KNN (c) NBT-0.045BT-0.023KNN (d) NBT-0.14KNN.[134]

Furthermore, it was also reported by Jo that adding only 1 to 3% KNN into NBT-BT solid solution can enhance the electric field-induced volume change.[135] For example, the strain components, S_{33} and S_{11}, for NBT-6BT-2KNN under an electric field of 8 kV mm^{-1} can reach up to 0.45 % and 0.34 % respectively, resulting in a volume change of 0.11% (Figure 2.36 (a)). Furthermore, an even higher but irreversible S_{33} value of 0.49 % was observed for NBT-6BT-1KNN under an electric field of 6 kV mm^{-1}, as presented in Figure 2.36(b).

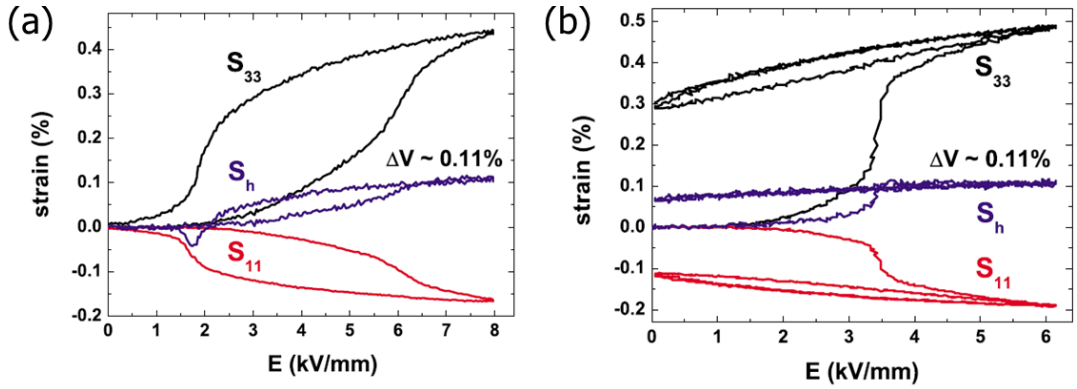

Figure 2.35 Unipolar strain for (a) 92NBT-6BT-2KNN and (b) 93NBT-6BT-1KNN from the unpoled state. S_{33} and S_{11} are the strains simultaneously measured parallel and perpendicular to the electric field, respectively, S_h denotes the volume change.[136]

In addition, the P-E loops for 92NBT-6BT-2KNN and 93NBT-6BT-1KNN are presented in Figure. 2.36. The maximum polarisation P_{max} under a poling field of 8kV mm^{-1} for both compositions reaches approximately the same value of 42 $\mu C\ cm^{-2}$. However, a different shape of ferroelectric P-E loop was observed. For 93NBT-6BT-1KNN, a saturated P-E loop was observed, indicating that it is an electric field-induced metastable FE state. on the other hand, a reversible transition between FE and RF states was found for 93NBT-6BT-2KNN, supported by the occurrence of a constricted P-E loop. For the remanent polarisation, P_{rem}, a high value of 33 $\mu C\ cm^{-2}$ was obtained for 93NBT-6BT-1KNN, which is much higher than the value for 92NBT-6BT-2KNN.

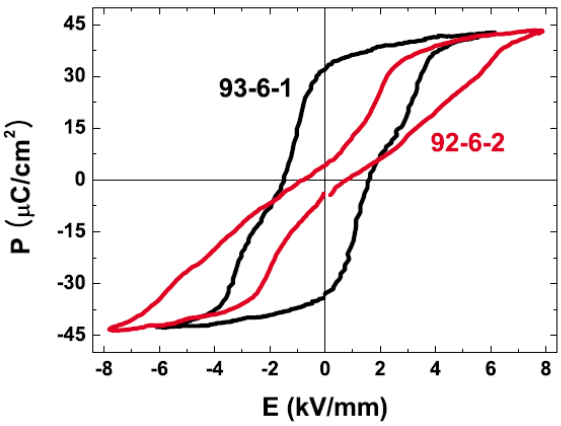

Figure 2.36 The ferroelectric P-E loop for 92NBT-6BT-2KNN under 8 kV mm^{-1} and 93NBT-6BT-1KNN under 6 kV mm^{-1}.[136]

Recently, it was also found that a constricted P-E loop with high maximum polarisation and low remanent polarisation was observed for NBT-BT-5KNN, as illustrated in Figure 2.37. This kind of behaviour contributes to a high temperature-stability in energy density, which can be used as the basis for lead-free energy storage dielectrics.[36, 56, 137]

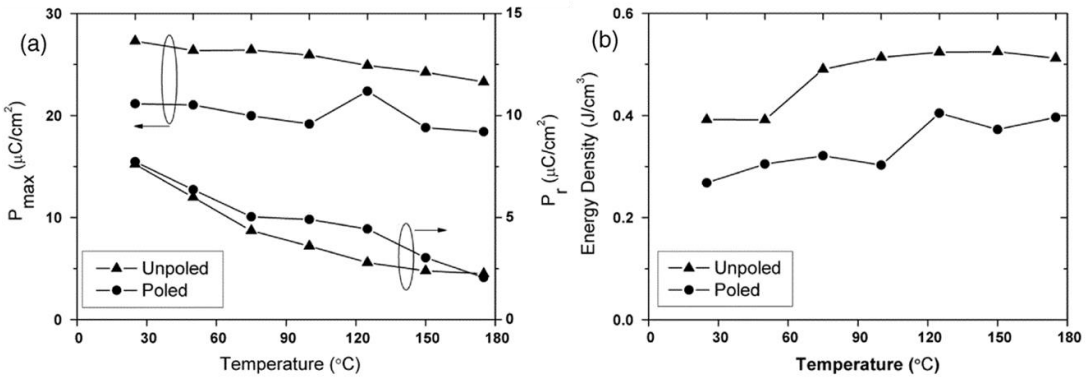

Figure 2.37 The temperature dependence of (a) maximum polarisation and remanent polarisation and (b) energy density of unpoled and poled states.[36]

2.8.2.6 NBT-BT-KN

It was reported by Ni that only a small amount of KN can enhance the electrical properties of NBT-BT ceramics.[138] The electromechanical coupling factor, k_t, and piezoelectric coefficient, d_{33}, for NBT-BT-KN solid solutions are presented in Figure 2.38. Both of them achieve the maximum value of 195 pC N^{-1} and 58.9% for a composition with x value of 0.01. With further increasing KN content, both parameters decrease slightly for NBT-BT-2KN then reduce significantly for x values over 0.02. With x values above 0.08, the materials only exhibit the electrorstrictive behaviour, as reported by Li.[139]

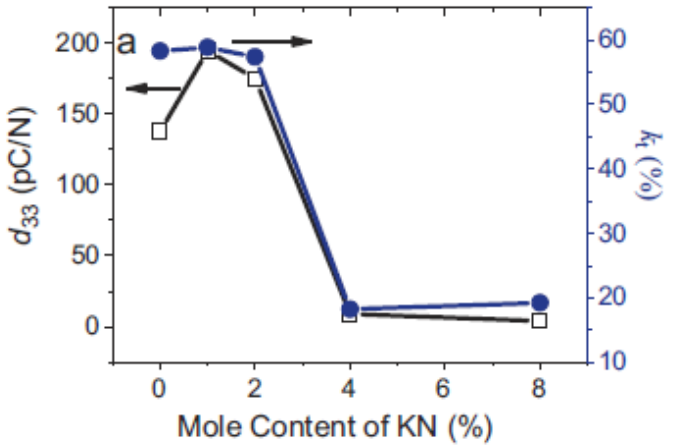

Figure 2.38 Piezoelectric coefficient d_{33} and the electromechanical coupling factor k_t of NBT-BT-KN ceramics as a function of KN mole content.[140]

Corresponding to the d_{33} and k_p, a well-saturated P-E loop was observed for compositions with x in the range from 0 to 0.02. The best electrical properties were obtained for NBT-BT-1KN, reaching a high P_{rem} value of 0.41 C m^{-2} and E_c of 1.95 kV mm^{-1}, as displayed in Figure 2.39. Less-pronounced hystere and weaker ferroelectricity for compositions having x over 0.04 in the NBT-BT-KN system are due to two reasons: (1) possible of non-polar regions exist due to substitution of K^{1+} on the A-site and Nb^{5+} on the B-site in ABO_3 perovskite ferroelectrics at room temperature. (2) high concentrations of KN generate more chemical disorder and convert the long-range FE state into PNRs.[140]

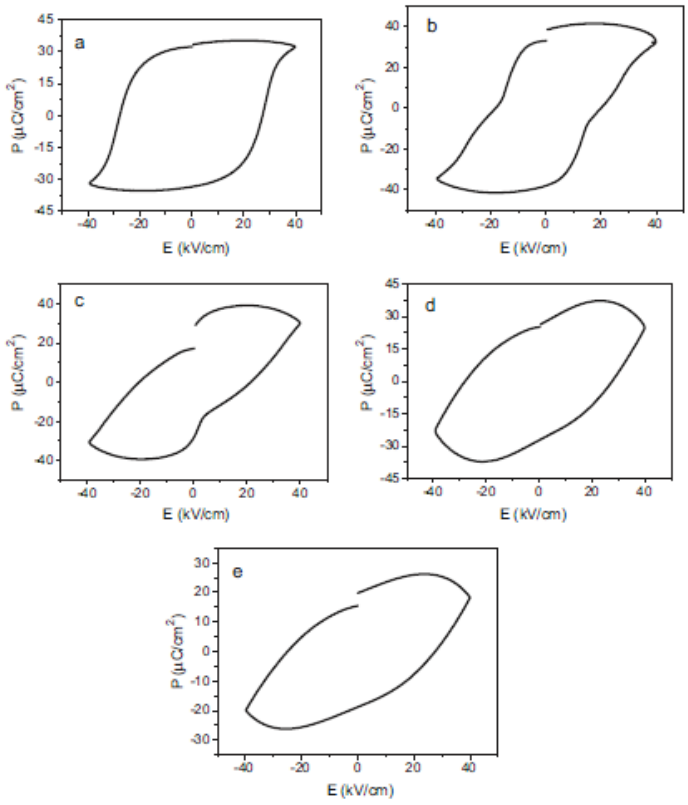

Figure 2.39 The ferroelectric hysteresis P-E loop for NBT-BT-xKN ceramics (a) x=0, (b) x=0.01, (c) x=0.02, (d) x=0.04, (e) x=0.08.[138]

2.8.3 Summary

It has been found that the electrical properties obtained for binary and ternary systems are often superior to those of unitary systems, due to the presence of an MPB. Materials compositions near to the MPB tend to yield higher polarisation values. However, most of the lead-free materials are still in the process of fundamental research, which is still far away from practical applications.[141] Only a few unique compositions can possess extraordinary and stable properties that might rival those of PZT-based ceramics, for example the 'giant' electric field-induced strain for NBT-BT-KNN.[142]

To reveal the origin of such interesting properties, fundamental research has played an important role to push lead-free piezoelectric materials towards real applications. Furthermore, from the point of view of the material itself, it is necessary to probe the structure of a material fo fully understand the

mechanisms that contribute to electrical and mechanical properties. Therefore, there are still many problems that need to be solved by the complementary use of advanced characterisation techiniques together with functional property measurements.

3 Characterisation techniques

This chapter introduces the characterisation techniques that have been used in this study to analyse the structural and electrical properties of the NBT-KN, NBT-NN and NBT-BT systems.

3.1 Density measurement

The diameter, r, and the thickness, t, were measured using a micrometer screw gauge. These dimensions are used to calculate the volume, V. The sample mass, m, was measured using an OHAUS Adventurer Pro AV213 balance. The density of the sample is calculated using Equation 3.1

$$\rho_m = m/v \tag{3.1}$$

In order to find the theoretical density, ρ_t, the mass in one unit cell according to the formula ABO_3, m, the unit cell volume, V, and Avogadro's constant $N_A=6.023x10^{23}$ molecules mol^{-1} were used following Equation 3.2 below.

$$\rho_t = m/v \tag{3.2}$$

The relative dentity, p_r, is defined as the ratio of measured density to the theoretical density in order to give a percentage of sample densification, given in Equation 3.3.

$$\rho_r = \rho_m / \rho_t \tag{3.3}$$

3.2 X-ray diffraction

X-ray diffraction (XRD) is one of the most commonly used material characterisation techniques for phase identification and lattice parameters determination both in powders and ceramics.[143] The principle of XRD is that a beam of monochromatic X-rays with high energy and short wavelength is targeting directly the surface of the sample, as illusrated in Figure 3.1.

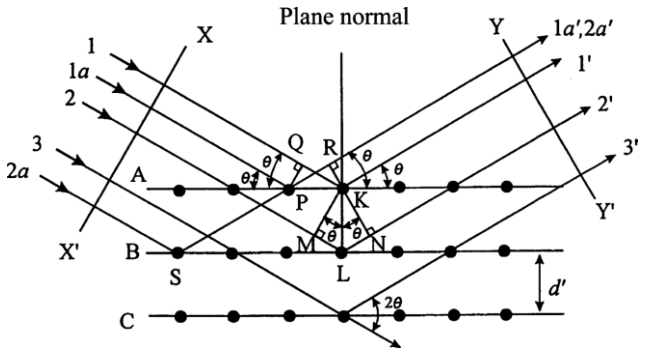

Figure 3.1 Theoretical illustration of X-Ray Diffraction.[144]

The most important and familiar method to analyse the mechanism of x-ray diffraction is represented by the Bragg law.[145] If the incident X-rays of wavelength, λ, strike a crystal where all atoms are placed in a regular periodic array with interplanar spacing d, the Bragg law is satisfied by:

$$2d \sin\theta = n\lambda \tag{3.4}$$

For fixed λ and d, the diffraction occurs at each angle such that θ_1, θ_2, θ_3 correspond to n=1,2,3. For example, when n=1, the path difference between two scattered X-rays denoted as 1′ in Figure 3.1 is one wavelength, λ. the path difference between X-rays 1′ and 3′ is two wavelengths, 2λ. Therefore, the diffracted X-rays from all atoms are considered to be in-phase in order to produce a maximum in intensity in a particular direction that satisfies the Bragg law.

In general, the diffraction angle 2θ of any set of planes (hkl) can be calculated by plane-spacing Equations which correspond to Miller indices and lattice parameters for each crystal system, as shown in Table 3.1.[143] It was found that the diffraction angle and diffraction directions can be determined from the shape and size of the unit cell, which is essential for structural analysis.

Table 3.1 Diffraction angle and directions in different unit cell.[144]

Cubic	$\frac{1}{d^2} = \frac{h^2+k^2+l^2}{a^2}$
Tetragonal	$\frac{1}{d^2} = \frac{h^2+k^2}{a^2} + \frac{l^2}{c^2}$
Hexagonal	$\frac{1}{d^2} = \frac{4}{3}\left(\frac{h^2+hk+k^2}{a^2}\right) + \frac{l^2}{c^2}$
Trigonal	$\frac{1}{d^2} = \frac{(h^2+k^2+l^2)\sin^2\alpha+2(hk+kl+hl)(\cos^2\alpha-\cos\alpha)}{a^2(1-3\cos^2\alpha+2\cos^3\alpha)}$
Orthorhombic	$\frac{1}{d^2} = \frac{h^2}{a^2} + \frac{k^2}{b^2} + \frac{l^2}{c^2}$
Monoclinic	$\frac{1}{d^2} = \frac{1}{\sin^2\beta}\left(\frac{h^2}{a^2} + \frac{k^2\sin^2\beta}{b^2} + \frac{l^2}{c^2} - \frac{2hl\cos\beta}{ac}\right)$
Triclinic	$\frac{1}{d^2} = \frac{1}{V^2}(S_{11}h^2 + S_{22}k^2 + S_{23}k^2 + 2S_{12}hk + 2S_{23}kl + 2S_{13}hl)$

On the triclinic system, V is the volume of a unit cell and the coefficients are given below.

$$S_{11} = b^2c^2\sin^2\alpha, \quad S_{12} = abc^2(\cos\alpha\cos\beta - \cos\gamma),$$
$$S_{22} = a^2c^2\sin^2\beta, \quad S_{23} = a^2bc(\cos\beta\cos\gamma - \cos\alpha),$$
$$S_{33} = a^2b^2\sin^2\gamma, \quad S_{13} = ab^2c(\cos\gamma\cos\alpha - \cos\beta)$$

In general, X-rays are generated within sealed high-vacuum X-ray tubes which consists of 3 components, which are the source of electrons, metal target and large accelerating voltage. These electrons are accelerated under application of voltages of around 30 to 60 kV to strike the target, which normally is a piece of pure metal.[146] For example, "hard" x-rays have shorter wavelengths and long penetration depths, which can be used to probe further below the surface of a sample. The penetration depth also depends strongly on the X-ray absorption coefficient of the sample at a particular wavelength. The most commonly used target metals are summarised in Table 3.2 below with their characteristic wavelengths.[143] A Cu target was used among this lab XRD study and a monochromator was used to reduce the noise of background.

Table 3.2 Typical metal target materials and x-ray wavelengths.

Metal	Cr	Fe	Co	Cu	Mo	Au	Ag
Wavelength(Å)	2.2909	1.9373	1.7902	1.5418	0.7107	0.5594	0.1801

3.3 Synchrotron x-ray diffraction

A synchrotron is an extremely powerful source of X-rays. These are produced by highly energetic electrons moving in a circle in the synchrotron. The mechanism is that a moving electron can emit energy when it changes direction. When a electron is moving fast enough, the emitted energy is at X-ray wavelengths. Therefore, compared to conventional XRD, the synchrotron source can generate a much higher intensity of X-rays, which allows a better resolution and accuracy.

3.3.1 Synchrotron components

All facilities contain mainly four components, beamline, storage ring, booster synchrotron and linac. The electrons are produced from an electron gun then start in Linac, which is a device similar to a cathode tube. These electrons are packed in "bunches" and then accelerated to 200 million electron volts to be energetic enough for injection into the booster synchrotron. The booster synchrotron is a 300-metre-long pre-accelerator where the electrons are accelerated to an energy of 6 billion electron-volts before being injected into the storage ring. For the storage ring, it is a tube where the electrons circle for hours until the speed reaches close that of light. This tube is controlled under extremely low pressure and all electrons pass through different type of magnet as they travel around the ring. Finally, the X-ray beams emitted by the electrons are directed toward various "beamlines", which surround the storage ring. Each beamline is designed for a specific type of research. High-energy X-rays can transmit through the sample deeply to probe the structure of the material inside bulk ceramics instead of being confined to the surface.

3.3.2 Diamond light source, UK

Diamond light source is the UK's national synchrotron facility. It provides intensive high-energy x-rays to charactise many scientific reasearch areas from materials science, engineering and proteins. Since it became operational in 2007, the Diamond synchrotron uses electrons travelling at an energy of 3 GeV and it

has nearly 22 beamlines and will increase the number of operational beamlines to 32 by 2017.[147]

3.3.2.1 Beamline I11-Diamond light source, UK

The purpose of the I11 beamline is to measure high-resolution powder x-ray diffraction patterns for different materials, such as metal-organic-frameworks, alloys, ceramics and superconductors. Furthermore, with a combination of very high-resolution, high count rates and controlled temperature conditions on I11, it is possible to perform detailed structural analysis of complex materials, which is extremly important to my fundamental research on structural phase transformations.[148]

3.3.2.2 Beamline I15-Diamond light source, UK

The I15 beamline is an 'extreme conditions' beamline with high-energy x-ray photon range from 20 to 80 keV. It is designed to carry out x-ray powder and bulk diffraction under extreme pressure, electric field and temperature, which enables 'in-situ' electric field experiments to be carried out in order to determine phenaomena associated with electric field-driven structural phase transformations and ferroelectric domain switching. A Perkin Elmer area detector was employed, which has 2048x2048 pixels, and the x-ray photon energy was 67 kev.[147]

3.4 Polarisation-electric field measurements

The ferroelectric hysteresis polarisation-electric field (P-E) measurement is a fundamental characterisation technique for ferroelectric materials under application of external electric field. The polarisation can be switched direction under application of electric field, as illustrated in Section 2.2.4. The normally ferroelectrics exhibit a square polarisation hysteresis loop while a constricted loop is obtained for relaxor ferroelectrics due to a reversible switching between PNRs and microdomain structure.

3.5 Permittivity-temperature measurements

The permittivity-temperature measurement is a commonly used characterisation techniques for ceramics to determine Curie temperature and other phase transition temperatures. In practice, the capacitance of a specimen is measured over a range of temperature between two parallel plate of sliver or platinum wires. At the same time, the relative permittivity will be calculated, as well as the dielectric loss.

3.6 Depolarisation-temperature measurements

The depolarisation temperature (T_d) is an important feature for both ferroelectric and piezoelectric materials, especially for applications such as sensors and actuators. At elevated temperature, materials will experience phase transition and structural transformation, leading to the loss of remanent polarisation as well as electromechanical properties. Based on European standard,[149] the depolarisation is defined as reducing polarisation due to temperature and other influences. However, it has found to be more complex for relaxor ferroelectrics due to existence of PNRs. Here, in terms of NBT-based relaxor ferroelectrics, the depolarisation temperature is defined as the steepest change of the polarisation.[73]

3.7 Scanning Electron Microscopy

A scanning electron microscope (SEM) is used to examine both powder and bulk ceramics samples. In SEM, a beam of electrons is generated by an electron gun and focused using apertures and electromagnetic lenses, as illustrated in Figure 3.2. Compared to optical microscopy, the SEM is able to obtain high-resolution images because electrons have a much shorter wavelength than light.[150] Furthermore, the resolution is determined by many reasons, such as accelerating voltage, working distance and imaging conditions.

In order to identify phases using SEM, back scattered and secondary electrons are most common imaging modes. The secondary electrons mainly detect the

surface information of the samples, which is used for topographical imaging mostly. However, the back scattered electrons are higher energy than secondary electrons and used for phase identification. Due to the variation in the atomic number, the back scattering made is able to distinguish phases by observing different contrast in the image.[151]

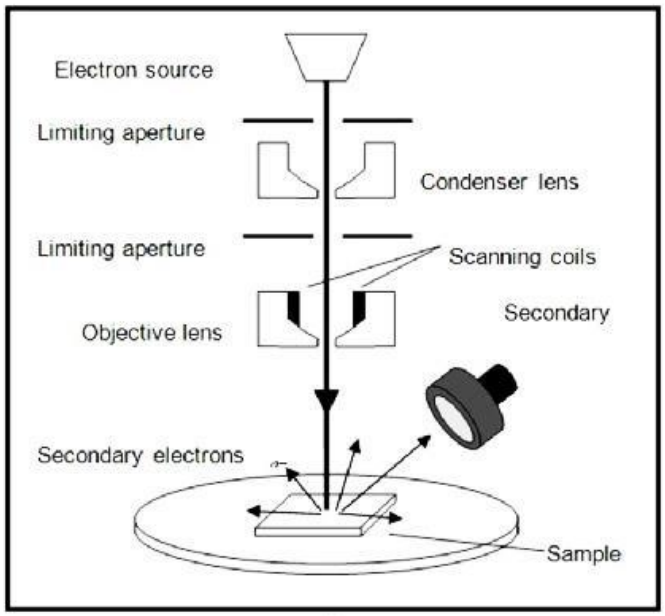

Figure 3.2 Scanning electron microscopy mechanisms.[152]

4 Experimental procedures

4.1 Synthesis of NBT-based ceramics

4.1.1 $Na_{0.5}Bi_{0.5}TiO_3$-$KNbO_3$ ceramics

Analytical-grade powders: Na_2CO_3(99.8%), K_2CO_3(99%), Bi_2O_3(99%), TiO_2(99%), Nb_2O_5(99%) were used as raw materials to prepare NBT-xKN (x=0.01 to 0.09) ceramics.

These powders were dried at 300 ºC to remove moisture before weighing into stoichiometric amounts to produce compositions ranging from (1-x)NBT-xKN with x=0.01 to 0.09. The mixed powders were milled for 24 h in propan-2-ol using zirconia milling balls and calcined for 10 h at 900 °C to finish the reaction process. Then the as-calcined powders were milled again for 24 h to break down large agglomerates. The final dry powders were pressed into pellets of 6.5 mm diameter, 1.5 mm in thickness and weighing approximately 0.15 g under pressure of 150 MPa for 30 seconds. Before sintering, the pellets were embedded in powders of the same composition to prevent the loss of volatile elements of bismuth, sodium and potassium. The pellets were heated using a rate of 300 ºC h^{-1} up to 1200 ºC for 3 hours and then cooled at 150 ºC h^{-1} to room temperature. During the sintering process, the ceramic pellets shrank by approximately 20 % in volume, resulting in a relative density of 90 % to 96 %.

4.1.2 $Na_{0.5}Bi_{0.5}TiO_3$-$NaNbO_3$ ceramics

Analytical-grade powders: Na_2CO_3(99.8%), Nb_2O_5(99%), Bi_2O_3(99%), TiO_2(99%) were used as raw materials to prepare (1-x) NBT-xNN (x=0.02 to 0.08) ceramics. The materials were processed in a similar manner to that described above (Section 4.1.1) but with slightly lower calcination and sintering temperatures of 850 °C and 1180 °C respectively.

4.1.3 $Na_{0.5}Bi_{0.5}TiO_3$-$BaTiO_3$ ceramics

Analytical-grade powders: Na_2CO_3(99.8%), $BaTiO_3$(99%), Bi_2O_3(99%), TiO_2(99%) were used as raw material to prepare NBT-xBT (x=0.04 to 0.11) ceramics. The calcination and sintering conditions for these compositions were identical to those described above in Section 4.1.1.

4.2 In-house characterisation techniques

4.2.1 X-ray diffraction

The ceramic pellet samples were polished mechanically first by using abrasive paper. However, the mechanical grinding process can generate significant residual stresses on the surface, which may changes in structure and preferred orientation. Thus, the ceramic pellets were annealed at 600 ºC for 30 mins before the XRD test to release the residual stress generated during sintering and polishing on the surface.

Powder samples were made from crushed sintered pellets by using a mortar and pestle. After crushing, a randomly-textured powder was obtained, which yielded diffraction patterns suitable for full-pattern refinement.

For this research study, calcined powders, sintered powders and sintered ceramic pellets were studied using XRD to identify crystal structures. A Philips PW1830 generator and PW3710 mpd controller were used for XRD measurements, using a Cu-Kα X-ray radiation tube which had a beam of wavelength of 1.54060 Å, a current of 40 mA and 40 kV voltage. The diffraction step was 0.05º per second between scanning angles of 10º to 80º.

The XRD results were analysed by X'pert HighScore Plus software using pattern fitting from the international centre for diffraction date database (ICDD) and *Topas* program to refine pattern peak from the inorganic, mineral & metal structure in National chemical service database (NCSD).

4.2.2 Scanning electron microscopy

For SEM sample preparation, bulk ceramics mounted first in resin and then ground using 240 to 2500-grade SiC grinding paper, followed by polishing on 6 μm then 1 μm diamond paste, then polishing with dilute OPS (oxide polishing suspension) colloidal silica solution for 20 mins. The sample was washed with soap and ethanol and also observed under optical microscopy to make sure no obvious scratches occurred at each stage. The sample was stuck onto an aluminum SEM holder using conductive carbon adhesive, and a carbon coating was deposited using GATAN Model 682 Precision etching coating system to avoid charging. Finally, silver paste was painted between the sample surface and the stub in order to be fully conductive during SEM imaging. For some other samples after polishing, the bulk sample was subsequently etched in dilute acid (1% HF, 3% HNO_3, 96% water) for few minutes in order to observe the domain structure. However, this etching solution was not effective for the materials investigated in this project. Furthermore, thermal etching was found to be difficult to control in terms of the appropriate heat treatment conditions. Hence, eventually the samples were examined in the SEM without any etching.

The electron microscopy was carried on a Phillips XL30. During the experiment, the accelerating voltages used were between 8 kV to 10 kV and the working distance was approximately 9 mm, depending on the specimens. Images of each specimen were taken under magnifications of 2000X and 5000X. Polished cross sections were taken in order to observe grain size and phase distribution.

To observed the effect of composition on grain size, the average grain size was calculated using the linear intercept method reported by Abrams et al.[153] Furthermore, a more accurate method for especially polycrystalline ceramics was proposed by Mendelson as illustrated in Equation below.[154]

$$\overline{D} = 1.57\ L \qquad (4.1)$$

L is the average intercept length over a large number of grain measured on a

polished surface.

4.2.3 Electrical measurements

Sintered samples were ground using 800-grade SiC grinding paper; the diameters and thicknesses were measured using a micrometer . Then both pellet faces were coated with silver paste (Gwent Group, UK), dried at 100 ºC for 30 mins and then fired in a furnace for 15 mins at 700 ºC. The sample was then cleaned around the edges using 1200 SiC grinding paper in order to avoid short-circuiting.

4.2.3.1 Ferroelectric hysteresis P-E measurements

Ferroelectric polarisation-electric field (P-E) hysteresis measurements were carried out using the method described by Stewart et al[155] using a HP33120A Function Generator and a Chevin Research HVA1B HV amplifier. The applied voltage and current waveforms were recorded using a Measurement Computing USB-1608FS-Plus A/D card and analysed using LabVIEW-based software. For measurement of ferroelectric properties, the specimens were poled in a silicone oil bath by applying at least 40 cycles of a sinusoidal AC electric field of 5 kV mm^{-1} at a frequency of 2 Hz, until a stable state was achieved.

4.2.3.2 Permittivity-temperature measurements

A ceramic pellet sample with a surface area A and thickness t was coated by sliver paste, as shown in Figure. 4.1. The sample was placed between two electrode platinum wires and placed into a Carbolite CWF 1200 Furnace.

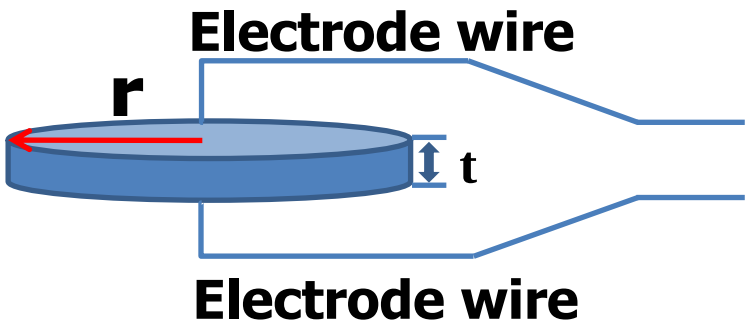

Figure 4.1 The electric circuit for temperature-dependent permittivity measurements.

A HP4284A LCR Meter was used to measure the capacitance, C, and loss tangent, tanδ. The measurements were conducted over a range of temperatures, from 50 to 300 ºC, at frequencies of 1 kHz, 10 kHz and 100 kHz with a HP 4284A LCR meter, using a heating rate of 2 ºC min^{-1}. The real part of permittivity, ε_r, was calculated using Equation 4.2 below.

$$C = \frac{\pi r^2 \varepsilon_0 \varepsilon_r}{t} \tag{4.2}$$

4.2.3.3 Depolarisation-temperature measurements

The poled ceramic pellets were placed into a Carbolite CWF 1200 furnace and connected in parallel with a high-impedance voltmeter (Keithley 6512) and another capacitor of approximately 10 μF which was chosen to be significantly greater than the capacitance of the samples (C_s in Figure 4.2). With this arrangement, the pyroelectric charge, ΔQ, developed on the sample is effectively transferred to the parallel capacitor and can be calculated from the measured voltage, V_C, using the standard Equation for capacitance, as follows:

$$\Delta Q = V_C C_S \tag{4.3}$$

The temperature was recorded by a thermocouple placed in a MACOR bottom substrate next to the samples, as illustrated in Figure 4.2.

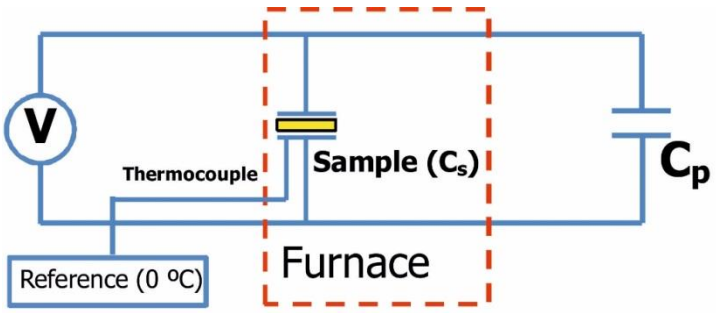

Figure 4.2 Electric circuit for thermally-depolarisation measurement.

The charge released from a sample was recorded during heating from 40 to

300 °C and converted into a change in remanent polarisation, ΔP, using the sample's surface area, A:

$$\Delta P = \Delta Q / A \quad (4.4)$$

4.3 Synchrotron x-ray diffraction experiments

4.3.1 High-resolution SXPD in I11

Powder-type samples were employed for high-resolution synchrotron x-ray diffraction (SXPD) measurements at beamline I11, Diamond Light Source Ltd., UK.[156] *Unpoled* ceramic powders were prepared by crushing and grinding as-sintered ceramic pellets by hand using a pestle and mortar, followed by annealing at 550 °C for 30 mins. *Poled* ceramic powders were also prepared by a similar method from poled ceramic pellets, but without the annealing procedure. It was shown in previous publications that this procedure provides the means to identify the crystal structure of a poled sample after a field-induced transformation, as noted above.[90, 157] The powder samples were loaded into glass capillaries of 0.3 mm diameter.

A photon energy of 25 keV was selected to reduce the effect of sample absorption ($\mu \cdot r \sim 2.5$. where μ is the absorption coefficient and r is the diameter if the capillary sample) and the resulting diffraction patterns were recorded using ~~a~~ multi-analyser crystal (MAC) detector at room temperature. The wavelength of $\lambda = 0.494731(10)$ Å was calibrated using the diffraction pattern of a high quality Si standard powder (SRM640c). The experimental apparatus within the I11 beamline hutch is displayed in Figure 4.3. Full-pattern refinements were carried out using *Topas* refinement software, v3.0.[158] In addition to crystallographic parameters and structural parameters, the lattice parameters and relative phase quantity were obtained from refinements of the SXPD patterns.

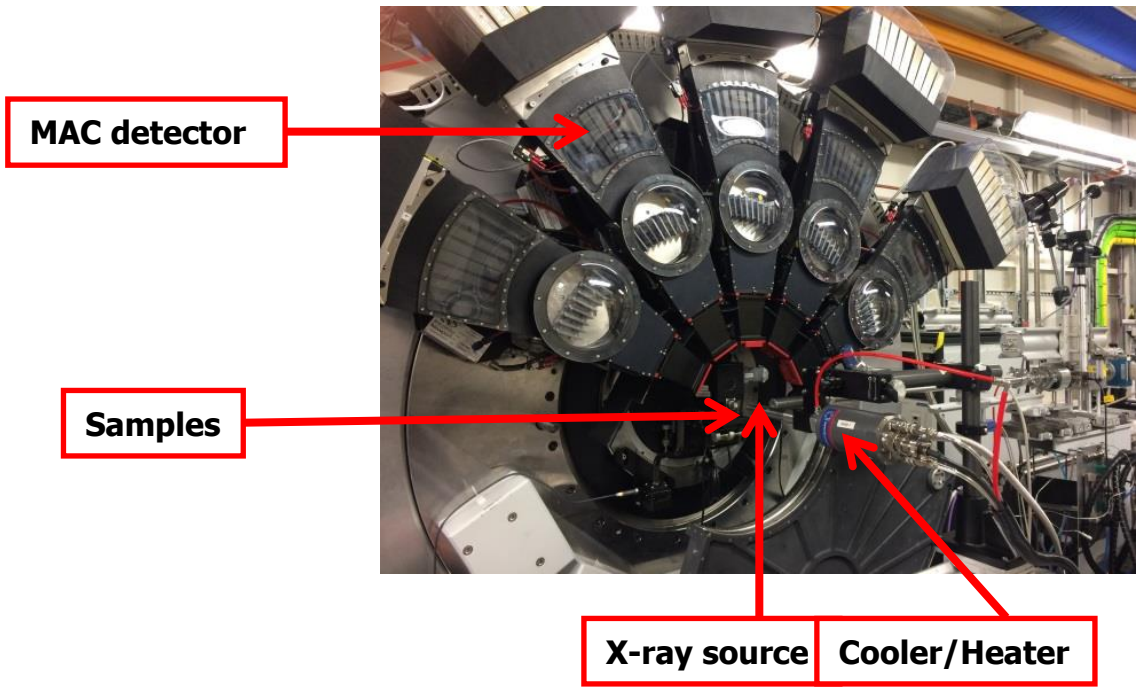

Figure 4.3 The arrangement of sample and detector within beamline I11.

4.3.2 High-energy synchrotron x-ray diffraction in I15

The sample preparation for in-situ experiments in I15, Diamond, followed the same procedures mentioned above. The sintered ceramic pellets were mechanical ground below 1 mm thickness, followed by firing silver electrodes on both faces at 550 ºC (Gwent Group, UK). Square-ended rod specimens having dimensions of 1mmx1mmx3.5mm were machined using a diamond dicing saw at Morgan Advanced Materials (Wrexham, UK). As illustrated in Figure 4.4, the specimen was inserted between an upper brass pin and a lower copper plate electrode in order to connect the output leads of the high voltage amplifier. The specimen and electrodes were immersed in silicone oil within an insulating polyimide bath. A soldering iron was used to heat up the oil via a heated steel block, which was also immersed in the oil bath. The x-ray beam was transmitted through the specimen and through a rounded rectangular aperture in the PTFE outer frame of the specimen holder. All samples were been poled from 0 to $\pm$6 kV mm^{-1} with a step of 0.5 kV mm^{-1} per half second. At least 15 cycles of maximum electric field was applied to each sample.

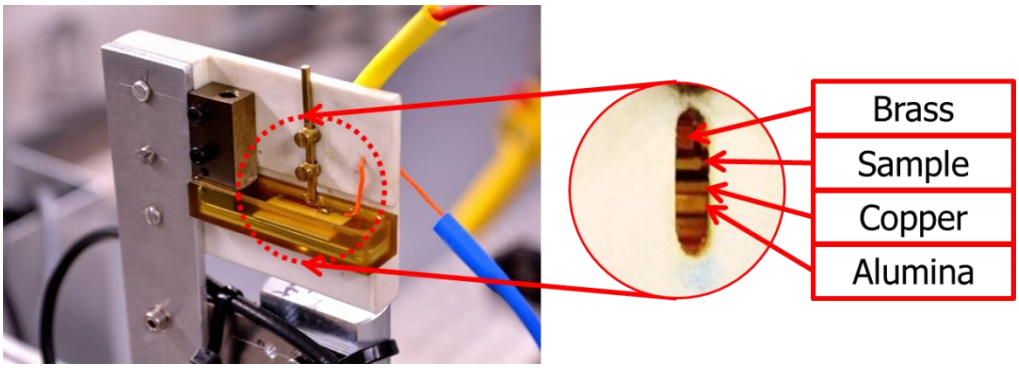

Figure 4.4 The sample holder for experiment in beamline I15.

The high-energy synchrotron XRD studies were performed at beamline I15 of the Diamond Light Source using monochromatic X-rays with a photon energy of 67 keV and wavelength of 0.1771 Å. The X-ray beam was focused down to 70 micron in diameter and cleaned up with the pinhole directly in front of the sample. 2-dimensional XRD images were recorded using a Perkin Elmer flat-panel detector positioned approximately 1 m from the sample. The experimental arrangement within beamline I15 is shown in Figure 4.5. The recorded images (diffraction rings) can provide the grain orientation information to analyse the influence of electric field.[159] They were converted into conventional 1-dimensional XRD patterns corresponding to a range of grain orientations, ψ, relative to the poling direction, using Fit2D.[160] The profiles for selected diffraction peaks were fitted using X-fit.[161]

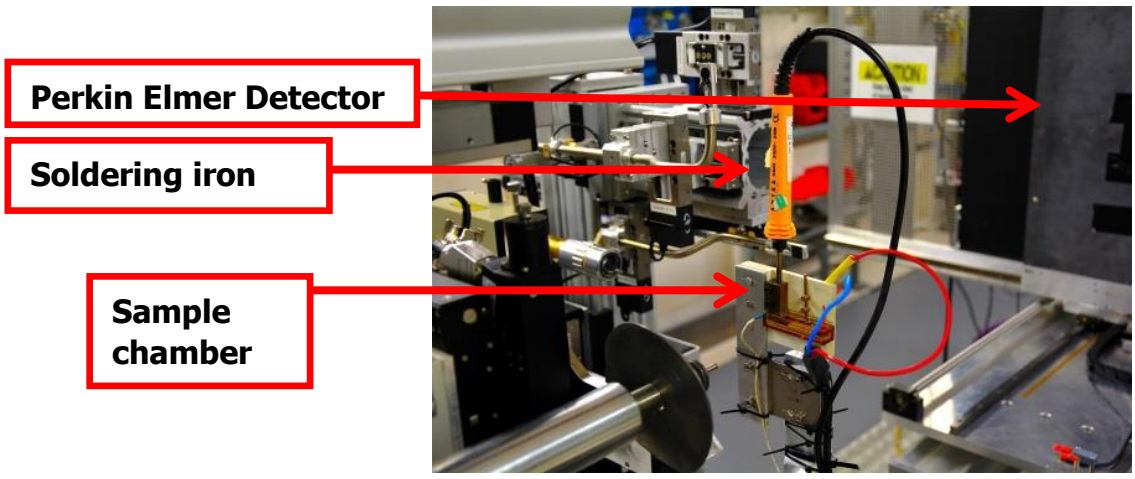

Figure 4.5 The arrangement of sample and detector within Beamline I15.

The sample preparation for ex-situ experiments in I15, Diamond, followed the same procedures for the in-situ experiment described above. However, instead of poling in-situ at Diamond, the bar-shaped specimens were poled in advance at the University of Manchester using the in-house ferroelectric hysteresis P-E measurement equipment. The specimens were poled using an electric field of at least 6 kV mm^{-1} and ex-situ diffraction measurements carried on at beamline I15, Diamond with beamline energy of 67 keV and wavelength of 0.1771 Å.

4.3.3 Data reduction

For analysis of the diffraction data, each two-dimensional image was converted into a sequence of conventional one-dimensional diffraction patterns by integration over an angular range of ±5° around the nominal angle of orientation using Fit2D and then the intensities and positions of individual peaks were determined by means of X-fit.[161] Changes in the diffraction patterns were monitored at the end of each cycle of 6 kV mm^{-1}, which was controlled remotely during the experiment so that the changes in domain configuration and lattice strain in response to the applied electric field could be determined *in-situ*, with an acquisition time for each image being of the order of 20 s. Some of the samples were previously poled in-house at the University of Manchester, and hence were scanned *ex-situ* without application of the electric field. After scanning, individual peaks were fitted to a combination of pseudo-Voigt-type peaks, using the either X-fit software[161] or a Matlab peak-fitting script that was developed in-house.

5 Phase switching behaviour in $Na_{0.5}Bi_{0.5}TiO_3$-$KNbO_3$ ceramics

In this chapter, the structural and electrical properties of the (1-x)NBT-xKN system are fully investigated as function of composition and temperature. The phase transition between RF and metastable FE states are examined using temperature-dependent electrical measurements. High resolution synchrotron SXPD is used to identify the crystal structures for poled and unpoled states at room temperature and to observe the structural transformations. Additionally, 'in-situ' experiments are performed using high energy synchrotron XRD to observe the structural transformations induced by an AC electric field and analyse the development of preferred ferroelectric domain orientations.

5.1 Density analysis

The relative densities of different compositions in the NBT-xKN (x=0.01 to 0.09) system sintered at different temperatures are presented in Figure 5.1. After calcination, the pressed ceramic pellets were sintered at temperatures ranging from 1100 to 1250 ºC. At 1100 ºC, the relative density obtained was no more than 93% for all compositions. With increasing sintering temperature, the relative density increased to approximately 95% at 1200 ºC, followed by a dramatic drop to 88% at 1250 ºC. Thus, 1200 ºC was selected as the optimum sintering temperature for the NBT-xKN system. It is assumed that the reduction in density at the highest sintering temperatures is caused by the loss of volatile oxides, such as Na_2O, K_2O and Bi_2O_3.[162-166]

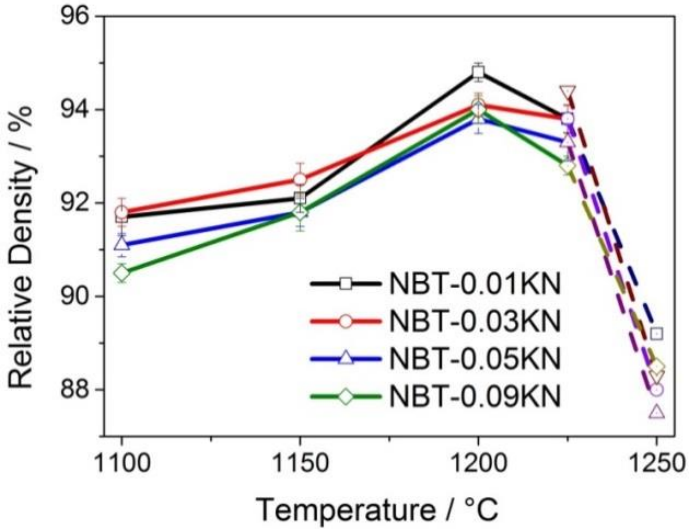

Figure 5.1 Relative density as a function of sintering temperature for NBT-xKN ceramics.

5.2 Lab XRD results

5.2.1 Calcined powders

The XRD patterns of NBT-xKN (x=0.01 to 0.09) powders calcined at a temperature of 900 ºC for 10 hours are presented in Figure 5.2.

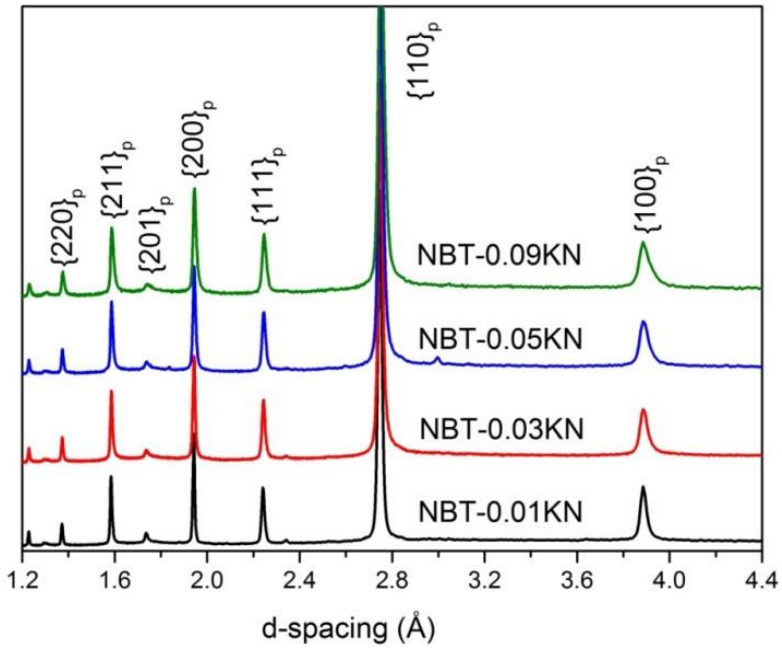

Figure 5.2 The XRD full patterns of calcined powders for NBT-xKN.

The peak profiles of $\{111\}_p$ and $\{200\}_p$ for all compositions in the NBT-xKN (x=0.01 to 0.09) system are displayed in Figure 5.3. It is evident that single $\{111\}_p$ and $\{200\}_p$ peaks are observed for all compositions. Furthermore, the positions of both peaks shift slightly to larger d-spacing with increasing KN content.

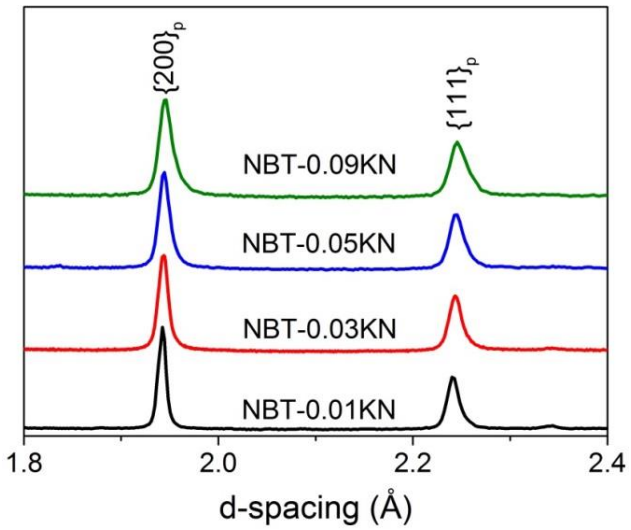

Figure 5.3 The representative $\{111\}_p$ and $\{200\}_p$ XRD peaks of calcined powders for the NBT-xKN system.

5.2.2 Sintered ceramic pellets

The crystal structures for both poled and unpoled NBT-xKN (x=0.01 to 0.09) ceramic pellets were investigated using lab XRD, as displayed in Figure 5.4. All compositions are observed to be single phase with a perovskite structure. For the unpoled state (Figure 5.4 a), all the peaks are single, indicating a cubic structure. In contrast, a rhombohedral structure was identified for compositions with low KN contents in the poled state (Figure 5.4 b), characterised by a split $\{111\}_p$ and a single $\{200\}_p$ peak. For compositions with high KN content, all peaks are observed to be single.

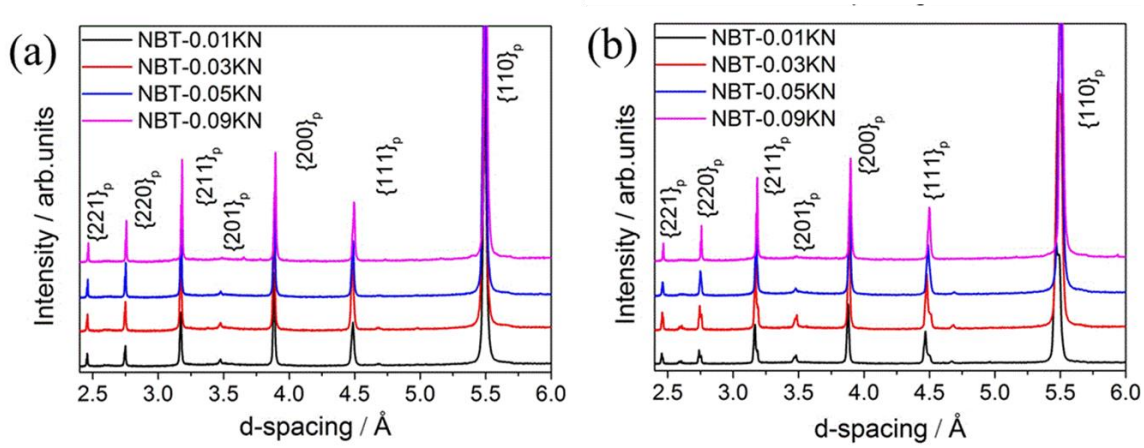

Figure 5.4 The XRD full patterns of (a) unpoled and (b) poled states for all compositions in NBT-xKN system.

Therefore, it was found that an irreversible electric field-induced structural transformation from cubic to rhombohedral occurred for compositions with low KN content. However, there is no obvious influence of the poling procedure on the structure for high KN contents. To further investigate this structural transformation induced by poling, high resolution synchrotron powder x-ray diffraction (SPXD) was conducted in beamline I11 at Diamond, as described in Section 5.6 below.

5.3 SEM

The cross-Sectional SEM images for NBT-xKN (x=0.01 to 0.09) ceramics were recorded under BSE and are presented in Figure 5.5. The average grain size for all compositions in NBT-xKN system is listed in Table 5.1. The grain size decreases with increasing KN content so that the KN is estimated to inhibit the grain growth. Similar behaviour was reported that adding KNN into NBT solid solution inhibited the grain growth due to lower diffusion rate for Nb[167, 168] and 'pinning effect' at the grain boundary.[169]

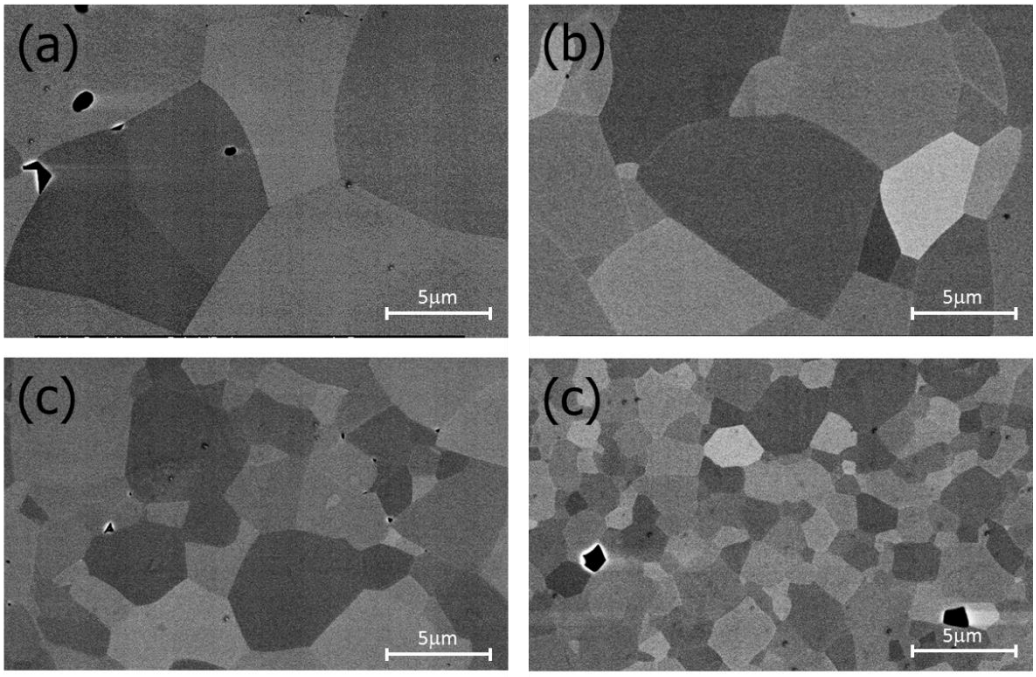

Figure 5.5 Cross-Sectional SEM images for (a) NBT-0.02NN (b) NBT-0.04NN (c) NBT-0.06NN and (d) NBT-0.08NN.

Table 5.1 Average grain sizes for NBT-xKN ceramics.

Compositions	Grain size / μm
NBT-0.01KN	8.55±0.34
NBT-0.03KN	5.38±0.43
NBT-0.05KN	4.11±0.19
NBT-0.09KN	2.05±0.26

5.4 Temperature-dependent ferroelectric properties

5.4.1 Polarisation-current density-electric Field (P-J-E) loops

The ferroelectric hysteresis loops (P-E) and current density curves (J-E) for NBT-0.01KN ceramic over the temperature range from 30 to 120 ºC are presented in Figure 5.6. From 30 to 90 ºC, this material behaves as a typical ferroelectric with saturation of the P-E loop and an unsplit switching peak in the J-E curve. With increasing temperature, the coercive field drops while both P_{max} and P_{rem} increase, indicating enhanced domain switching. At 120 ºC, a slight constriction and a doublet switching peak are observed for the P-E and J-E loops respectively, indicating that a reversible transformation between PNRs and long-range ordered metastable FE state was induced under the high electric-field at this temperature.

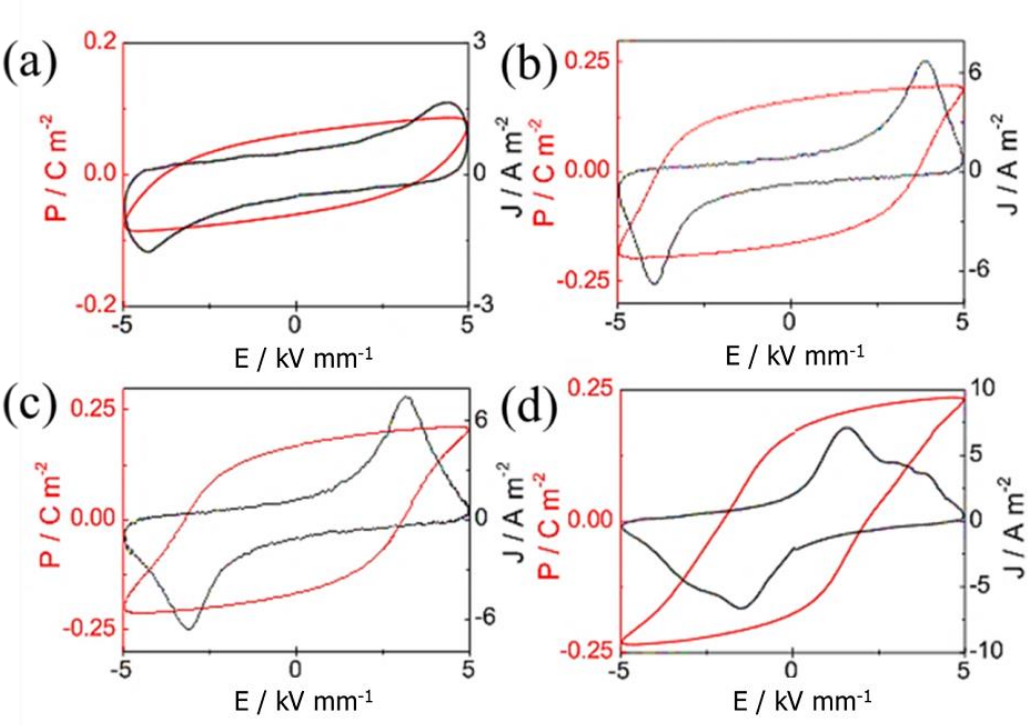

Figure 5.6 The P-J-E curves for NBT-0.01KN ceramic at temperatures of (a) 30 ºC (b) 65 ºC (c) 90 ºC and (d) 120 ºC.

The P-E loops and J-E curves for the NBT-0.03KN ceramic over the temperature range from 30 to 120 ºC are illustrated in Figure 5.7. At room temperature, a well-defined P-E loop is observed with relatively high P_{max} and P_{rem} values of 0.29 C m^{-2} and 0.26 C m^{-2} respectively, indicating an electric field-induced metastable ferroelectric order. With increasing temperature to 65 ºC, a slightly constricted P-E loop is observed and split polarisation switching peaks are present on the J-E curves for both positive and negative field, suggesting that the switching between PNRs and long-range ordered FE state becomes reversible at 65 ºC. The E_f and E_b values at this temperature are estimated as 3.4 mm^{-1} and 1.6 kV mm^{-1}. Here, E_f represents the forward and E_b the backward switching field between weak-polar PNRs and long-range ordered FE states.

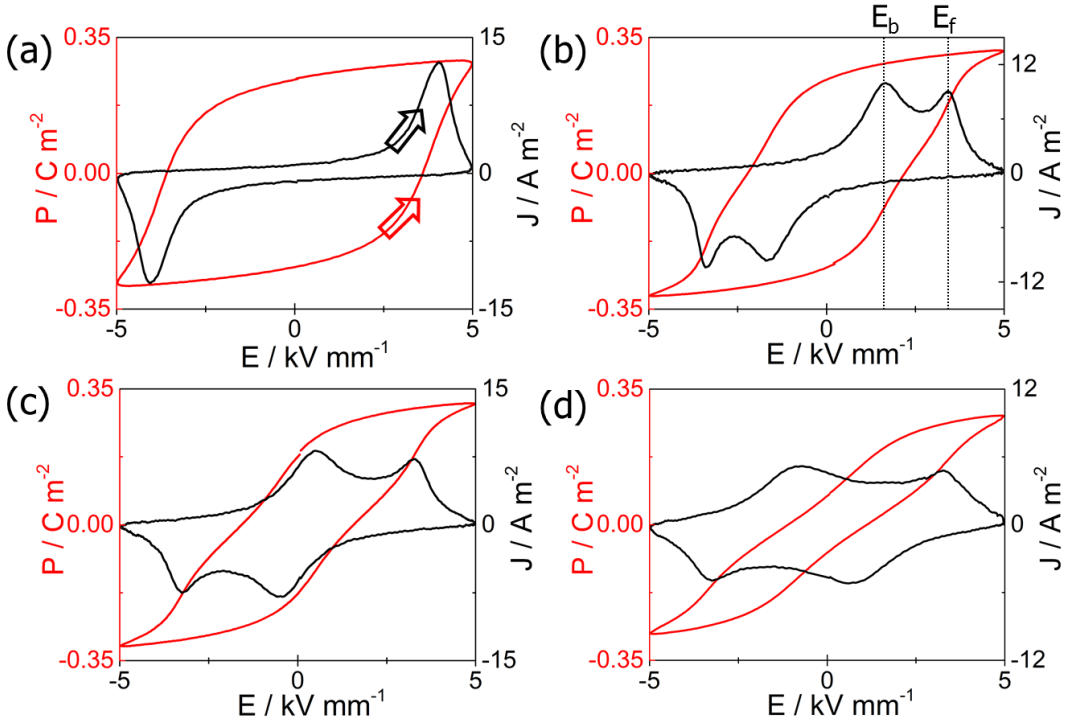

Figure 5.7 The P-J-E curves for NBT-0.03KN ceramic at temperatures of (a) 30 ºC (b) 65 ºC (c) 90 ºC and (d) 120 ºC.

With further heating, a more constricted P-E loop is observed and the separation between the two polarisation switching peaks in the J-E curve becomes greater. However, P_{max} retains approximately the same value from 30 ºC to 120 ºC, indicating that the polarisation can reach a similar maximum value after the PNRs switch to the long-range ordered FE state with the electric field on. In contrast,

P_{rem} declines dramatically from 0.28 C m^{-2} at 65 ºC to approximately zero at 120 ºC, indicating that the long-range ordered FE state is lost on removing the electric field and the PNRs become more stable with increasing temperature. Therefore, an irreversible electric field-induced transformation to long-range ordered metastable FE state occurred at 30 ºC. However, the transition between PNRs and long-range ordered FE state became reversible at temperatures of 65 ºC and above.

The P-E and J-E loops for NBT-0.05KN in the temperature range from 30 to 120 ºC are shown in Figure 5.8. Unlike NBT-0.01KN and NBT-0.03KN, the split polarisation switching peaks in the J-E loop and a constricted P-E loop are evident at room temperature, indicating that the reversible transition between PNRs and long-range ordered FE state occurred under the applied electric field. With increasing temperature, the P-E loop develops further constriction and the separation of the split switching peaks in J-E curves becomes more pronounced. At 120 ºC, a very slim loop is observed with a P_{rem} value of 0.02 C m^{-2}, indicating a weak ferroelectric behaviour.

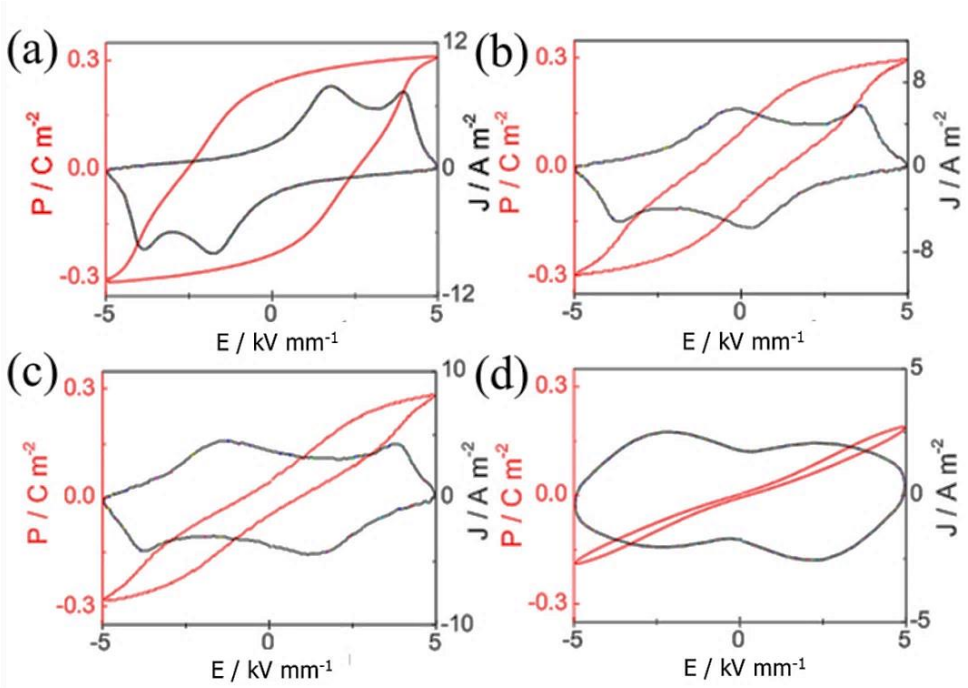

Figure 5.8 The P-J-E curves for NBT-0.05KN ceramic at temperatures of(a) 30 ºC (b) 65 ºC (c) 90 ºC and (d) 120 ºC.

The P-E loops and J-E curves for NBT-0.09KN in the temperature range from 30 to 120 ºC are shown in Figure 5.9. At room temperature, a slim P-E loop is observed with P_{max} and P_{rem} values of 0.18 C m^{-2} and 0.07 C m^{-2} respectively. At elevated temperatures, the P-E loops become slimmer, indicating a weaker ferroelectric behaviour, but the P_{max} value remains at approximately 0.14 C m^{-2}. These observations indicate that it might be possible to achieve high electric field-induced strain in these materials, with low hysteresis, and that this strain may be relatively temperature-independent. It is evident that increasing KN content leads to increasing disorder and the occurrence of more-stable PNRs in the unpoled materials, which cannot be switched irreversibly into a long-range ordered ferroelectric phase under the application of a high electric field.

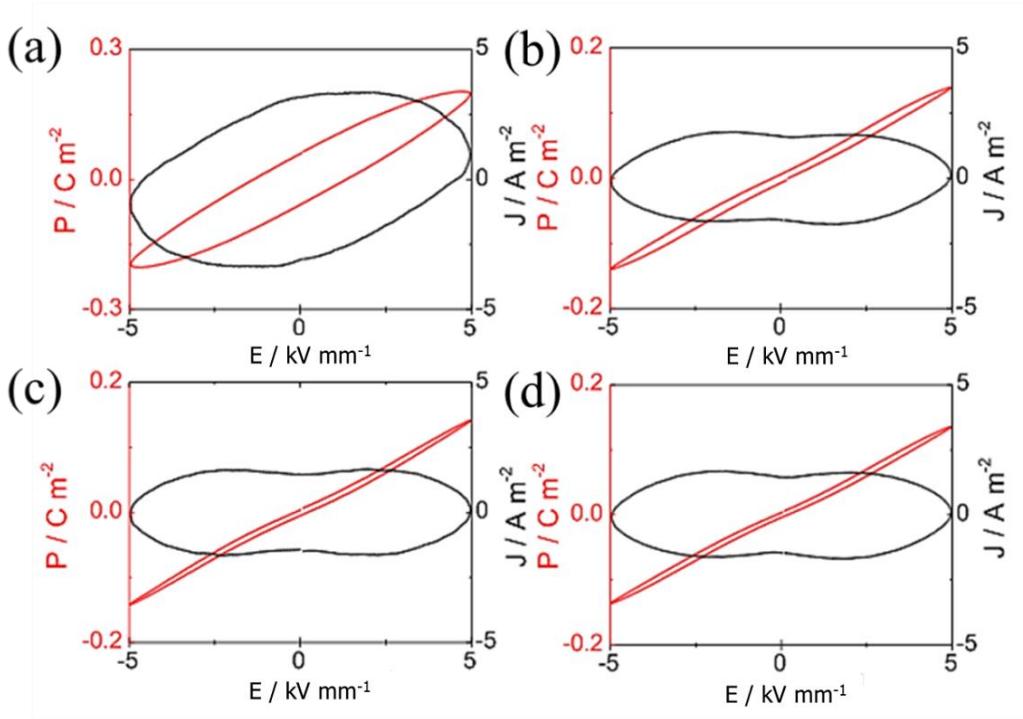

Figure 5.9 The P-J-E curves for NBT-0.09KN ceramic at temperatures of (a) 30 ºC (b) 65 ºC (c) 90 ºC and (d) 120 ºC.

5.4.2 Summary

Both P-E and J-E ferroelectric hysteresis loops were obtained for NBT-xKN (x=0.01 to 0.09) ceramics in the temperature range from 30 to 120 ºC. The polarisation switching field (E_c or E_b/E_f), remanent polarisation (P_{rem}) and maximum polarisation (P_{max}) values are summarized in Table 5.2 below.

Table 5.2 The (a) polarisation switching field (b) maximum polarisation and (c) remanent polarisation for NBT-xKN ceramics at different temperatures.

(a) E / kV mm^{-1}

x	30 ºC	65 ºC	90 ºC	120 ºC
0.01	4.4	3.7	3.1	2.0
0.03	4.1	3.4/1.6	3.3/0.5	3.3/0.7
0.05	3.9/1.8	3.7/0.4	3.7/1.4	N/A
0.09	N/A	N/A	N/A	N/A

(b) P_{max} / C m^{-2}

x	30 ºC	65 ºC	90 ºC	120 ºC
0.01	0.08	0.18	0.20	0.23
0.03	0.29	0.32	0.31	0.28
0.05	0.31	0.30	0.28	0.19
0.09	0.18	0.14	0.14	0.13

(c) P_{rem} / C m^{-2}

x	30 ºC	65 ºC	90 ºC	120 ºC
0.01	0.06	0.15	0.17	0.18
0.03	0.26	0.29	0.19	0.07
0.05	0.24	0.13	0.05	0.01
0.09	0.07	0.01	0.01	0.01

As noted above, the x-ray diffraction peak profiles for all of the as-sintered ceramics appeared to be single without splitting, indicating a cubic structure. However, for certain compositions, such as NBT-0.01KN and NBT-0.03KN, well-developed ferroelectric hysteresis loops with a relatively high remanent polarisation were observed. A similar phenomenon was reported by Daniels,[12] who observed an irreversible electric field-induced structural transformation from cubic to tetragonal in NBT-0.07$BaTiO_3$ ceramics. The tetragonal phase also

exhibited orientation-dependent ferroelectric domain switching behaviour.[12] It is proposed that an electric field-induced phase transition and structural transformation occurred for low KN contents in the present study. For NBT-0.01KN and NBT-0.03KN, the PNRs can be transformed irreversibly into the metastable long-range FE order at room temperature even after removing the external electric field.

With increasing temperature, a constricted P-E loop and a split polarisation switching peak in the J-E curves were observed at 120 ºC and 65 ºC for NBT-0.01KN and NBT-0.03KN respectively, which are similar to those of NBT-0.05KN at room temperature, indicating that the transformation from weak-polar PNRs to metastable FE order became reversible. A similar result was obtained by Viola,[36, 170] for the $CaTiO_3$-modified NBT-BT system. Specifically, the occurrence of forward and backward switching peaks, E_f and E_b, in the J-E curves represents the electric field-induced switching between PNRs and the long-range ordered FE state. For example, J-t and E-t profiles were reported for Mn-modified NBT-BT to illustrate the phase transition during the application of the AC electric field.[171] At lower temperatures, the nonergodic-RF (NR) state was transformed irreversibly to FE state. However, it was found that the NR state evolved into an ergodic-RF (ER) state with increasing temperature, which could transform reversibly between ER and FE states under the influence of an AC electric field.[171]

Finally, the NBT-0.09KN ceramic exhibited a weak ferroelectric behaviour with slim P-E loops at all of the temperatures used in this investigation.

5.5 Temperature-dependent depolarisation

Thermal depolarisation results for NBT-0.01KN and NBT-0.03KN are presented in Figure 5.10. The samples were poled prior to the measurements using at least 30 cycles of an AC electric field with amplitude 5 kV mm^{-1} at room temperature. The poled samples lost the majority of their remanent polarisation at approximately 133 ºC and 74 ºC for NBT-0.01KN and NBT-0.03KN respectively.

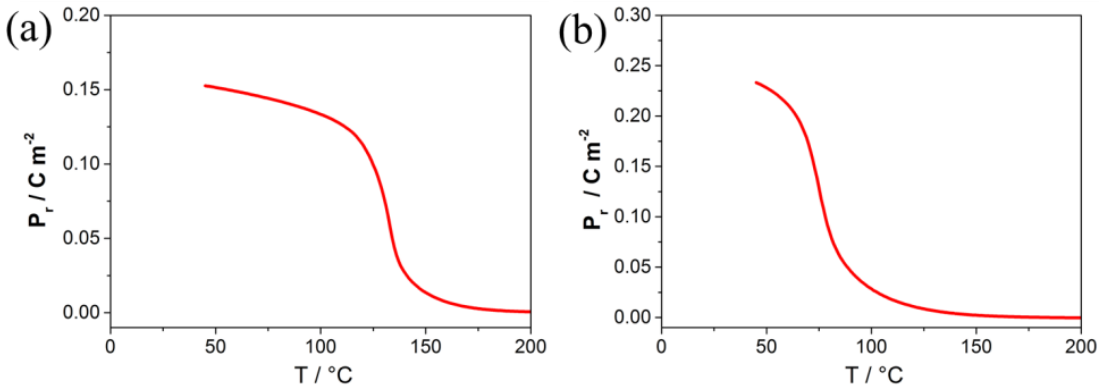

Figure 5.10 Temperature-dependent depolarisation curves for (a) NBT-0.01KN and (b) NBT-0.03KN ceramics.

The depolarisation temperature, T_d, in NBT-xKN decreases with increasing KN content. It was found that both compositions previously experienced an irreversible transformation from weak-polar PNRs to metastable FE order under the high electric field, indicating a nonergodic-RF state. In contrast, for compositions with x=0.05 and x=0.09, a thermal depolarisation temperature could not be obtained due to the reversible transformation between weak-polar PNRs and ferroelectric order during poling at room temperature, indicating an ergodic-RF state. To summarise, the depolarisation temperature and maximum depolarisation rate for NBT-xKN are listed in Table 5.3 below.

Table 5.3 The thermally-induced depolarisation temperature and maximum depolarisation rate for all compositions in the NBT-xKN system.

Compositions	T_d / °C	dP / dT / mC m^{-2} $°C^{-1}$
NBT-0.01KN	133	8
NBT-0.03KN	71	9
NBT-0.05KN	N/A	N/A
NBT-0.09KN	N/A	N/A

It has been reported that adding BT nanowires into a NBT-KBT-BT solid solution can maintain the electrical properties and enhance the depolarisation temperature by approximately 20 °C.[172] More recently, it was reported by Zhang[173] that a 'depolarisation-free' 0-3 type composite was made by adding semiconducting ZnO particles into a NBT-BT solid solution. It was proposed that the presence of ZnO particles at the grain boundary can reduce the porosity of the ceramic and, most importantly, the charges generated during poling can compensate the depolarisation field after removing the external field.[173] Such an approach would provide a potentially useful means of tailoring the stability of the FE phase in NBT-based solid solutions.

5.6 Dielectric properties

5.6.1 Poled states

The changes in dielectric permittivity and loss tangent with temperature for poled NBT-xKN (x=0.01 to 0.09) specimens are shown in Figure 5.11. All compositions exhibit significant variations in permittivity with temperature.

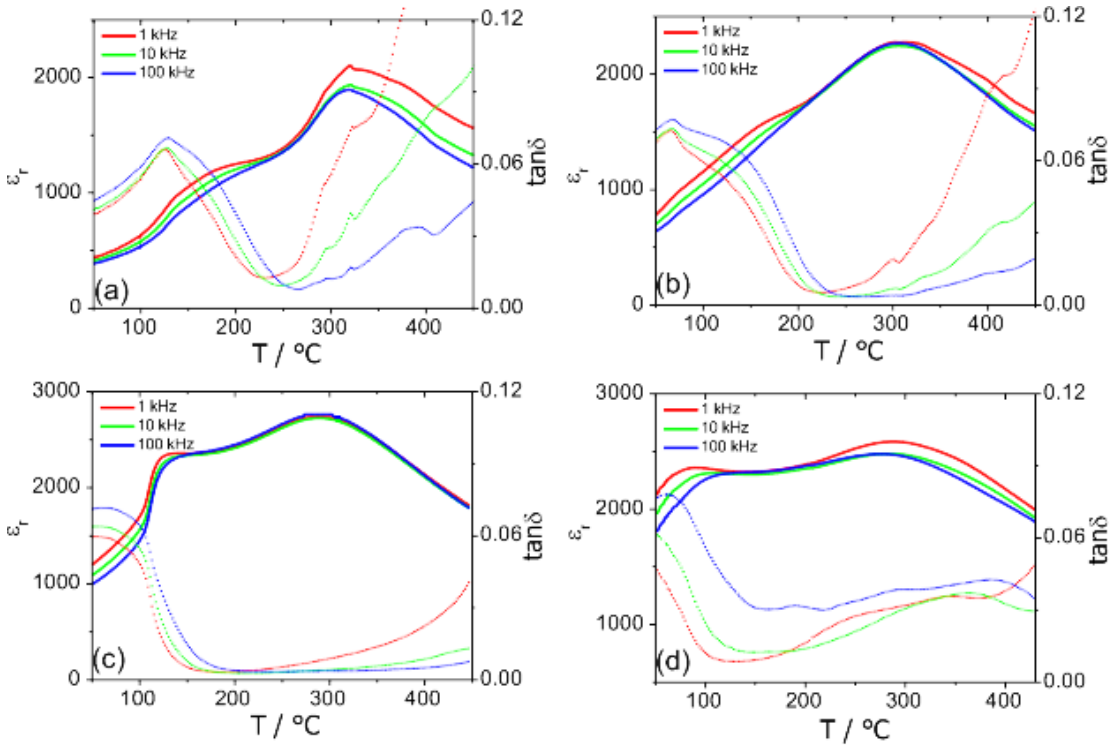

Figure 5.11 Temperature-dependent permittivity and loss curves for poled NBT-xKN ceramics (a) x=0.01 (b) x=0.03 (c) x=0.05 (d) x=0.09.

For the composition with x=0.01, the initial ε_r value is in the region of 450; it increases steadily up to 1050 at approximately 130 ºC, at which temperature the frequency dispersion is enhanced. With further increasing temperature, ε_r increases sharply up to the dielectric peak value of 2058 at approximately 310 ºC, followed by a decrease with reappearance of frequency dispersion upon further heating. The frequency dispersion at lower temperatures can be attributed to the influence of the PNRs, while that at higher temperatures is most likely associated with increasing electronic conductivity and the associated space-charge polarisation; the strong increase in loss tangent at low frequencies (see below) provides supporting evidence for the latter.

The loss tangent, tanδ, also exhibits frequency-dependent behaviour and the transition temperature from metastable ferroelectric order to RF state, T_{F-R}, is indicated by the relatively sharp peak at 127 ºC.[73] The tanδ starts at approximately 0.05 and increases up to 0.065 at T_{F-R}, followed by a significant decrease down to 0.02 at a temperature of 230 ºC. The tanδ increases with increasing measurement frequency before T_{F-R} but then exhibits an inverse dependence on frequency at high temperatures, consistent with a contribution from electronic conductivity.[174]

Upon increasing the KN content to 3%, the transition temperature, T_{F-R}, for NBT-0.03KN decreased to 68 ºC and the maximum permittivity, ε_{max}, was enhanced to 2280 at approximately 305 ºC, which is similar to that of NBT-0.01KN. The dielectric loss, tanδ, shows a similar behaviour to that of NBT-0.01KN but slightly less frequency dispersion above 210 ºC.

With further increase in KN content to 5% and 9%, the T_{F-R} transition becomes less pronounced on both ε_r-T and tanδ–T curves, while ε_r starts higher at approximately 1000 and 2000 respectively. For NBT-0.05KN, ε_r increases sharply to the first anomaly at approximately 135 ºC, followed by a progressive enhancement to a frequency-independent ε_{max} at 295 ºC and then a decrease with further heating. For NBT-0.09KN, the shape of the ε_r-T relation was relatively flatter than other compositions. It experiences a slight increase to the first frequency-dependent anomaly at approximately 100 ºC and then reduces slightly to a frequency-independent value of 2350 up to 200 ºC. With further heating, the frequency dispersion reappears up to the highest temperature of 450 °C.

5.6.2 Unpoled states

The ε_r-T, and tanδ–T relations for unpoled NBT-xKN (x=0.01 to 0.09) specimens within the temperature range from 50 to 450 ºC are illustrated in Figure 5.12. Compared to the results for the poled states described above, no obvious T_{F-R} is observed for any composition and ε_{max} was almost frequency-independent. The ε_r values for all compositions show less frequency dispersion at lower temperatures until reaching the first anomaly, followed by a frequency-independent enhancement to T_m. Eventually, the ε_r values decrease with the reappearance of slight frequency dispersion upon further heating.

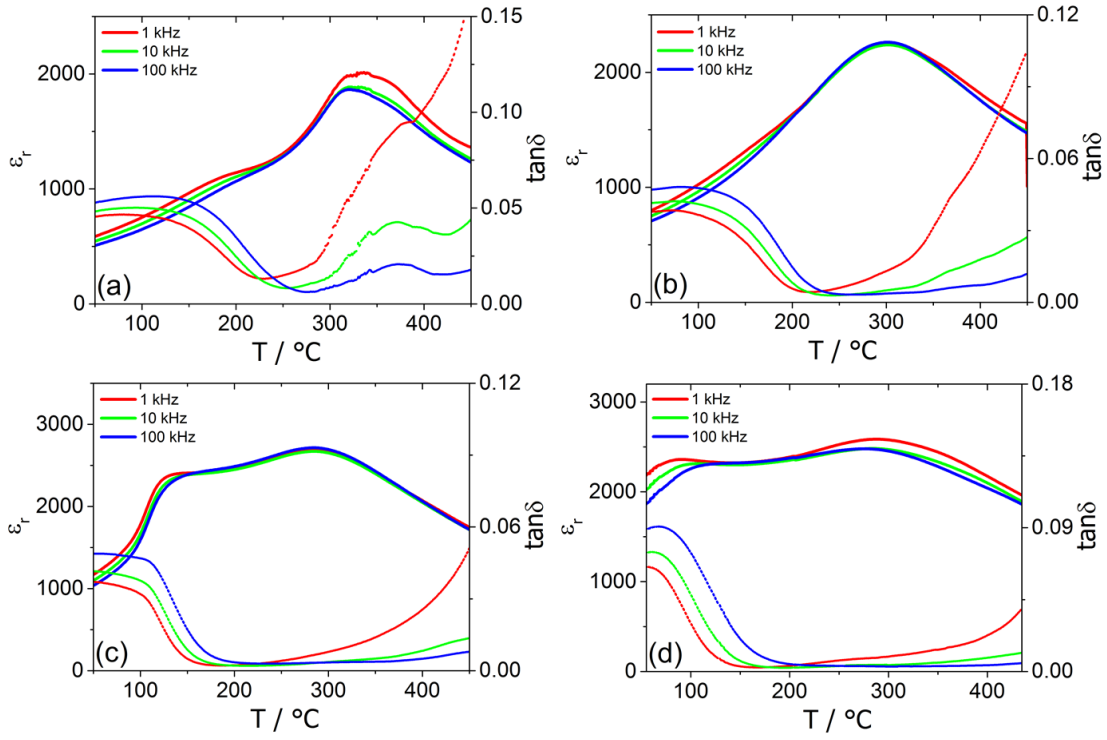

Figure 5.12 Temperature-dependent permittivity and loss curves for unpoled NBT-xKN specimens (a) x=0.01 (b) x=0.03 (c) x=0.05 (d) x=0.09.

5.6.3 Summary

The important dielectric parameters including transition temperature, T_{F-R}, the maximum permittivity, ε_{max}, and the dielectric peak, T_{max}, for poled NBT-xKN were obtained from the data illustrated in the Figures above and are listed in Table 5.4 below.

Table 5.4 The transition temperature, maximum permittivity and the temperature for dielectric peak for poled NBT-xKN ceramics.

Compositions	T_{F-R} / °C	ε_{max}	T_{max}
x=0.01	127	2058	310
x=0.03	68	2280	310
x=0.05	N/A	2763	295
x=0.09	N/A	3085	288

It was found that a prominent peak in the tanδ-T plot for the transition temperature, $T_{F-R,}$ was only observed for poled NBT-0.01KN and NBT-0.03KN ceramics, which can be attributed to the electric field-induced metastable FE phase. Under application of a high electric field, the PNRs can transform to long-range metastable FE order with the presence of a micro-domain structure. This kind of behaviour is referred to as nonergodic-relaxor behaviour (NR), as explained by Dittmer.[29] However, the metastable FE order can be destabilised under heat treatment. It was found that the transition from the metastable FE to RF state is the reason for the loss of remanent polarisation, evidenced by constricted P-E loops and a split polarisation switching peak in the J-E curves. Furthermore, the T_{F-R} decreased with increasing compositional disorder with the result that no T_{F-R} could be detected for NBT-0.05KN and NBT-0.09KN.

Another notable phenomenon is the lower-temperature shoulder in the ε_r-T relationship, which was observed for all compositions in the NBT-xKN system. Furthermore, this low-temperature shoulder was less prominent with increasing frequency. A number of possibilities have been proposed to explain the occurrence of this low-temperature shoulder, including the depolarisation,[125] phase transition,[126] and ageing effects. As shown above, the phase transition

temperature from the electric field-induced metastable ferroelectric order to RF states was determined by the tanδ-T curve. Furthermore, the lower-temperature shoulder for the poled state did not correspond to the structural transformation temperature, which is discussed in the following Section. It was reported previously that ageing effects can cause the appearance of a low temperature shoulder in the ε_r-T curve, for example in $Sr_{0.75}Ba_{0.25}Nb_2O_6$,[175] $Pb(Mg_{1/3}Nb_{2/3})O_3$-$PbTiO_3$[176] and La-PZT.[177] However, the mechanism of ageing for lead-free piezoelectric ceramics is not necessarily the same as that in lead-based materials. For example, it was found that the ageing for the unpoled and poled states for NBT-based materials were different due to the existence of PNRs.[178] Furthermore, no significant domain stabilisation effects were observed in the present study during the ferroelectric measurements on NBT-KN ceramics.

This kind of behaviour has been reported in many NBT-based systems, such as Pr-modified NBT-0.07BT,[179] NBT-BT-$SrTiO_3$,[180] and Mn-modified NBT-BT.[181] In addition, a new phase transition temperature, referred to as T_{DV}, was identified where the low-temperature shoulder disappeared.[179] Due to the existence of localised structure in NBT-based materials, an in-depth study was conducted for NBT-0.06BT to investigate different states of PNRs in different temperature regimes by using high-resolution TEM.[11] The PNRs were said to exist as a single phase, which experiences a phase transition between the lower-temperature states to the high-temperature states, or co-existence. Both states of PNRs contributed to the frequency-dependent shoulder in the ε_r-T curve and the materials were defined as being in a "frustrated state". For example, both low-temperature PNRs with the rhombohedral R3c symmetry, and high-temperature PNRs with the tetragonal P4bm symmetry, were present in NBT-0.06BT ceramics at room temperature.[11].

Therefore, it is concluded that potentially different kinds of PNRs, for example with rhombohedral and monoclinic symmetries on a local scale, could be present for all compositions in the NBT-xKN system, leading to the low-temperature

shoulder. The transformation between different PNR symmetries is the most likely cause for the frequency-independent peak in dielectric permittivity at higher temperatures. Further investigation is required using TEM to detect the nano-scale structures in NBT-xKN ceramics.

5.7 High resolution SXPD experiments (Diamond beamline I11)

The aim of this investigation was to identify the effect of poling on the crystal structures in NBT-xKN ceramics by using high resolution SXPD. Based on Garg's studies,[182] the use of crushed poled specimens provides a way to obtain a random texture in a specimen, which facilitates the use of full-pattern refinement procedures. By comparing the results obtained for the unpoled and poled states, it is possible to determine whether the poling procedure resulted in an irreversible structural phase transformation.

5.7.1 Poling procedure

Prior to the diffraction experiments, an alternating electric field with an amplitude 5.5 kV mm^{-1} was applied to the NBT-xKN virgin sample at room temperature. Taking NBT-0.03KN as an example, it was observed that several cycles of the electric field were required in order to obtain a saturated P-E loop, as shown by the results presented in Figure 5.13. A maximum polarisation, P_{max}, of 0.30 C m^{-2} was obtained after approximately 20 cycles of the electric field, remaining approximately constant thereafter. It was noted in Section 5.3.1 above that a saturated P-E loop would not normally be expected for a relaxor ferroelectric such as NBT-xKN, in which the crystal structure appeared as a pseudo-cubic phase, indicating that an electric field-induced structural transformation occurred during the measurement procedure. Also, it is evident that both the remanent polarisation, P_{rem} and the maximum value, P_{max}, increased gradually from 0.05 C m^{-2} to 0.26 C m^{-2} and 0.12 C m^{-2} to 0.31 C m^{-2} respectively after 20 cycles, suggesting that this was a progressive transformation.

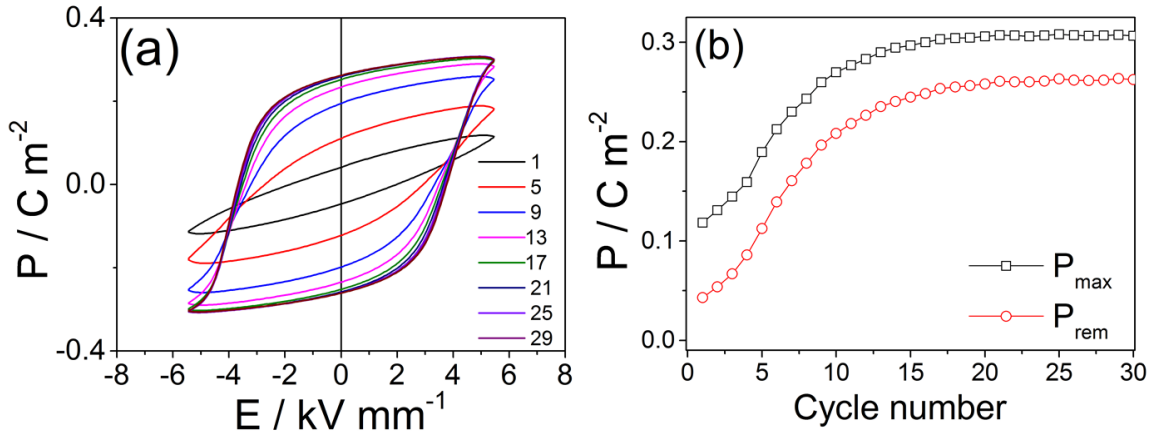

Figure 5.13 Changes in (a) P-E loops and (b) polarisation values obtained for NBT-0.03KN ceramics after cycling under an AC electric field.

5.7.2 Influence of composition at room temperature

The SXPD full patterns for unpoled and poled NBT-xKN ceramics with x=0.01 to 0.09 are illustrated in Figure 5.14. No secondary phase was detected for all compositions. For the unpoled state, all compositions were identified as cubic phase with single peaks for all reflections. The diffraction peaks shifted to higher d-spacing with increasing KN content, indicating expansion of the lattice due to the larger ionic radii. The ionic radius of K^+ is 1.51 Å, which is larger those for Na^+ (1.18 Å) and Bi^{3+} (1.17 Å). Furthermore, the ionic radius of Nb^{5+} is 0.64 Å, which is larger than Ti^{4+} (0.605 Å).[183] Hence, the observed expansion of the lattice with increasing KN content in (1-x)NBT-xKN ceramics is in accordance with the change in average ion size.

In contrast, for the poled specimens it was found that several diffraction peaks showed evidence of splitting, indicating the occurrence of an irreversible structural transformation during poling. Superlattice peaks corresponding to the $(\frac{3}{2}\frac{1}{2}\frac{1}{2})_p$ reflection of the R3c phase are also observed at a d-spacing of approximately 2.38 Å.

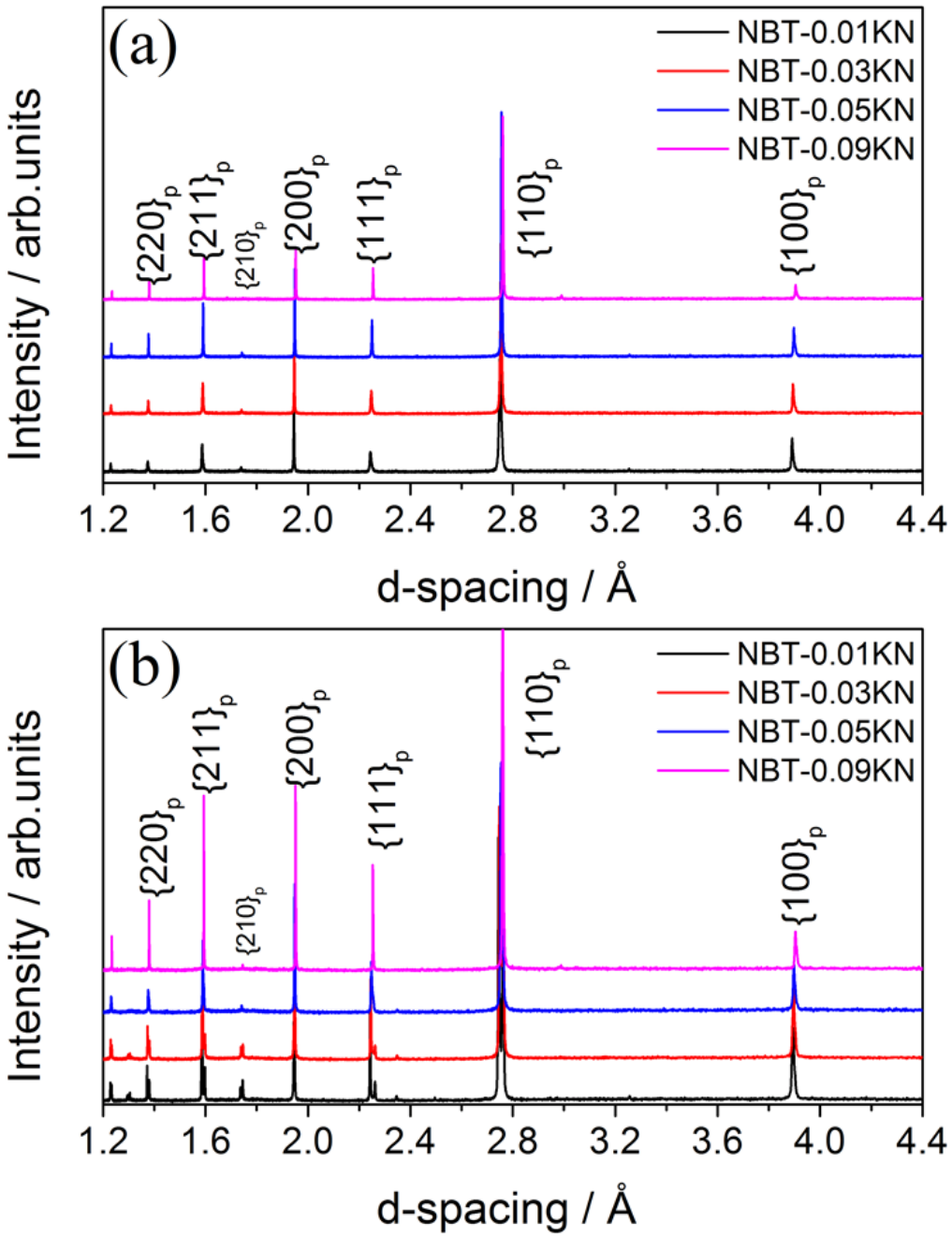

Figure 5.14 The full SXPD patterns for (a) unpoled and (b) poled NBT-xKN ceramics.

To be specific, the peak profiles of $\{111\}_p$, $\{200\}_p$ and $\{211\}_p$ for NBT-xKN are presented in Figure 5.15. For the unpoled state, asymmetric $\{111\}_p$ and $\{211\}_p$ single peaks are observed for NBT-0.01KN, indicating a pseudo-cubic structure with a slight rhombohedral distortion. All other compositions are identified as cubic structure, characterised by all single peaks.

In contrast, a well-defined rhombohedral structure was detected for poled NBT-0.01KN and NBT-0.03KN, characterised by a double $\{111\}_p$ peak, single

$\{200\}_p$ peak and triple $\{211\}_p$, as shown in Figure 5.14. For NBT-0.05KN, a single $\{200\}_p$ peak and asymmetric $\{111\}_p$ and $\{211\}_p$ peaks with a shoulder are observed, indicating a small rhombohedral distortion. The crystal structure for poled NBT-0.09KN retains the cubic structure after the poling procedure. In summary, a structural transformation from cubic to rhombohedral was observed for NBT-0.01KN, NBT-0.03KN and NBT-0.05KN, even after crushing into powders. There is no influence of poling on crystal structure for NBT-0.09KN.

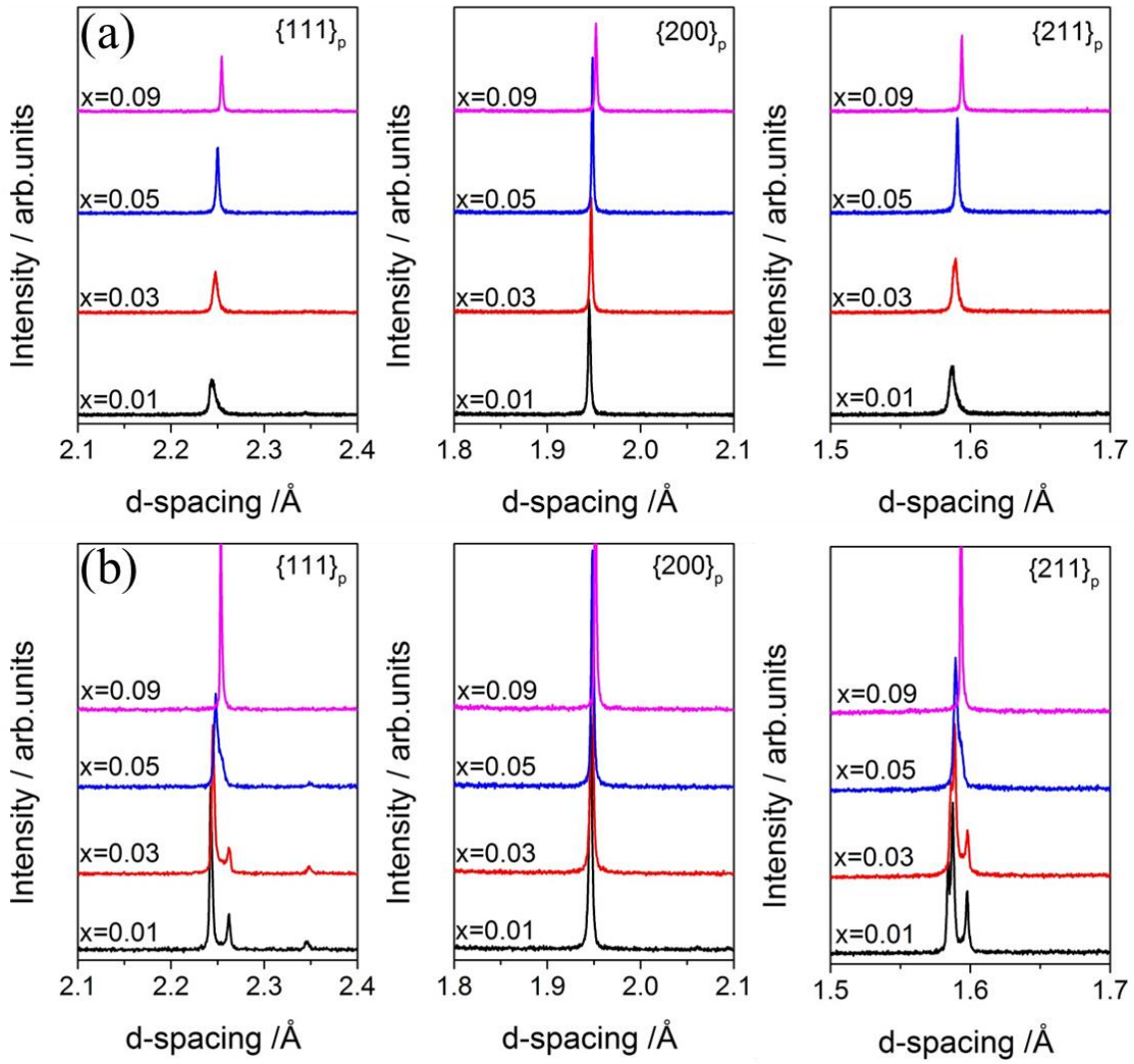

Figure 5.15 The representative peaks $\{111\}_p$, $\{200\}_p$ and $\{211\}_p$ of SXPD for (a) unpoled and (b) poled NBT-xKN (x=0.01 to 0.09).

5.7.3 Temperature-dependent study

5.7.3.1 Poled NBT-0.01KN

The temperature-dependent SPXD full patterns for poled NBT-0.01KN are presented in Figure 5.16. The structure at all temperatures appears to be single phase perovskite without any secondary phase.

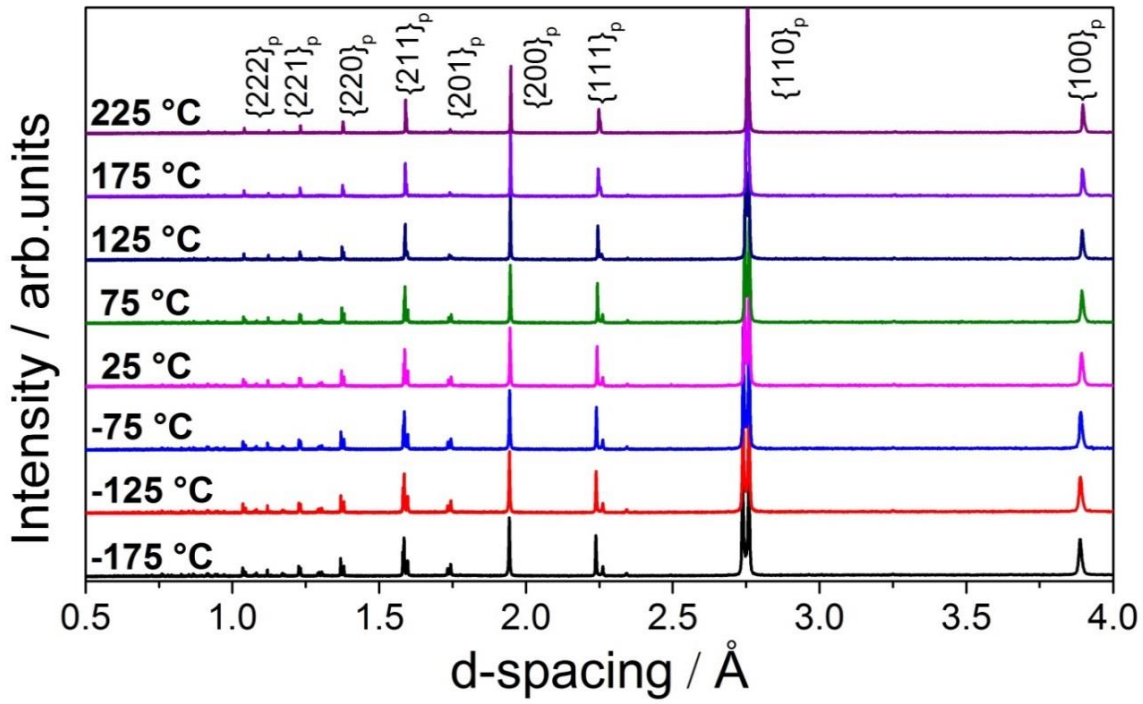

Figure 5.16 The full SXPD patterns for poled NBT-0.01KN at temperature from -175 ºC to 225 ºC.

Selected regions of the SXPD peak reflections for poled NBT-0.01KN in the temperature range from -175 ºC to 225 ºC are presented in Figure 5.17. A well-defined rhombohedral structure is identified at -175 ºC, evidenced by double $\{111\}_p$, single $\{200\}_p$, triple $\{211\}_p$ and double $\{220\}_p$ peaks. With increasing temperature, the separation between (111) and $(\bar{1}11)$ peaks becomes smaller and the $\{200\}_p$ peak shifts to higher d-spacing, indicating a reduction of rhombohedrality. Furthermore, the triple $\{211\}_p$ and double $\{220\}_p$ peaks gradually change to double and single peaks respectively. At 225 ºC, a remaining rhombohedral structure is characterised by doublet $\{111\}_p$ and $\{211\}_p$, indicating that the thermally-induced structural transformation from rhombohedral to cubic was incomplete for the poled NBT-0.01KN ceramic.

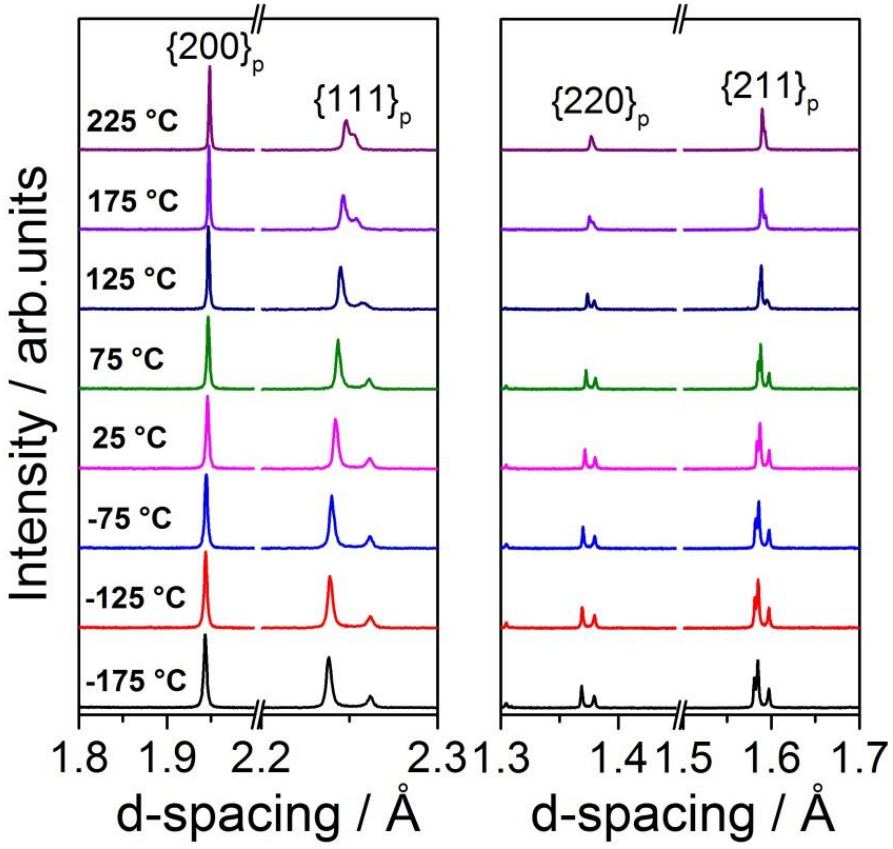

Figure 5.17 Temperature-dependent SXPD representative peak reflections for poled NBT-0.01KN.

5.7.3.2 Unpoled NBT-0.01KN

The temperature-dependent SXPD full patterns for unpoled NBT-0.01KN are presented in Figure 5.18. The structure at all temperatures appears to be single perovskite structure without any secondary phase.

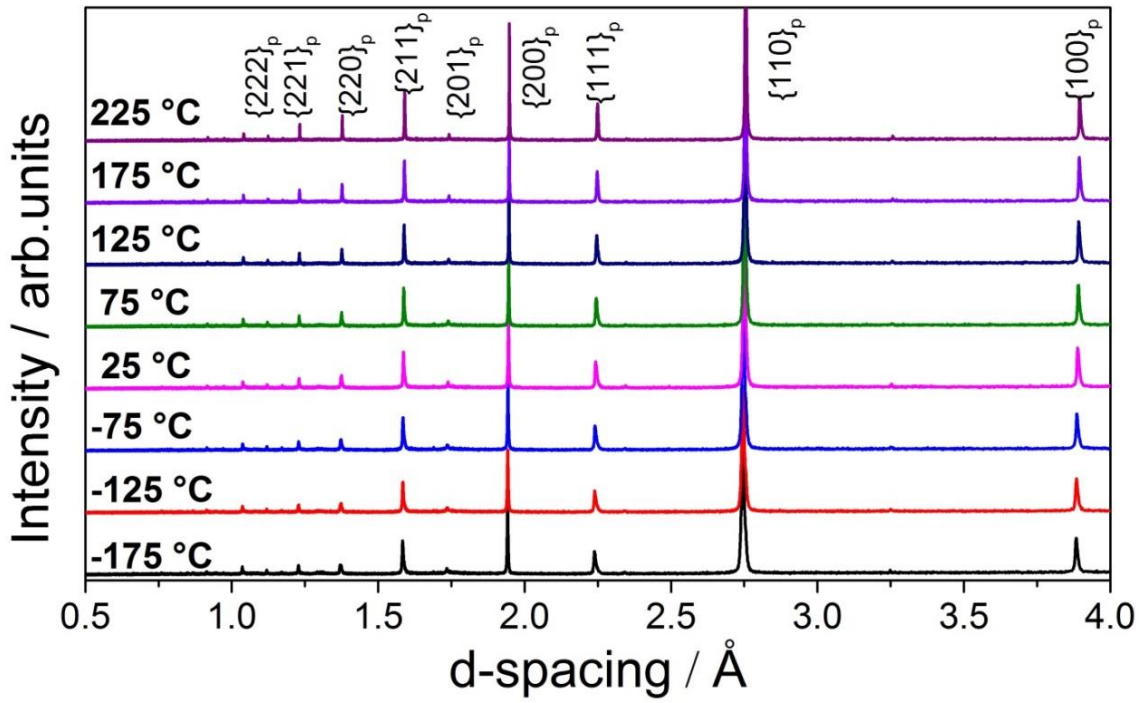

Figure 5.18 The full SXPD patterns for unpoled NBT-0.01KN at temperature from -175 ºC to 225 ºC.

Selected regions of the SXPD patterns for unpoled NBT-0.01KN in the temperature range from -175 ºC to 225 ºC are illustrated in Figure 5.19. Asymmetric $\{111\}_p$, $\{211\}_p$ and $\{220\}_p$ peaks are observed at -175 ºC, indicating a pseudo-cubic structure with a slight rhombohedral distortion. It is notable that a transformation to the rhombohedral phase was not observed for the unpoled powders on cooling below room temperature, even at -175 °C, which is approximately 375 degrees below T_{F-R} for the poled state. Therefore the nanopolar state remains remarkably stable on cooling in the absence of an electric field. During heating, the asymmetric peak becomes more symmetric especially at temperatures greater than 175 ºC, indicating that the slight rhombohedral distortion transforms gradually to cubic structure.

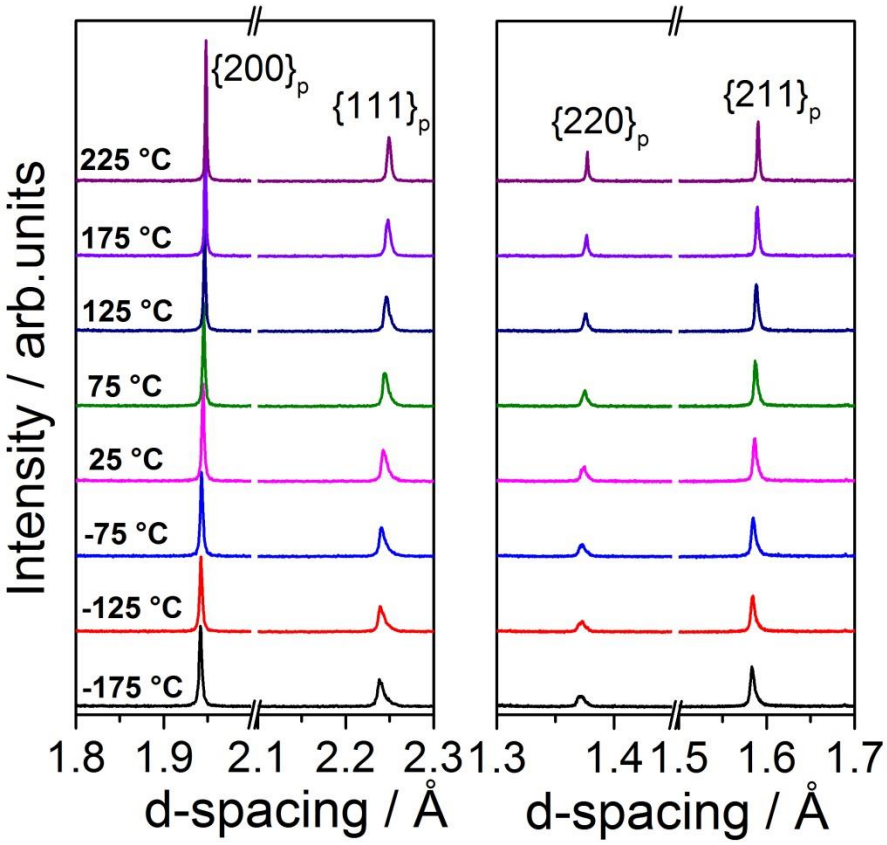

Figure 5.19 Temperature-dependent SXPD representative peak reflections for unpoled NBT-0.01KN.

5.7.3.3 Poled NBT-0.03KN

The selected regions of the SXPD patterns obtained for poled NBT-0.03KN in the temperature range from 25 ºC to 225 ºC are presented in Figure 5.20. A well-defined rhombohedral structure is observed at 25 ºC, characterised by the double $\{111\}_p$, single $\{200\}_p$, triple $\{211\}_p$ and double $\{220\}_p$ peaks. With increasing temperature, all multiple peaks transformed gradually to single peaks at 225 ºC, indicating that the thermally-induced structural transformation from rhombohedral to cubic completed between 175 ºC and 225 ºC.

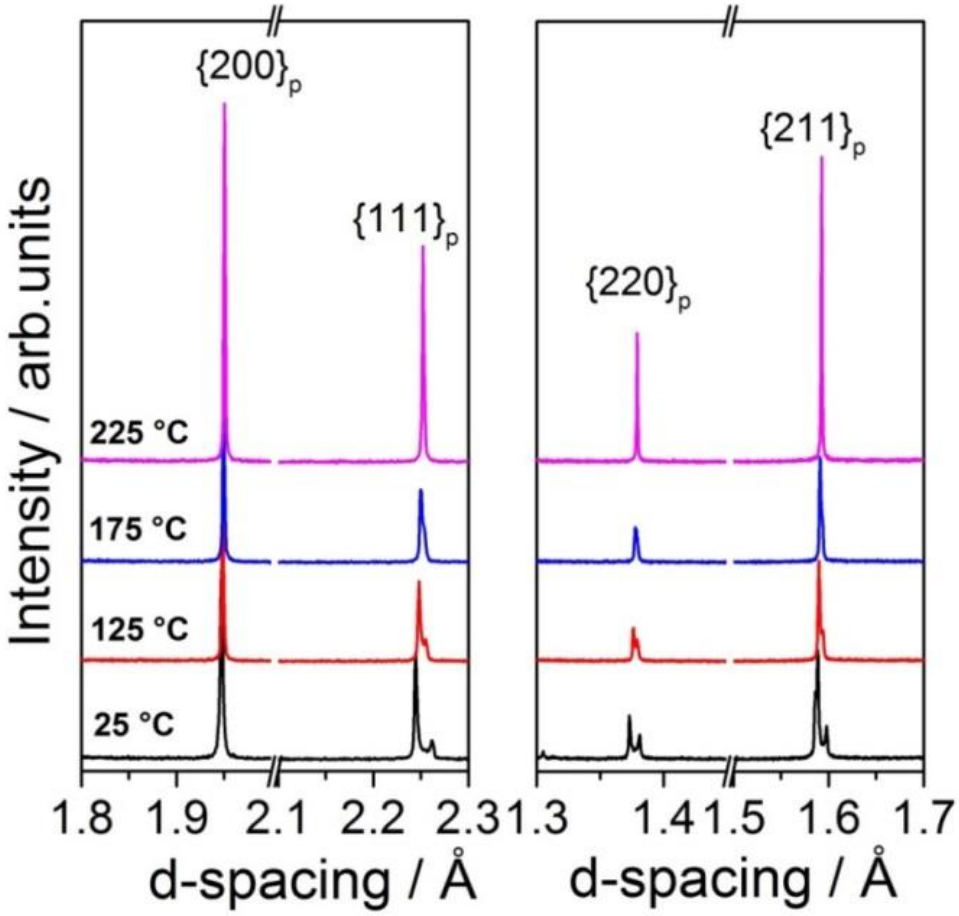

Figure 5.20 Temperature-dependent SXPD representative peak reflections for poled NBT-0.03KN.

5.7.3.4 Poled NBT-0.05KN

The selected regions of the SXPD patterns for poled NBT-0.05KN in the temperature range from -175 ºC to 225 ºC are illustrated in Figure 5.21. A rhombohedral structure is identified by double $\{111\}_p$ and single $\{200\}_p$ peaks at -175 ºC. With increasing temperature, the doublet $\{111\}_p$, $\{211\}_p$ and $\{220\}_p$ peaks transformed to single peaks at 125 ºC, indicating that the structural transformation from rhombohedral to cubic completed between 75 ºC and 125 ºC. Furthermore, the $\{200\}_p$ peak shifts to larger d-spacing during heating from -175 ºC to 225 ºC.

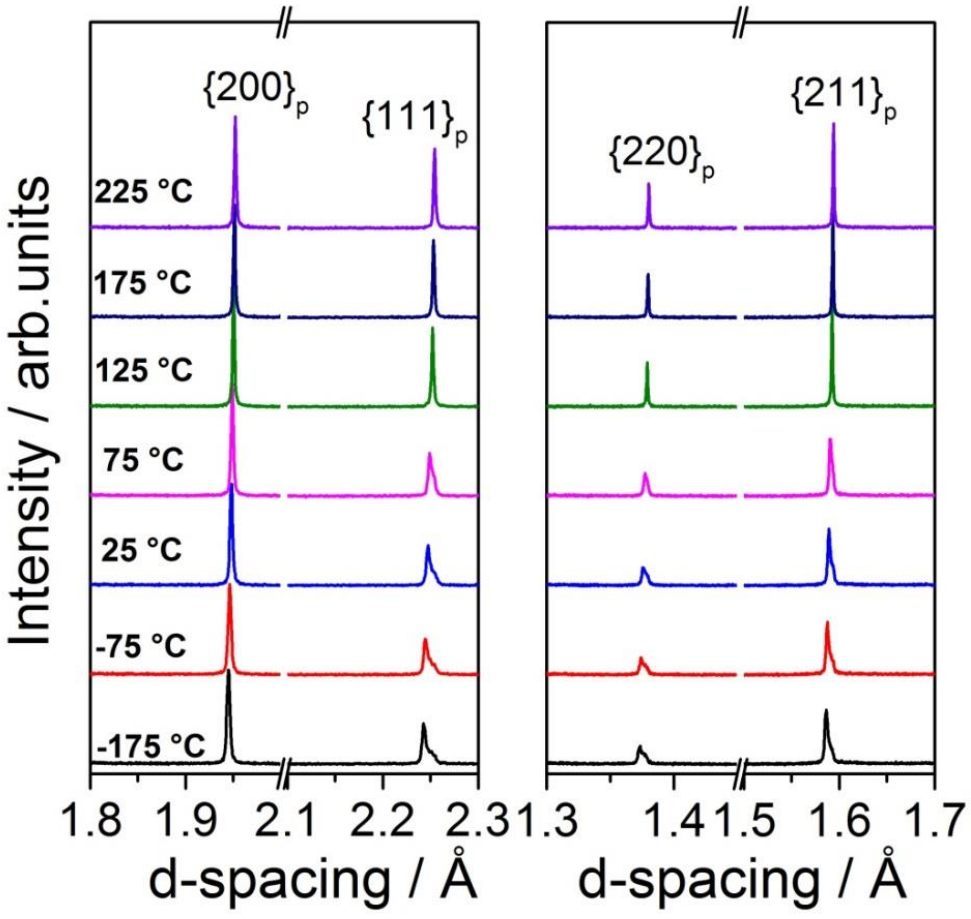

Figure 5.21 Temperature-dependent SXPD representative peak reflections for poled NBT-0.05KN.

5.7.3.5 Poled NBT-0.09KN

The selected regions of the SXPD patterns for poled NBT-0.09KN in the temperature range from -175 ºC to 225 ºC are presented in Figure 5.22. All peaks at three temperatures are observed to be single, indicating a cubic structure. Compared to the other compositions, increasing KN content in NBT-xKN system enhances the compositional disorder and stabilises the PNRs. Furthermore, there is no observable effect of the applied electric field on crystal structure for NBT-0.09KN.

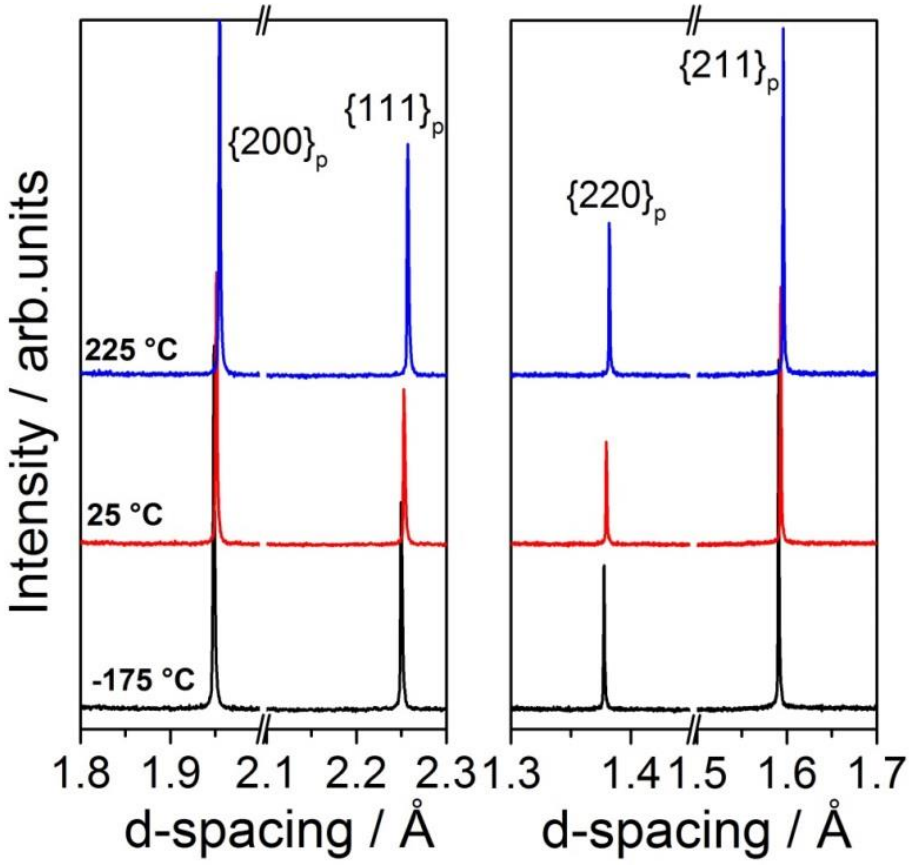

Figure 5.22 Temperature-dependent SXPD representative peak reflections for poled NBT-0.09KN.

5.7.4 Refinement of SXPD profiles

In order to obtain refined crystallographic parameters for NBT-xKN, such as lattice parameters, inter-axial angle and unit cell volume, the full XRD patterns have been fitted with several single or mixed phase models including R3c rhombohedral, Cc monoclinic and Pm3m cubic structures. The best refined full patterns for poled NBT-0.01KN at 25 ºC are presented as an example in Figure 5.23 with an inset of peak profiles of $\{111\}_p$ and $\{200\}_p$ and the results for other temperatures and compositions are illustrated in Appendix 11.1. The results obtained after refinement will be discussed in the next section.

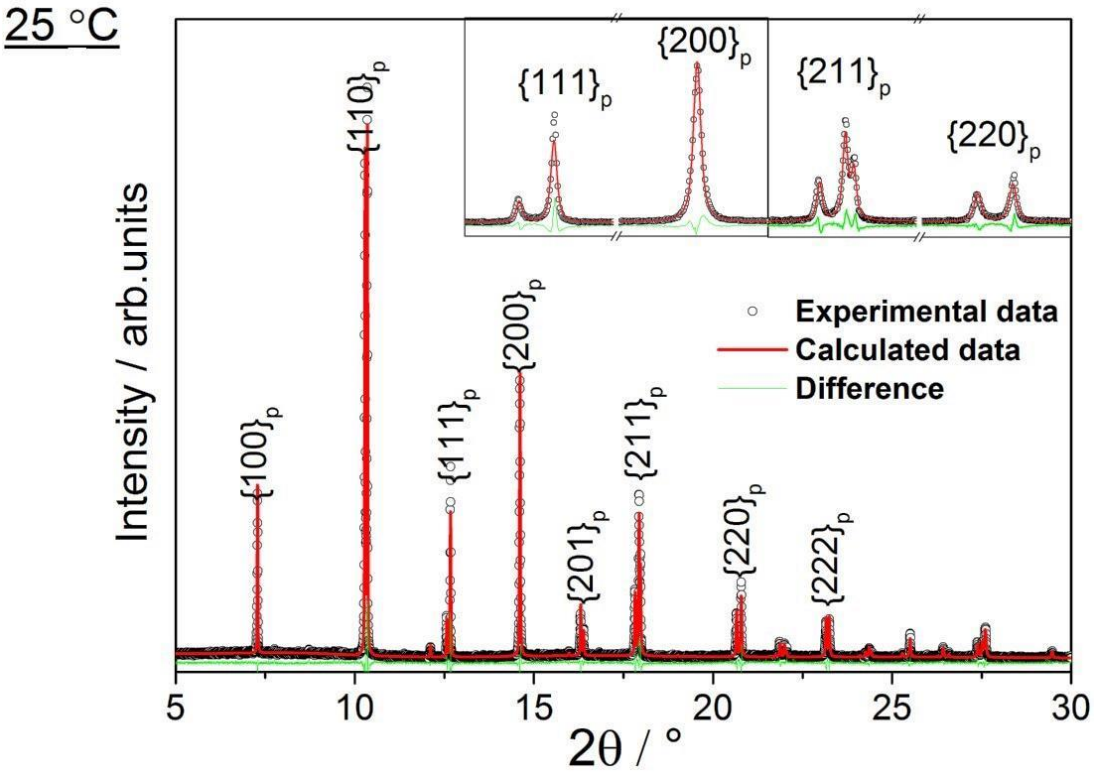

Figure 5.23 The SXPD full patterns refinement for poled NBT-0.01KN powders at 25 ºC. The black circles are experimental data, the red line is the calculated results from Rietveld refinement, and the green line is the difference profile between experimental and calculated diffraction patterns.

To facilitate a comparison between the unpoled and poled states, the rhombohedral phase, which is normally indexed according to the hexagonal unit cell, can be transformed to an equivalent pseudo-cubic unit cell through the rhombohedral unit cell, using the relationships given by Megaw[184] and

Cullity.[143] The lattice parameter, a_R, and interaxial angle, α_R, were calculated using equations 5.1 and 5.2. Note that the volume of the hexagonal unit cell is three times greater than that of the rhombohedral one.[143]

$$a_R = \frac{1}{3}\sqrt{3a_H^2 + {c_H}^2} \tag{5.1}$$

$$\sin\frac{\alpha_R}{2} = \frac{3}{2\sqrt{3+(c_H/\alpha_H)^2}} \tag{5.2}$$

Subsequently, a_R and α_R for the rhombohedral unit cell can be transformed into a_{pc} and α_{pc} for the pseudo-cubic unit cell according to Equations 5.3 and 5.4. Furthermore, the volume of the rhombohedral unit cell is double that of the pseudo-cubic unit cell.[184]

$$a_{pc} = \frac{a_R}{\sqrt{2}} \tag{5.3}$$

$$\alpha_{pc} = 90 - \frac{\sqrt{3}}{2}(60 - \alpha_R) \tag{5.4}$$

5.7.4.1 Poled NBT-0.01KN

The lattice parameter, a_{pc}, and the interaxial angle, α_{pc}, for poled NBT-0.01KN ceramic powder in the temperature range from -175 ºC to 225 ºC are presented in Figure 5.24. A rhombohedral phase is identified for poled NBT-0.01KN at -175 ºC with a_{pc} =3.898 Å and α_{pc}=89.58º. With increasing temperature, the rhombohedral phase is retained and both a_{pc} and α_{pc} increase steadily up to 25 ºC. Upon further heating, the value of a_{pc} declines dramatically from 3.902 Å to 3.895 Å while α_{pc} increases significantly from 89.68º to 89.93º until 225 ºC, indicating a reduction of rhombohedral distortion. However, a remaining rhombohedral phase is observed at 225 ºC due to an incomplete structural transformation from rhombohedral to cubic.

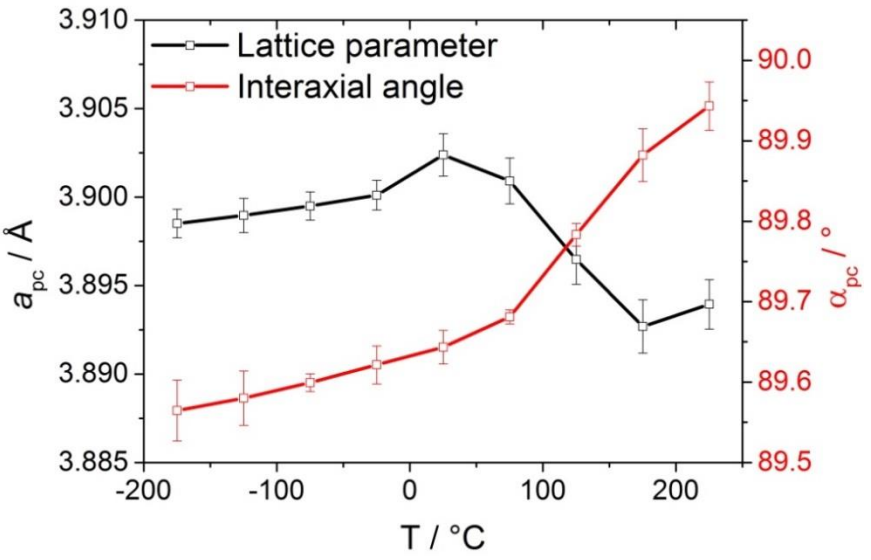

Figure 5.24 The variation of crystallographic parameters at temperatures from -175 ºC to 225 ºC for poled NBT-0.01KN.

5.7.4.2 Unpoled NBT-0.01KN

The lattice parameter, a_{pc}, and the interaxial angle, α_{pc}, for unpoled NBT-0.01KN ceramic powders in the temperature range from -175 ºC to 225 ºC are presented in Figure 5.25. Compared to the poled NBT-0.01KN, the unpoled NBT-0.01KN was characterised as a pseudo-cubic phase with slight rhombohedral distortion at all temperatures. There was no significant structural transformation during heating. Furthermore, both a_{pc} and α_{pc} increase slightly and progressively from 3.885 Å to 3.893 Å and 89.85º to 89.97º respectively.

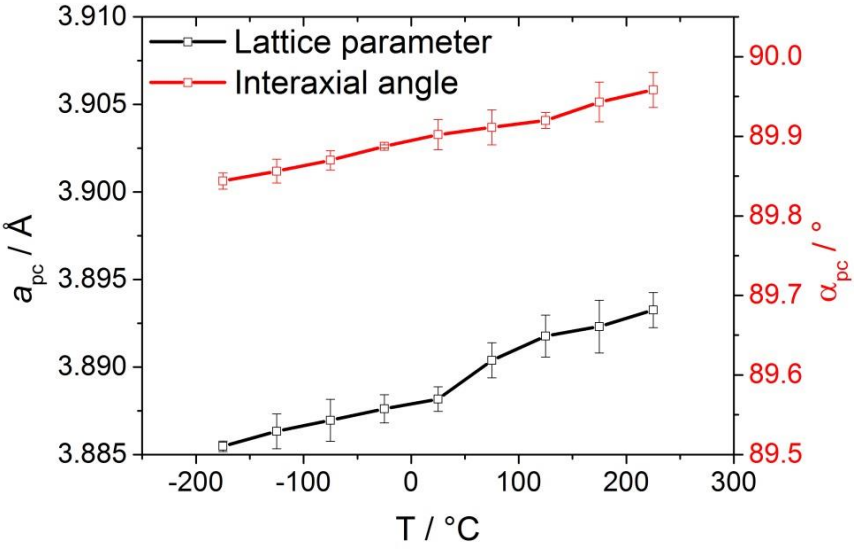

Figure 5.25 The variation of crystallographic parameters at temperatures from -175 ºC to 225 ºC for unpoled NBT-0.01KN.

5.7.4.3 Poled NBT-0.03KN

The lattice parameter, a_{pc}, and the interaxial angle, α_{pc}, for poled NBT-0.03KN ceramic powder in the temperature range from 25 ºC to 225 ºC are presented in Figure 5.26. The structure was identified as a rhombohedral phase at 25 ºC with a α_{pc}=89.73º. Then the α_{pc} value increases steadily with increasing temperature to approximately 90º at 225 ºC, indicating that the structural transformation from rhombohedral to cubic was completed by this temperature. On the other hand, the lattice parameter, a_{pc}, starts at approximately 3.901 Å at 25 ºC, followed by a slight decrease to 3.895 Å at 125 ºC. With further heating, the a_{pc} increases again slightly to 3.898 Å at 225 ºC.

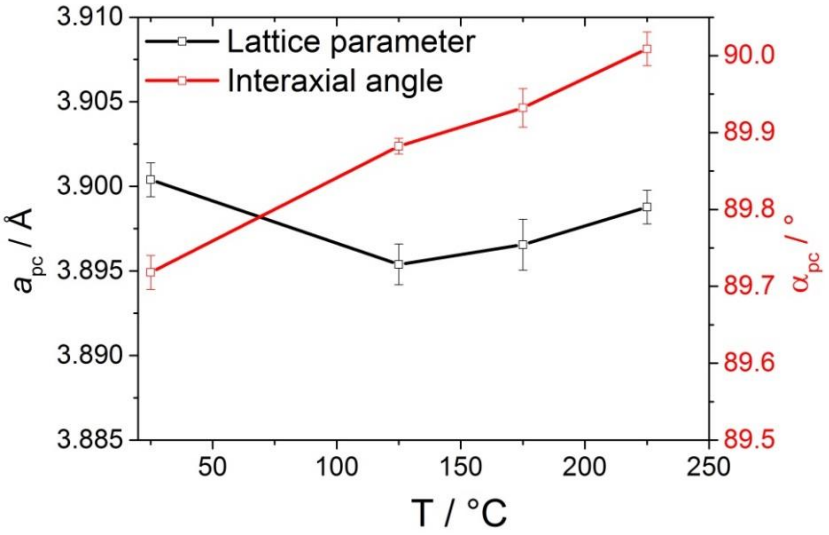

Figure 5.26 The variation of crystallographic parameters in a temperature 25 ºC to 225 ºC for poled NBT-0.03KN.

5.7.4.4 Poled NBT-0.05KN

The lattice parameter, a_{pc}, and the interaxial angle, α_{pc}, for poled NBT-0.05KN ceramics powder in the temperature range from -175 ºC to 225 ºC are illustrated in Figure 5.27. A slight rhombohedral distortion was observed with α_{pc}=89.85º at -175 ºC. During heating, the rhombohedral distortion was retained and both a_{pc} and α_{pc} experience slight increase up to 25 ºC. With further heating, the value of a_{pc} decreases slightly at 75 ºC, followed by a steady increase up to 225 ºC. For α_{pc}, it is increases significantly up to approximately 90º at 125 ºC, indicating a completion of the structural transformation from rhombohedral to cubic phase.

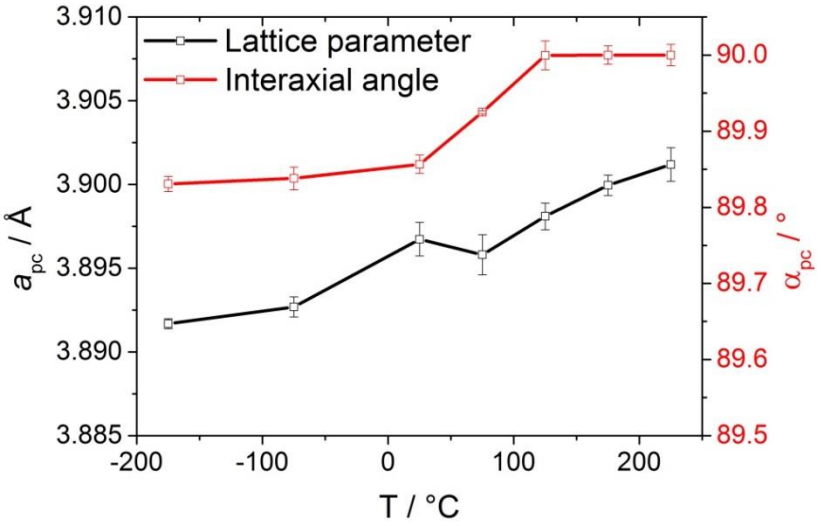

Figure 5.27 The variation of crystallographic parameters at temperatures from -175 ºC to 225 ºC for poled NBT-0.05KN.

5.7.4.5 Poled NBT-0.09KN

The lattice parameter, a_{pc}, and the interaxial angle, α_{pc}, for poled NBT-0.09KN ceramic powder in the temperature range from -175 ºC to 225 ºC are illustrated in Figure 5.28. The α_{pc} remains at approximately 90º for all temperatures, indicating the presence of the cubic structure. The lattice parameter, a_{pc}, increased from 3.899 Å at -175 ºC to approximately 3.903 Å at 25 ºC, followed by a further increase to 3.906 Å at 225 ºC.

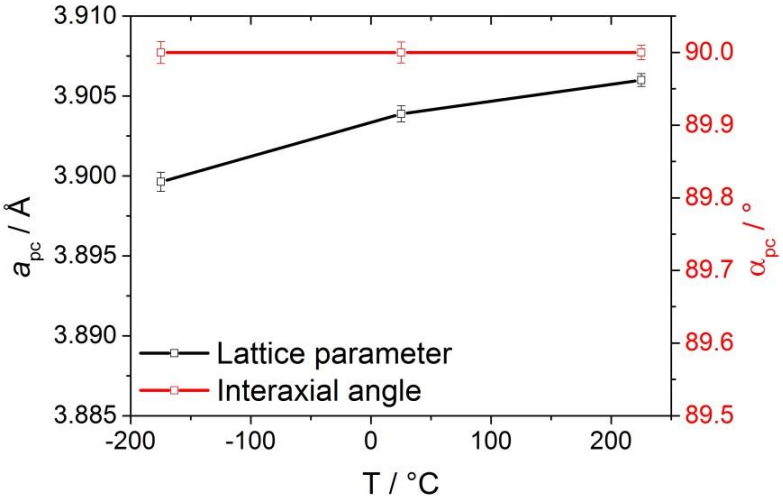

Figure 5.28 The variation of crystallographic parameters in a temperature -175 ºC to 225 ºC for poled NBT-0.09KN.

5.7.5 Overview of structural transformations induced by electric field and temperature

Based on the results discussed above, a ferroelectric hysteresis loop was observed for NBT-xKN with low KN content, indicating the occurrence of an electric field-induced structural transformation from cubic to rhombohedral. With heating up to 225 ºC, NBT-0.01KN retained a slight rhombohedral structure but NBT-0.03KN and NBT-0.05KN transformed reversibly to cubic phase. Hence, the changes in crystallographic parameters resulting from the electric field and thermally-induced structural transformations were studied and calculated after *Topas* refinement.

The results obtained for the crystallographic parameters for all NBT-KN compositions during heating from 25 °C to 225 °C and subsequent cooling to 25 °C, are presented in Figure 5.29. For NBT-0.01KN, a_{pc} decreases with increasing temperature up to 175 °C and then increases slightly up to 225 °C. Simultaneously, α_{pc} increases consistently from 89.68º to 89.93º up to the maximum temperature of 225 ºC. Both parameters reduce during cooling down to 25 ºC. A rhombohedral phase, with $\alpha_{pc} \approx 89.85º$, is retained after cooling back to room temperature, indicating that an irreversible structural transformation occurred on heating. However, the maximum temperature of 225 °C was insufficient to complete the transformation to the cubic phase for the NBT-0.01KN composition. It is shown in Figure 5.10 above that this transformation was associated with disruption of the ferroelectric order by thermal depoling.

Similar results were obtained for NBT-0.03KN and NBT-0.05KN, although in these cases a complete transformation to the cubic phase was observed, as indicated by the tendency for α_{pc} towards 90°. The structural transformation temperatures, T_{ST}, were determined as approximately 225 °C and 125 °C for NBT-0.03KN and NBT-0.05KN respectively. After completion of the rhombohedral to cubic structural transformation, α_{pc} remained approximately equal to 90º during subsequent heating and cooling while a_{pc} varied in a manner consistent with

thermal expansion.

Another interesting point, which was observed for all compositions apart from NBT-0.09KN, was that a_{pc} initially reduced on heating followed by an increase up to the maximum temperature, as shown in Figure 5.29 (a) to (c). The temperature ranges over which this reduction in a_{pc} was observed were 25 to 175 ºC, 25 to 125 ºC, and 25 to 75 ºC for NBT-0.01KN, NBT-0.03KN and NBT-0.05KN respectively. The reduction in a_{pc} was generally associated with an increase in the interaxial angle, α_{pc}, resulting in an overall increase in unit cell volume with increasing temperature, as illustrated in Figure 5.29 (e) to (h).

With reference to the unpoled state of ceramics (red open-circle), the electric field-induced structural transformation from pseudo-cubic to rhombohedral produced a volume increase of 0.24%, 0.22% and 0.14% for NBT-0.01KN, NBT-0.03KN and NBT-0.05KN respectively. After heating to 225 ºC and cooling back to 25 ºC, the thermally-induced phase transformation from rhombohedral back to cubic resulted in a volume decrease of 0.25% and 0.15% for NBT-0.03KN and NBT-0.05KN respectively. A relatively small volume decrease of 0.14% was obtained for NBT-0.01KN, indicating that the thermally-induced rhombohedral to cubic transformation was incomplete at 225 °C. In this case, an overall increase in volume of 0.10% was observed compared to the initial unpoled state. It is evident that the irreversible increase in volume caused by the electric field-induced phase transformation for both NBT-0.03KN and NBT-0.05KN can be recovered completely upon heating above 225 °C. In contrast, there is no significant volume change or structural transformation for NBT-0.09KN.

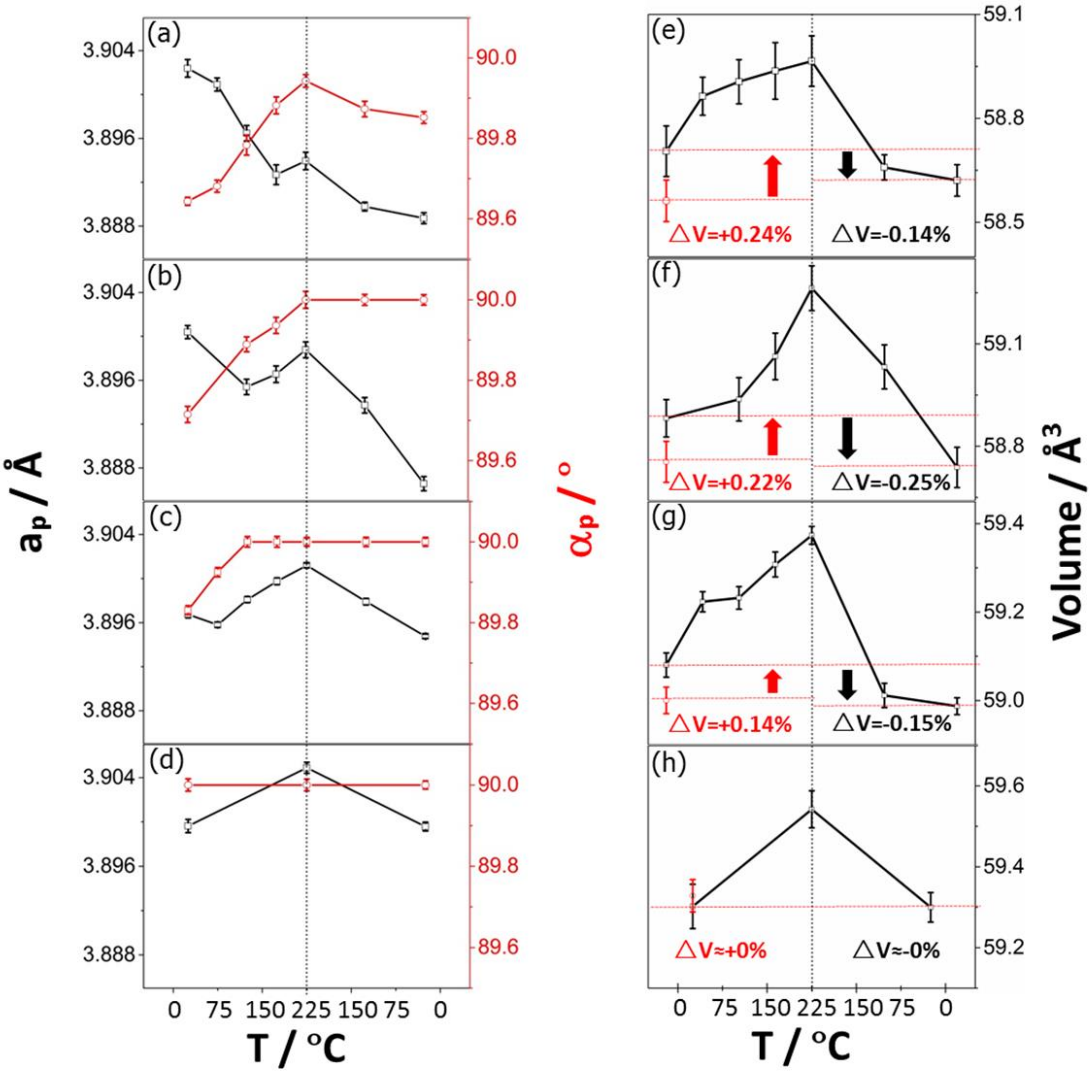

Figure 5.29 Lattice parameter r(a_{pc}) and interaxial angle (α_{pc}) for (a) NBT-0.01KN (b) NBT-0.03KN (c) NBT-0.05KN (d) NBT-0.09KN and volume change for (e) NBT-0.01KN (f) NBT-0.03KN (g) NBT-0.05KN (h) NBT-0.09KN ceramic powders as a function of temperature.

5.7.6 Summary

At room temperature, an electric field-induced structural transformation from cubic to rhombohedral was found for NBT-0.01KN, NBT-0.03KN and NBT-0.05KN ceramics. Furthermore, these materials retained a ferroelectric state with R3c rhombohedral symmetry after removing the external electric field, which provides evidence of the nonergodic-RF behaviour at room temperature. With increasing temperature, the electric field-induced rhombohedral structure transformed gradually back to cubic. The structural transformation temperature, T_{ST}, decreased with increasing KN content. In contrast, on increasing KN content to 9%, the material returned subsequently to its initial state with cubic structure regardless of the strength or polarity of the external electric field applied, which provides evidence of the ergodic-RF state.

5.8 In-situ high energy XRD experiments during electrical poling (Diamond beamline I15)

5.8.1 Influence of composition at room temperature

5.8.1.1 XRD patterns during electric poling

In order to investigate the electric field-induced structural transformation in NBT-xKN, the in-situ electric poling experiment was employed using high-energy synchrotron XRD in Diamond beamline I15. The diffraction patterns were taken at the end of each bipolar cycle without field and the diffraction image was caked using Fit2D software to obtain the conventional 1-D diffraction patterns for each grain orientation from ψ=-90º to ψ=270º, ψ being the angle between the scattering vector (plane normal) and the poling direction. The degree of poling and/or the cubic to rhombohedral phase transformation is expected to increase progressively during AC cycling, as indicated by the ferroelectric hysteresis measurements shown in Figure 5.13 above.

For ψ=0º, which is the direction parallel to the electric field, the peak profiles of

$\{111\}_p$ and $\{200\}_p$ for NBT-xKN (x=0.01 to 0.09) are plotted as function of the number of applied cycles in Figure 5.30. It is evident that the $\{111\}_p$ peak splits progressively while the $\{200\}_p$ peak shifts slightly with increasing cycle number for NBT-0.01KN and NBT-0.03KN, indicating that a structural transformation from cubic to rhombohedral phase completed gradually. In contrast, there are no significant changes in both peaks for NBT-0.05KN and NBT-0.09KN.

Compared to the high-resolution SXPD results reported in Section 5.7.2 above, in terms of crystal structure, the results obtained for both NBT-0.01KN and NBT-0.03KN were in agreement with those from I11, showing cubic and rhombohedral structures for the unpoled and poled states respectively. However, a slight rhombohedral distortion was observed in the poled NBT-0.05KN ceramic powders whereas there was no obvious structural change in the in-situ test on NBT-0.05KN ceramics after 20 cycles. This could be due to the limitation of the low-resolution detector on I15. No significant changes in structure were observed for NBT-0.09KN, in agreement with the SXPD results and the slim-loop ferroelectric behaviour.

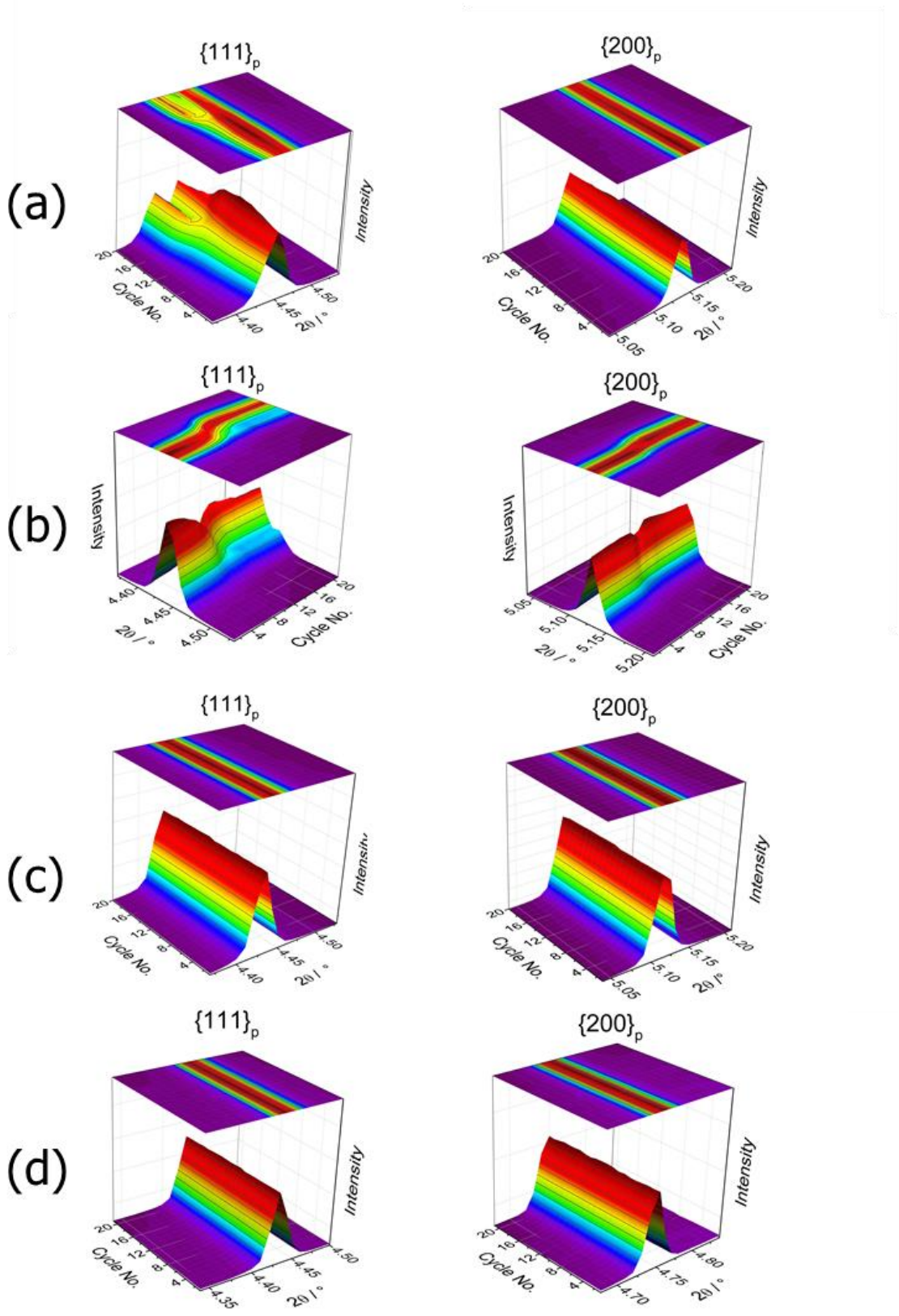

Figure 5.30 Evolution of $\{111\}_p$ and $\{200\}_p$ diffraction peaks for NBT-xKN ceramics as function of increasing electric field cycle number for (a) x=0.01 (b) x=0.03 (c) x=0.05 (d) x=0.09, at ψ = 0°.

5.8.1.2 Texture development during in-situ electric poling

To analyse the intermediate state induced by in-situ electric poling, an attempt was made to identify the texture- and strain-free orientation so that full pattern refinement procedures could be used to obtain and calculate the crystallographic parameters. In the absence of a structural transformation, in-situ electric field-driven experiments are normally conducted on an initially unpoled specimen (assumed to be texture- and strain-free), which is then poled under a high electric field. However, due to the existence of PNRs in NBT-xKN ceramics, the cubic phase was present in the unpoled state for all compositions, which makes it difficult to determine the $\{111\}_p$ peak intensity ratio and the $\{200\}_p$ lattice parameter for the rhombohedral phase in the unpoled state. To resolve this issue, the SPXD results obtained from beamline I11 for poled NBT-xKN ceramic powders were used to represent the texture-free and unstrained state of the rhombohedral phase.

NBT-0.01KN and NBT-0.03KN ceramics required approximately 15 and 11 cycles of electric field respectively to complete the structural transformation from cubic to rhombohedral. Comparing these two compositions, the variation of peak intensity ratio for $\{111\}_p$ peak and shift for $\{200\}_p$ peak changed more significantly for NBT-0.03KN than NBT-0.01KN, indicating a better domain switching. Furthermore, it was found that there was no significant change in the diffraction patterns for NBT-0.05KN and NBT-0.09KN. Therefore, the intermediate states for NBT-0.03KN were selected for further analysis of the changes induced by in-situ electric poling.

The peak profiles of $\{111\}_p$ and $\{200\}_p$ reflections for NBT-0.03KN after different numbers of bipolar electric field cycles are plotted as function of ψ, which is the grain orientation, as shown in Figure 5.31 below. For the unpoled state, there are no differences between each grain orientation. During in-situ electric poling, the texture developed progressively during AC cycling due to the structural transformation and domain switching.

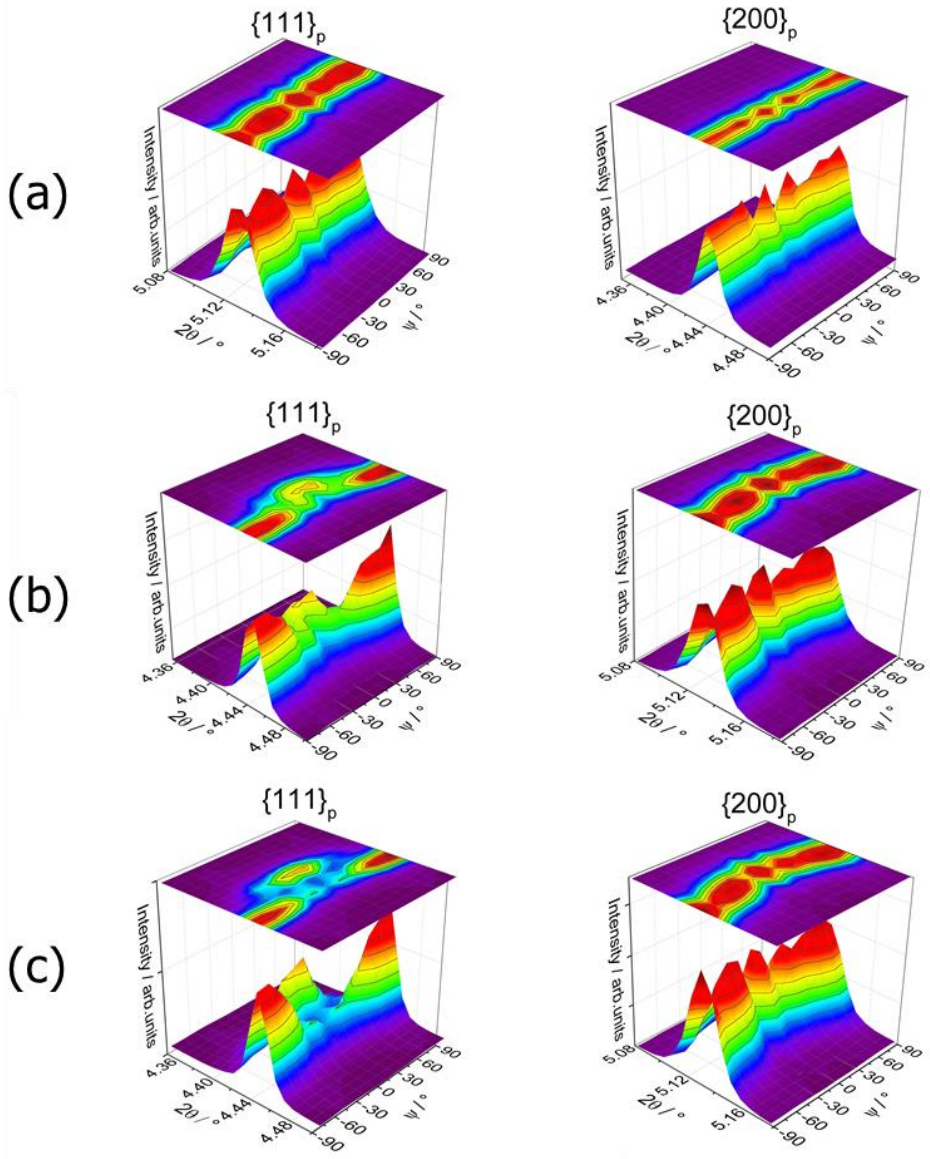

Figure 5.31 Changes in $\{111\}_p$ and $\{200\}_p$ XRD peak profiles as a function of grain orientation for NBT-0.03KN after (a) 2 (b) 7 and (c) 11 cycles of a bipolar electric field with E_0 = 5.5 kV mm^{-1}.

After 2 cycles of electric field, both $\{111\}_p$ and $\{200\}_p$ peaks are observed to be single for all ψ from -90º to 90º, indicating that no texture effect was developed. After 7 cycles of electric field, a double $\{111\}_p$ peak is observed for grains with orientation ψ=0º, while a single peak is present at grain orientations with ψ=-90º / 90º, indicating the onset of the structural transformation from cubic to rhombohedral. The $\{200\}_p$ peak shifts consistently with grain orientation, ψ. After 11 cycles of electric field, the separation between the $(111)_p$ and $(\bar{1}11)_p$ peaks

becomes wider and the position of the $\{200\}_p$ peak shifts more significantly. Additionally, there is no effect of further cycles of electric field on diffraction peaks, indicating the saturation of poling.

5.8.1.3 Identification of texture- and strain-free bank

In order to identify the texture- and strain-free bank, the integrated intensity ratio was refined and calculated by *Topas*. The domain fraction, ν_{111}, was calculated more accurately using the method described by Jones[185]. According to this approach, the fraction of [111]-oriented domains in a rhombohedral specimen is given by Equation 5.5.

$$\nu_{111} = \frac{I_{111}/I'_{111}}{I_{111}/I'_{111} + 3I_{\bar{1}11}/I'_{\bar{1}11}} \tag{5.5}$$

where I_{hkl} represents the intensity of the (hkl) reflection for the specimens after 20 bipolar electric field cycles and I'_{hkl} represents the intensity of the (hkl) reflection for the randomly oriented specimen, using the SXPD data obtained from I11 for the crushed poled pellet to provide the latter values.

The calculated domain fraction, ν_{111}, for poled NBT-0.03KN is plotted below as function of $\cos^2\psi$ in Figure 5.32. The banks for ψ=-90º/90º were neglected because the intensity of the $(111)_p$ peak was close to zero and could not be determined at these angles.

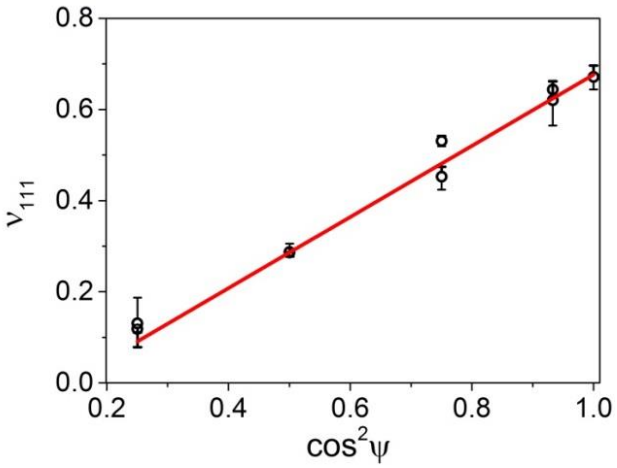

Figure 5.32 Dependence of domain fraction on grain orientation, ψ. The black

circle is experimental data and the red line is calculated using a squared cosine function.

The value of ν_{111} for NBT-0.03KN in the unpoled state, calculated using the data from beamline I11 obtained above, was determined as 0.2477. Based on the linear fit shown in Figure 5.33 above, the specific orientation which had a domain fraction value of 0.2477 was calculated as $\cos^2\psi$=0.228, which gives ψ=61.5º. Therefore, the texture- and strain-free bank for in-situ electric poling was determined and the crystallographic parameters were obtained by *Topas* using full pattern refinement. The refinement was conducted on diffraction patterns after 2, 7, 9, 10 and 11 cycles of electric field to illustrate how the crystallographic parameters vary with the number of electric field cycles.

The peak profiles of $\{111\}_p$, $\{200\}_p$, $\{211\}_p$ and $\{220\}_p$ after certain cycles of electric field are presented in Figure 5.33. All peaks appear to be single after two cycles of electric field, indicating no structural transformation. After 7 cycles of electric field, all peaks still remain single but become asymmetric apart from the $\{200\}_p$ peak, indicating a small rhombohedral distortion. After 10 cycles of electric field, a significant rhombohedral distortion is observed, characterised by a double $\{111\}_p$, $\{211\}_p$, $\{220\}_p$ peaks and a single $\{200\}_p$ peak. After 11 cycles of electric field, there are no significant changes on diffraction peaks, indicating that the structural transformation was completed.

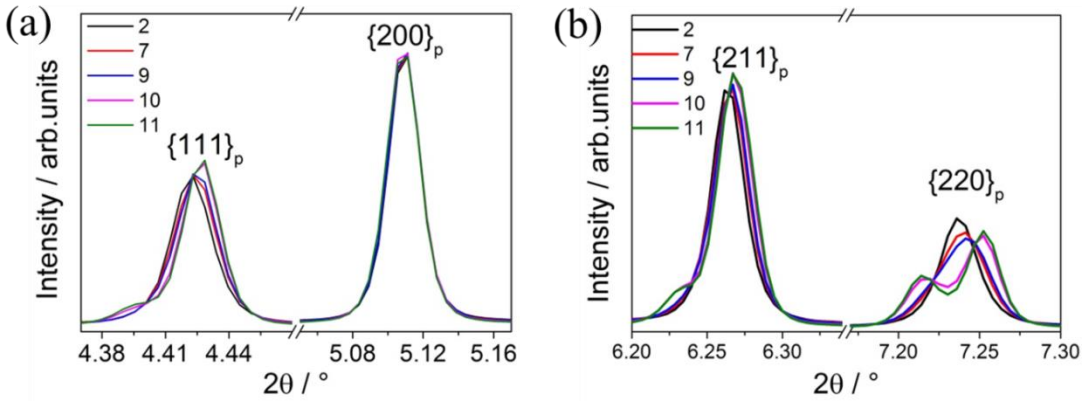

Figure 5.33 The in-situ cycle-dependent XRD representative peaks of (a) $\{111\}_p$ (b) $\{200\}_p$ (c) $\{211\}_p$ and (d) $\{220\}_p$ for NBT-0.03KN.

It is evident that the position of the $\{200\}_p$ peak remains invariant during the transformation, which is a good indication that the choice of the strain- and texture-free bank was relatively accurate. All patterns were fitted using either single- and mixed-phase models, including Cc monoclinic, R3c rhombohedral and Pm3m cubic phase. Based on the best fitting results, the cubic phase was identified for NBT-0.03KN before 7 cycles of electric field, followed by a coexistance of both cubic and rhombohedral structure. After 11 cycles of electric field onwards, a single rhombohedral phase was obtained.

5.8.1.4 Determination of crystallographic parameters

The lattice parameters for cubic and rhombohedral phases, a_C and a_R respectively, and the interaxial angle for rhombohedral distortion, α_R, are presented as a function of the number of cycles in Figure 5.34. The value of a_C decreases with increasing cycles of electric field up to 11 cycles, where all cubic is transformed into rhombohedral structure. After the appearance of the rhombohedral phase after 7 cycles of electric field, the a_R value increases slightly then remains stable at approximately 3.896 Å after 11 cycles of electric field. On the other hand, the inter-axial angle for rhombohedral phase, α_R, decreased from 89.83º to 89.70º during cycles 7 to 11 of the electric field, indicating the enhancement of the rhombohedral distortion. Furthermore, it was also found that the proportion of rhombohedral phase increased during cycling.

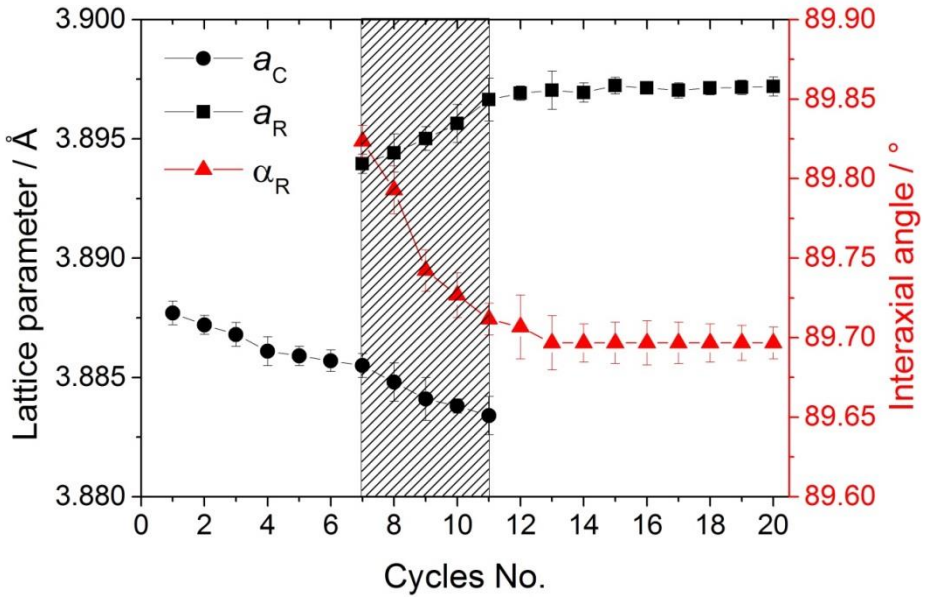

Figure 5.34 The crystallographic parameters for NBT-0.03KN during in-situ cyclic poling experiments.

As shown in Table 5.5, the phase fraction started with 100% cubic until 7 cycles of electric field. Then the phase fraction of rhombohedral increased while at the same time that of the cubic decreased from 7 to 11 cycles of electric field. Eventually, a single rhombohedral phase was obtained with a lattice parameter value of 3.896 Å and an interaxial angle of 89.70º. These results are similar to the values obtained from I11 and reported in Section 5.7.4.3 which were 3.901 Å and 89.73º.

Table 5.5 The phase fractions for NBT-0.03KN ceramic during in-situ poling.

Cycle No.	R phase fraction / %	C phase fraction / %
2	0	100
7	26	74
8	35	65
9	55	45
10	84	16
11	100	0
12-20	100	0

5.8.1.5 Domain orientation distribution (DOD) analysis

The changes in domain orientation distribution and lattice strain for the NBT-0.01KN and NBT-0.03KN ceramics in the poled rhombohedral state are examined further in the following section to evaluate the influence of the KN content on domain switching behaviour and to allow a comparison with previous results for conventional rhombohedrally-distorted PZT ceramics.

First, consider the origin of the lattice strain, which is most clearly evident for the $\{200\}_p$ peak. In polycrystalline ferroelectric ceramics, the process of poling leads to domain reorientation with an associated macroscopic strain. After removal of the applied electric field, the piezoelectric strain reduces to zero but a tensile remanent strain, $\bar{\varepsilon}$, remains along the poling direction, ψ = 0°. Assuming a volume conservative domain switching mechanism and transverse isotropy of the material, the transverse strain (ψ = 90°) is $-\bar{\varepsilon}/2$. Therefore, the macroscopic strain due to poling can be represented in the co-ordinate system *X* of the specimen as[186]

$$\varepsilon^P(X) = \begin{pmatrix} -\bar{\varepsilon}/2 & 0 & 0 \\ 0 & -\bar{\varepsilon}/2 & 0 \\ 0 & 0 & \bar{\varepsilon} \end{pmatrix} \tag{5.6}$$

The X_3 axis is chosen as the direction of the applied electric field, which corresponds to ψ = 0°. In the modified co-ordinate system, *Y*, in which the axis Y_3 is rotated by an angle ψ relative to the axis X_3, the elongation along Y_3 is given by[186]

$$\varepsilon_{33}^P(Y) = \bar{\varepsilon}\left(\frac{3}{2}\cos^2\psi - \frac{1}{2}\right) \tag{5.7}$$

In rhombohedrally-distorted perovskite ferroelectrics, the <h00> orientation of a grain has the special property that its dimension is independent of the fractions of different domain variants present within the grain and consequently it would

remain unchanged after poling in an unconstrained state. However, each grain in a polycrystalline ceramic is constrained by its neighbours. Therefore, after the removal of the electric field and the associated piezoelectric strain, the observed lattice strain for a {200}-oriented grain is due solely to the macroscopic strain of its surroundings and the local inter-granular residual stresses.[186] For this reason, it is anticipated that the {200} lattice spacing, d_{200} and the lattice strain, ε_{200}, should both exhibit a dependence on grain orientation, ψ, that is similar in form to Equation 5.7 (neglecting the influences of crystalline anisotropy and initial residual stresses).[187]

Determination of the lattice strain demands knowledge of the unstrained lattice parameter, d^0_{200}, which is usually obtained from diffraction measurements on an unpoled specimen. Unfortunately, it is not possible to use this approach in the present case due to the nature of the poling process for the NBT-0.01KN and NBT-0.03KN ceramics, which involved both a cubic to rhombohedral phase transformation and ferroelectric domain reorientation in the rhombohedral phase, as explained above in Section 5.8.1.1. Also, it was found that attempts to create a random domain structure by thermal depolarisation caused a reversion to the cubic phase, as discussed Section 5.7.3 above. As an alternative approach, it is possible to estimate the value of d^0_{200} by utilizing the relationship given in Equation 5.7 above, since it is evident that the macroscopic elongation due to poling is zero when $\cos^2\psi = 1/3$, or $\psi = 54.7°$.

5.8.1.5.1 NBT-0.01KN

The peak profiles of $\{111\}_p$ and $\{200\}_p$ for a range of different grain orientations are illustrated in Figure 5.35. The split $\{111\}_p$ peak after poling confirmed the presence of the rhombohedral phase. The variations in the relative intensities of the $\{111\}_p$ peaks as a function of the azimuthal angle, ψ, indicated that the [111]-oriented domains were oriented preferentially along the electric field direction at ψ = 0°. Furthermore, the $\{200\}_p$ peak shifts as function of ψ, indicating a small elastic lattice strain. These observations are similar to those made previously for poled rhombohedral PZT ceramics.[186]

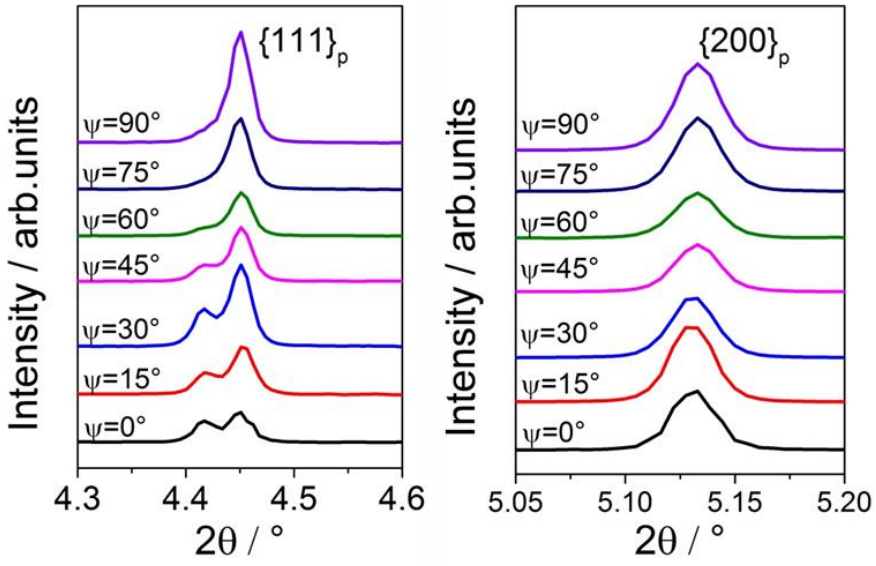

Figure 5.35 $\{111\}_p$ and $\{200\}_p$ XRD peak profiles for poled NBT-0.01KN ceramic as a function of azimuthal angle, ψ.

The positions of the $\{200\}_p$ diffraction peaks were determined by peak profile fitting using *Topas* and the lattice spacing, $d_{\{200\}}$, calculated using the Bragg Equation. Plotting $d_{\{200\}}$ as a function of $\cos^2\psi$ yielded a linear relationship, as illustrated in Figure 5.36. The value of the strain-free {200} lattice spacing, $d^0_{(200)}$, was determined as the d-spacing at which $\cos^2\psi = 1/3$, according to Equation 5.7. Subsequently, the change in lattice strain, ε_{200}, as a function of ψ was calculated using this value of d^0_{200}; the results of these calculations are illustrated in Figure 5.36. It is apparent that the dependence of ε_{200} on ψ exhibited a good fit to Equation 5.7, although it should also be noted that the lattice strain is not exactly

equal to the macroscopic strain due to the effects of elastic anisotropy.

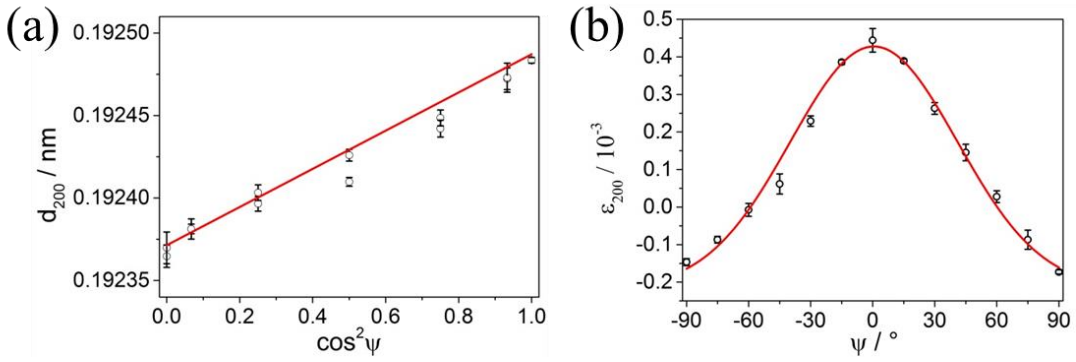

Figure 5.36 Dependence of (a) d_{200} and (b) ε_{200} on azimuthal angle, ψ. Symbols are experimental data points and solid lines are calculated according to Equation 5.3.

Next, consider the change in the differently-oriented domain variants as a function of grain orientation. The simplest method to calculate the intensity fraction of [111]-oriented domains, $R_1(111)$, involves using the ratio of the integrated intensities of the {111} diffraction peaks.[188]

$$R_1(111) = \frac{I_{111}}{I_{111} + I_{\bar{1}11}} \tag{5.8}$$

Note that $I_{\bar{1}11}$ includes contributions from the, $(\bar{1}11)$ $(1\bar{1}1)\ and\ (11\bar{1})$ reflections. It is found that the ratio, R_1, exhibited an approximately linear dependence on $\cos^2\psi$, as shown in Figure 5.37.

For reasons similar to those given above, it is anticipated that the value of R_1 should be equal to that of an unpoled specimen, having random domain orientations, when $\cos^2\psi$ = 1/3. However, the linear fit to the data shown in Figure 5.37 indicates that the intensity ratio is approximately equal to 0.195 at $\cos^2\psi$ = 1/3, which is slightly smaller than the value of approximately 0.25 expected for random domain texture. This apparent discrepancy can be understood as being due to slight differences in the structure factors for the (111) and $(\bar{1}11)$ diffraction peaks.

The fractions of differently-oriented domains, denoted as the *domain orientation*

distribution (DOD) can be calculated according to Equation 5.5 above. The Equation 5.8 can also be expressed in terms of the simple peak intensity ratio $R_2(111)$, defined as

$$R_2(111) = \frac{I_{111}}{I_{\bar{1}11}} \tag{5.9}$$

Substituting Equation 5.9 into Equation 5.5 results in the following expression for the [111]-orientated domain fraction, ν_{111}.

$$\nu_{111} = \frac{R_2}{R_2 + 3R_2^{/}} \tag{5.10}$$

The value of the peak intensity ratio in the unpoled state, $R_2^{/}$, can be obtained from $R_1^{/}$ since R_2 and R_1 are generally related according to

$$R_2 = \frac{R_1}{(1 - R_1)} \tag{5.11}$$

The value of $R_1^{/}$ was determined as approximately 0.195, as discussed above, which yields a value of 0.242 for $R_2^{/}$.

The variations in ν_{111}, calculated from the measured diffraction peak intensities according to Equation 5.8 and Equation 5.10, are presented in Figure 5.37. These results indicate that the degree of non-180° domain switching in the remanent state was not very high, with a maximum ν_{111} value of approximately 0.55 being achieved for ψ = 0°. This level of saturation indicates that the NBT-0.01KN processed a higher spontaneous strain, which caused higher elastic strain energy during non-180º domain switching and higher coercive field. Furthermore, it is evident that the DOD function follows closely the form of the macroscopic strain, according to Equation 5.7. Therefore, we can conclude that the electric field-induced metastable rhombohedral phase of the NBT-0.01KN ceramic exhibited both structural and functional characteristics that are typical of a conventional long-range ordered ferroelectric.

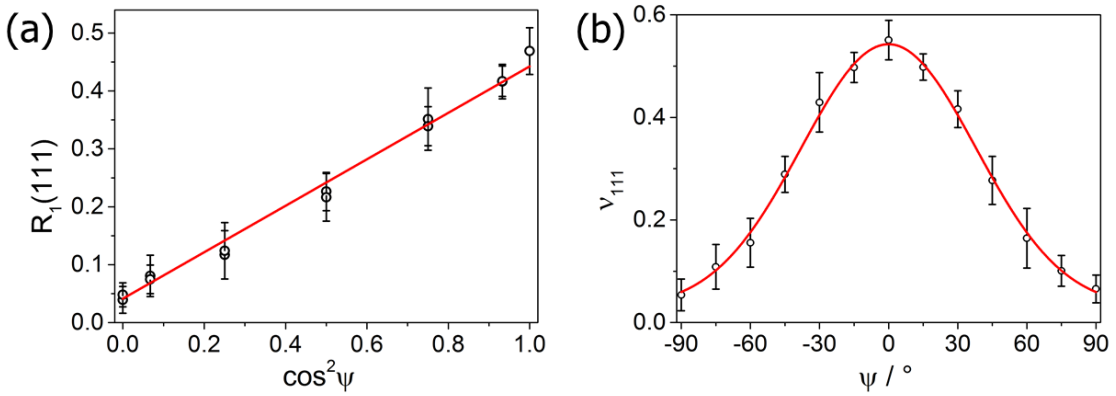

Figure 5.37 Dependence of (a) peak intensity ratio, $R_1(111)$, and (b) domain fraction, ν_{111}, on azimuthal angle, ψ. Symbols are experimental data points and solid lines are calculated using a squared cosine relation.

5.8.1.5.2 NBT-0.03KN

The XRD peak profiles of $\{111\}_p$ and $\{200\}_p$ for a range of different grain orientations are illustrated in Figure 5.38. A rhombohedral phase was observed for poled NBT-0.03KN, characterised by a double $\{111\}_p$ and single $\{200\}_p$ peak. The variations in the relative intensities of the $\{111\}_p$ peaks as a function of the azimuthal angle ψ indicated that the [111]-oriented domains were oriented preferentially along the electric field direction at ψ = 0°. Furthermore, similar to NBT-0.01KN, the $\{200\}_p$ shifts more significantly as function of ψ, indicating a higher lattice strain due to domain switching.

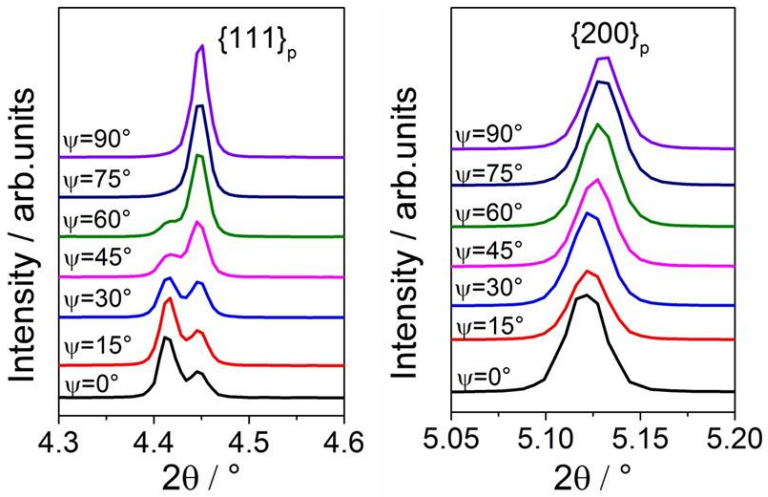

Figure 5.38 The representative XRD peak reflections for poled NBT-0.03KN.

The d-spacing, lattice strain, intensity ratio and [111]-oriented domain fraction for the poled NBT-0.03KN ceramic were calculated using the method described

above for NBT-0.01KN. The results obtained for $d_{\{200\}}$ and $\varepsilon_{(200)}$, as a function of ψ are illustrated in Figure 5.39. It is apparent that the dependence of ε_{200} on ψ exhibited a good fit to Equation 5.7. As a comparison, the value of lattice strain for NBT-0.03KN reaches of 1.4 x 10^{-3} at ψ = 0º, which was much higher than for NBT-0.01KN (0.4 x 10^{-3}).

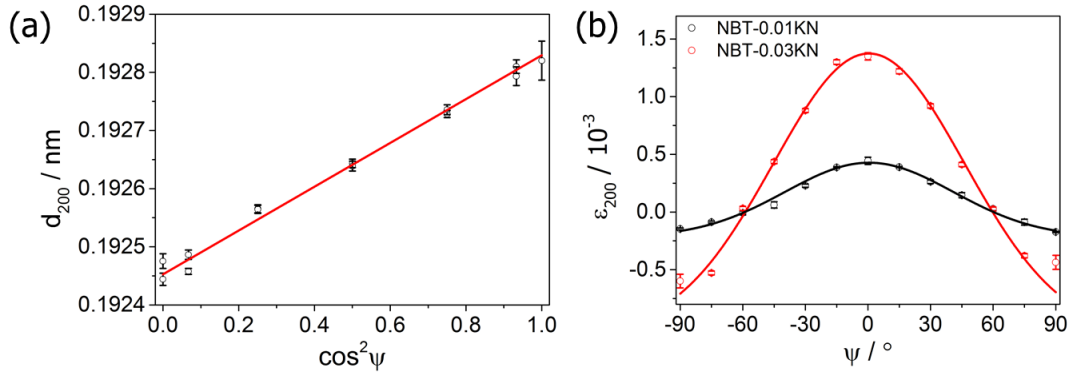

Figure 5.39 Dependence of (a) d_{200} for NBT-0.01KN and (b) ε_{200} for NBT-0.01KN and NBT-0.03KN on azimuthal angle, ψ.

The results for $R_1(111)$ and ν_{111} are calculated using the same method for NBT-0.01KN described above and plotted as function of ψ, as shown in Figure 5.40. The linear fit to the data indicated that the intensity ratio was approximately equal to 0.214 at $\cos^2\psi$ = 1/3. Furthermore, The degree of non-180° domain switching in the remanent state for poled NBT-0.03KN is higher than poled NBT-0.01KN, with a maximum ν_{111} value of approximately 0.76 (0.55 for NBT-0.01KN) being achieved for ψ = 0°. This level of saturation was similar to that of the *soft* rhombohedral PZT, reported by Hall.[186]

This level of saturation is even better than that of NBT-0.02KN, reported previously by Wang.[67] Also, it is clearly evident that the domain orientation distribution function follows closely the form of the macroscopic strain, according to Equation 5.7. The enhanced degree of ferroelectric domain switching in the NBT-0.03KN ceramic can be attributed to the relatively low coercive field of this composition, which itself is due to the lower rhombohedral distortion.

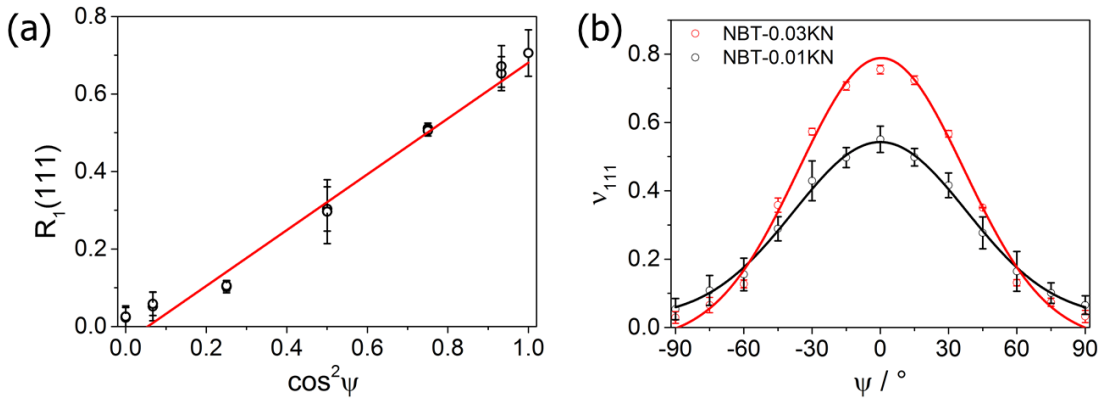

Figure 5.40 Dependence of (a) peak intensity ratio, $R_1(111)$, and (b) domain fraction, ν_{111}, on azimuthal angle, ψ. Symbols are experimental data points and solid lines are calculated using a squared cosine relation.

5.8.2 Influence of composition at high temperature

The in-situ poling experiments were also carried out using high-energy synchrotron XRD in Diamond at 100 ºC for NBT-xKN specimens. The domains with grain orientation ψ= 0º were selected to illustrate the effect of electric field on the domain orientation distribution.

5.8.2.1 Changes in XRD patterns during electric poling

5.8.2.1.1 NBT-0.01KN

The cycle-dependent peak profiles of $\{111\}_p$ and $\{200\}_p$ for NBT-0.01KN are illustrated in Figure 5.41. It is evident that both peaks are single in the unpoled state (cycle number 0), indicating the presence of the cubic structure. After the first cycle of electric field, a rhombohedral structure was observed, characterised by double $\{111\}_p$ and single $\{200\}_p$ peaks. Similar to the transformation at room temperature, cycles of electric field can induce the structural transformation from cubic to rhombohedral. However, much fewer cycles were required at 100 ºC due to the lower coercive field and lower spontaneous strain at high temperature. This leads to easier domain switching and a more rapid phase transformation. Hence, the structural transformation started immediately after the first cycle and was completed within 3 cycles.

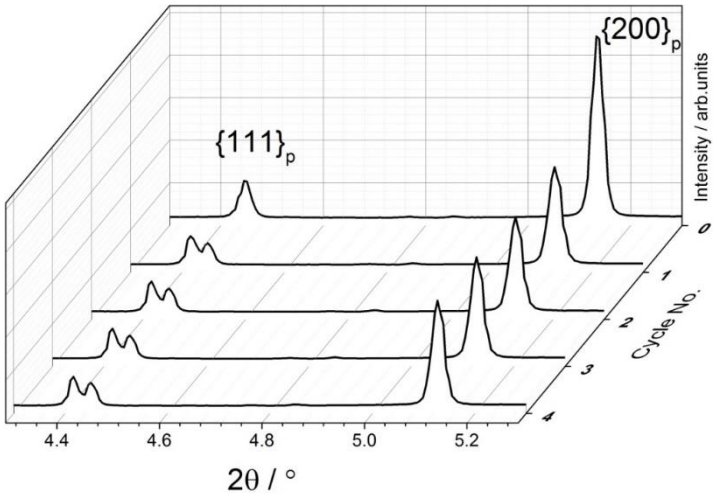

Figure 5.41 The 'in-situ' cycle-dependent peak profiles of $\{111\}_p$ and $\{200\}_p$ for NBT-0.01KN at 100 ºC.

5.8.2.1.2 NBT-0.03KN

The cycle-dependent peak profiles of $\{111\}_p$ and $\{200\}_p$ for NBT-0.03KN are displayed in Figure 5.42. Similar to the case of NBT-0.01KN, both peaks are single in the unpoled state, indicating the presence of the cubic structure. After the first cycle of electric field, a slight shoulder is observed on $\{111\}_p$ peak, which develops gradually with increasing cycles. The $\{200\}_p$ peak remains single. Corresponding to the ferroelectric results reported in 5.4.1, the poling procedure at 100 ºC induced a reversible transformation from PNRs to the metastable FE state, resulting in a constricted P-E loop and split polarisation switching peak. Even though the temperature of 100 ºC is above the depolarisation temperature (T_d) and phase transition temperature (T_{F-R}), as reported in Section 5.5 and 5.6, the rhombohedral distortion was still retained after the poling procedure, which is in agreement with the temperature-dependent XRD study (Section 5.7.3).

It is proposed that this reversible transformation still induce structural transformation from cubic to pseudo-cubic with slight rhombohedral-distortion, evidenced by a weak shoulder on the $\{111\}_p$ peak. This transformation occurred after applying 1 cycle and was complete within 3 cycles.

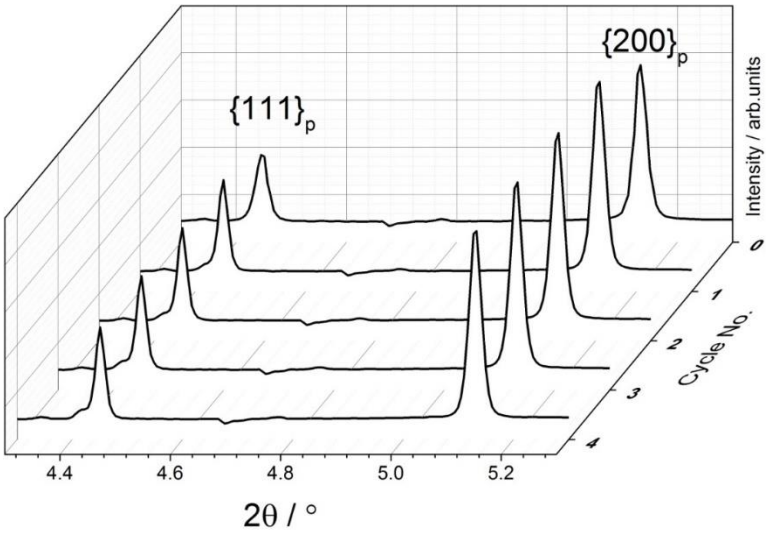

Figure 5.42 The 'in-situ' cycle-dependent peak profiles of $\{111\}_p$ and $\{200\}_p$ for NBT-0.03KN at 100 ºC.

5.8.2.1.3 NBT-0.05KN

The cycle-dependent representative peak profiles of $\{111\}_p$ and $\{200\}_p$ for NBT-0.05KN are displayed in Figure 5.43. It is apparent that both peaks are single in the unpoled state, indicating the presence of the cubic structure. After 5 cycles of electric field, both peaks remain single, indicating that no structural transformation occurred. Hence, the in-situ poling has no influence on structure for NBT-0.05KN at room temperature and at 100 ºC.

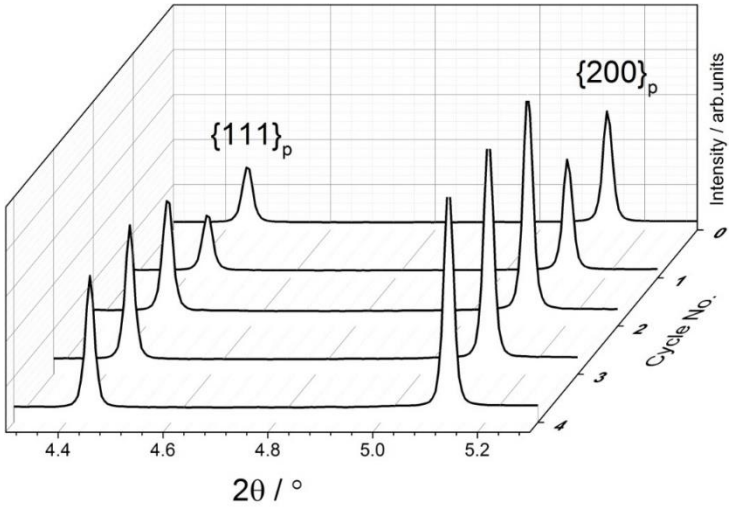

Figure 5.43 The 'in-situ' cycle-dependent peak profiles of $\{111\}_p$ and $\{200\}_p$ for NBT-0.05KN at 100 ºC.

5.9 Summary

The (1-x)NBT-xKN (x=0.01 to 0.09) ceramics were synthesized by solid state reaction, obtaining a relatively density of 93% or greater. The average grain size in the sintered ceramics ranges from 2.05 to 8.55 μm and decreases with enhancing KN content. The XRD results for as-sintered ceramics pellets indicated the presence of a cubic phase for all compositions. However, for compositions with low KN content, a well-defined P-E loop was observed during ferroelectric hysteresis measurements under a high electric field, indicating that a structural transformation must have occurred. It was shown using high resolution SXPD that an irreversible structural transformation to rhombohedral occurred for NBT-0.01KN and NBT-0.03KN even after mechanical crushing, indicating a nonergodic-RF state at room temperature. In contrast, there was a less significant influence of electric field on crystal structure for NBT-0.05KN and no effect for NBT-0.09KN due to the ergodicity, which is associated with constricted P-E loops and split polarisation switching peaks in the J-E curve.

To further investigate the structural transformation for (1-x)NBT-xKN during poling, an in-situ poling experiment was conducted in beamline I15 (Diamond). Each diffraction pattern was recorded after a quick bipolar electric field cycle and the diffraction image was caked into conventional XRD patterns by Fit2D. It was

found that the structural transformation could not be observed using the conventional in-situ experimental method, in which the XRD pattern is obtained during application of the electric field. Hence, this kind of structural transformation only can be observed by applying several cycles of the electric field, similar to procedure employed during the P-E measurements. A similar time-dependent in-situ structural transformation experiment was performed on NBT-KBT by Royles.[189] It was found that low-frequency poling induced domain switching first while the structural transformation was more easily induced under high-frequency poling.

It took approximately 15 and 11 cycles of the bipolar electric field to complete the structural transformation from cubic to rhombohedral for NBT-0.01KN and NBT-0.03KN respectively. After poling, it was found that the electric field-induced metastable rhombohedral phase exhibited both structural and functional characteristics that are typical of a conventional long-range ordered ferroelectric. Furthermore, the texture- and strain-free XRD patterns for NBT-0.03KN during poling were obtained to analyse the intermediate state. The NBT-0.03KN was identified as a cubic structure before applying 7 cycles of electric field, then a mixed-phase of rhombohedral and cubic were obtained between 7 and 11 cycles, followed by the presence of a single rhombohedral phase from 11 cycles onward.

With increasing temperature, the electric field-induced rhombohedral structure can transform back to cubic for low KN contents in (1-x)NBT-xKN ceramics. The structural transformation temperature, T_{ST}, was determined on poled specimens by investigating the thermally-induced structural transformation on beamline I11, Diamond. In addition, the depolarisation temperature for poled specimens, T_d, and the phase transition temperature, T_{F-R}, were obtained on poled specimens. It was proposed that the T_{ST} is higher than T_d and T_{F-R} for NBT-0.01KN, NBT-0.03KN and NBT-0.05KN, indicating that the rhombohedral structure can be retained even after depolarisation. In contrast, the NBT-0.09KN retained its cubic structure corresponding to the RF state for all temperatures.

Further evidence was obtained by conducting a high energy in-situ poling experiment and ferroelectric hysteresis measurements as a function of temperature. Split polarisation switching peaks in the J-E curve were observed for NBT-0.01KN, NBT-0.03KN and NBT-0.05KN at certain temperatures, corresponding to T_d and T_{F-R}, indicating a reversible phase transition between PNRs and long-range ferroelectric order. However, the maximum polarisation still reaches high values for these compositions even over T_d and T_{F-R}. Additionally, the irreversible transformation from cubic to rhombohedral phase was obtained at 100 ºC during in-situ electric poling for NBT-0.01KN and NBT-0.03KN, which is in agreement with the results obtained in the temperature-dependent SXPD study.

Therefore, by combining the phase transition temperatures, T_{F-R}, T_{ST} and T_m (dielectric peak), for pure NBT, as reported by Hiruma,[126] with results obtained in this work for poled (1-x)NBT-xKN (x=0.01 to 0.09), a phase diagram is plotted, as presented in Figure 5.44.

For NBT-KN compositions with low KN content, a metastable FE state with rhombohedral structure was observed below transition temperature, T_{F-R}, for poled specimens. With increasing temperature, this metastable FE state becomes unstable and transforms back to the ergodic-RF (ER) state with a remaining rhombohedral distortion. The structural transformation temperature, T_{ST}, for these compositions is approximately 150 ºC above T_{F-R}, resulting in an ER state with cubic structure. In contrast, an ER state with cubic structure was identified for compositions with high KN content for all temperatures. Even though the structure was observed to be cubic above T_{ST}, it assumed that the local structure of the PNRs possesses different symmetries, which transform into the cubic structure at higher temperatures.

Another transition temperature, representing the transformation from the ER state to a non-polar paraelectric (PE) state is defined as the Burns temperature, T_B, which was not determined in the present work. Additionally, the dielectric

peak, T_m, was determined using the ε_r-T relationship. All transition temperatures decrease with increasing KN content, consistent with increasing disorder on both A- and B- cation sites in the ABO_3 perovskite structure.

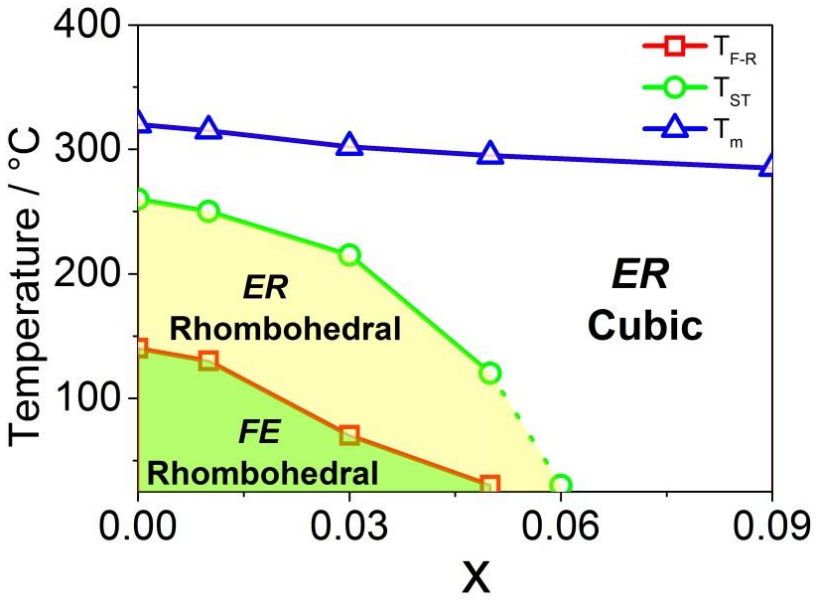

Figure 5.44 Phase diagram obtained from analysis of dielectric and structural studies on poled (1-x)NBT-xKN ceramics.

6 Phase switching behaviour in $Na_{0.5}Bi_{0.5}TiO_3$-$NaNbO_3$ ceramics

In this chapter, the structural and electrical properties of the (1-x)NBT-xNN system are fully investigated as function of composition and temperature. The phase transition between RF and metastable FE states are examined using temperature-dependent electrical measurements. The synchrotron SXPD is used to properly identify crystal structure for compositions exhibiting a well-defined P-E loop at room temperature. Furthermore, an electric poling experiment is examined 'in-situ' using high energy synchrotron XRD to observe the structural transformation and analyse crystallographic texture.

6.1 Density analysis

The changes in relative density for different compositions in the NBT-xNN (x=0.02 to 0.08) system as a function of the sintering temperature are presented in Figure 6.1. After calcination, the ceramic pellets were sintered at temperatures from 1120 ºC to 1220 ºC. At 1120 ºC, the relative density of approximately 92 % was achieved, followed by a slight increase with increasing sintering temperature. The best relative densities were obtained by sintering at 1180 ºC, reaching approximately 94 % to 96 % for all compositions. With further increasing temperature, the relative density decreases significantly to 92 %, especially for compositions with high NN content. The low densification at temperatures over 1180 ºC is assumed to be due the volatilisation of Na_2O and Bi_2O_3. Thus, 1180 ºC was selected as the optimum sintering temperature for the NBT-xNN system. Similar assumption as NBT-KN ceramics was adapted to consider that the reduction in density at the highest sintering temperatures is caused by the loss of volatile oxides, such as Na_2O and Bi_2O_3.[162, 163]

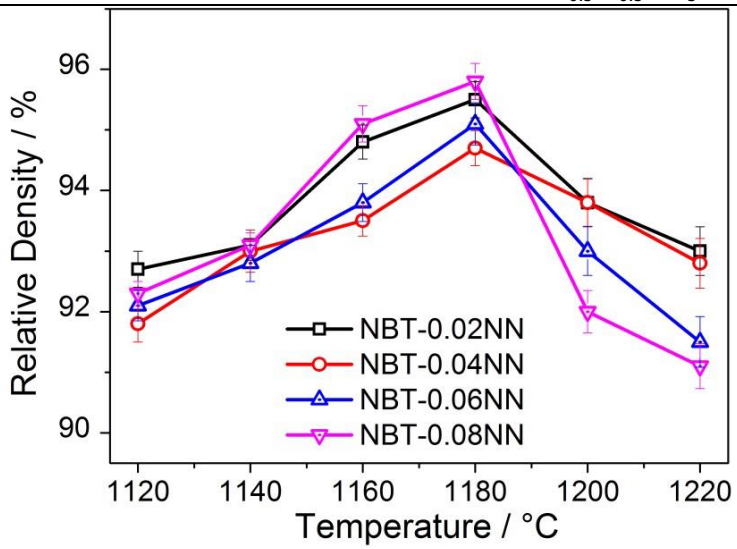

Figure 6.1 Relative densities for different sintering temperatures for NBT-xNN ceramics.

6.2 Lab XRD results

6.2.1 Calcined powders

The XRD profiles of NBT-xNN (x=0.02 to 0.08) powders calcined at a temperature of 850 ºC for 10 hours are illustrated in Figure 6.2. All peaks appear to be single and peak position shifts slightly to lower d-spacing with increasing NN content.

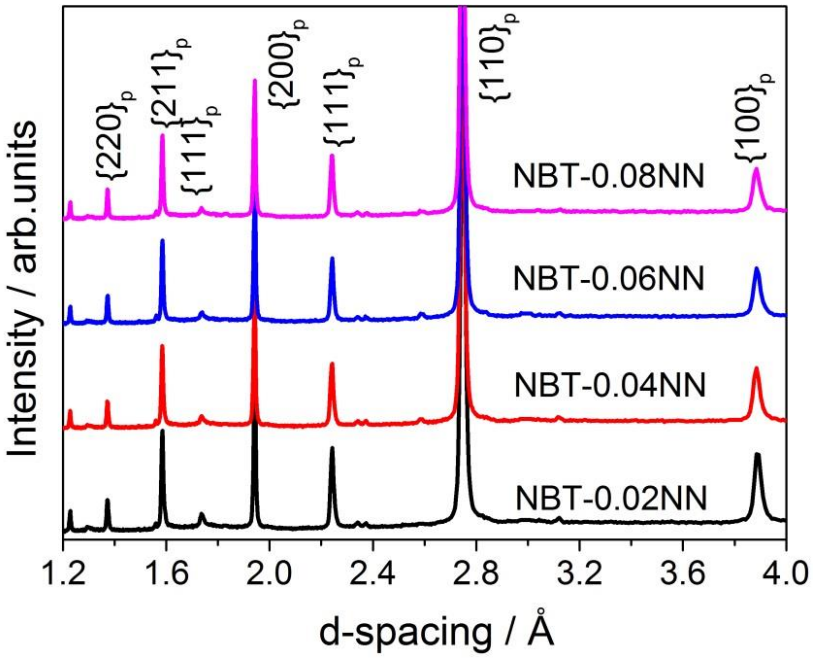

Figure 6.2 The XRD full patterns for calcined NBT-xNN powders.

6.2.2 Sintered ceramic pellets

The crystal structures for unpoled NBT-xNN (x=0.02 to 0.08) ceramic pellets were examined using lab XRD, as illustrated in Figure 6.3. All compositions were found to be single phase cubic with a perovskite structure, indicated by the presence of unsplit diffraction peaks.

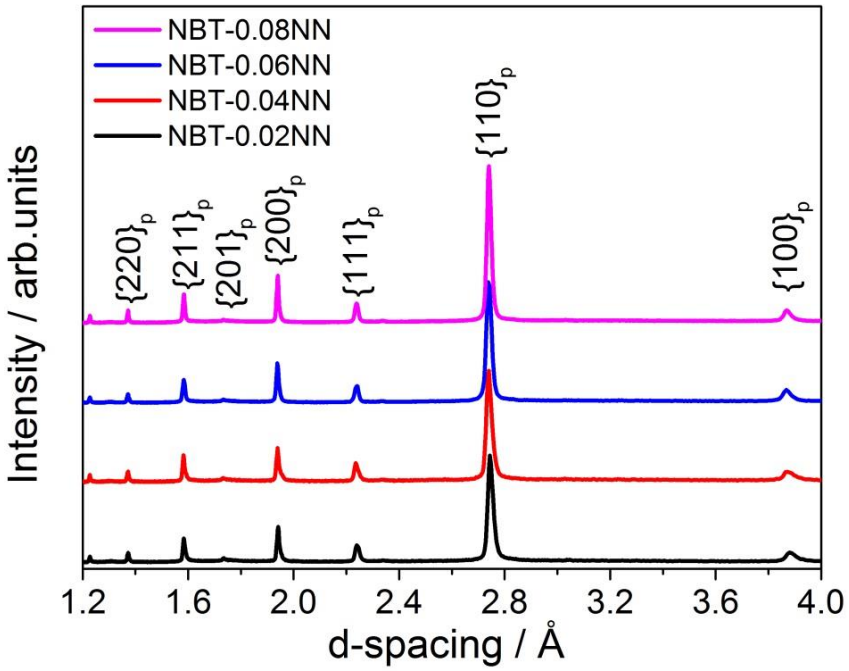

Figure 6.3 The XRD full patterns of the unpoled state for all compositions in the NBT-xNN system sintered at 1180 ºC for 3 hours.

6.3 SEM

The cross-Sectional SEM images for NBT-xNN (x=0.02 to 0.08) bulk ceramics were recorded under BSE imaging mode and are illustrated in Figure 6.4. The average grain sizes for all compositions in NBT-xNN system are listed in Table 6.1. Results similar to those of NBT-KN were obtained in that the grain size decreases slightly with increasing NN content, indicating that adding NN content inhibits the grain growth.

Table 6.1 The average grain size for NBT-xNN ceramics.

Compositions	Grain size / μm
NBT-0.02NN	8.28±0.71
NBT-0.04NN	7.73±0.54
NBT-0.06NN	6.87±0.58
NBT-0.08NN	5.81±0.54

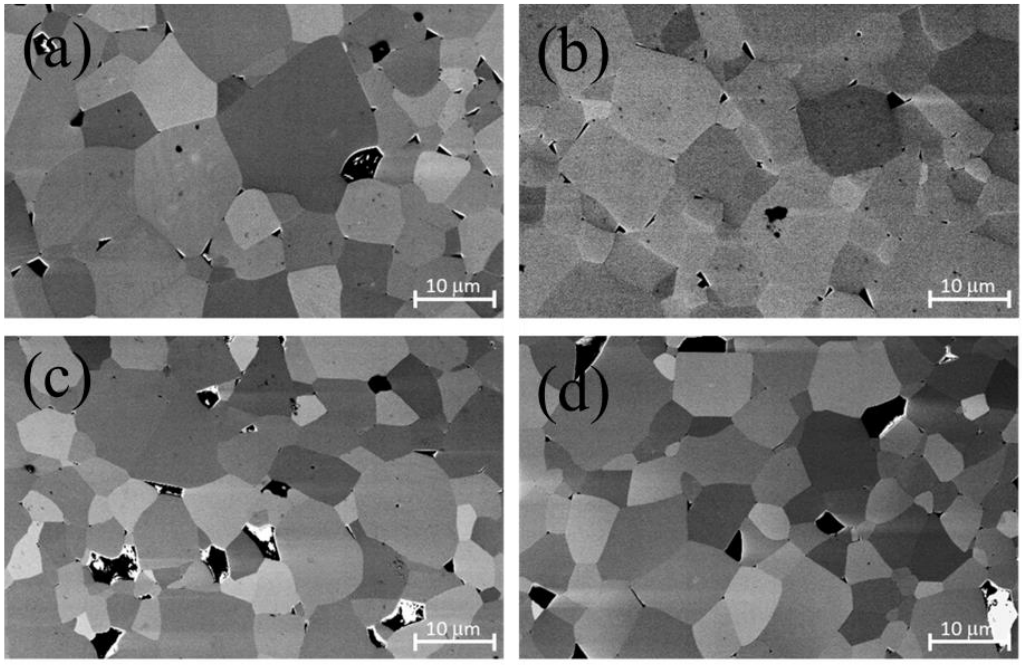

Figure 6.4 The cross-Sectional SEM images for (a) NBT-0.02NN (b) NBT-0.04NN (c) NBT-0.06NN and (d) NBT-0.08NN ceramics.

6.4 Temperature-dependent ferroelectric properties

6.4.1 Polarisation-Current density-Field (P-J-E) loops

The ferroelectric hysteresis loops (P-E) and current density curves (J-E) for NBT-0.02NN over the temperature range from 30 to 120 ºC are shown in Figure 6.5. From 30 to 75 ºC, this material behaves as a typical ferroelectric with saturation of the P-E loop and an unsplit switching peak in the J-E curve. With increasing temperature, the coercive field drops but both P_{max} and P_{rem} increase. At 120 ºC, a constricted P-E loop and split polarisation switching peaks in the J-E loop are apparent, indicating that a reversible transformation between PNRs and long-range ordered FE state was induced under the high electric-field at this temperature.

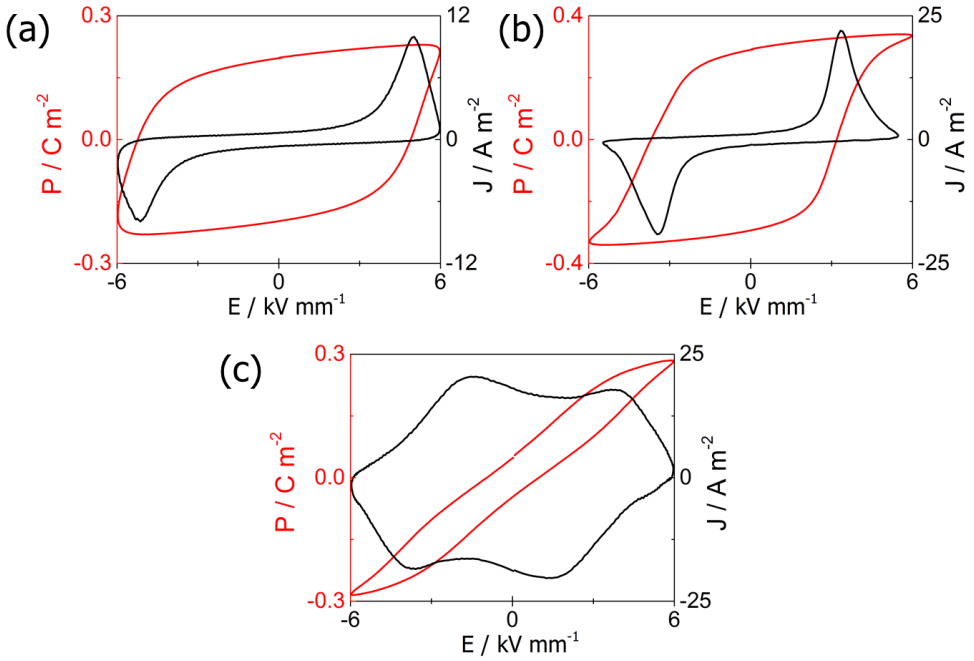

Figure 6.5 The P-J-E curves for NBT-0.02NN ceramic at temperatures of (a) 30 ºC (b) 75 ºC and (c) 120 ºC.

The P-E loops and J-E curves for NBT-0.04NN in the temperature range from 30 to 120 ºC are illustrated in Figure 6.6. A similar behaviour to NBT-0.03KN is observed. At room temperature, a well-defined P-E loop is observed with relatively high P_{max} and P_{rem} values of 0.36 C m^{-2} and 0.33 C m^{-2} respectively. With increasing temperature to 75 ºC, a slightly constricted P-E loop is observed and split polarisation switching peaks are present on the J-E curves for both positive and negative field, suggesting that the switching between PNRs and long-range ferroelectric order became reversible at 75 ºC. The E_f and E_b values at this temperature were approximately 4.5 kV and 1.6 kV mm^{-1}.

With further heating, a more slim and constricted P-E loop was observed. During the heat treatment, the P_{max} retains approximately the same value of 0.35 C m^{-2} from 30 ºC to 120 ºC, indicating that the polarisation can reach a similar maximum value after the PNRs switch to the long-range ferroelectric order with the electric field on. However, the P_{rem} declines dramatically from 0.34 C m^{-2} at 30 ºC to approximately zero at 120 ºC, indicating that the long-range ferroelectric order is destabilised on removing the electric field and the destabilisation rate enhances with increasing temperature.

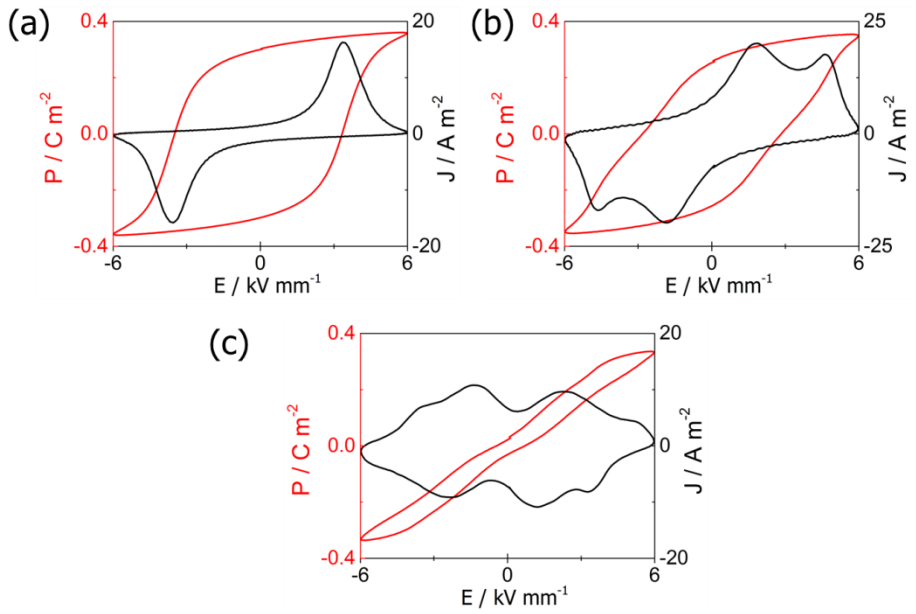

Figure 6.6 The P-J-E curves for NBT-0.04NN ceramic at temperatures of (a) 30 ºC (b) 75 ºC and (c) 120 ºC.

The P-E and J-E loops for NBT-0.06NN in the temperature range from 30 to 120 ºC are shown in Figure 6.7. A similar behaviour to NBT-0.05KN was observed. The split polarisation switching peaks in the J-E loop and a constricted P-E loop are observed for all temperatures. In addition, the P-E loop develops more constriction, with low remanent polarisation values, with increasing temperature.

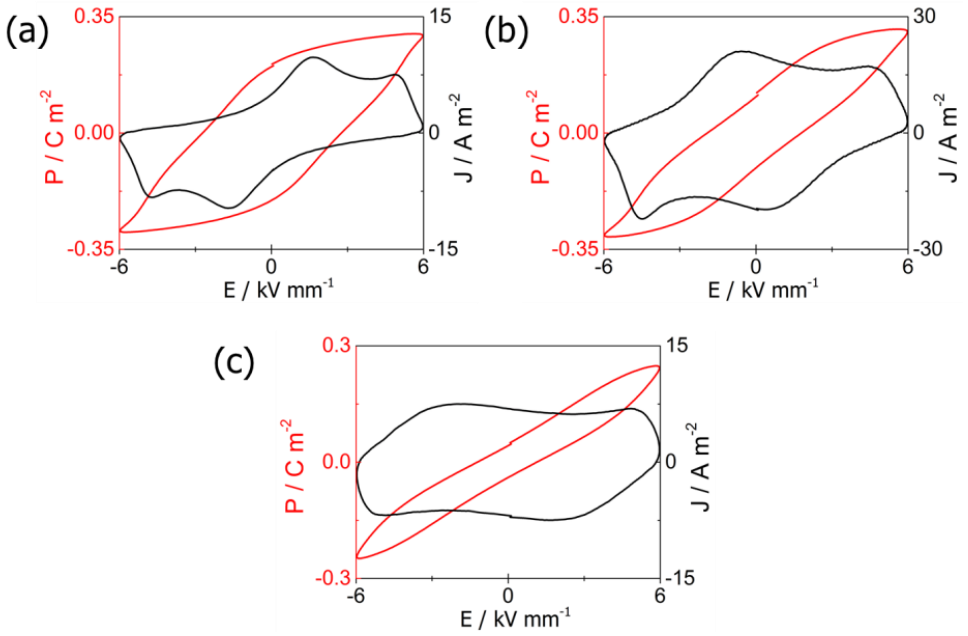

Figure 6.7 The P-J-E curves for NBT-0.06NN ceramic at temperatures of (a) 30 ºC (b) 75 ºC and (c) 120 ºC.

The P-E loops and J-E curves for NBT-0.08NN in the temperature range from 30 to 120 ºC are shown in Figure 6.8. The P-E loops are observed to be slim and constricted for all temperatures. The shape of the P-E loop becomes slimmer while the maximum and remanent polarisation values decrease with increasing temperature. Compared to NBT-0.09KN, the P_r and P_{max} values are slightly higher.

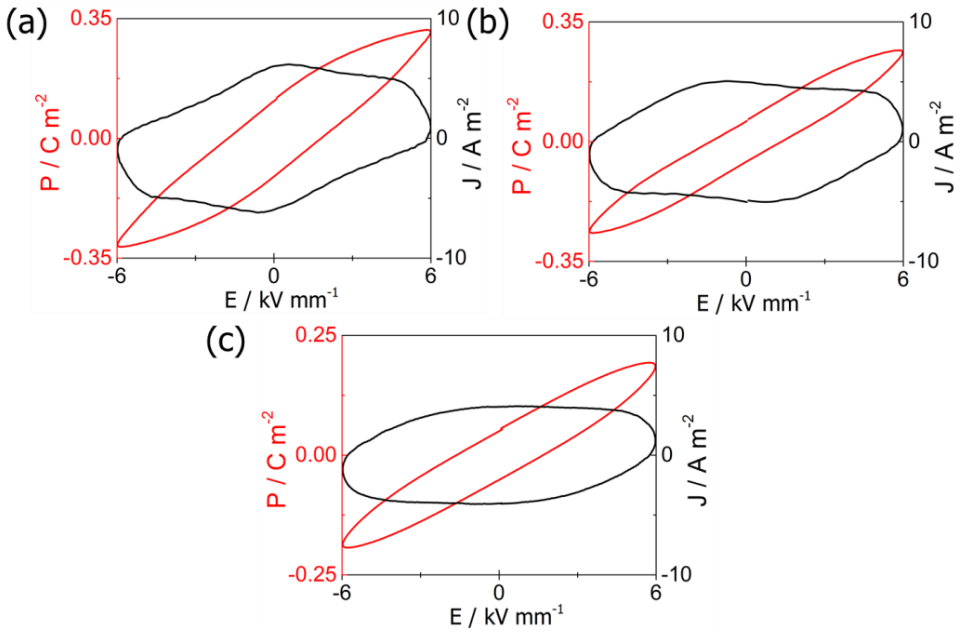

Figure 6.8 The P-J-E curves for NBT-0.06NN ceramic at temperatures of (a) 30 ºC (b) 75 ºC and (c) 120 ºC.

6.4.2 Summary

Both P-E and J-E ferroelectric hysteresis loops were obtained for NBT-xNN (x=0.02 to 0.08) in the temperature range from 30 to 120 ºC. The polarisation switching field (E_c or E_b/E_f), maximum polarisation (P_{max}) and remanent polarisation (P_{rem}) values are summarised in Table 6.2 below.

Table 6.2 The (a) polarisation switching field, (b) maximum polarisation and (c) remanent polarisation for NBT-xKN ceramics at different temperatures.

(a) E / kV mm^{-1}

x	30 ºC	75 ºC	120 ºC
0.02	4.5	3.8	3.4/1.5
0.04	3.1	4.5/1.6	N/A
0.06	4.9/1.4	4.7/0.7	N/A
0.08	N/A	N/A	N/A

(b) P_{max} / C m^{-2}

x	30 ºC	75 ºC	120 ºC
0.02	0.22	0.33	0.28
0.04	0.36	0.35	0.33
0.06	0.33	0.34	0.27
0.08	0.31	0.22	0.18

(c) P_{rem} / C m^{-2}

x	30 ºC	75 ºC	120 ºC
0.02	0.17	0.31	0.08
0.04	0.33	0.29	0.04
0.06	0.22	0.15	0.05
0.08	0.14	0.08	0.09

As illustrated above, the XRD results for all of the unpoled ceramics appeared to show single unsplit diffraction peaks, indicating a cubic structure. However, well-developed ferroelectric hysteresis P-E loops were obtained for compositions with low NN content. This behaviour was similar to that of the NBT-xKN ceramics, as described in Section 5.4. Hence, it is proposed that an electric field-induced phase transition and structural transformation occurred for low NN contents in the present study. For low NN contents, the PNRs can be transformed irreversibly into the metastable long-range FE state, which is retained after removing the external electric field. However, for high NN contents, this transformation from PNRs to metastable long-range FE state becomes reversible.

With increasing temperature, a constricted P-E loop and a split polarisation switching peak in the J-E curve were observed at 120 ºC and 75 ºC for NBT-0.02NN and NBT-0.04NN respectively, which are similar to those of NBT-0.06NN at room temperature, indicating a reversible transformation from PNRs to the long-range ordered metastable FE state. Hence, it is proposed that the NBT-0.02NN and NBT-0.04NN ceramics exhibited a nonergodic-RF (NR) state at room temperature then transformed into an ergodic-RF (ER) state at elevated temperatures. Finally, the NBT-0.08NN ceramic exhibits an ER state at all temperatures, showing a weak ferroelectric behaviour with slim P-E loops.

6.5 Temperature-dependent depolarisation

Thermal depolarisation results for poled NBT-0.02NN and NBT-0.04NN ceramics are illustrated in Figure 6.9. The samples were poled using at least 20 cycles of an AC electric field with amplitude 6 kV mm^{-1} at room temperature. The poled specimens lost the majority of their remanent polarisation at approximately 123 ºC and 60 ºC for NBT-0.02NN and NBT-0.04NN respectively.

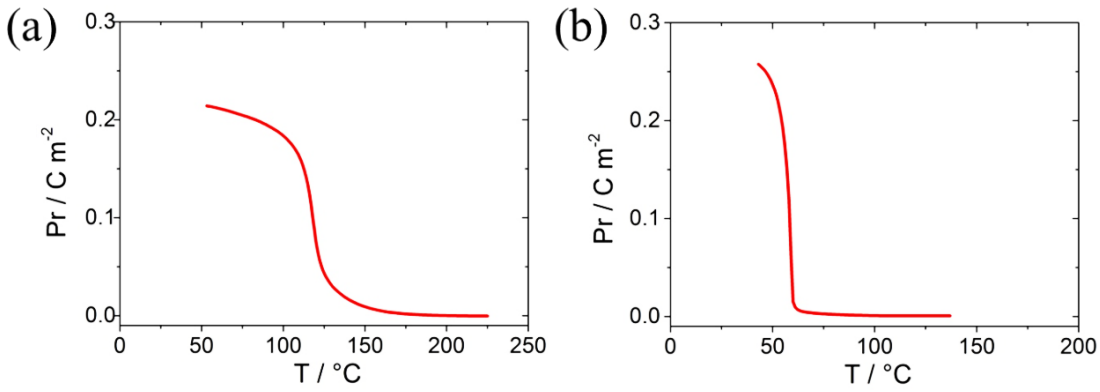

Figure 6.9 The thermally-induced depolarisation results for (a) NBT-0.02NN and (b) NBT-0.04NN poled ceramics.

The depolarisation temperature, T_d, in NBT-xNN decreases with increasing NN content for low NN contents. A thermal depolarisation temperature could not be obtained for compositions with x=0.06 and x=0.08, due to the ergodic-RF state. To summarise, the depolarisation temperature and maximum depolarisation rate for poled NBT-xNN ceramics are listed in Table 6.3 below.

Table 6.3 The thermally-induced depolarisation temperature and maximum depolarisation rate for all compositions in the NBT-xNN system.

Compositions	T_d / ºC	dP/dT / mC m^{-2} $ºC^{-1}$
NBT-0.02NN	123	13
NBT-0.04NN	60	58
NBT-0.06NN	N/A	N/A
NBT-0.08NN	N/A	N/A

6.6 Dielectric measurements

6.6.1 Poled states

The changes in dielectric permittivity and loss tangent with temperature from 50 to 420 ºC for poled NBT-xNN (x=0.02 to 0.08) ceramics are displayed in Figure 6.10. All compositions exhibit significant variations in permittivity and loss tangent with increasing temperature, which can be attributed to changes in crystal structure and local ferroelectric order i.e. to the evolution of the FE domain structure and PNRs.

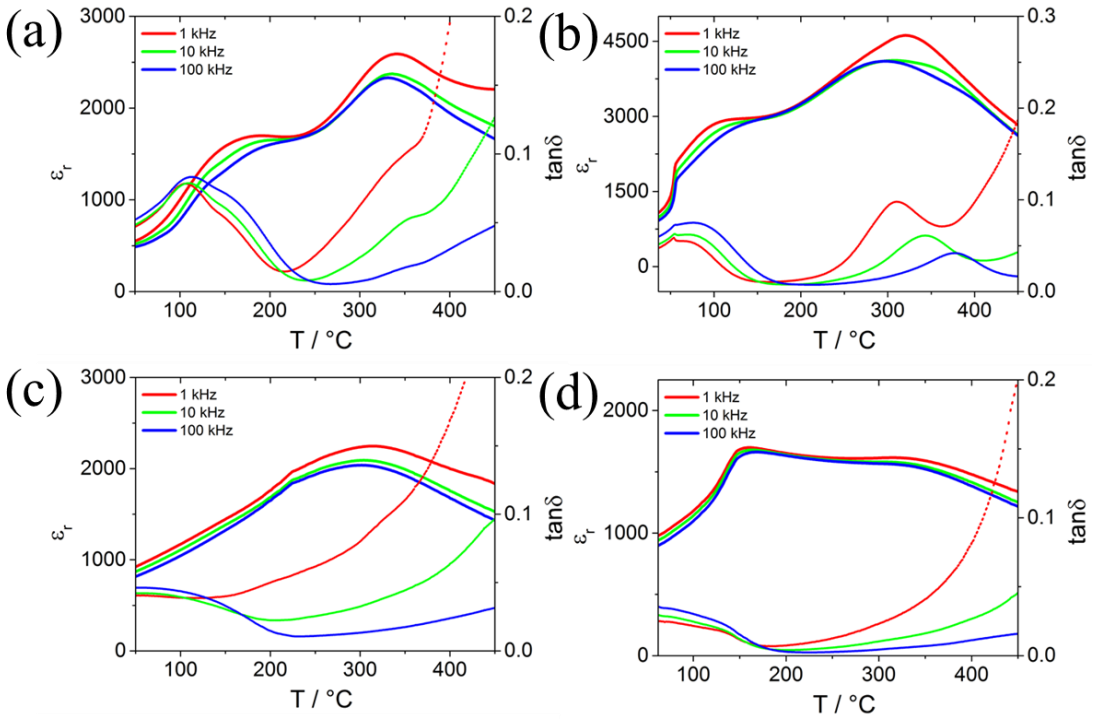

Figure 6.10 The temperature-dependent permittivity and loss curves for poled NBT-xNN specimens (a) x=0.02 (b) x=0.04 (c) x=0.06 and (d) x=0.08.

For NBT-0.02NN, the initial frequency-independent ε_r value is in the region of 500. ε_r increases steadily up to a value of approximately 1700 at 185 ºC, at which temperature some frequency dispersion appears. The permittivity remains stable until approximately 230 ºC, with less frequency dispersion. With further increase in temperature, ε_r increases sharply up to a peak value of 2560 at approximately 345 ºC with reappearance of frequency dispersion, followed by a decrease upon further heating. Similar to NBT-xKN ceramics, the frequency dispersion in the

lower temperature region can be attributed to the evolution of the PNRs, while that at higher temperatures is most likely due to increasing electronic conductivity and the associated space-charge polarisation.

The loss tangent, tanδ, shows frequency-dependent behaviour and the transition temperature from metastable FE state to RF state, T_{F-R}, indicated by the sharp peak at approximately 118 ºC. The value of tanδ begins at approximately 0.05 and increases up to 0.075 at T_{F-R}, followed by a decrease to 0.02 at approximately 230 ºC. The tanδ increases with increasing measurement frequency before T_{F-R} but then exhibits an inverse dependence on frequency at high temperatures, consistent with a contribution from electronic conductivity.[174]

Upon increasing the NN content to 4%, it was found that the phase transition temperature for NBT-0.04NN, T_{F-R}, decreased to 55 ºC and a significant increase in the maximum permittivity value was observed. The temperature for maximum permittivity, T_m, decreases to 322 ºC. The frequency-dependence tanδ exhibits a similar behaviour to that of NBT-0.02NN but less frequency dispersion after 230 ºC.

With further increases in NN concentration to 6% and 8%, there was no T_{F-R} observed on both ε_r-T and tanδ–T. For NBT-0.06NN, ε_r starts at approximately 950 with slight frequency dispersion, then increases to the first anomaly at approximately 210 ºC, followed by a progressive increase to ε_{max} at 310 ºC with frequency-dependence and a reduction upon further heating. The tanδ value starts at 0.05 then increases significantly above 200 ºC with strong frequency dispersion. For NBT-0.08NN, the shape of the ε_r-T relation was relatively flatter than that of the other compositions. There is a rapid increase to the first anomaly at approximately 150 ºC but then a relatively stable value up to the second anomaly at approximately 325 ºC, followed by further reductions with further heating. The tanδ value starts at 0.03 then reduces up to 175 ºC, followed by a dramatic increase above 300 ºC with strong frequency dispersion. These results

are in general agreement with those of Xu,[131] who investigated the dielectric behaviour for (1-x)NBT-xNN ceramics with x value ranging from 0.25 to 0.35. It was reported that such materials show good potential for use in high temperature capacitors, due to their temperature-stable and high permittivity values.

6.6.2 Unpoled states

The ε_r-T, and tanδ–T relations for unpoled NBT-xNN (x=0.02 to 0.08) specimens within the temperature range from 50 to 450 ºC are illustrated in Figure 6.11.

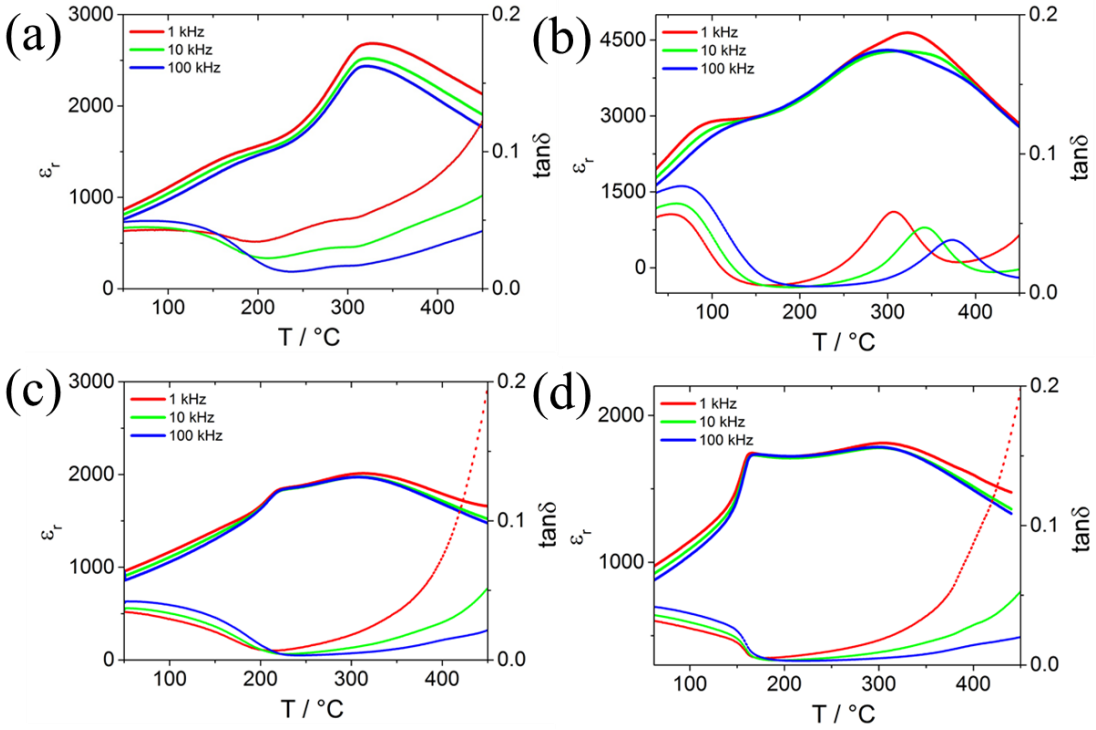

Figure 6.11 The temperature-dependent permittivity and loss curves for unpoled NBT-xNN specimens (a) x=0.02 (b) x=0.04 (c) x=0.06 (d) x=0.08.

In this case, no obvious T_{F-R} transition was observed for any composition, while both ε_{max} and T_{max} values remained approximately the same as those of the poled specimens. The ε_r values for all compositions show less frequency dispersion at lower temperatures until reaching the first anomaly, followed by a frequency-independent enhancement to T_m. Eventually, the ε_r values decrease with the reappearance of slight frequency dispersion upon further heating.

6.6.3 Summary

The important dielectric parameters including transition temperature, T_{F-R}, the maximum permittivity (1kHz), ε_{max}, and the temperature of the dielectric peak (1kHz), T_{max}, for poled NBT-xNN, obtained from the Figures above, are listed in Table 6.4 below.

Table 6.4 The transition temperature, maximum permittivity and temperature of dielectric peak for poled NBT-xNN ceramics.

Composition	T_{F-R} / °C	ε_{max}	T_{max}
x=0.02	118	2562	331
x=0.04	55	4551	326
x=0.06	N/A	2277	312
x=0.08	N/A	1665	322

Compared with the results of NBT-xKN ceramics discussed in Section 5.6, very similar ε_r-T and $\tan\delta$–T relationships were obtained for the NBT-xNN system. The transition temperature, $T_{F-R,}$ was only observed for compositions with low-NN content, NBT-0.02NN and NBT-0.04NN ceramics, which can be attributed to the electric field-induced metastable FE phase. Associated with the ferroelectric hysteresis measurements reported in Section 6.4, the destabilisation of the FE state at higher temperatures induces the reversible transformation, resulting in a significant drop in remanent polarisation. Furthermore, the T_{F-R} decreased with increasing compositional disorder with the result that no T_{F-R} could be detected for NBT-0.06NN and NBT-0.08NN.

A similar explanation can be given to explain the low-temperature and high-temperature anomalies in the ε_r-T relationship, which are due to the gradual destabilisation of the FE state and the transition between different PNR symmetries respectively.

6.7 High resolution SXPD experiments (Diamond beamline I11)

The aim of this investigation was to determine the effect of poling on the crystal structures in NBT-xNN ceramics by using high resolution SXPD. Only compositions exhibiting an irreversible transformation from PNRs to the long-range ordered metastable FE state, which were NBT-0.02NN and NBT-0.04NN, were studied. Similar to the study on NBT-KN ceramics, reported in Section 5.7 above, the crushed powders for both unpoled and poled states were evaluated using high resolution XRD and analysed by a full pattern refinement procedure in *Topas*.

6.7.1 Influence of composition at room temperature

The SXPD full patterns for unpoled and poled NBT-xNN ceramic powders with x=0.02 and x=0.04 are shown in Figure 6.12. For the unpoled state, all compositions were identified as cubic structure, characterised by all single peak reflections. In contrast, some split peaks were observed for powders in the poled state, indicating that an irreversible structural transformation had occurred during poling.

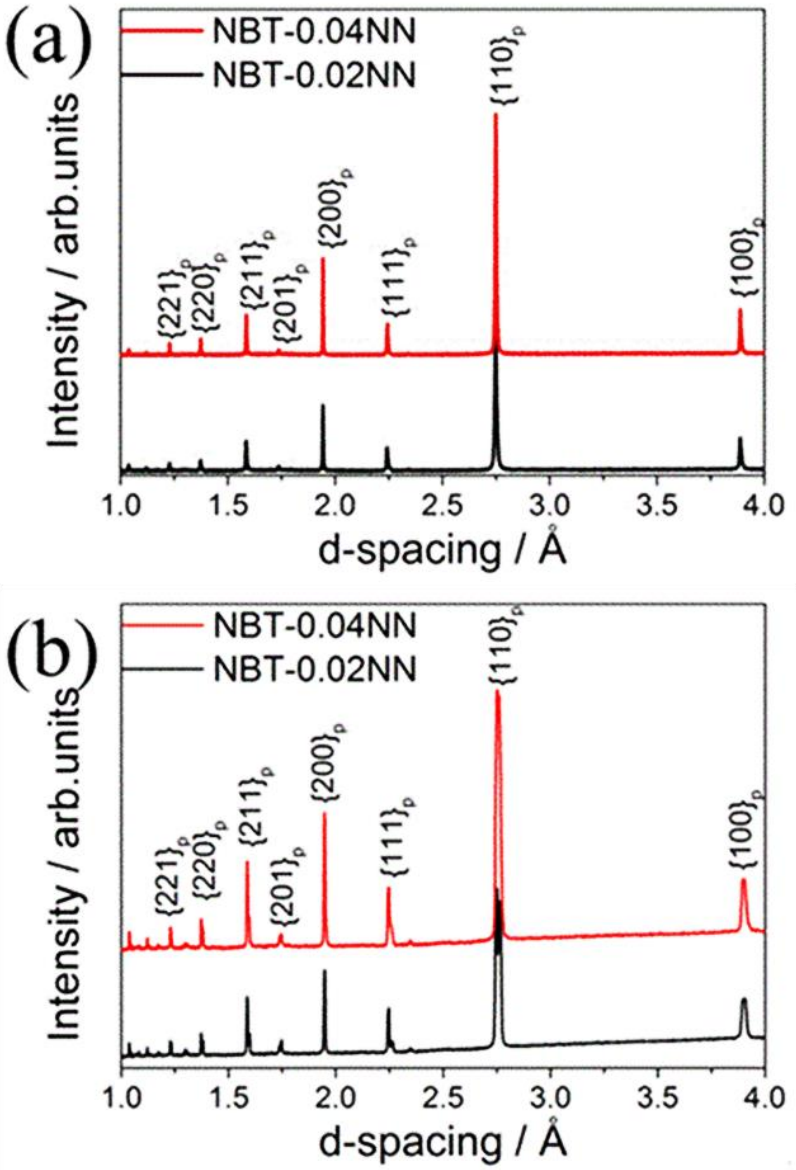

Figure 6.12 The SXPD full patterns for (a) unpoled and (b) poled NBT-0.02NN and NBT-0.04NN.

To examine the diffraction patterns in more detail, the peak profiles for $\{111\}_p$, $\{200\}_p$ and $\{211\}_p$ for both NBT-0.02NN and NBT-4NN are displayed in Figure 6.13. For the unpoled state, single $\{111\}_p$ and $\{200\}_p$ peaks are observed for both compositions, indicating a cubic structure. However, significant splitting of the $\{111\}_p$ and $\{211\}_p$ peaks, together with a single $\{200\}_p$ peak were obtained for poled NBT-0.02NN, indicating an electric field-induced rhombohedral phase. For poled NBT-0.04NN, a mixed-phase of rhombohedral and tetragonal is observed, characterised by a single peak with a broad shoulder on both $\{111\}_p$ and $\{200\}_p$ peak reflections. Superlattice peaks corresponding to the $(\frac{3}{2}\frac{1}{2}\frac{1}{2})_p$

reflection of the R3c phase are also observed for both compositions at a d-spacing of approximately 2.35 Å. In summary, an irreversible structural transformation from cubic to rhombohedral and cubic to mixed-phase of rhombohedral and tetragonal were observed for NBT-0.02NN and NBT-0.04NN respectively, even after crushing into powders, which results in the well-defined ferroelectric P-E loops observed above.

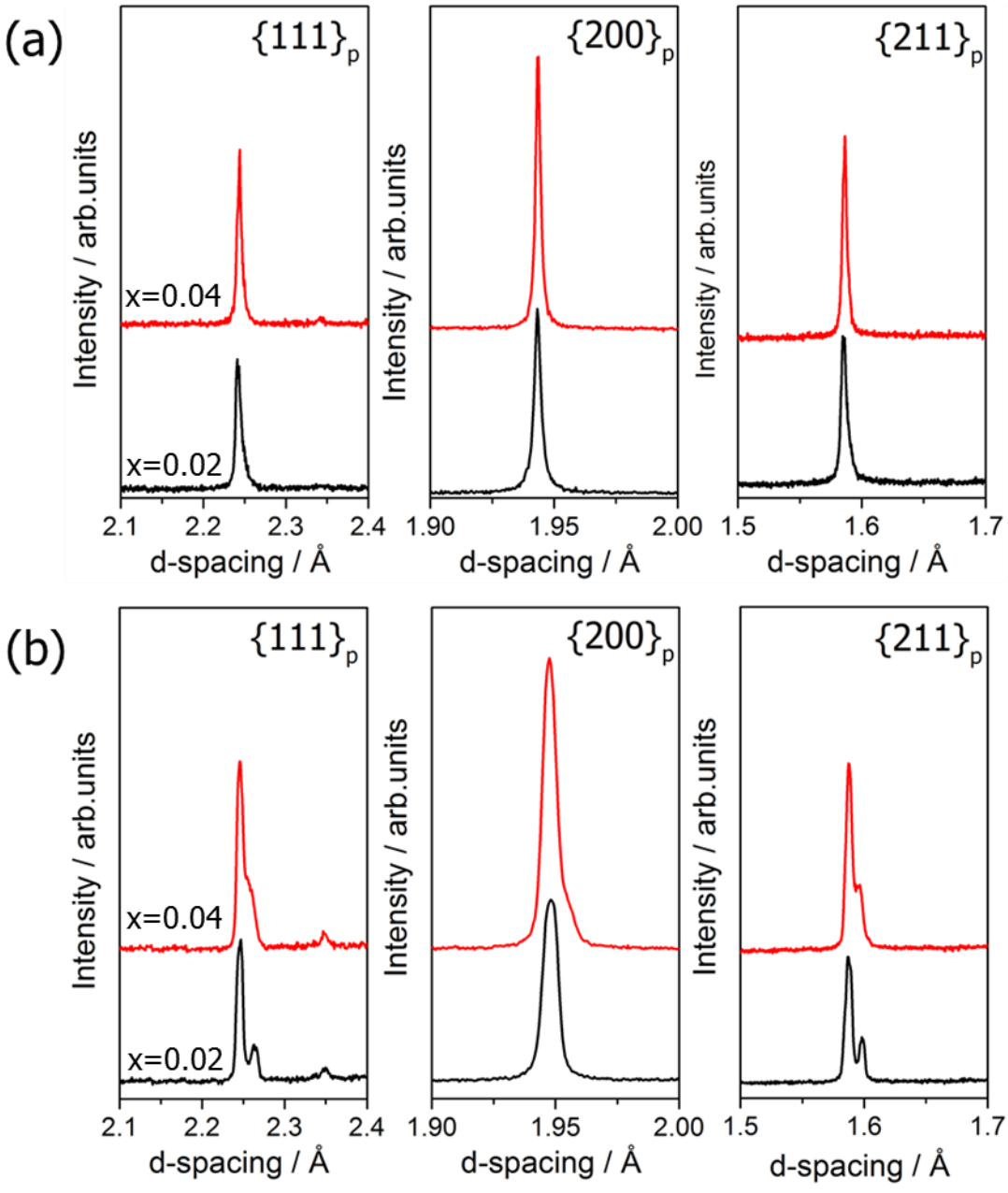

Figure 6.13 The representative peaks $\{111\}_p$, $\{200\}_p$ and $\{211\}_p$ of SXPD for (a) unpoled and (b) poled NBT-xKN (x=0.02 and 0.04).

6.7.2 Full pattern refinement

Full pattern refinement was carried out using *Topas* in order to obtain the crystallographic parameters for unpoled and poled NBT-xNN (x=0.02 and 0.04) ceramics. The refinement results are presented in Figure 6.14.

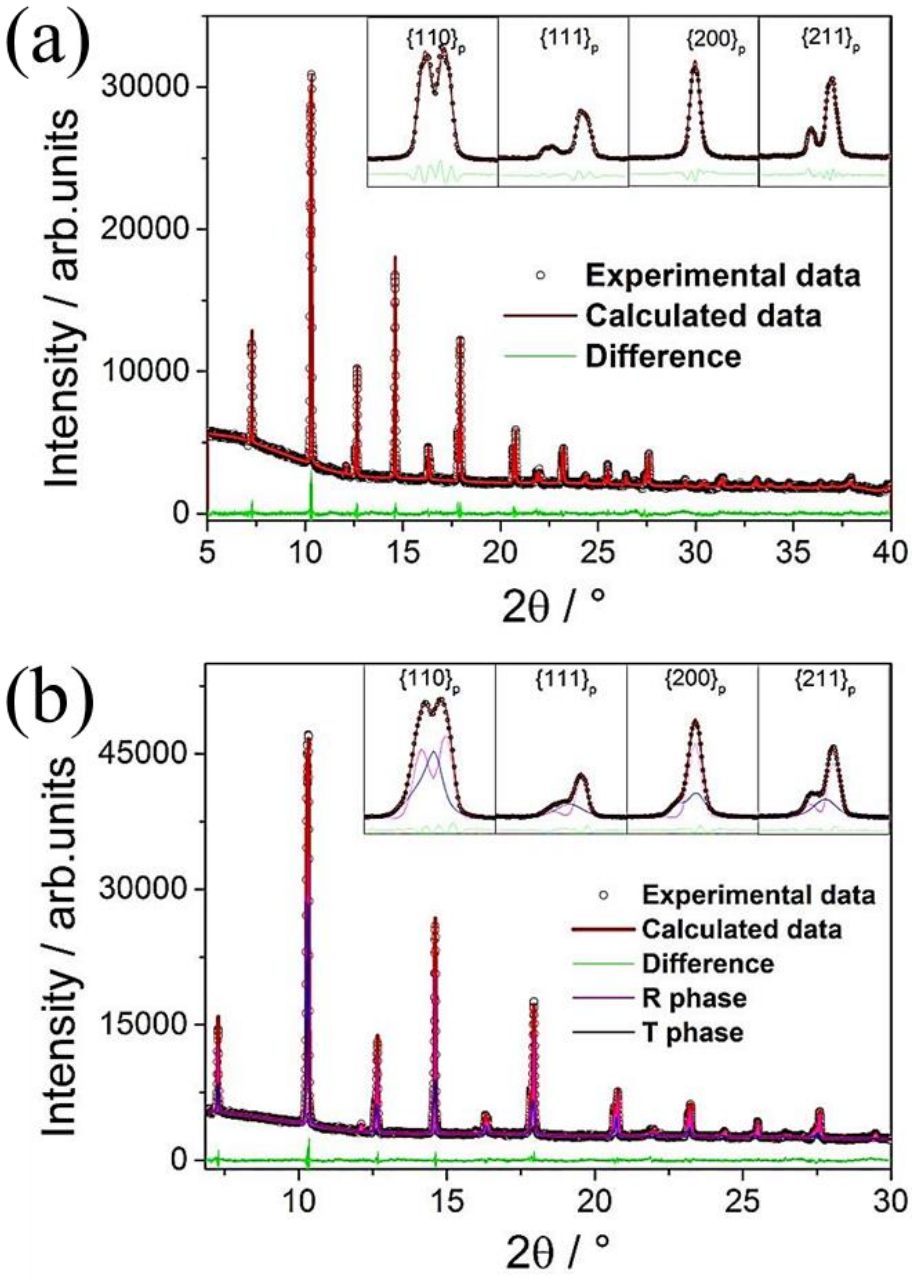

Figure 6.14 The SXPD full pattern refinements for poled (a) NBT-0.02NN and (b) NBT-0.04NN. The black circles are experimental data, the red line is the calculated results from Rietveld refinement, and the green line is the difference profile between experimental and calculated diffraction patterns.

The experimental diffraction data was fitted using several single or mixed-phase models, such as the rhombohedral R3m/R3c, monoclinic Cc, tetragonal P4bm and cubic Pm3m. The best fitting for poled NBT-0.02NN was obtained using a single phase rhombohedral R3c structure while the best refinement for poled NBT-0.04NN was obtained using a mixed-phase of rhombohedral (52%) and tetragonal (48%). The refined crystallographic parameters are listed in Table 6.5.

Table 6.5 The refined crystallographic parameters for NBT-0.02NN and NBT-0.04NN.

Refined parameters	NBT-0.02NN	NBT-0.04NN
GOF	1.87	1.85
R_{wp}	3.54	3.12
Lattice parameter(Ra) / Å	5.4825925(5)	5.4838167(3)
Lattice parameter(Rc) / Å	13.5477477(11)	13.5394777(9)
Lattice parameter(Ta) / Å	N/A	5.4965854(4)
Lattice parameter(Tc) / Å	N/A	3.9030918(8)
Phase fraction	Rhombohedral 100%	Rhombohedral 52% Tetragonal 48%

6.8 In-situ high-energy XRD experiments during electrical poling (Diamond beamline I15)

6.8.1 XRD patterns during electric poling

In order to investigate the electric field-induced structural transformation in NBT-xNN ceramics with x=0.02 and 0.04, the in-situ electric poling experiment was conducted using high-energy synchrotron XRD in Diamond beamline I15. The diffraction patterns were recorded following the same method described in Section 5.8.1.1. Based on the results presented in Section 6.7 above, it is anticipated that the structural transformation from cubic to rhombohedral in NBT-0.02NN and cubic to mixed-phase rhombohedral and tetragonal for NBT-0.04NN should be observed during high-field AC cycling.

For ψ=0°, which is the direction parallel to the electric field, the peak profiles of $\{111\}_p$ and $\{200\}_p$ for NBT-xNN (x=0.02 and 0.04) are plotted as a function of the number of applied cycles in Figure 6.15. It is evident that the $\{111\}_p$ peak

splits progressively while the $\{200\}_p$ peak shifts slightly with increasing cycle number for NBT-0.02NN, indicating that a structural transformation from cubic to rhombohedral phase completed gradually. On the other hand, for NBT-0.04NN both $\{111\}_p$ and $\{200\}_p$ peaks exhibit a broad shoulder after 2 cycles of electric field, indicating the occurrence of a structural transformation from cubic to mixed-phase of rhombohedral and tetragonal. These results provide direct evidence of the irreversible electric field-driven phase transformations in these materials and are in good agreement with the high-resolution SXPD patterns reported in Section 6.7 above, which were used to evaluate the crystal structures before and after the transformation.

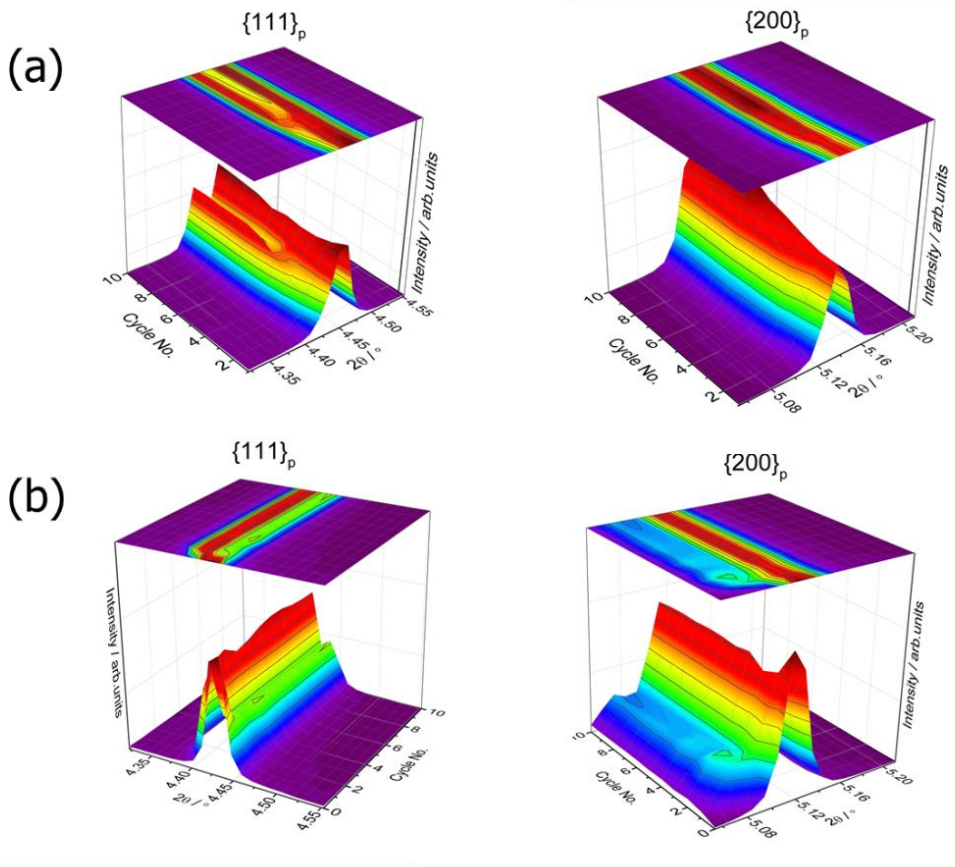

Figure 6.15 Evolution of $\{111\}_p$ and $\{200\}_p$ diffraction peaks for NBT-xNN ceramics as function of increasing electric field cycle number for (a) x=0.02 (b) x=0.04, at ψ = 0°.

6.8.2 Domain orientation distribution (DOD) analysis

The changes in crystallographic texture and lattice strain for the NBT-0.02NN and NBT-0.04NN ceramics in the poled state are examined further in the following Section to evaluate the influence of the NN content on domain switching behaviour and to allow a comparison with previous results for NBT-xKN. The domain fraction and lattice strain were calculated following the same method reported in Section 5.8.1.5.

6.8.2.1 NBT-0.02NN

The diffraction peak profiles of $\{111\}_p$ and $\{200\}_p$ for a range of different grain orientations in poled NBT-0.02NN ceramics are illustrated in Figure 6.16. The split $\{111\}_p$ and single $\{200\}_p$ peaks confirmed the presence of the rhombohedral structure. The variations in the relative intensities of the $\{111\}_p$ peaks as a function of the azimuthal angle, ψ, indicated that the [111]-oriented domains are oriented preferentially along the electric field direction at ψ=0°. Additionally, the $\{200\}_p$ peak exhibited a slight shift as function of ψ, indicating a small elastic lattice strain. These observations are similar to those made previously for poled NBT-xKN (Section 5.8.1.5).

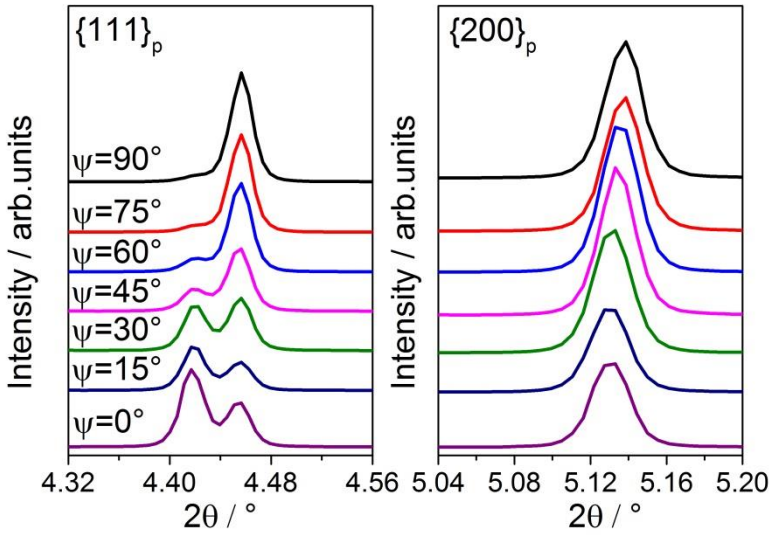

Figure 6.16 The representative XRD peak reflections for NBT-0.02NN ceramic.

The same method described in Section 5.8.1.5 above was adapted to calculate the d-spacing and lattice strain. The results for $d_{\{200\}}$ and $\varepsilon_{(200)}$, as a function of ψ

are shown in. Figure 6.17. The lattice strain reached a value of 1.1 x 10^{-3} at ψ = 0º, which is slightly lower than that of the NBT-0.03KN ceramic.

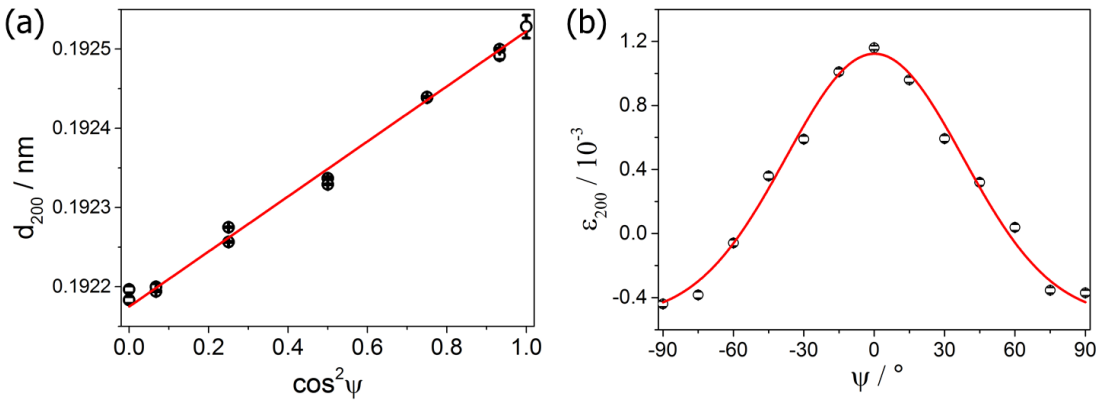

Figure 6.17 Dependence of (a) d_{200} and (b) ε_{200} on azimuthal angle, ψ. Symbols are experimental data points and solid lines are calculated according to Equation 5.3.

In addition, the DOD was calculated according to Equation 5.8-5.10, following the same method described in Section 5.8.1.5. The linear fit to the $R_1(111)$ data indicated that the intensity ratio was approximately equal to 0.233 at $\cos^2\psi$ = 1/3.The results obtained for the domain fraction, $\nu_{111,}$ are plotted as function of ψ in Figure 6.18. The degree of non-180° domain switching in the remanent state reaches a maximum ν_{111} value of approximately 0.70 at ψ = 0°, which is lower than that of NBT-0.03KN (0.76) but higher than that of NBT-0.01KN (0.55).

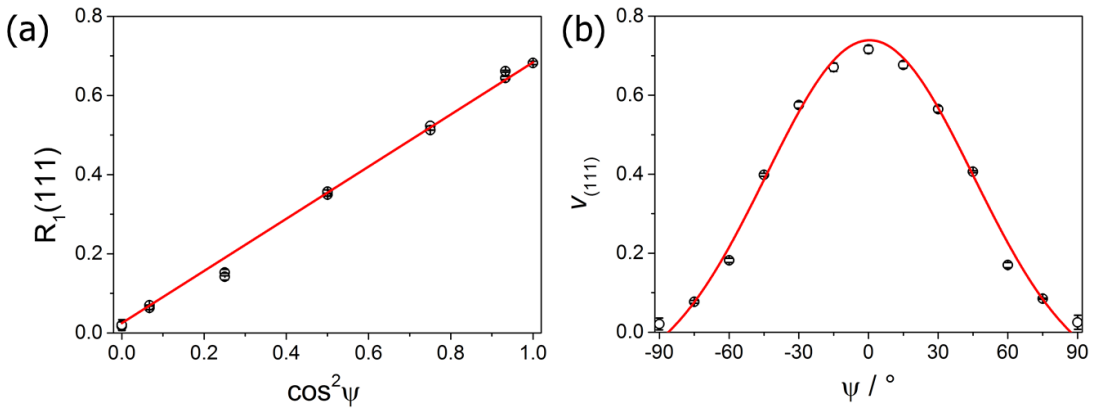

Figure 6.18 Dependence of (a) peak intensity ratio, $R_1(111)$, and (b) domain fraction, ν_{111}, on azimuthal angle, ψ. Symbols are experimental data points and solid lines are calculated using a squared cosine relation.

6.8.2.2 NBT-0.04NN

The diffraction peak profiles for $\{111\}_p$ and $\{200\}_p$ for a range of different grain orientations are illustrated in Figure 6.19. The splitting of both $\{111\}_p$ and $\{200\}_p$ peaks suggest the presence of the rhombohedral and tetragonal phases. The variations in the relative intensities of the $\{111\}_p$ and $\{200\}_p$ peaks as a function of the azimuthal angle, ψ, indicated that the [111]-oriented domains were oriented preferentially along the electric field direction at ψ=0° in the rhombohedral phase and the [002]-oriented domains were orientated preferentially along the electric field in the tetragonal phase. Furthermore, both $\{111\}_p$ and $\{200\}_p$ peaks exhibited a slight shift as function of ψ, indicating that an elastic lattice strain developed due to domain switching. In these circumstances, the analysis of lattice strain and crystallographic texture by means of single peak profile fitting is not feasible. Ongoing developments in full-pattern refinement methods with provision for anisotropic lattice strain could enable such an analysis to be carried out in the near future.

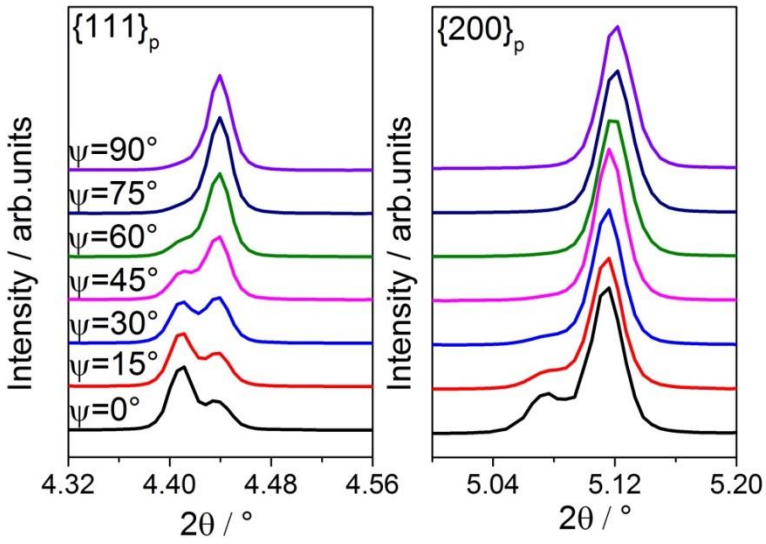

Figure 6.19 The representative XRD peak reflections for poled NBT-0.04NN ceramic.

6.9 Summary

The NBT-xNN (x=0.02 and 0.04) ceramics were synthesized by solid state reaction and relatively densities of approximately 94 % were obtained after sintering. The average grain size for sintered ceramics ranged from 5.81 to 8.28

μm and decreases with increasing NN content. The XRD results for as-sintered ceramic pellets indicated the presence of a cubic perovskite phase for all compositions. However, for compositions with low NN content, the observation of well-developed ferroelectric hysteresis loops under the influence of a high electric field at room temperature indicated the occurrence of an irreversible phase transition from PNRs to a metastable FE state, similar to that found in the NBT-KN system. In contrast, a reversible transformation between PNRs and a field-induced metastable FE state occurred for NBT-0.06NN and NBT-0.08NN, characterised by constricted P-E loops and split polarisation switching peaks in the J-E curves.

To reveal the origin of the well-defined P-E loops for ceramics with apparent cubic structure, both unpoled and poled NBT-0.02NN and NBT-0.04NN ceramic powders were examined using high resolution SXPD. After full pattern refinement, it was confirmed that a cubic structure was present for both NBT-0.02NN and NBT-0.04NN in the unpoled state, while a rhombohedral phase and a mixed-phase of rhombohedral and tetragonal were observed for poled NBT-0.02NN and poled NBT-0.04NN respectively. Furthermore, the poled states can retain the structure after removing the electric field and subsequent mechanical crushing, indicating that a nonergodic-RF (NR) state exists in these compositions at room temperature.

To further investigate the structural transformation and texture development for NBT-0.02NN and NBT-0.04NN during AC cycling, an in-situ electric poling experiment was conducted in beamline I15, Diamond. It was observed that the diffraction profiles changed progressively with increasing cycle number, taking 5 and 3 cycles of the electric field waveform to complete the structural transformation from cubic to rhombohedral and cubic to mixed-phase of rhombohedral and tetragonal for NBT-0.02NN and NBT-0.04NN respectively. After 20 cycles of electric poling, it was found that the electric field-induced metastable rhombohedral phase for the NBT-0.02NN ceramic exhibited orientation-dependent lattice strain and ferroelectric domain orientation, similar

to those found in NBT-0.01 and NBT-0.03KN ceramics. The NBT-0.04NN ceramic also exhibits lattice strain and texture as a result of the applied electric field, but it was not feasible to conduct the texture analysis by single peak profile fitting due to the overlapping diffraction peaks and anisotropic lattice strain.

The temperature-dependent ferroelectric and dielectric properties were also investigated for NBT-xNN ceramics. Constricted P-E loops and split polarisation switching peaks in the J-E curves were observed at 120 ºC and 75 ºC for NBT-0.02NN and NBT-0.04NN respectively, indicating that the transformation between PNRs and metastable FE state become reversible during heating. For NBT-0.06NN and NBT-0.08NN, the constriction in the middle of P-E loop and the separation between E_f and E_b were greater, indicating a more hysteretic reversible transition.

For compositions with the NR state at room temperature, the high remanent polarisation was obtained and retained due to the formation of the metastable FE state after removing the electric field. In order to investigate the influence of temperature on the metastable FE state, the thermal depolarisation and dielectric measurements were conducted on poled specimens. The depolarisation temperature, T_d, was determined as 123 ºC and 60 ºC for NBT-0.02NN and NBT-0.04NN respectively. The depolarisation temperature was not obtained for NBT-0.06NN and NBT-0.08NN due to the reversible nature of the transformation between weak-polar PNRs and ferroelectric order during poling at room temperature. Furthermore, the phase transition temperatures from the metastable FE state to RF state, T_{F-R}, were determined as 115 ºC and 55 ºC for NBT-0.02KN and NBT-0.04NN respectively, which are similar to the T_d values. It was suggested that the gradual phase transition from metastable FE order to RF state on heating is the primary reason for the occurrence of constricted P-E loops with a significant loss in remanent polarisation.

7 Phase switching behaviour in $Na_{0.5}Bi_{0.5}TiO_3$-$BaTiO_3$ ceramics

In this chapter, the temperature-dependent electrical properties are examined to illustrate the phase transition in (1-x)NBT-xBT ceramics. Additionally, NBT-0.05BT ceramic powder is re-examined using high resolution SXPD to clarify the nature of the crystal structure. Furthermore, 'ex-situ' experiments are conducted on NBT-0.05BT and NBT-0.06BT ceramics to analyse the domain orientation distribution (DOD) using high energy synchrotron XRD.

7.1 Lab XRD results

7.1.1 Calcined powders

The XRD patterns of NBT-xBT (x=0.04 to 0.11) ceramic powders calcined at a temperature of 900 ºC for 10 hours are presented in Figure 7.1.

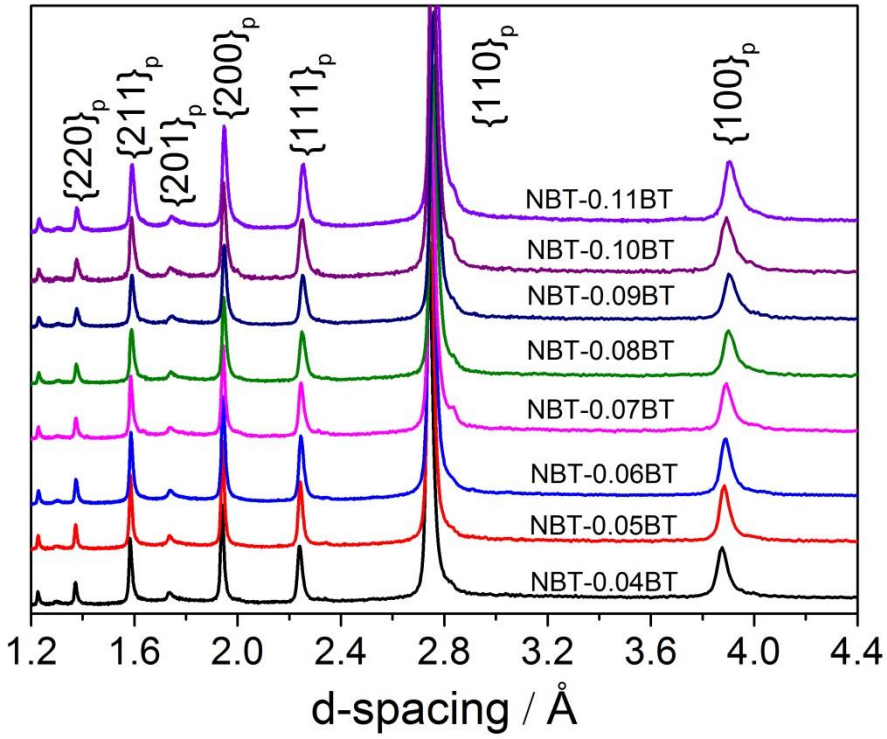

Figure 7.1 The XRD full patterns of NBT-xBT calcined powders.

The peak profiles of $\{111\}_p$ and $\{200\}_p$ for all compositions are illustrated in Figure 7.2. Both $\{111\}_p$ and $\{200\}_p$ peaks are observed to be asymmetric and shift slightly to larger d-spacing with increasing BT content, which is consistent with previous reports.[10] This trend can be understood in terms of the change in average ionic radius, since the ionic radius of Ba^{2+} is 1.42 Å, which is larger than those of Na^+ and Bi^{3+}, which 1.18 Å and 1.17 Å respectively.[183]

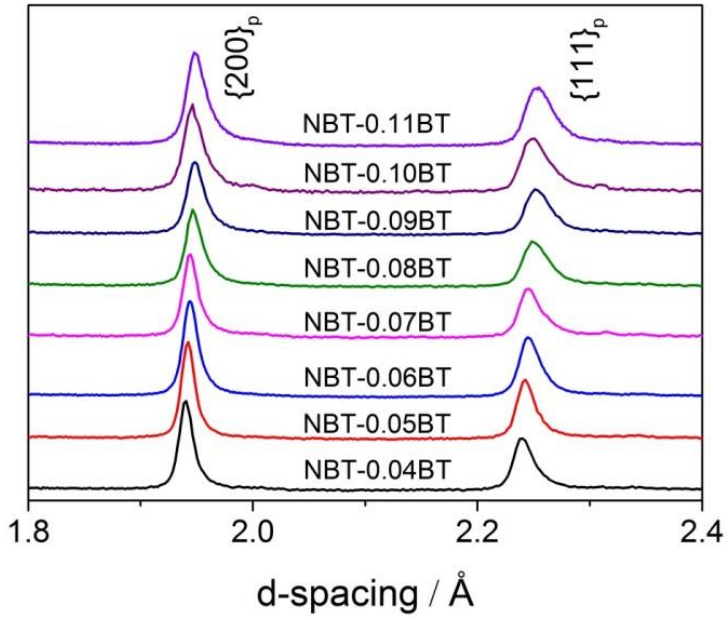

Figure 7.2 The representative $\{111\}_p$ and $\{200\}_p$ peaks of calcined powders for NBT-xBT system.

7.1.2 Sintered ceramic pellets

The crystal structures for unpoled NBT-xBT (x=0.04 to 0.11) ceramic pellets were investigated using lab XRD, as displayed in Figure 7.3. All compositions are observed to be single phase with a perovskite structure.

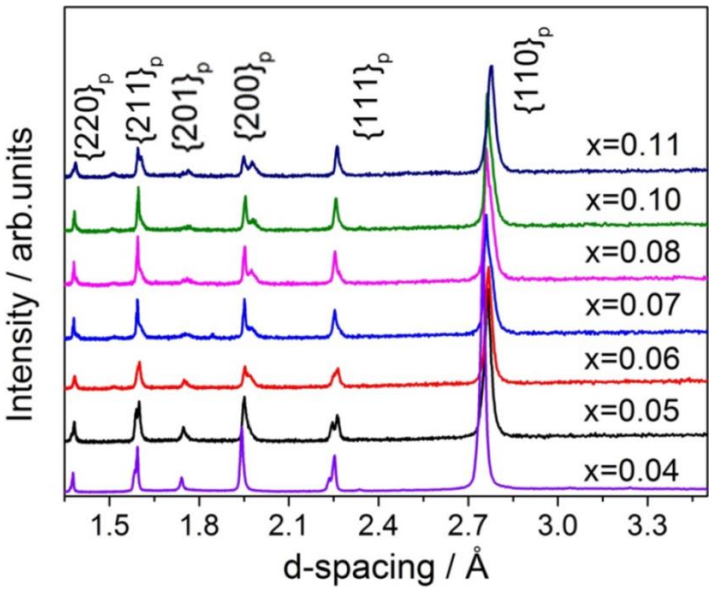

Figure 7.3 The XRD full patterns of sintered ceramic pellets for all compositions in NBT-xBT system, after sintering at a temperature of 1200 °C.

A double $\{111\}_p$ and single $\{200\}_p$ peaks are observed for NBT-0.04BT, indicating a rhombohedral structure. For compositions with x=0.05 to 0.11 in NBT-xBT system, mixed-phases of rhombohedral and tetragonal are present, characterised by splitting in both $\{111\}_p$ and $\{200\}_p$ peaks. All of the structures agreed with those reported in previous publications apart from NBT-0.05BT.[10] In this case, broadening/splitting of both $\{111\}_p$ and $\{200\}_p$ is evident, whereas only $\{111\}_p$ peak splitting would be expected for the single R3c rhombohedral phase reported by Jo.[10] Hence, the crystal structure of the as-sintered NBT-0.05BT (unpoled) ceramic is re-examined using high resolution SXPD.

7.2 SEM

The cross-Sectional SEM images for NBT-xBT ceramics were examined under BSE mode, as presented in Figure 7.4. The relative density of the ceramic reaches approximately 94%. The average grain size for NBT-xBT bulk ceramics is listed in Table 7.1, which varies from 1.86 μm to 3.74 μm. This result indicates that Ba^{2+} inhibits the grain growth in the NBT-BT solid solution.[112, 190]

Table 7.1 The average grain size for all compositions in NBT-xBT system.

Compositions	Grain size / μm
NBT-0.04BT	3.74±0.41
NBT-0.06BT	2.58±0.21
NBT-0.08BT	2.48±0.42
NBT-0.10BT	1.86±0.23

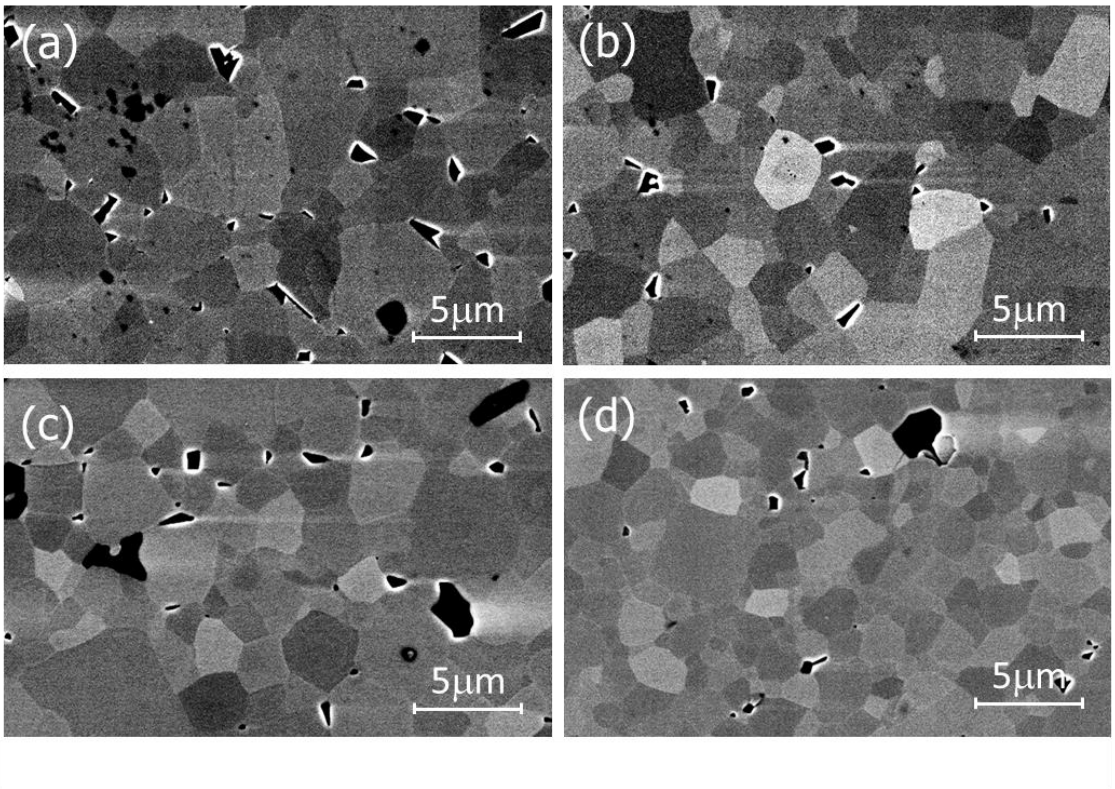

Figure 7.4 The cross-Sectional SEM images for (a) NBT-0.04BT (b) NBT-0.06BT (c) NBT-0.08BT and (d) NBT-0.10BT.

7.3 Temperature-dependent ferroelectric properties

7.3.1 Polarisation-current density-field (P-J-E) loops

The ferroelectric P-E hysteresis loops and J-E current density curves for NBT-0.04BT over the temperature range from 30 to 120 ºC are presented in Figure 7.5. For all temperatures, a saturated P-E loop and a single polarisation switching peak in the J-E curve are apparent, indicating the presence of a long-range ordered FE state. With increasing temperature, the coercive field decreases from 3.7 kV mm^{-1} at 65 ºC to 2.3 kV mm^{-1} at 120 ºC while the remanent polarisation (P_r) increases from 0.18 C m^{-2} to 0.30 C m^{-2}. The FE state is clearly stable for this composition up to a temperature of 120 °C.

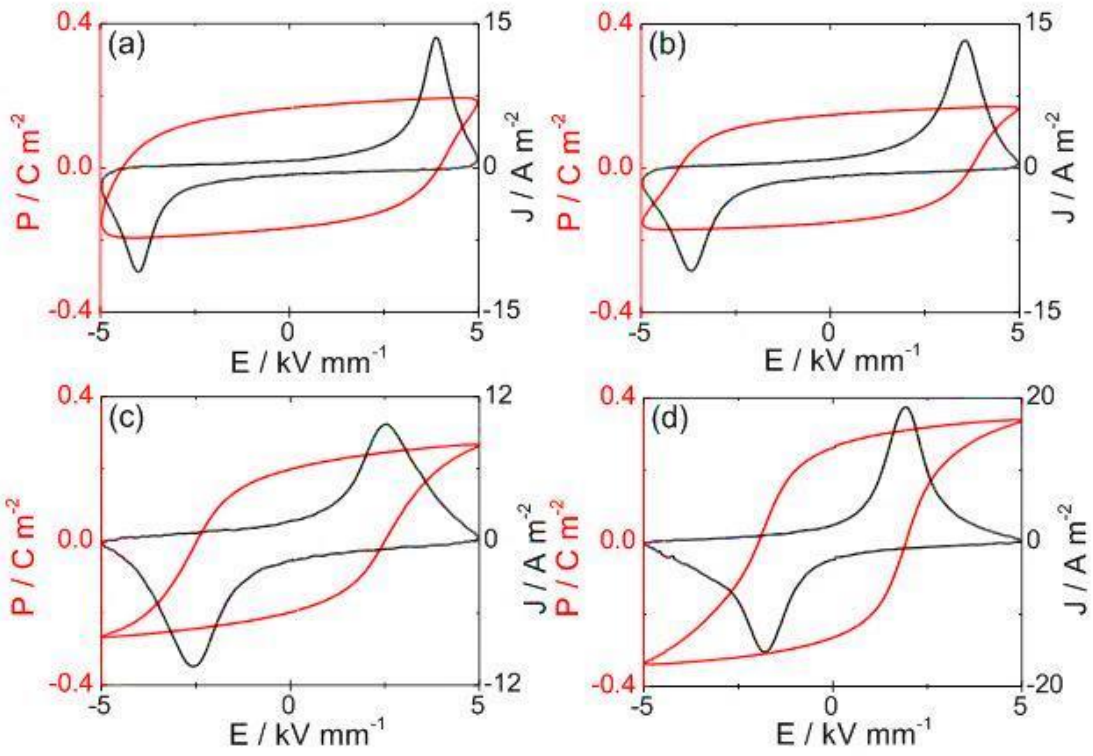

Figure 7.5 The P-J-E curves for NBT-0.04BT ceramic at temperature of (a) 30 ºC (b) 65 ºC (c) 90 ºC and (d) 120 ºC.

Similar results for NBT-0.05BT are illustrated in Figure 7.6. At 30 ºC, a well-defined ferroelectric P-E loop is observed with high P_{max} and P_{rem} values of 0.37 C m^{-2} and 0.33 C m^{-2} respectively. With increasing temperature to 90 ºC, the E_c drops from 3.7 kV mm^{-1} to 2.6 kV mm^{-1} but the P_{max} and P_{rem} values remain the same. At 120 ºC, a significant constriction in the middle of the P-E loop and a split polarisation switching peak in the J-E curve are present, indicating a reversible phase transition between PNRs and a long-range ordered FE state. It is evident that two pairs of polarisation switching peaks are observed. One set of peaks occurs at approximately $E_f \approx \pm 4.3$ kV mm^{-1}, where a transition from PNRs into long-range ordered FE state occurred while the other pair of peaks occurs approximately $E_b \approx \pm 0.4$ kV mm^{-1}, where the long-range ordered FE phase transformed reversibly back to PNRs.

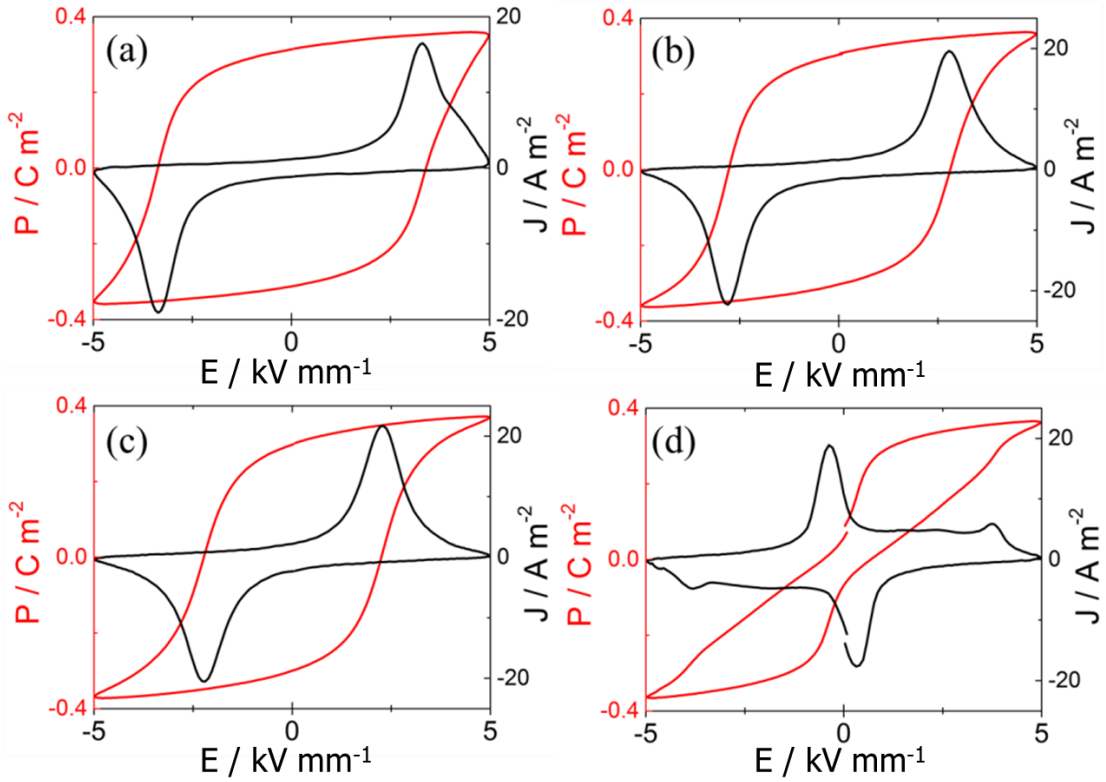

Figure 7.6 The P-J-E curves for NBT-0.05BT ceramic at temperature of (a) 30 ºC (b) 65 ºC (c) 90 ºC and (d) 120 ºC.

Similar results for NBT-0.06BT are presented in Figure 7.7. At room temperature, a well-defined P-E loop with a high P_{max} value of approximately 0.40 C m^{-2} is obtained, indicating a FE state. With increasing temperature up to 65 ºC, a constricted P-E loop and a split polarisation switching peak in the J-E curve are observed. Similar to NBT-0.05BT, here, the E_f and E_b were determined as approximately $\pm$3.8 kV mm^{-1} and zero field. With further increasing temperature up to 90 and 120 ºC, more-constricted P-E loops were observed with similar P_{max} but extremely low P_{rem} values. Therefore, FE state was destabilised with increasing temperature, leading to a more reversible transition between PNRs and long-range ordered ferroelectric state.

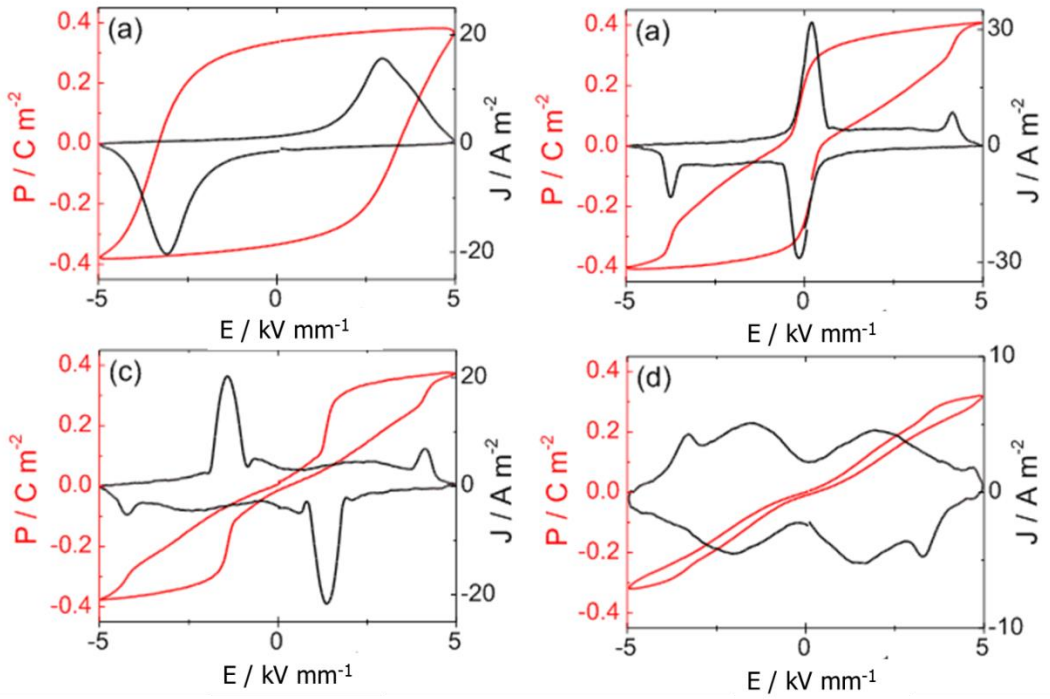

Figure 7.7 The P-J-E curves for NBT-0.06BT ceramic at temperatures of (a) 30 ºC (b) 65 ºC (c) 90 ºC and (d) 120 ºC.

The P-E loops and J-E curves for NBT-0.08BT are presented in Figure 7.8. In this case, constricted P-E loops and split polarisation switching peaks in the J-E loops are evident for all temperatures. With increasing temperature, a more constricted P-E loop with a significant drop in P_{max} and P_{rem} values was obtained. At 120 ºC, a slim P-E loop is apparent, exhibiting approximately zero remanent polarisation.

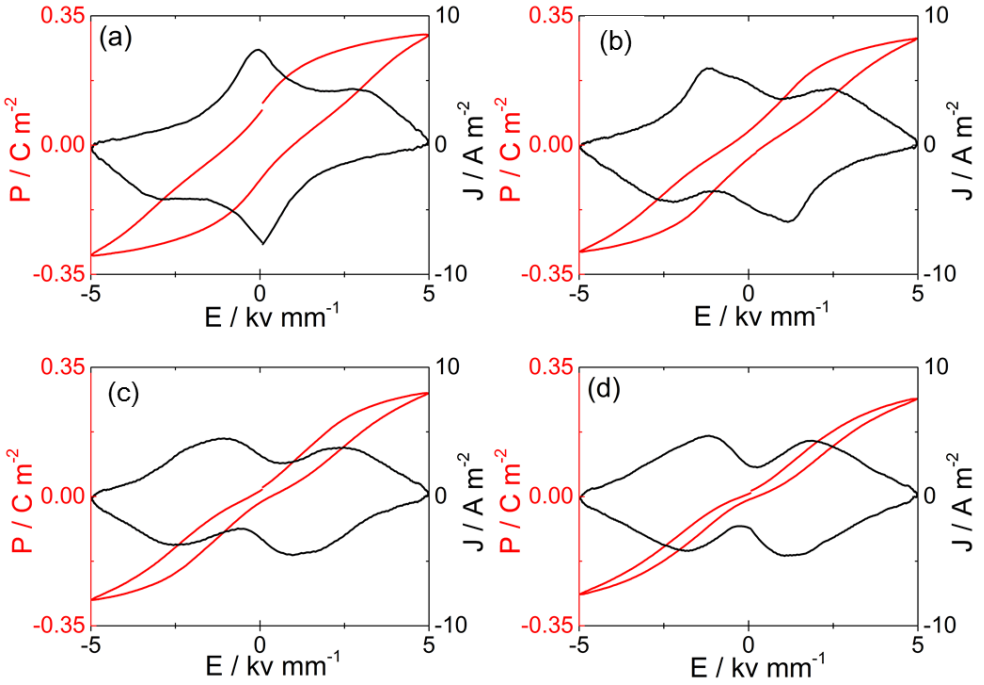

Figure 7.8 The P-J-E curves for NBT-0.08BT ceramic at temperature of (a) 30 ºC (b) 65 ºC (c) 90 ºC and (d) 120 ºC.

The P-E loops and J-E curves for NBT-0.11BT are illustrated in Figure 7.9. At room temperature, ferroelectric P-E and J-E loops are present, indicating an FE state. At 65 ºC, the P-E loop becomes slimmer with an increase in P_{max} and P_{rem} values. With further increasing temperature to 90 ºC, the reversible transition between PNRs to FE state occurred, characterised by a slightly constricted P-E loop and a split polarisation switching peak in the J-E curve. At 120 ºC, a more pronounced constriction in the P-E loop and a split polarisation switching peak in the J-E curve are observed, indicating that the reversible transition between PNRs and long-range ordered ferroelectric state developed more significantly.

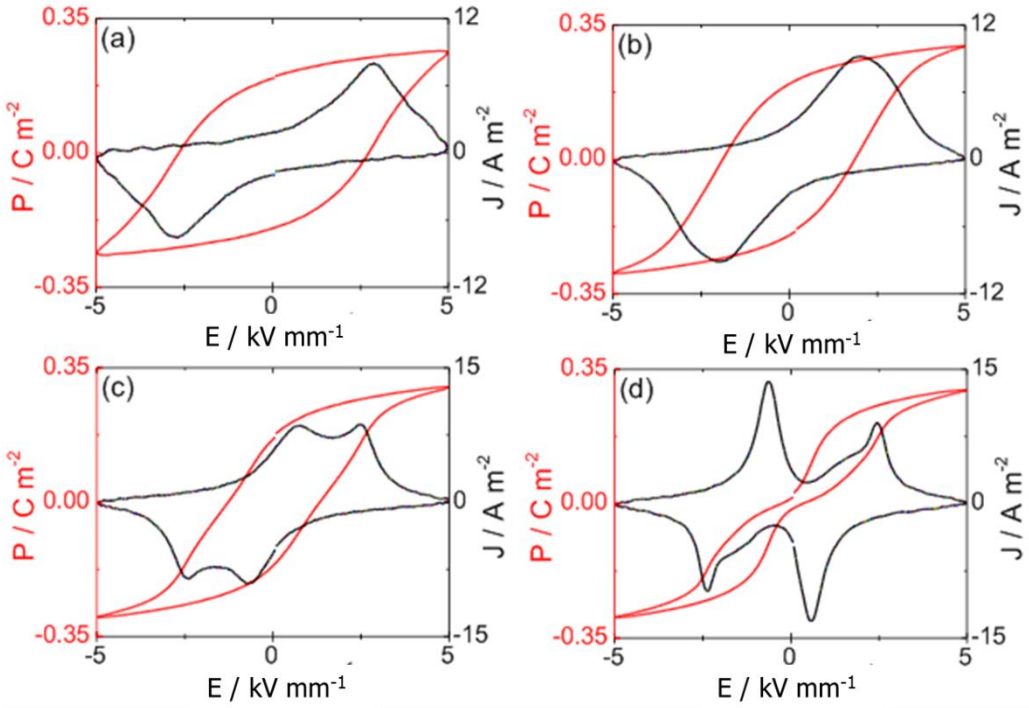

Figure 7.9 The P-J-E curves for NBT-0.11BT ceramic at temperature of (a) 30 ºC (b) 65 ºC (c) 90 ºC and (d) 120 ºC.

7.3.2 Summary

Both P-E and J-E ferroelectric hysteresis loops were obtained for NBT-xBT (x=0.04 to 0.11) in the temperature range from 30 to 120 ºC. The polarisation switching field (E_c or E_b/E_f), remanent polarisation (P_{rem}) and maximum polarisation (P_{max}) values are summarised in Table 7.2 below.

Table 7.2 (a) The polarisation switching field, (b) maximum and (c) remanent polarisation for NBT-xBT in a temperature range of 30 to 120 ºC.

(a) Polarisation switching field (E / kV mm^{-1})

x	30 ºC	65 ºC	90 ºC	120 ºC
0.04	3.9	3.7	2.6	2.3
0.05	3.7	2.6	2.2	3.8/0.8
0.06	3.2	3.8/0.2	4.2/1.5	N/A
0.08	3.2/0.1	2.5/1.3	2.5/1.2	1.8/1.2
0.11	2.8	1.9	2.4/0.7	2.3/0.6

(b) Maximum Polarisation (P_{rem} / C m^{-2})

x	30 ºC	65 ºC	90 ºC	120 ºC
0.04	0.19	0.18	0.27	0.31
0.05	0.37	0.39	0.38	0.38
0.06	0.38	0.40	0.38	0.32
0.08	0.30	0.29	0.28	0.27
0.11	0.26	0.30	0.30	0.30

(c) Remanent Polarisation (P_{rem} / C m^{-2})

x	30 ºC	65 ºC	90 ºC	120 ºC
0.04	0.17	0.17	0.20	0.27
0.05	0.33	0.30	0.30	0.10
0.06	0.33	0.26	0.02	0.01
0.08	0.12	0.07	0.04	0.01
0.11	0.20	0.20	0.18	0.02

For NBT-0.04BT, a saturated P-E loop and a single polarisation switching peak in the J-E curve were observed for all temperatures, indicating the presence of an FE state.

It was reported by Jo that two MPBs were observed in the NBT-BT system, at x=0.06 and x=0.11.[10] Between compositions with x=0.06 to 0.11, a mixed-phase region of rhombohedral and tetragonal was identified. Here, for

compositions close to the MPB, which were NBT-0.05BT, NBT-0.06BT and NBT-0.11BT, an FE state was present with high P_{rem} and P_{max} values. With increasing temperature, the FE state can be destabilised to the RF state and the reversible transition was indicated by the constricted P-E loops and split polarisation switching peaks in J-E curves.

For NBT-0.08BT, a reversible transition between PNRs and metastable FE state occurred at all temperatures, indicated by the constricted P-E loop and split polarisation switching peaks in the J-E curve.

7.4 Temperature-dependent depolarisation

Thermal depolarisation results for NBT-0.04BT, NBT-0.05BT and NBT-0.06BT are presented in Figure 7.10. The samples had been poled using at least 30 cycles of an AC electric field with amplitude 5 kV mm^{-1} at room temperature. The poled sample lost the majority of its remanent polarisation at temperatures of 137 ºC, 95 ºC and 66 ºC for NBT-0.04BT, NBT-0.05BT and NBT-0.06BT respectively. Compared to previous reports, the obtained T_d for NBT-0.06BT is lower due to the different sample preparation and experimental methods.[7, 112, 191]

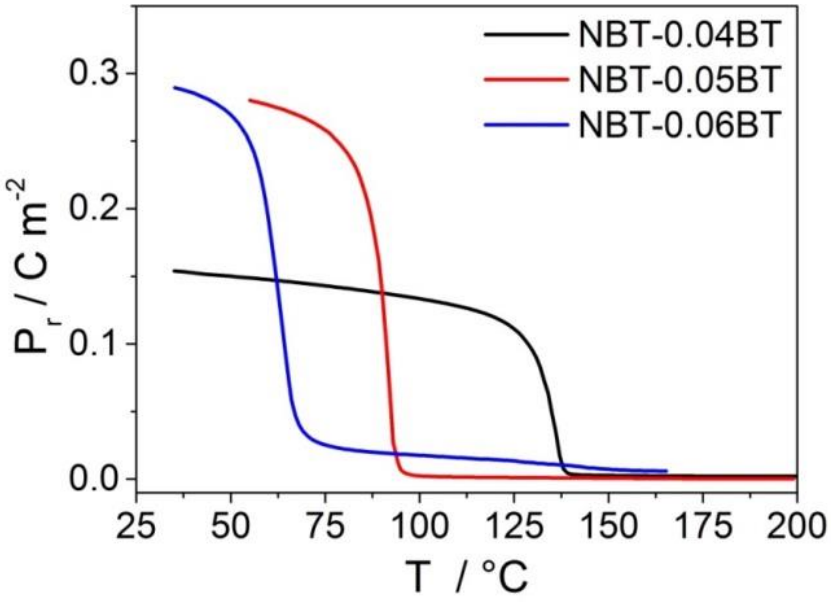

Figure 7.10 The thermally-induced depolarisation curves for NBT-xBT.

The depolarisation temperature, T_d, for NBT-xBT ceramics decreases with increasing BT content. The preferred domain orientation was induced by poling

for these three compositions, then the remanent polarisation was lost due to the transformation to a weak-polar state upon heating. In contrast, a thermal depolarisation temperature could not be obtained for the composition with x=0.08 due to the reversible transformation between weak-polar PNRs and ferroelectric order during poling at room temperature, indicating an ergodic-RF state. To summarise, the depolarisation temperature and maximum depolarisation rate for NBT-xBT ceramics are listed in Table 7.3 below. The reductions in T_d with increasing BT content can be understood generally in terms of the increasing disorder in composition and ionic charge associated with the substitution of Ba^{2+} for Na^{+}/Bi^{3+}.

Table 7.3 The depolarisation temperature and depolarisation rate for NBT-xBT.

Compositions	T_d / ^oC	dP/dT / mC m^{-2} $^oC^{-1}$
x=0.04	137	25
x=0.05	95	40
x=0.06	66	23
x=0.08	N/A	N/A

7.5 Dielectric properties

7.5.1 Poled states

The changes in dielectric permittivity and loss tangent for poled NBT-xBT (x=0.04 to 0.11) over the temperature range from 50 to 420 ºC are shown in Figure 7.11. Two anomalies are observed in the ε_r-T relationship for all compositions, including the higher-temperature peak, defined as maximum permittivity peak (T_m), and the lower-temperature shoulder.

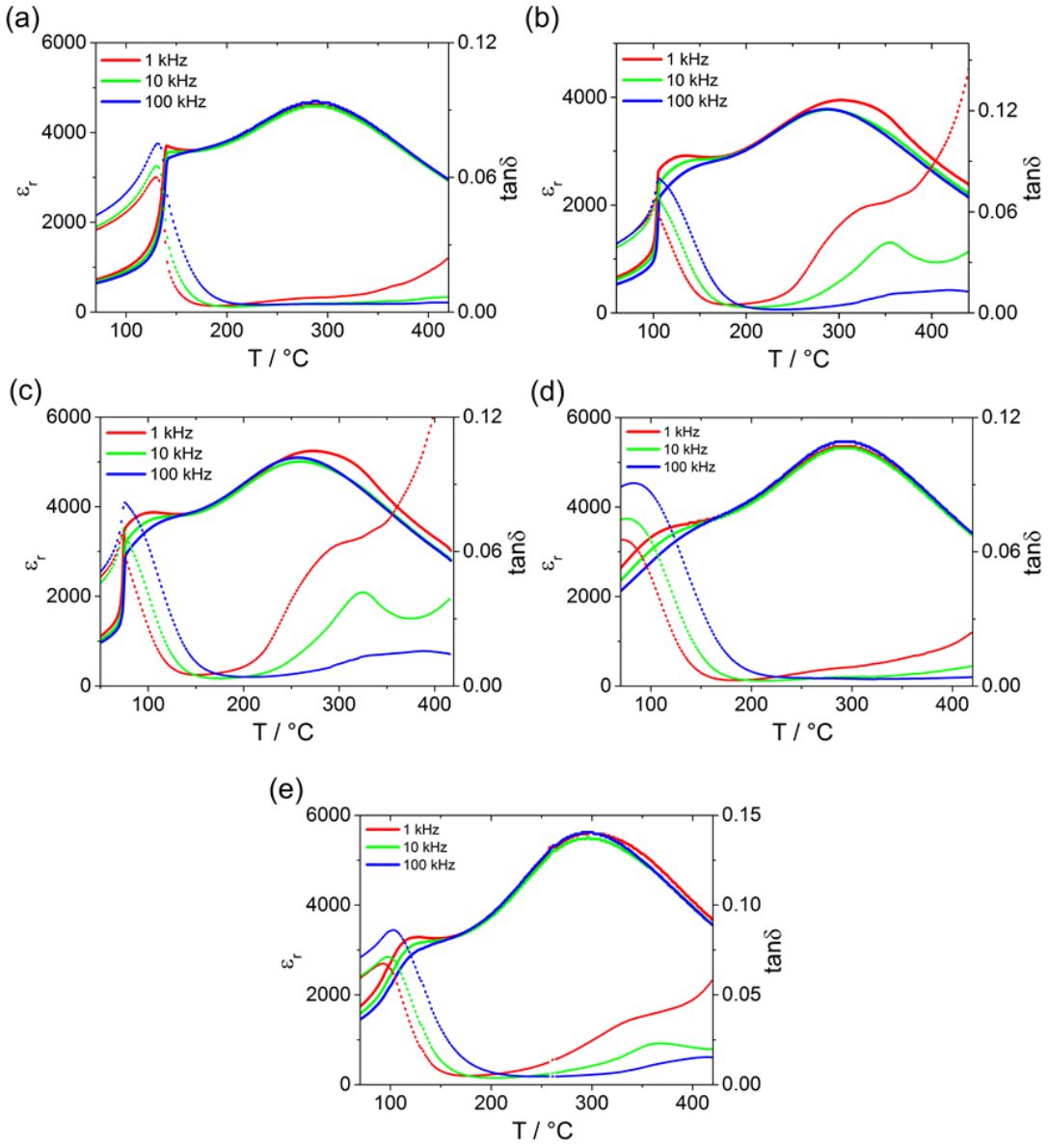

Figure 7.11 Temperature-dependent permittivity and loss curves for poled NBT-xBT ceramics (a) x=0.04 (b) x=0.05 (c) x=0.06 (d) x=0.08 (e) x=0.11.

For the composition with x=0.04, the ε_r value is around 800 at room temperature, increasing sharply to 3800 at approximately 145 °C. Above this temperature, the permittivity increases progressively and significant frequency dispersion appears up to 160 ºC. With further increasing temperature, it is frequency-independent and increases steadily to a peak of 4800 at 295 °C, followed by a gradual decline up to 450 °C.

The tanδ–T relationship displays a similar characteristic to those in the NBT-KN system, with noticeable frequency-dependence and a transition temperature from FE to RF states, T_{F-R}, being evident at 141 ºC. The tanδ values reduce with increasing frequency up to 210 ºC, characteristic of a RF, while above this temperature the trend reverses in accordance with an increasing contribution from electronic conduction.

Upon increasing BT content to 5% and 6%, the T_{F-R} values decrease to 110 ºC and 73 ºC respectively while the temperature of maximum permittivity remains at approximately 295 ºC. The tanδ-T characteristics are similar to those of the NBT-0.04BT system, but significantly higher losses are present at high temperatures indicating higher electronic conductivity.

With further increase of the BT content to 8%, the T_{F-R} transition is not evident in both the ε_r-T and tanδ-T relationships. The ε_r value starts higher at approximately 2000 with frequency dispersion up to 170 ºC. Beyond this temperature a frequency-independent ε_r increases progressively to the maximum value of approximately 5100, followed by a decline on further heating. For tanδ, it starts at a relatively high value of 0.08 and decreases with increasing temperature until around 210 ºC and exhibits relatively low values at high temperature, indicating a reduced conductivity for this composition.

Similar results were obtained for NBT-0.11BT, although the low temperature shoulder in the ε_r-T relationship and the peak in the tanδ-T relationship became more prominent, suggesting that a transition from FE to RF states could occur for this composition, in agreement with the ferroelectric P-E results reported above.

7.5.2 Unpoled states

The ε_r-T, and tanδ–T relations for unpoled NBT-xBT (x=0.04 to 0.11) ceramics over the temperature range from 50 to 420 ºC are shown in Figure 7.12. Compared to the results for poled ceramic pellets, no significant T_{F-R} is evident for any of the compositions and ε_{max} was almost frequency-independent. The ε_r for all compositions shows frequency dispersion at lower temperatures up to the low temperature shoulder, followed by a gradual increase and loss of frequency-dependence up to T_m and finally a gradual decline on further heating.

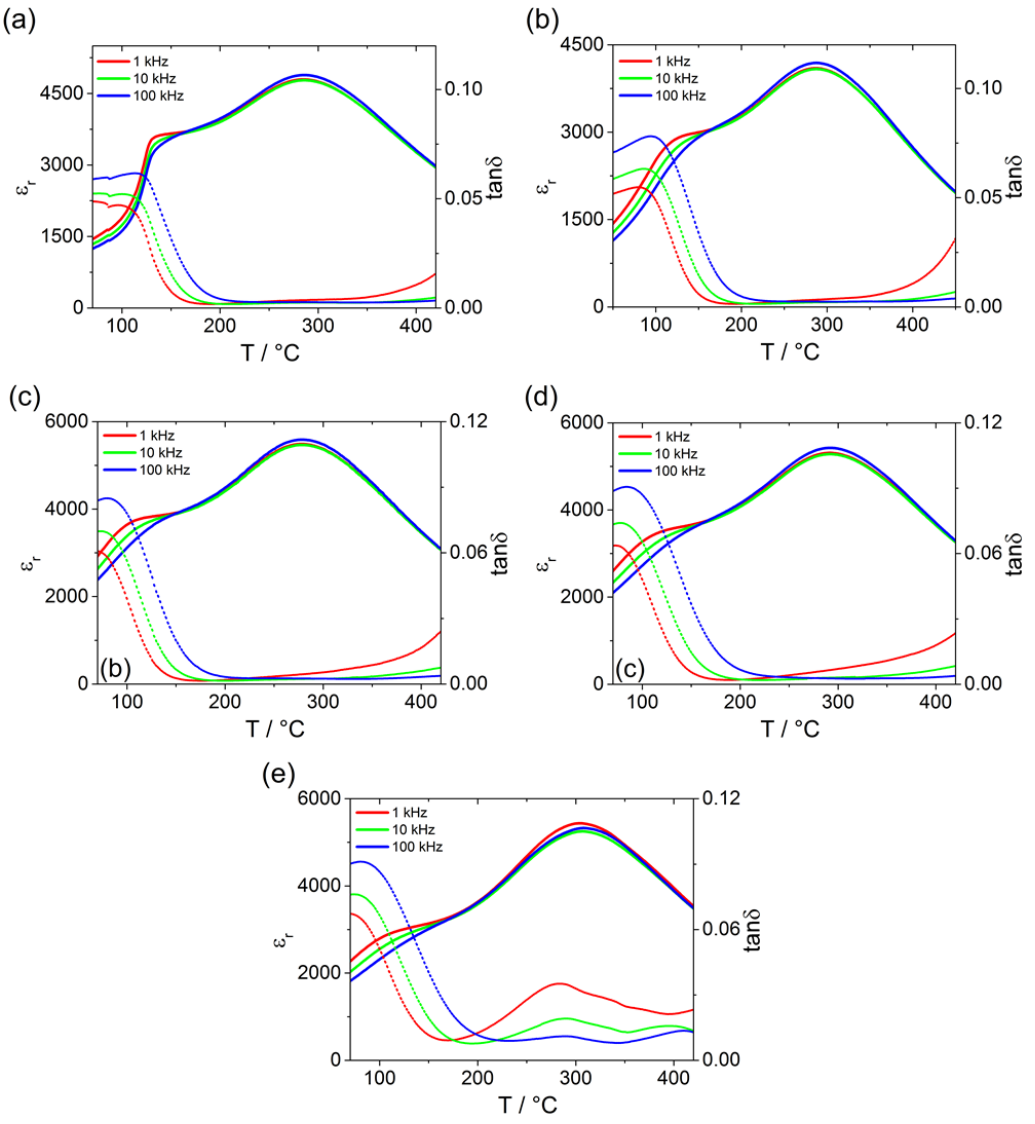

Figure 7.12 Temperature-dependent permittivity and loss curves for unpoled NBT-xBT ceramics (a) x=0.04 (b) x=0.05 (c) x=0.06 (d) x=0.08 (e) x=0.11.

7.5.3 Summary

The important dielectric parameters including the transition temperature, T_{F-R}, the maximum permittivity, ε_{max}, and the temperature of the dielectric peak, T_{max}, for poled NBT-xBT ceramics were obtained from the data illustrated in Figure 7.12 above and are listed in Table 7.4 below.

Table 7.4 The transition temperature, the maximum permittivity and the temperature of the dielectric peak for poled NBT-xBT.

Compositions	T_{F-R} / °C	ε_{max}	T_{max}
x=0.04	141	4700	292
x=0.05	110	4000	292
x=0.06	73	5050	280
x=0.08	N/A	5263	292
x=0.11	N/A	5620	295

It was found that the transition temperature peak in the tanδ-T relationship, T_{F-R}, was present for poled NBT-0.04BT, NBT-0.05BT and NBT-0.06BT, and possibly for NBT-0.11BT. The transition temperature decreases with increasing BT content. Furthermore, it was found that the transition from the FE to RF state is the reason for the loss of remanent polarisation, indicated by constricted P-E loops and split polarisation switching peaks in the J-E curves, which are similar to those of other NBT-based ceramics.[192]. For the ε_r-T relationship, a low-temperature shoulder was found for all compositions in NBT-xBT ceramics. This phenomenon was discussed by Jo for the specific case of NBT-0.06BT.[11] It was suggested that the first (low-temperature) anomaly, ε_{FA}, and the second (high-temperature) anomaly, ε_{SA}, can be deconvoluted into three contributions by using a phenomenological model.[11] Due to the presence of coexisting R3c rhombohedral and P4bm tetragonal phases, the mixed-phase state experiences thermal evolution of PNRS and/or a FE to RF transition, which both contribute to the ε_{FA} anomaly. At higher temperatures, the phase transition between R3c PNRs and P4bm PNRs can be induced during heating, which was identified as the cause of the ε_{SA} peak. The latter transformation is assumed to be frequency-independent.

7.6 High resolution SXPD experiments (Diamond beamline I11)

The aim of this investigation was to re-examine the crystal structure for NBT-0.05BT ceramic due to the discrepancy between results reported in the literature[10] and the lab XRDs result reported above in Section 7.1.2. Similar to the approach used for the NBT-KN and NBT-NN systems, a crushed powder obtained from unpoled ceramic specimens was used to obtain a strain- and texture-free diffraction pattern, which was used to conduct the full pattern refinement by *Topas*.

The SXPD full pattern for unpoled NBT-0.05BT was obtained and the crystallographic parameters were refined by *Topas*, as illustrated in Figure 7.13. The raw diffraction pattern was fitted with several different models and the best refinement value was obtained using single rhombohedral phase with *R3c* space group.

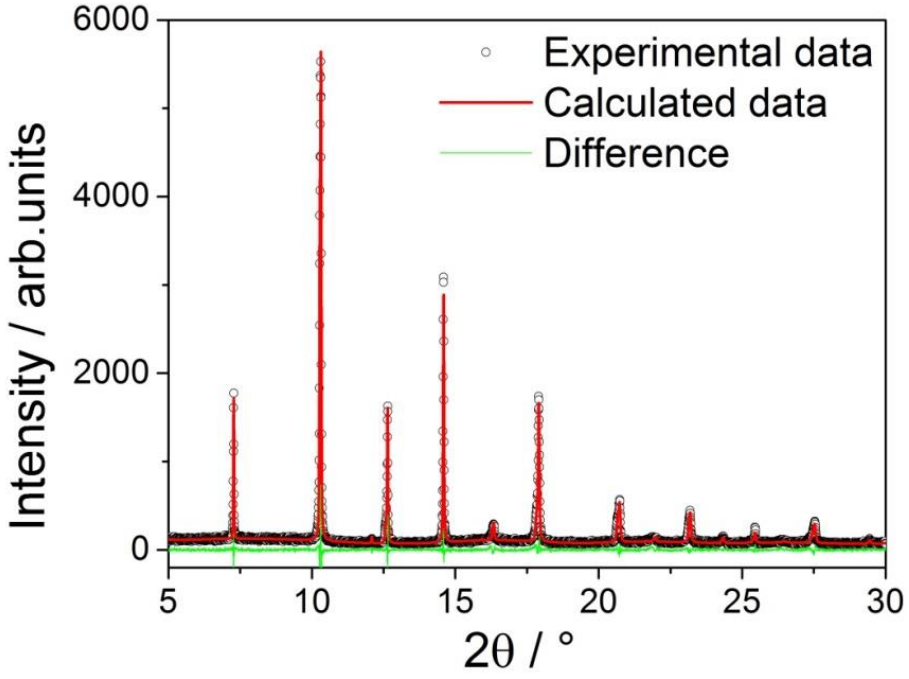

Figure 7.13 Room-temperature SPXD patterns for unpoled NBT-0.05BT powders. The black circles are experimental data, the red line is the calculated results from Rietveld refinement, and the green line is the difference profile.

The diffraction peak profiles for $\{111\}_p$, $\{200\}_p$, $\{211\}_p$ and $\{200\}_p$ are illustrated in Figure 7.14. It was found that the double $\{111\}_p$, $\{211\}_p$ and $\{220\}_p$ are fitted well with R3c space group, especially the small superlattice reflection $(\frac{3}{2}\frac{1}{2}\frac{1}{2})_p$. The refined crystallographic parameters are listed in Table 7.5.

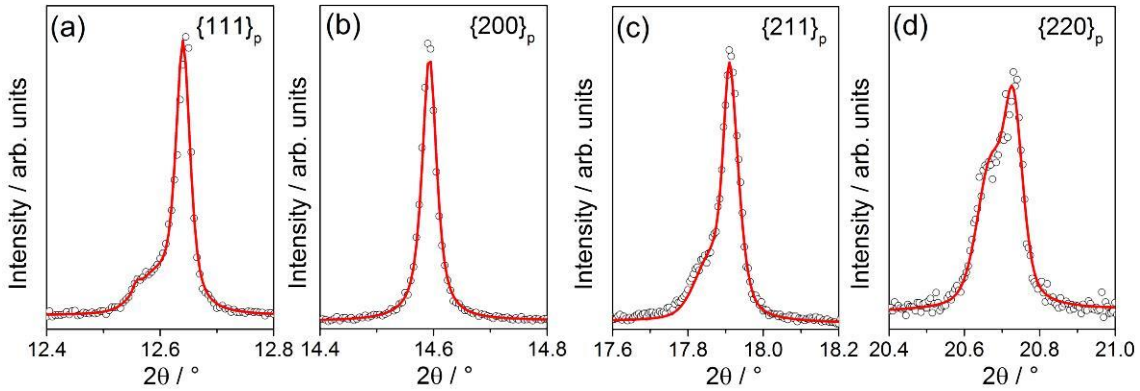

Figure 7.14 The representative peak profiles for (a) $\{111\}_p$ (b) $\{200\}_p$ (c) $\{211\}_p$ and (d) $\{220\}_p$ for unpoled NBT-0.05BT powders.

Table 7.5 The crystallographic parameters for unpoled NBT-0.05BT ceramic powder after full pattern refinement.

Crystallographic parameters	Value
GOF	1.17
R_{exp} / %	8.67
R_{wp} / %	10.44
Lattice parameter a / Å	5.4969(6)
Lattice parameter c / Å	13.5258(14)

7.7 Ex-situ high-energy XRD experiments (Diamond beamline I15)

7.7.1 Domain orientation distribution (DOD) analysis

The changes in crystallographic texture and lattice strain for the NBT-0.05BT and NBT-0.06BT ceramics in the poled state are examined further in the following Section to evaluate the influence of the BT content on domain switching behaviour and to allow a comparison with previous results for NBT-xKN and NBT-xNN ceramics. The lattice strain and preferred orientation due to ferroelectric domain switching were determined using high energy XRD and

calculated following the method reported in Section 5.8.1.5 above.

7.7.1.1 NBT-0.05BT

The diffraction peak profiles for $\{111\}_p$ and $\{200\}_p$ for a range of different grain orientations are exhibited in Figure 7.15. The split $\{111\}_p$ and single $\{200\}_p$ peaks indicate the presence of the rhombohedral structure, consistent with the high resolution SXPD results reported in the previous section. The variations in the relative intensities of the $\{111\}_p$ peaks as a function of the azimuthal angle, ψ, indicated that the [111]-oriented domains are oriented preferentially along the electric field direction at ψ=0°. Additionally, the $\{200\}_p$ peak exhibited a slight shift as function of ψ, indicating a small elastic lattice strain.

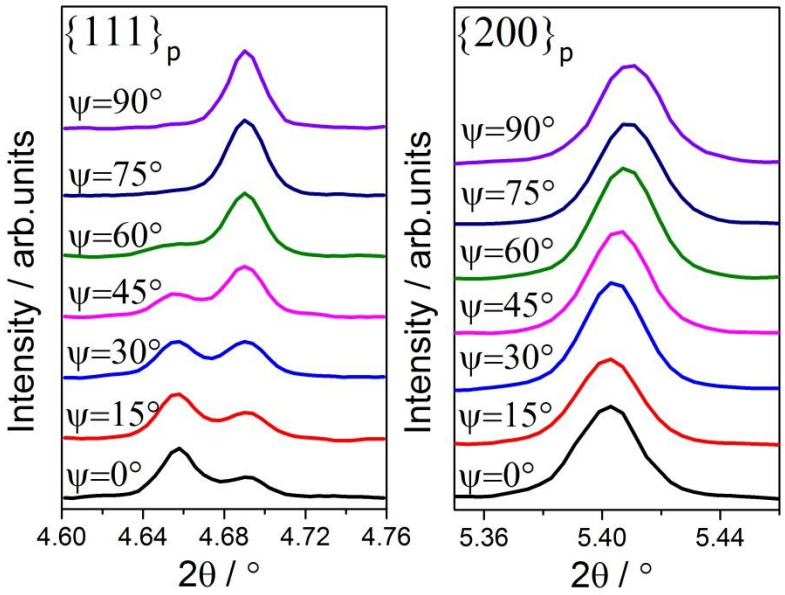

Figure 7.15 The representative XRD peak reflections for poled NBT-0.05BT ceramic.

Both $d_{\{200\}}$ and $\varepsilon_{(200)}$ were calculated following same method in Section 5.8.1.5 and plotted as function of ψ, as illustrated in Figure 7.16. It is evident that that the dependence of ε_{200} on ψ exhibited a good fit to Equation 5.7, yielding a maximum lattice strain of 1.1×10^{-3} at ψ = 0°.

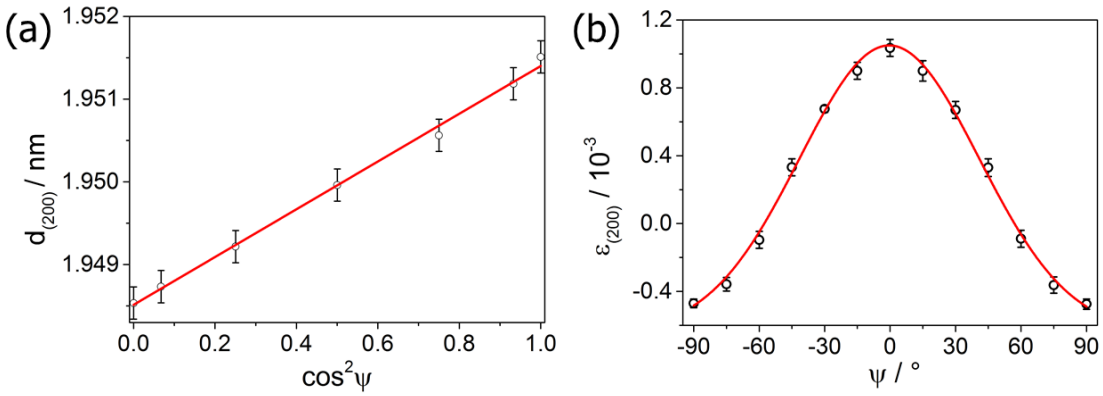

Figure 7.16 Dependence of (a) d_{200} and (b) ε_{200} on azimuthal angle, ψ. Symbols are experimental data points and red lines are calculated according to Equation 5.3.

Additionally, the DOD was calculated according to Equation 5.8-5.10 following the same method described in Section 5.8.1.5. The results obtained for ν_{111} was plotted as function of ψ, as shown in Figure 7.18. The linear fit to the $R_1(111)$ data indicated that the intensity ratio was approximately equal to 0.205 at $\cos^2\psi$ = 1/3. With a maximum ν_{111} value of approximately 0.72 being achieved for ψ=0°, these results indicated that the degree of non-180° domain switching in the remanent state was relatively high. This level of saturation was similar to that of the NBT-0.03KN (0.76) and NBT-0.02NN (0.70) ceramics.

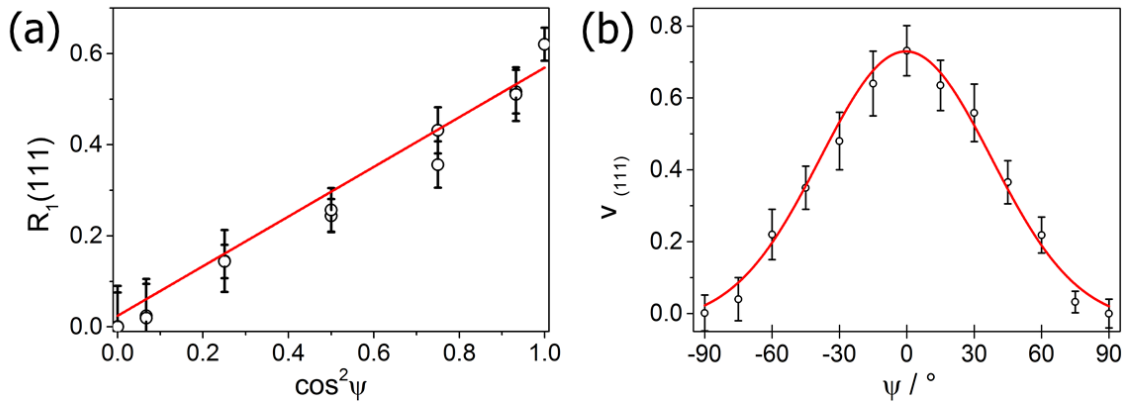

Figure 7.17 Dependence of (a) peak intensity ratio, $R_1(111)$, and (b) domain fraction, $\nu_{(111)}$, on azimuthal angle, ψ. Symbols are experimental data points and red lines are calculated data.

7.7.1.2 NBT-0.06BT

The diffraction peak profiles of $\{111\}_p$ and $\{200\}_p$ over a range of different grain orientations are displayed in Figure 7.19. A mixed-phase of rhombohedral and tetragonal is observed, characterised by the splitting of both $\{111\}_p$ and $\{200\}_p$ peaks. The variations in the relative intensities of the $\{111\}_p$ and $\{200\}_p$ peaks as a function of the azimuthal angle, ψ, indicated that the [111]-oriented domains were oriented preferentially along the electric field direction at ψ=0° in rhombohedral phase and the [002]-oriented domains were orientated preferentially along the electric field in the tetragonal phase. Furthermore, both $\{111\}_p$ and $\{200\}_p$ peaks exhibit a slight shift as function of ψ, indicating that an elastic lattice strain was generated due to domain switching. Quantitative analysis of the domain fractions and lattice strain was not undertaken in this case, for the reasons outlined above in Section 6.8.2.2.

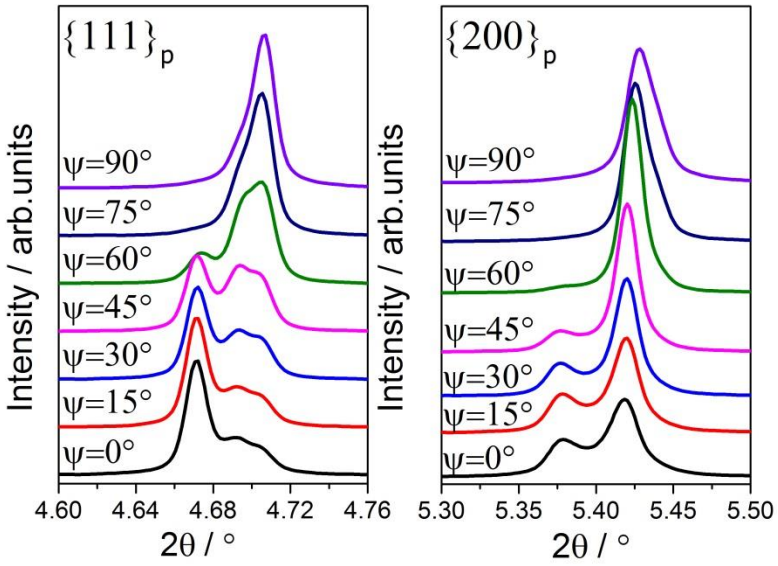

Figure 7.18 The representative XRD peak reflections for poled NBT-0.06BT ceramic.

7.8 Summary

The NBT-xBT (x=0.04 to 0.11) ceramics were synthesized by solid state reaction, reaching a relative density of greater than 94%. The average grain size for sintered ceramics ranged from 1.86 to 3.74 μm. For NBT-0.04BT, a single phase rhombohedral structure was observed, characterised by double $\{111\}_p$ and single

$\{200\}_p$ peaks. For compositions with x=0.05 to 0.11 in NBT-xBT ceramics, a mixed-phase region of rhombohedral and tetragonal structure was identified by lab XRD. However, a single phase with R3c rhombohedral structure was obtained for NBT-0.05BT using high resolution SXPD. Furthermore, the poled NBT-0.05BT and NBT-0.06BT ceramic specimens were examined using high-energy synchrotron XRD. It was found that NBT-0.05BT exhibits lattice strain and preferred ferroelectric domain orientations that are consistent with a conventional long-range ordered rhombohedral ferroelectric. The NBT-0.06BT ceramic showed strong texture in both rhombohedral and tetragonal phases, but the occurrence of anisotropic lattice strain and the overlapping of diffraction peaks hindered the quantitative texture analysis.

For the ferroelectric behaviour, well-defined P-E loops were obtained for compositions with x=0.04 to 0.06 at room temperature, indicating the presence of the FE state. On increasing the BT content to 8%, the transition between PNRs and long-range ferroelectric order became reversible, characterised by a constricted loop and a split polarisation switching peak. For NBT-0.11BT, a typical ferroelectric P-E loop and J-E curve were obtained again.

Upon heating, the NBT-0.05BT, NBT-0.06BT and NBT-0.11BT ceramics exhibited constricted P-E loops, indicating a reversible transition between PNRs and the metastable FE state. Further investigations were conducted on poled specimens using depolarisation and dielectric measurements to illustrate the influence of composition and temperature on the phase stability. The depolarisation temperature, T_d, was determined as 137, 95 and 66 °C for NBT-0.04BT, NBT-0.05BT and NBT-0.06BT respectively. The depolarisation temperature could not be obtained for NBT-0.08BT due to the reversible nature of the field-induced RF to FE transformation. Furthermore, the phase transition temperature, T_{F-R}, was obtained from the additional peak in the $\tan\delta$-T relationship, which was found to be close to T_d. It was proposed that the thermally-induced phase transition from the metastable FE to RF state is directly related to the development of constricted P-E loops and loss of remanent polarisation.

8 Overall summary and conclusions

8.1 Overall summary

8.1.1 Comparison of temperature-dependent polarisation for NBT-KN, NBT-NN and NBT-BT systems

For compositions in the non-ergodic RF state at room temperature, the bipolar poling procedure induced an irreversible transformation from the NR to metastable FE state, resulting in high P_{max} and P_{rem} values. With increasing temperature, the FE state becomes unstable and transforms back to the ergodic-RF (ER) state, evidenced by constricted P-E loops and split polarisation switching peaks the in J-E curves.

To compare between ceramics with different compositions, the P_{max} and P_{rem} values for NBT-0.03KN, NBT-0.05BT, NBT-0.06BT, NBT-0.02NN and NBT-0.04NN poled specimens, are plotted in Figure 8.1 as function of temperature.

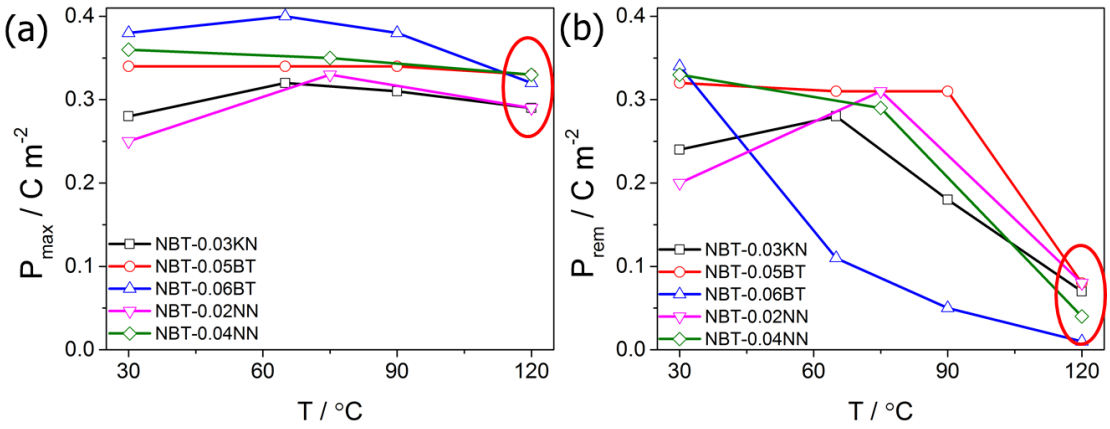

Figure 8.1 Comparison of temperature-dependent (a) maximum polarisation and (b) remanent polarisation for different NBT-based compositions.

For NBT-0.03KN and NBT-0.02NN ceramics, the P_{max} and P_{rem} values increase with increasing temperature from 30 to 65 ºC and 30 to 75 ºC respectively due to reduction of E_c value. With further increase temperature, the P_{max} values for all compositions remain the same, in the range from 0.25 C m^{-2} to 0.42 C m^{-2}. However, the P_{rem} values decline dramatically due to thermally-induced phase

transition from FE to RF states. The combination of low P_{rem} and high P_{max} values could be opportunity for actuators and energy storage applications utilizing reversible transformation. Furthermore, it was found that the transition temperatures, T_{F-R}, decrease with increasing KN, NN and BT contents due to effect of compositional or charge disorder.

8.1.2 Comparison of DOD for NBT-KN, NBT-NN and NBT-BT systems

The distributions of domain orientation and lattice strain were analysed on poled specimens with single R3c rhombohedral phase in order to evaluate the effect of KN, NN and BT on domain reorientation. The ferroelectric hysteresis loop, P-E, grain orientation-dependent lattice strain, ε_{200}-ψ, and domain fraction, ν_{111}-ψ, relationships for four compositions are illustrated in Figure 8.2.

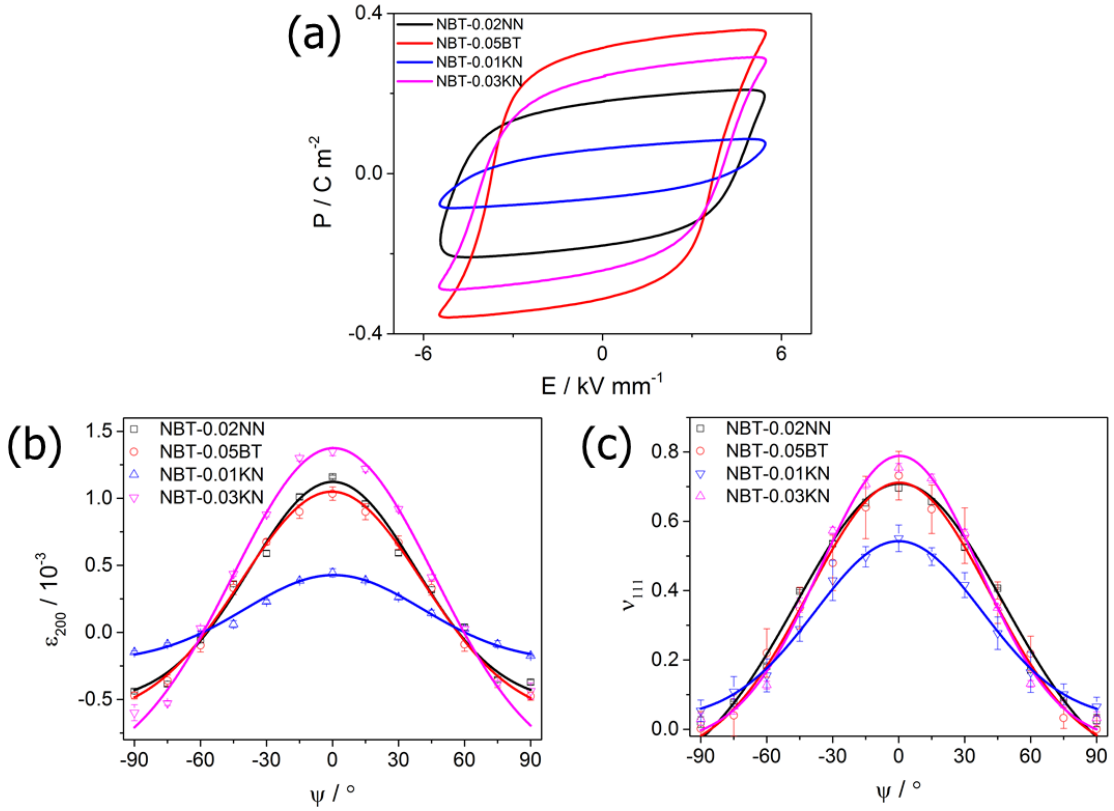

Figure 8.2 Comparison of (a) ferroelectric hysteresis P-E loops (b) orientation-dependent lattice strain and (c) orientation-dependent domain fraction.

It is shown below that NBT-0.05BT, NBT-0.03KN and NBT-0.02NN possess a well-defined P-E loop, resulting in a high fraction of [111]-oriented domains of approximately 72%, 76% and 70% respectively being achieved for ψ = 0°. The lattice strain, ε_{200}, is observed to be very high for these compositions as well, with maximum values of $1.4x10^{-3}$, $1.1x10^{-3}$ and $1.1\ x10^{-3}$ respectively for ψ = 0°. In contrast, NBT-0.01KN is not well-poled due to the high coercive field, leading to a low degree of domain reorientation and lattice strain for ψ = 0°.

8.2 Conclusions

Numerous questions concerning NBT-based relaxor ferroelectrics were addressed in this PhD project, relating to both structural and electrical characteristics. Three ceramic systems were investigated, specifically the newly developed systems (1-x)NBT-xKN and (1-x)NBT-xNN and the well-known system (1-x)NBT-xBT.

At room temperature, all compositions of NBT-KN ceramics in the unpoled state were observed to be cubic. However, for compositions with low KN content, a well-defined ferroelectric hysteresis P-E loop was observed, indicating that an irreversible transformation from PNRs to a long-range ordered FE state occurred during the measurement procedure. Subsequently, the crystal structures of NBT-KN ceramic powders in both the unpoled and poled states were examined using high resolution SXPD. It was confirmed that an irreversible structural transformation from cubic to rhombohedral had occurred for compositions with low KN content during application of the high bipolar electric field. Similar behaviour was observed for NBT-NN solid solutions with low NN content, resulting in structural transformations from cubic to rhombohedral for NBT-0.02NN and from cubic to mixed-phase rhombohedral and tetragonal for NBT-0.04NN. In contrast, a cubic structure was observed in both poled and unpoled states for high KN content due to the reversible transition, associated with a constricted P-E loop and split polarisation switching peaks in the J-E curve.

To thoroughly investigate the structural transformation, an ‘in-situ’ electric field poling experiment was conducted using high-energy synchrotron XRD. It was

found that the crystal structure can be transformed progressively with increasing cycles of a bipolar electric field. For example, it took 15 and 11 cycles of electric field to complete the structural transformation from cubic to rhombohedral for NBT-0.01KN and NBT-0.03KN respectively. It was demonstrated that the structure transformed from single phase cubic to mixed-phase of cubic and rhombohedral and finally to single phase rhombohedral during the structural transformation. Similar behaviour was observed for NBT-0.02NN and NBT-0.04NN, which required approximately 5 and 3 cycles of electric field respectively to complete the structural transformation.

Furthermore, the crystallographic texture analysis has been conducted on poled state in order to evaluate the effect of KN and NN on domain switching behaviour and the resulting DOD. For compositions exhibiting well-defined P-E loops with single phase rhombohedral structure after poling, the lattice strain and domain orientation distribution are similar to those of conventional rhombohedral PZT ceramics. The highest ν_{111} values, greater than 70%, were obtained for NBT-0.03KN and NBT-0.02NN. The lattice strain, ε_{200}, was also found to be the highest for NBT-0.03KN and NBT-0.02NN. A coexistence of rhombohedral and tetragonal phases was observed for poled NBT-0.04NN, which exhibited systematic variations in intensity ratio and peak positions with grain orientation. However, the quantitative crystallographic texture analysis was not undertaken due to the combination of anisotropic lattice strain, strong crystallographic texture and overlapping of diffraction peaks.

In terms of the phase transition temperatures for poled specimens, both T_{F-R} and T_d were obtained from dielectric and thermal depolarisation measurements respectively for compositions with low KN and NN contents due to the irreversible transformation from nonergodic-RF to metastable FE states. Both T_{F-R} and T_d were observed to decrease with increasing KN and NN content. No T_{F-R} and T_d values could be obtained for compositions with high KN and NN contents due to their ergodicity. An additional transition temperature, T_{ST}, representing the structural transformation from rhombohedral to cubic was obtained for poled

(1-x)NBT-xKN (x=0.01 to 0.05) using high resolution SPXD. Finally, a phase diagram for poled NBT-xKN was constructed to illustrate the stability regions of the different types of ferroelectric phase and crystal structures.

The structural, ferroelectric and dielectric properties of the well-studied NBT-BT system were also investigated to provide a reference point for comparison with the more novel NBT-KN and NBT-NN systems. For NBT-xBT compositions with x=0.04 to 0.06 and 0.11, an FE state was observed, featuring well-defined P-E loops and single polarisation switching peak in the J-E curves. With increasing temperature, the FE state was destabilised and transformed to an RF state, characterised by a constricted P-E loop and split polarisation switching peaks in the J-E curve. This caused a significant drop in remanent polarisation, P_r, which was correlated with reductions in the thermal depolarisation temperature, T_d, and the FE to RF transition temperature, T_{F-R}.

For NBT-0.08BT, an ergodic-RF state was present, which was found to undergo a reversible transition between PNRs and metastable FE states for all temperatures, characterised by a constricted P-E and split polarisation switching peaks in the J-E curve.

For the structural characterisation, the unpoled NBT-0.05BT ceramic powder was re-examined using SXPD. A single rhombohedral phase was obtained after full pattern refinement, which was in agreement with previous reports. Furthermore, an 'ex-situ' high-energy synchrotron XRD experiment was conducted on NBT-0.05BT and NBT-0.06BT ceramic pellets to illustrate the effect of poling on crystallographic texture effect. It was concluded that a high domain fraction value of 0.72 and a lattice strain value of 1.1×10^{-3} were achieved for $\psi=0^{o}$, which was similar to those of NBT-0.02NN and NBT-0.03KN. Similar to the case of NBT-0.04NN, the quantitative crystallographic texture analysis could not be undertaken for NBT-0.06BT due to the presence of a highly textured mixed-phase structure.

9 Future work

The work presented in the thesis has attempted to explain the fundamental nature of the electric field-induced phase switching and domain switching mechanisms in lead-free NBT-based ceramics. So far, three material systems, (1-x)NBT-xKN, (1-x)NBT-xNN and (1-x)NBT-xBT, have been characterised by both structural and electrical measurements. However, there is still a considerable amount of experimental work that could be done to complement the research results reported here. The experiments listed below would help to address the issues raised by these investigations.

1. It was found that different kinds of localised structure or symmetries of PNR exist in NBT and NBT-based ceramics.[11, 193] Therefore, the pair distribution function (PDF) analysis and transmission electron microscopy (TEM) are potential characterisation techniques that could be employed to determine the short-range atomic order and nano-scale local structure. This is an important step to determine the nature of the pseudo-cubic structure for unpoled NBT-xKN and NBT-xNN ceramics as well as to evaluate the irreversible and reversible phase transition between PNRs and long-range ordered ferroelectric state.

2. Similar to the NBT-xKN, a temperature-dependent study can be devised to determine the structural transformation temperature, T_{ST}, for the (1-x)NBT-xNN system in order to construct the phase diagram.

3. The focus of this project has been to evaluate the effect of electric field on structural and functional properties of NBT-based materials. However, as a piezoelectric ceramic, another interesting opportunity would be to evaluate the effect of pressure. It was observed that a substantial increase in unit cell volume occurred due to the electric field-induced structural transformation from cubic to rhombohedral. It is proposed that it may be possible to induce the reverse transformation under the application of hydrostatic pressure. Furthermore, it was reported that mechanical pressure can induce the phase transition from

metastable ferroelectric order to the RF state in (1-x) NBT-xBT ceramics.[194] Hence, a similar experiment could be conducted on poled NBT-KN and NBT-NN ceramics with low KN and NN contents to investigate the characteristics of such a pressure-induced transformation.

4. Another characterisation technique that could be used to measure the strain during application of an electric field is Digital image correlation (DIC). Such a technique could be employed to confirm the variations in axial and volumetric strains for NBT-based ceramics during electric field-induced phase switching.

5. A ternary solid solution or doping could be used to tailor the functional properties of NBT-based ceramics. Based on an improved understanding of the mechanisms involved in the NBT-KN and NBT-NN systems, a suitable choice of dopants could be introduced to improve the properties further with respect to specific applications. For example, the addition of another end member such as $BiFeO_3$ or even the addition of a conductive second phase could be employed to enhance the stability of the FE state for sensor applications. On the other hand, stabilisation of the PNRs at high NN contents could result in better energy storage and reversible actuation characteristics.

10 References

[1] J. Rödel, W. Jo, K. T. P. Seifert, E.-M. Anton, T. Granzow, and D. Damjanovic, Perspective on the Development of Lead-free Piezoceramics, *Journal of the American Ceramic Society,* vol. 92, pp. 1153-1177, 2009.

[2] Verordnung zur Reduktion von Risiken beim Umgang mit bestimmten besonders gefaöhrlichen Stoffen, Zubereitungen und Gegenstaönden (Chemikalien-Risikoreduktions-Verordnung,ChemRRV), *Amtliche Sammlung des Bundesrechts (Swiss Federal Legislation),* vol. [AS 2005 2917], 2005.

[3] Regulations Relating to Restrictions on the Manufacture, Import, Export, Sale and Use of Chemicals and Other Products Hazardous to Health and the Environment, *Produktforskriften,* 2004.

[4] Solid Waste: Hazardous Electronic Waste, *U.S. California Senate Bill No.20,* 2003.

[5] Solid Waste: Hazardous Electronic Waste, *U.S. California Senate Bill No.50,* 2004.

[6] Restriction of the Use of Certain Hazardous Substances in Electrical and Electronic Equipment, *Ministry of Environment and Forestry Turkey Regulation No. 26891,* 2008.

[7] T. Tadashi, M. Kei-ichi, and S. Koichiro, $(Bi_{1/2}Na_{1/2})TiO3$-$BaTiO_3$ System for Lead-Free Piezoelectric Ceramics, *Japanese Journal of Applied Physics,* vol. 30, p. 2236, 1991.

[8] Y. Saito, H. Takao, T. Tani, T. Nonoyama, K. Takatori, T. Homma, T. Nagaya, and M. Nakamura, Lead-free piezoceramics, *Nature,* vol. 432, pp. 84-87, Nov 2004.

[9] W. Jo, R. Dittmer, M. Acosta, J. D. Zang, C. Groh, E. Sapper, K. Wang, and J. Rodel, Giant electric-field-induced strains in lead-free ceramics for actuator applications - status and perspective, *Journal of Electroceramics,* vol. 29, pp. 71-93, Aug 2012.

[10] W. Jo, J. E. Daniels, J. L. Jones, X. Tan, P. A. Thomas, D. Damjanovic, and J. r. Rödel, Evolving morphotropic phase boundary in lead-free $(Bi_{1/2}Na_{1/2})TiO_3$–$BaTiO_3$ *Journal of Applied Physics,* vol. 109, p. 014110, 2011.

[11] W. Jo, S. Schaab, E. Sapper, L. A. Schmitt, H.-J. Kleebe, A. J. Bell, and J. r. Rödel, On the phase identity and its thermal evolution of lead free $(Bi_{1/2}Na_{1/2})TiO3$-6 mol% $BaTiO_3$, *Journal of Applied Physics,* vol. 110, p. 074106, 2011.

[12] J. E. Daniels, W. Jo, J. Rödel, and J. L. Jones, Electric-field-induced phase transformation at a lead-free morphotropic phase boundary: Case study in a 93%$(Bi_{0.5}Na_{0.5})TiO3$-7%$BaTiO_3$ piezoelectric ceramic, *Applied Physics Letters,* vol. 95, p. 032904, 2009.

[13] A. R. West, *Basic Solid State Chemistry (Second Edition)*: Wiley, 1999.

[14] A. J. Moulson and J. M. Herbert, Electroceramics: Materials, Properties, Applications, 1990.

[15] V. M. Goldschmidt, Geochemische verteilungsgesetze der elemente, *Skrifter utg. Av det Norske Viedenskaps-akademii Oslo,* vol. 2, pp. 1-117, 1926.

[16] W. R. J. C. B. Jaffe, H. Jaffe, Piezoelectric ceramics, *Academic Press, London,* 1971.

[17] E. K. A. Ahmad Safari, Piezoelectric and Acoustic Material for Transdecer applications.

[18] A. Glazer, The classification of tilted octahedra in perovskites, *Acta Crystallographica Section B,* vol. 28, pp. 3384-3392, 1972.

[19] A. M. Glazer, THe classification of tilted octahedra in perovskite, *Acta Crystallographica.Section.B,* vol. B28, pp. 3384-3392, 1972.

[20] K. E. Johnston, C. C. Tang, J. E. Parker, K. S. Knight, P. Lightfoot, and S. E. Ashbrook, The

Polar Phase of $NaNbO_3$: A Combined Study by Powder Diffraction, Solid-State NMR, and First-Principles Calculations, *Journal of the American Chemical Society,* vol. 132, pp. 8732-8746, 2010/06/30 2010.

[21] D. Damjanovic, Ferroelectric, dielectric and piezoelectric properties of ferroelectric thin films and ceramics, *Reports on Progress in Physics,* vol. 61, pp. 1267-1324, Sep 1998.

[22] L. J. Gauckler, Ingenieurskeramik 3-Funktionskeramik, *Swiss Federal Institute of Technology Zurich, Zurich,* 2001.

[23] D. A. Hall, Rayleigh behaviour and the threshold field in ferroelectric ceramics, *Ferroelectrics,* vol. 223, pp. 319-328, 1999.

[24] AN AMERICAN NATIONAL STANDARD - IEEE STANDARD DEFINITIONS OF PRIMARY FERROELECTRIC TERMS, *Ieee Transactions on Ultrasonics Ferroelectrics and Frequency Control,* vol. 38, pp. 7-21, Nov 1991.

[25] Y. H. Bing, A. A. Bokov, and Z. G. Ye, Diffuse and sharp ferroelectric phase transitions in relaxors, *Current Applied Physics,* vol. 11, pp. S14-S21, 2011.

[26] G. A. Smolenskii, V. A. Isupov, A. I. Agranovskaya, and S. N. Popov, Ferroelectrics with Diffuse Phase Transition, *Soviet Physics Solid State,* vol. 2, pp. 2584-2594, 1961.

[27] G. A. Samara, The relaxational properties of compositionally disordered ABO_3 perovskites, *Journal of Physics Condensed Matter,* vol. 15, pp. R367-R411, 2003.

[28] L. E. Cross, Relaxorferroelectrics: An overview, *Ferroelectrics,* vol. 151, pp. 305-320,

[29] R. Dittmer, Lead-Free Piezoceramics Ergodic and Nonergodic Relaxor Ferroelectrics Based on Bismuth Sodium Titanate, PhD Thesis, University of Darmstadt, 2013.

[30] S. J. L. Billinge and I. Levin, The Problem with Determining Atomic Structure at the Nanoscale, *Science,* vol. 316, pp. 561-565, 2007.

[31] I. Levin, I. M. Reaney, E. M. Anton, W. Jo, J. Rödel, J. Pokorny, L. A. Schmitt, H. J. Kleebe, M. Hinterstein, and J. L. Jones, Local structure, pseudosymmetry, and phase transitions in $Na_{1/2}Bi_{1/2}TiO_3$-$K_{1/2}Bi_{1/2}TiO_3$ ceramics, *Physical Review B,* vol. 87, p. 024113, 2013.

[32] B. N. Rao, L. Olivi, V. Sathe, and R. Ranjan, Electric field and temperature dependence of the local structural disorder in the lead-free ferroelectric $Na_{0.5}Bi_{0.5}TiO_3$: An EXAFS study, *Physical Review B,* vol. 93, p. 024106, 2016.

[33] W. Ge, C. Luo, C. P. Devreugd, Q. Zhang, Y. Ren, J. Li, H. Luo, and D. Viehland, Direct evidence of correlations between relaxor behavior and polar nano-regions in relaxor ferroelectrics: A case study of lead-free piezoelectrics $Na_{0.5}Bi_{0.5}TiO_3$-x%$BaTiO_3$, *Applied Physics Letters,* vol. 103, p. 241914, 2013.

[34] C. Ma, H. Guo, S. P. Beckman, and X. Tan, Creation and Destruction of Morphotropic Boundaries through Electrical Poling: A Case Study of Lead-Free $Bi_{1/2}Na_{1/2}TiO_3$-$BaTiO_3$ Piezoelectrics, *Physical Review Letters,* vol. 109, p. 107602, 2012.

[35] J. Yao, N. Monsegue, M. Murayama, W. Leng, W. T. Reynolds, Q. Zhang, H. Luo, J. Li, W. Ge, and D. Viehland, Role of coexisting tetragonal regions in the rhombohedral phase of $Na_{0.5}Bi_{0.5}TiO_3$-x$BaTiO_3$ crystals on enhanced piezoelectric properties on approaching the morphotropic phase boundary, *Applied Physics Letters,* vol. 100, p. 012901, 2012.

[36] G. Viola, H. Ning, M. J. Reece, R. Wilson, T. M. Correia, P. Weaver, M. G. Cain, and H. Yan, Reversibility in electric field-induced transitions and energy storage properties of bismuth-based perovskite ceramics, *Journal of Physics D: Applied Physics,* vol. 45, p. 355302, 2012.

[37] W. Kleemann, The relaxor enigma-charge disorder and random fields in ferroelectrics,

Journal of Materials Science, vol. 41, pp. 129-136, 2006.

[38] M. D. Glinchuk and R. Farhi, A random field theory based model for ferroelectric relaxors, *Journal of Physics: Condensed Matter,* vol. 8, p. 6985, 1996.

[39] L. E. Cross, Relaxor Ferroelectrics, *Ferroelectrics,* 1987.

[40] G. A. Smolenskii and V. A. Isupov, Segnetoelektricheskie Svoistva Tverdykh Rastvorov Stannata Bariya V Titanate Bariya, *Zhurnal Tekhnicheskoi Fiziki,* vol. 24, pp. 1375-1386, 1954.

[41] C. G. F. Stenger and A. J. Burggraaf, Order-disorder reactions in the ferroelectric perovskites $Pb(Sc_{1/2}Nb_{1/2})O_3$ and $Pb(Sc_{1/2}Ta_{1/2})O_3$. II. Relation between ordering and properties, *Physica Status Solidi A: Applied research,* vol. 61, pp. 653-664, 1980.

[42] C. G. F. Stenger and A. J. Burggraaf, Order-disorder reactions in the ferroelectric perovskites $Pb(Sc_{1/2}Nb_{1/2})O_3$ and $Pb(Sc_{1/2}Ta_{1/2})O_3$. I. Kinetics of the ordering process, *Physica Status Solidi A: Applied research,* vol. 61, pp. 275-285, 1980.

[43] Z. G. Ye, Relaxor Ferroelectric Complex Perovskites: Structure, Properties and Phase Transitions, *Key Engineering Materials,* vol. 155-156, pp. 81-122, 1998.

[44] B. Chu, X. Zhou, K. Ren, B. Neese, M. Lin, Q. Wang, F. Bauer, and Q. M. Zhang, A Polymer with High Electric Energy Density and Fast Discharge Speed, *Science,* vol. 313, 334-336, 2006.

[45] W. J. Sarjeant, J. Zirnheld, and F. W. MacDougall, Capacitors, *IEEE Transactions on Science,* vol. 26, pp. 1368-1392, 1998.

[46] N. H. Fletcher, A. D. Hilton, and B. W. Ricketts, Optimization of energy storage density in ceramic capacitors, *Journal of Physics D: Applied Physics,* vol. 29, p. 253, 1996.

[47] T. M. Correia, M. McMillen, M. K. Rokosz, P. M. Weaver, J. M. Gregg, G. Viola, and M. G. Cain, A Lead-Free and High-Energy Density Ceramic for Energy Storage Applications, *Journal of the American Ceramic Society,* vol. 96, pp. 2699-2702, 2013.

[48] J. B. Lim, S. Zhang, N. Kim, and T. R. Shrout, High-Temperature Dielectrics in the $BiScO_3$–$BaTiO_3$–$(K_{1/2}Bi_{1/2})TiO_3$ Ternary System, *Journal of the American Ceramic Society,* vol. 92, pp. 679-682, 2009.

[49] H. Ogihara, C. A. Randall, and S. Trolier-McKinstry, High-Energy Density Capacitors Utilizing 0.7 $BaTiO_3$–0.3 $BiScO_3$ Ceramics, *Journal of the American Ceramic Society,* vol. 92, pp. 1719-1724, 2009.

[50] G. Yao, X. Wang, Y. Wu, and L. Li, Nb-Doped $0.9BaTiO_3$–$0.1(Bi_{0.5}Na_{0.5})TiO_3$ Ceramics with Stable Dielectric Properties at High Temperature, *Journal of the American Ceramic Society,* vol. 95, pp. 614-618, 2012.

[51] R. Dittmer, W. Jo, D. Damjanovic, and J. Rödel, Lead-free high-temperature dielectrics with wide operational range, *Journal of Applied Physics,* vol. 109, p. 034107, 2011.

[52] W. P. Cao, W. L. Li, X. F. Dai, T. D. Zhang, J. Sheng, Y. F. Hou, and W. D. Fei, Large electrocaloric response and high energy-storage properties over a broad temperature range in lead-free NBT-ST ceramics, *Journal of the European Ceramic Society,* vol. 36, pp. 593-600, 2016.

[53] P. Chen and B. Chu, Improvement of dielectric and energy storage properties in $Bi(Mg_{1/2}Ti_{1/2})O_3$-modified $(Na_{1/2}Bi_{1/2})0.92Ba0.08TiO_3$ ceramics, *Journal of the European Ceramic Society,* vol. 36, pp. 81-88, 2016.

[54] W. P. Cao, W. L. Li, D. Xu, Y. F. Hou, W. Wang, and W. D. Fei, Enhanced electrocaloric in lead-free NBT-based ceramics, *Ceramics International,* vol. 40, pp. 9273-9278, 2014.

[55] M. Chandrasekhar and P. Kumar, Synthesis and characterizations of BNT–BT and BNT–BT–KNN ceramics for actuator and energy storage applications, *Ceramics International,* vol. 41, pp. 5574-5580, 2015.

[56] F. Gao, X. Dong, C. Mao, W. Liu, H. Zhang, L. Yang, F. Cao, G. Wang, and J. Jones, Energy-Storage Properties of $0.89Bi_{0.5}Na_{0.5}TiO_3$-$0.06BaTiO_3$-$0.05K_{0.5}Na_{0.5}NbO_3$ Lead-Free Anti-ferroelectric Ceramics, *Journal of the American Ceramic Society,* vol. 94, pp. 4382-4386, 2011.

[57] L. Luo, B. Wang, X. Jiang, and W. Li, Energy storage properties of $(1 - x)(Bi_{0.5}Na_{0.5})TiO_3$–$xKNbO_3$ lead-free ceramics, *Journal of Materials Science,* vol. 49, pp. 1659-1665, 2013.

[58] M. Ahart, M. Somayazulu, R. E. Cohen, P. Ganesh, P. Dera, H.-k. Mao, R. J. Hemley, Y. Ren, P. Liermann, and Z. Wu, Origin of morphotropic phase boundaries in ferroelectrics, *Nature,* vol. 451, pp. 545-548, 2008.

[59] A. F. Devonshire, Theory of ferroelectrics, *Advances in Physics,* vol. 3, pp. 85-130, 1954.

[60] B. Noheda, J. A. Gonzalo, L. E. Cross, R. Guo, S. E. Park, D. E. Cox, and G. Shirane, Tetragonal-to-monoclinic phase transition in a ferroelectric perovskite: The structure of $PbZr_{0.52}Ti_{0.48}O_3$, *Physical Review B,* vol. 61, pp. 8687-8695, 2000.

[61] D. W. Baker, P. A. Thomas, N. Zhang, and A. M. Glazer, A comprehensive study of the phase diagram of $K_xNa_{1-x}NbO_3$, *Applied Physics Letters,* vol. 95, p. 091903, 2009.

[62] Jaffe B., W. R. a. Cook, and H. Jaffe, *Piezoelectric Ceramics*: Academic Press, 1971.

[63] D. Berlincourt, H. H. A. Krueger, and B. Jaffe, Stability of phases in modified lead with variation in pressure, electric field, temperature and composition, *Journal of Physics and Chemistry of Solids,* vol. 25, pp. 659-674, 1964.

[64] D. Berlincourt, H. Jaffe, H. H. A. Krueger, and B. Jaffe, Release of electric energy in $PbNb(Zr, Ti, Sn)O_3$ by temperature and by pressure enforced phase transitions, *Applied Physics Letters,* vol. 3, pp. 90-92, 1963.

[65] K. Uchino, Recent topics of ceramic actuators how to develop new ceramic devices, *Ferroelectrics,* vol. 91, pp. 281-292, 1989.

[66] A. J. Royles, A. J. Bell, A. P. Jephcoat, A. K. Kleppe, S. J. Milne, and T. P. Comyn, Electric-field-induced phase switching in the lead free piezoelectric potassium sodium bismuth titanate, *Applied Physics Letters,* vol. 97, p. 132909, 2010.

[67] G. Wang, D. A. Hall, T. P. Comyn, L. Daniel, and A. K. Kleppe, Structure and ferroelectric behaviour of $Na_{0.5}Bi_{0.5}TiO_3$-$KNbO_3$ ceramics, *Advances in Applied Ceramics,* vol. 115, pp. 89-95, 2016.

[68] W. Ge, D. Maurya, J. Li, S. Priya, and D. Viehland, Alternating and direct current field effects on the structure-property relationships in $Na_{0.5}Bi_{0.5}TiO_3$-x%$BaTiO_3$ textured ceramics, *Applied Physics Letters,* vol. 102, p. 222905, 2013.

[69] C. Ma, H. Guo, and X. Tan, A New Phase Boundary in $(Bi_{1/2}Na_{1/2})TiO_3$–$BaTiO_3$ Revealed a Novel Method of Electron Diffraction Analysis, *Advanced Functional Materials,* vol. 23, 5261-5266, 2013.

[70] D. Maurya, A. Pramanick, M. Feygenson, J. C. Neuefeind, R. J. Bodnar, and S. Priya, Effect of poling on nanodomains and nanoscale structure in A-site disordered lead-free piezoelectric $Na_{0.5}Bi_{0.5}TiO_3$-$BaTiO_3$, *Journal of Materials Chemistry C,* vol. 2, pp. 2014.

[71] D. A. Hall, J. D. S. Evans, S. J. Covey-Crump, R. F. Holloway, E. C. Oliver, T. Mori, and P. J. Withers, Effects of superimposed electric field and porosity on the hydrostatic

pressure-induced rhombohedral to orthorhombic martensitic phase transformation in PZT 95/5 ceramics, *Acta Materialia,* vol. 58, pp. 6584-6591, 2010.

[72] X. Jiang, L. Luo, B. Wang, W. Li, and H. Chen, Electrocaloric effect based on the depolarization transition in $(1-x)Bi_{0.5}Na_{0.5}TiO_3$–$xKNbO_3$ lead-free ceramics, *Ceramics International,* vol. 40, pp. 2627-2634, 2014.

[73] E.-M. Anton, W. Jo, D. Damjanovic, and J. r. Rödel, Determination of depolarization temperature of $(Bi_{1/2}Na_{1/2})TiO_3$-based lead-free piezoceramics, *Journal of Applied Physics,* vol. 110, p. 094108, 2011.

[74] W. Jo, J. Daniels, D. Damjanovic, W. Kleemann, and J. Rödel, Two-stage processes of electrically induced-ferroelectric to relaxor transition in $0.94(Bi_{1/2}Na_{1/2})TiO_3$-$0.06BaTiO_3$, *Applied Physics Letters,* vol. 102, p. 192903, 2013.

[75] Z. Luo, T. Granzow, J. Glaum, W. Jo, J. Rödel, and M. Hoffman, Effect of Ferroelectric Long-Range Order on the Unipolar and Bipolar Electric Fatigue in $Bi_{1/2}Na_{1/2}TiO_3$-Based Lead-Free Piezoceramics, *Journal of the American Ceramic Society,* vol. 94, pp. 2011.

[76] D. Dragan, Ferroelectric, dielectric and piezoelectric properties of ferroelectric thin films and ceramics, *Reports on Progress in Physics,* vol. 61, p. 1267, 1998.

[77] B. Noheda, D. E. Cox, G. Shirane, R. Guo, B. Jones, and L. E. Cross, Stability of the monoclinic phase in the ferroelectric perovskite$PbZr_{1-x}Ti_xO_3$, *Physical Review B,* vol. 63, 2000.

[78] G. A. I. Smolenskii, V.A.; Agranovskaya, A.I.; Krainik, N.N., New Ferroelectrics of Complex Composition.IV., *Sov. Phys.-Solid State,* vol. 2, 2651-2654., 1961.

[79] K. Roleder, J. Suchanicz, and A. Kania, Time dependence of electric permittivity in $Na_{0.5}Bi_{0.5}TiO_3$ single crystals, *Ferroelectrics,* vol. 89, pp. 1-5, 1989.

[80] J. Suchanicz and W. S. Ptak, On the phase transition in $Na_{0.5}Bi_{0.5}TiO_3$, *Ferroelectrics,* vol. 12, pp. 71-78, 1990.

[81] J. Suchanicz, Investigations of the phase transitions in $Na_{0.5}Bi_{0.5}TiO_3$, *Ferroelectrics,* vol. 172, pp. 455-458, 1995.

[82] J. A. Zvirgzds, P. P. Kapostin, J. V. Zvirgzde, and T. V. Kruzina, X-ray study of phase transitions in efrroelectric $Na_{0.5}Bi_{0.5}TiO_3$, *Ferroelectrics,* vol. 40, pp. 75-77, 1982/05/01 1982.

[83] G. O. Jones and P. A. Thomas, Investigation of the structure and phase transitions in the novel A-site substituted distorted perovskite compound $Na_{0.5}Bi_{0.5}TiO_3$, *Acta Crystallographica.Section.B,* vol. 58, pp. 168-178, 2002.

[84] J. A. Zvirgzds, P. P. Kapostin, J. V. Zvirgzde, and T. V. Kruzina, X-ray study of phase transitions in efrroelectric $Na_{0.5}Bi_{0.5}TiO_3$, *Ferroelectrics,* vol. 40, pp. 75-77, 2011.

[85] S. Gorfman and P. A. Thomas, Evidence for a non-rhombohedral average structure in the lead-free piezoelectric material $Na_{0.5}Bi_{0.5}TiO_3$, *Journal of Applied Crystallography,* vol. 43, pp. 1409-1414, 2010.

[86] E. Aksel, J. S. Forrester, J. L. Jones, P. A. Thomas, K. Page, and M. R. Suchomel, Monoclinic crystal structure of polycrystalline $Na_{0.5}Bi_{0.5}TiO_3$, *Applied Physics Letters,* vol. 98, p. 152901, 2011.

[87] I. Levin and I. M. Reaney, Nano- and Mesoscale Structure of $Na_{1\backslash 2}Bi_{1\backslash 2}TiO_3$: A TEM Perspective, *Advanced Functional Materials,* vol. 22, pp. 3445-3452, 2012.

[88] B. N. Rao and R. Ranjan, Electric-field-driven monoclinic-to-rhombohedral transformation

in $Na_{1/2}Bi_{1/2}TiO_3$, *Physical Review B,* vol. 86, 2012.

[89] D. Schütz, M. Deluca, W. Krauss, A. Feteira, T. Jackson, and K. Reichmann, Lone-Pair-Induced Covalency as the Cause of Temperature- and Field-Induced Instabilities in Bismuth Sodium Titanate, *Advanced Functional Materials,* vol. 22, pp. 2285-2294, 2012.

[90] B. N. Rao, R. Datta, S. S. Chandrashekaran, D. K. Mishra, V. Sathe, A. Senyshyn, and R. Ranjan, Local structural disorder and its influence on the average global structure and polar properties in $Na_{0.5}Bi_{0.5}TiO_3$, *Physical Review B,* vol. 88, 2013.

[91] Y. Hiruma, R. Aoyagi, H. Nagata, and T. Takenaka, Ferroelectric and Piezoelectric Properties of $(Bi_{1/2}K_{1/2})TiO_3$ Ceramics, *Japanese Journal of Applied Physics,* vol. 44, pp. 5040-5044, 2005.

[92] D. Q. Xiao, D. M. Lin, J. G. Zhu, and P. Yu, Studies on new systems of BNT-based lead-free piezoelectric ceramics, *Journal of Electroceramics,* vol. 21, pp. 34-38, 2008.

[93] D. Lin, D. Xiao, J. Zhu, and P. Yu, Piezoelectric and ferroelectric properties of $[Bi_{0.5}(Na_{1-x-y}K_xLi_y)_{0.5}]TiO_3$ lead-free piezoelectric ceramics, *Applied Physics Letters,* vol. 88, p. 062901, 2006.

[94] M. Otoničar, S. D. Škapin, B. Jančar, R. Ubic, and D. Suvorov, Analysis of the Phase Transition and the Domain Structure in K0.5Bi0.5TiO3 Perovskite Ceramics by In Situ XRD and TEM, *Journal of the American Ceramic Society,* vol. 93, pp. 4168-4173, 2010.

[95] E. Aksel and J. L. Jones, Advances in Lead-Free Piezoelectric Materials for Sensors and Actuators, *Sensors,* vol. 10, pp. 1935-1954, Mar 2010.

[96] G. Shirane, H. Danner, A. Pavlovic, and R. Pepinsky, Phase Transitions in Ferroelectric KNbO3, *Physical Review,* vol. 93, pp. 672-673, 1954.

[97] L. Liang, Y. L. Li, L.-Q. Chen, S. Y. Hu, and G.-H. Lu, Thermodynamics and ferroelectric properties of KNbO3, *Journal of Applied Physics,* vol. 106, p. 104118, 2009.

[98] Y. Hiruma, K. Yoshii, H. Nagata, and T. Takenaka, Phase transition temperature and electrical properties of $(Bi_{1/2}Na_{1/2})TiO3$-$(Bi_{1/2}A_{1/2})TiO3$ (A=Li and K) lead-free ferroelectric ceramics, *Journal of Applied Physics,* vol. 103, p. 084121, 2008.

[99] Y.-R. Zhang, J.-F. Li, and B.-P. Zhang, Enhancing Electrical Properties in NBT-KBT Lead-Free Piezoelectric Ceramics by Optimizing Sintering Temperature, *Journal of the American Ceramic Society,* vol. 91, pp. 2716-2719, 2008.

[100] Y. R. Zhang, J. F. Li, and B. P. Zhang, Enhancing electrical properties in NBT-KBT lead-free piezoelectric ceramics by optimizing sintering temperature, *Journal of the American Ceramic Society,* vol. 91, pp. 2716-2719, Aug 2008.

[101] W. Ge, Q. Zhang, Z. Wang, J. Yao, J. Li, H. Luo, and D. Viehland, In-situ X-ray diffraction study of an electric field induced phase transition and giant strain in $Na_{0.5}Bi_{0.5}TiO_3$-x%$BaTiO_3$ lead-free single crystals, *Physica Status Solidi,* vol. 5, pp. 356-358, 2011.

[102] H. Simons, J. E. Daniels, J. Glaum, A. J. Studer, J. L. Jones, and M. Hoffman, Origin of large recoverable strain in $0.94(Bi_{0.5}Na_{0.5})TiO_3$-$0.06BaTiO_3$ near the ferroelectric-relaxor transition, *Applied Physics Letters,* vol. 102, p. 062902, 2013.

[103] C. Luo, W. Ge, Q. Zhang, J. Li, H. Luo, and D. Viehland, Crystallographic direction dependence of direct current field induced strain and phase transitions in $Na_{0.5}Bi_{0.5}TiO_3$-x%$BaTiO_3$ single crystals near the morphotropic phase boundary, *Applied Physics Letters,* vol. 101, p. 141912, 2012.

[104] H. Simons, J. Daniels, W. Jo, R. Dittmer, A. Studer, M. Avdeev, J. Rödel, and M. Hoffman, Electric-field-induced strain mechanisms in lead-free 94%($Bi_{1/2}Na_{1/2}$)TiO_3–6%$BaTiO_3$, *Applied Physics Letters,* vol. 98, p. 082901, 2011.

[105] C. Groh, W. Jo, and J. Rödel, Frequency and temperature dependence of actuating performance of $Bi_{1/2}Na_{1/2}TiO_3$-$BaTiO_3$ based relaxor/ferroelectric composites, *Journal of Applied Physics,* vol. 115, p. 234107, 2014.

[106] W.-S. Kang and J.-H. Koh, (1−x)$Bi_{0.5}Na_{0.5}TiO_3$–x$BaTiO_3$ lead-free piezoelectric ceramics for energy-harvesting applications, *Journal of the European Ceramic Society,* vol. 35, pp. 2057-2064, 2015.

[107] Y. Bai, G.-P. Zheng, and S.-Q. Shi, Abnormal electrocaloric effect of $Na_{0.5}Bi_{0.5}TiO_3$–$BaTiO_3$ lead-free ferroelectric ceramics above room temperature, *Materials Research Bulletin,* vol. 46, pp. 1866-1869, 2011.

[108] G. Yao, X. Wang, Y. Wu, L. Li, and D. C. Lupascu, Nb-Doped 0.9$BaTiO_3$-0.1($Bi_{0.5}Na_{0.5}$)TiO_3 Ceramics with Stable Dielectric Properties at High Temperature, *Journal of the American Ceramic Society,* vol. 95, pp. 614-618, 2012.

[109] J. E. Daniels, W. Jo, J. Rödel, D. Rytz, and W. Donner, Structural origins of relaxor behavior in a 0.96($Bi_{1/2}Na_{1/2}$)TiO_3–0.04$BaTiO_3$ single crystal under electric field, *Applied Physics Letters,* vol. 98, p. 252904, 2011.

[110] M. E. Montero-Cabrera, L. Pardo, A. García, M. E. Fuentes-Montero, M. L. Ballinas-Casarrubias, and L. E. Fuentes-Cobas, The Global and Local Symmetries of Nanostructured Ferroelectric Relaxor 0.94($Bi_{0.5}Na_{0.5}$)TiO_3–0.06$BaTiO_3$, *Ferroelectrics,* vol. 469, pp. 50-60, 2014.

[111] R. Ranjan and A. Dviwedi, Structure and dielectric properties of ($Na_{0.50}Bi_{0.50}$)1−xBa_xTiO_3: 0⩽x⩽0.10, *Solid State Communications,* vol. 135, pp. 394-399, 2005.

[112] M. Chen, Q. Xu, B. H. Kim, B. K. Ahn, J. H. Ko, W. J. Kang, and O. J. Nam, Structure and electrical properties of ($Na_{0.5}Bi_{0.5}$)1−xBaxTiO_3 piezoelectric ceramics, *Journal of the European Ceramic Society,* vol. 28, pp. 843-849, 2008.

[113] S. S. Sundari, B. Kumar, and R. Dhanasekaran, Structural, Dielectric, Piezoelectric and Ferroelectric Characterization of NBT-BT Lead-Free Piezoelectric Ceramics, presented at the IOP Conference Series: Materials Science and Engineering, 2013.

[114] E. Sapper, N. Novak, W. Jo, T. Granzow, and J. Rödel, Electric-field–temperature phase diagram of the ferroelectric relaxor system $(1-x)Bi_{1/2}Na_{1/2}TiO_3 - xBaTiO_3$ doped with manganese, *Journal of Applied Physics,* vol. 115, p. 194104, 2014.

[115] F. Craciun, C. Galassi, and R. Birjega, Electric-field-induced and spontaneous relaxor-ferroelectric phase transitions in $(Na_{1/2}Bi_{1/2})_{1-x}Ba_xTiO_3$, *Journal of Applied Physics,* vol. 112, p. 124106, 2012.

[116] W. Jo and J. Rödel, Electric-field-induced volume change and room temperature phase stability of ($Bi_{1/2}Na_{1/2}$)TiO_3-x mol. % $BaTiO_3$ piezoceramics, *Applied Physics Letters,* vol. 99, p. 042901, 2011.

[117] J. Anthoniappen, C. H. Lin, C. S. Tu, P. Y. Chen, C. S. Chen, S. J. Chiu, H. Y. Lee, S. F. Wang, and C. M. Hung, Enhanced Piezoelectric and Dielectric Responses in 92.5%($Bi_{0.5}Na_{0.5}$) TiO_3 -7.5%$BaTiO_3$ Ceramics, *Journal of the American Ceramic Society,* vol. 97, pp. 1890-1894, 2014.

[118] J. Xijie, W. Baoyin, L. Laihui, L. Weiping, Z. Jun, and C. Hongbing, Electrical properties of (1-x)($Bi_{0.5}Na_{0.5}$)TiO_3-x$KNbO_3$ lead-free ceramics, *Journal of Solid state Chemistry,* vol. 213,

pp. 72-78, 2014.

[119] G. Fan, W. Lu, X. Wang, F. Liang, and J. xiao, Phase transition behaviour and electromechanical properties of $(Na_{1/2}Bi_{1/2})TiO_3$–$KNbO_3$ lead-free piezoelectric ceramics, *Journal of Physics D: Applied Physics,* vol. 41, p. 035403, 2008.

[120] X. Jiang, B. Wang, L. Luo, W. Li, J. Zhou, and H. Chen, Electrical properties of $(1-x)(Bi_{0.5}Na_{0.5})TiO_3$–$xKNbO_3$ lead-free ceramics, *Journal of Solid state Chemistry,* vol. 213, pp. 72-78, 2014.

[121] M. Jiang, X. Liu, and G. Chen, Phase structures and electrical properties of new lead-free $Na_{0.5}K_{0.5}NbO_3$–$LiSbO_3$–$BiFeO_3$ ceramics, *Scripta Materialia,* vol. 60, pp. 909-912, 2009.

[122] L. Luo, B. Wang, X. Jiang, and W. Li, Energy storage properties of $(1 - x)(Bi_{0.5}Na_{0.5})TiO_3$–$xKNbO_3$ lead-free ceramics, *Journal of Materials Science,* vol. 49, pp. 1659-1665, 2014.

[123] N. Pisitpipathsin, W. Koontasing, S. Eitssayeam, U. Intatha, G. Rujijanagul, K. Pengpat, and T. Tunkasiri, Morphotropic Phase Boundary of Lead-Free Piezoelectric Ceramics from BNT-KN System, *Advanced Materials Research,* vol. 55-57, pp. 225-228, 2008.

[124] G. Wang, D. A. Hall, Y. Li, C. A. Murray, and C. C. Tang, Structural characterization of the electric field-induced ferroelectric phase in $Na_{0.5}Bi_{0.5}TiO_3$-$KNbO_3$ ceramics, *Journal of the European Ceramic Society,* vol. 36, pp. 4015-4021, 2016.

[125] G. Fan, W. Lu, X. Wang, and F. Liang, Morphotropic phase boundary and piezoelectric properties of $(Bi_{1/2}Na_{1/2})TiO_3$–$(Bi_{1/2}K_{1/2})TiO_3$–$KNbO_3$ lead-free piezoelectric ceramics, *Applied Physics Letters,* vol. 91, p. 202908, 2007.

[126] Y. Hiruma, H. Nagata, and T. Takenaka, Phase diagrams and electrical properties of $(Bi_{1/2}Na_{1/2})TiO_3$-based solid solutions, *Journal of Applied Physics,* vol. 104, p. 124106, 2008.

[127] Y. Li, W. Chen, J. Zhou, Q. Xu, H. Sun, and R. Xu, Dielectric and piezoelecrtic properties of lead-free $(Na_{0.5}Bi_{0.5})TiO_3$–$NaNbO_3$ ceramics, *Materials Science and Engineering: B,* vol. 112, pp. 5-9, 2004.

[128] Y.-M. Li, W. Chen, J. Zhou, Q. Xu, X.-Y. Gu, and R.-H. Liao, Impedance spectroscopy and dielectric properties of $Na_{0.5}Bi_{0.5}TiO_3$–$NaNbO_3$ ceramics, *Physica B: Condensed Matter,* vol. 365, pp. 76-81, 2005.

[129] C. C. Wu, Y. H. Lin, P. S. Cheng, C. C. Chan, and C. F. Yang, The Influences of NaNbO3 on the Dielectric and Structure Characteristics of (1-X) $(Na_{0.5}Bi_{0.5})TiO_3$–x $NaNbO_3$ Ceramics, *Advanced Materials Research,* vol. 415-417, pp. 1064-1069, 2011.

[130] Q. Xu, T. Li, H. Hao, S. Zhang, Z. Wang, M. Cao, Z. Yao, and H. Liu, Enhanced energy storage properties of NaNbO3 modified $Bi_{0.5}Na_{0.5}TiO_3$ based ceramics, *Journal of the European Ceramic Society,* vol. 35, pp. 545-553, 2015.

[131] Q. Xu, Z. Song, W. Tang, H. Hao, L. Zhang, M. Appiah, M. Cao, Z. Yao, Z. He, H. Liu, and S. Troiler-McKinstry, Ultra-Wide Temperature Stable Dielectrics Based on $Bi_{0.5}Na_{0.5}TiO_3$-$NaNbO_3$ System, *Journal of the American Ceramic Society,* vol. 98, pp. 3119-3126, 2015.

[132] S.-T. Zhang, A. B. Kounga, E. Aulbach, H. Ehrenberg, and J. r. Rödel, Giant strain in lead-free piezoceramics $Bi_{0.5}Na_{0.5}TiO_3$-$BaTiO_3$-$K_{0.5}Na_{0.5}NbO_3$ system, *Applied Physics Letters,* vol. 91, p. 112906, 2007.

[133] S.-T. Zhang, A. B. Kounga, E. Aulbach, W. Jo, T. Granzow, H. Ehrenberg, and J. r. Rödel, Lead-free piezoceramics with giant strain in the system $Bi_{0.5}Na_{0.5}TiO_3$-$BaTiO_3$-$K_{0.5}Na_{0.5}NbO_3$. II. Temperature dependent properties, *Journal of*

Applied Physics, vol. 103, p. 034108, 2008.

[134] J. E. Daniels, W. Jo, J. Rödel, V. Honkimäki, and J. L. Jones, Electric-field-induced phase-change behavior in $(Bi_{0.5}Na_{0.5})TiO_3$–$BaTiO_3$–$(K_{0.5}Na_{0.5})NbO_3$: A combinatorial investigation, *Acta Materialia,* vol. 58, pp. 2103-2111, 2010.

[135] W. Jo, T. Granzow, E. Aulbach, J. Rödel, and D. Damjanovic, Origin of the large strain response in $(K_{0.5}Na_{0.5})NbO_3$-modified $(Bi_{0.5}Na_{0.5})TiO_3$-$BaTiO_3$ lead-free piezoceramics, *Journal of Applied Physics,* vol. 105, p. 094102, 2009.

[136] W. Jo, T. Granzow, E. Aulbach, J. Rodel, and D. Damjanovic, Origin of the large strain response in $(K_{0.5}Na_{0.5})NbO_3$-modified $(Bi_{0.5}Na_{0.5})TiO_3$-$BaTiO_3$ lead-free piezoceramics, *Journal of Applied Physics,* vol. 105, May 2009.

[137] F. Gao, X. Dong, C. Mao, F. Cao, G. Wang, and S. T. Zhang, c/a Ratio-Dependent Energy-Storage Density in $(0.9-x)Bi_{0.5}Na_{0.5}TiO_3$-$xBaTiO_3$-$0.1K_{0.5}Na_{0.5}NbO_3$ Ceramics, *Journal of the American Ceramic Society,* vol. 94, pp. 4162-4164, 2011.

[138] H. Ni, L. Luo, W. Li, Y. Zhu, and H. Luo, Preparation and electrical properties of $Bi_{0.5}Na_{0.5}TiO_3$–$BaTiO_3$–$KNbO_3$ lead-free piezoelectric ceramics, *Journal of Alloys and Compounds,* vol. 509, pp. 3958-3962, 2011.

[139] J. Li, F. Wang, X. Qin, M. Xu, and W. Shi, Large electrostrictive strain in lead-free $Bi_{0.5}Na_{0.5}TiO_3$–$BaTiO_3$–$KNbO_3$ ceramics, *Applied Physics A,* vol. 104, pp. 117-122, 2010.

[140] H. M. Ni, L. H. Luo, W. P. Li, Y. J. Zhu, and H. S. Luo, Preparation and electrical properties of $Bi_{0.5}Na_{0.5}TiO_3$-$BaTiO_3$-$KNbO_3$ lead-free piezoelectric ceramics, *Journal of Alloys and Compounds,* vol. 509, pp. 3958-3962, Mar 2011.

[141] J. Rödel, K. G. Webber, R. Dittmer, W. Jo, M. Kimura, and D. Damjanovic, Transferring lead-free piezoelectric ceramics into application, *Journal of the European Ceramic Society,* vol. 35, pp. 1659-1681, 2015.

[142] W. Jo, R. Dittmer, M. Acosta, J. Zang, C. Groh, E. Sapper, K. Wang, and J. Rödel, Giant electric-field-induced strains in lead-free ceramics for actuator applications – status and perspective, *Journal of Electroceramics,* vol. 29, pp. 71-93, 2012.

[143] B. Culity, *Elements of X-ray Diffraction*: Addison-Wesley 1978.

[144] W. D. Callister, Materials science and engineering: an introduction, Wiley 2003.

[145] B. D. Cullity and J. W. Weymouth, Elements of X-ray Diffraction, *American Journal of Physics,* vol. 25, pp. 394-395, 1957.

[146] D. Lin, K. W. Kwok, and H. L. W. Chan, Structure and electrical properties of $Bi_{0.5}Na_{0.5}TiO_3$–$BaTiO_3$–$Bi_{0.5}Li_{0.5}TiO_3$ lead-free piezoelectric ceramics, *Solid State Ionics,* vol. 178, pp. 1930-1937, 2008.

[147] A 10-year vision for diamond light source, *Diamond Light Source Ltd,* 2015.

[148] Paul Adamson, Alistair Lennie, Claire Murray, Julia Parker, Jonathan Potter, Chiu Tang, S. T. and, and F. Yuan, Beamline I11 User Manual, 2015.

[149] Piezoelectric properties of ceramic materials and components - Part 1: Definitions and classifications, EN 50324-1:2002 (British Standards Institution, London, 2002).

[150] L. Rayleigh, " XXXI. Investigations in optics, with special reference to the spectroscope," *London, Edinburgh, Dublin Philosophical Magazine,* vol. 8, pp. 261-274, 1879.

[151] I. W. H. R. W. Kelsall, M. Geoghegan, and J. Wiley, *Nanoscale science and technology*: Wiley, 2005.

[152] B. F. Kourosh Kalantar-zadeh, *Nanotechnology-Enabled Sensor: Springer 1 edition,* October 31, 2007.

[153] H. Abrams, Grain size measurement by the intercept method, *Metallography,* vol. 4, pp. 59-78, 1971.

[154] M. I. Mendelson, Average Grain Size in Polycrystalline Ceramics, *Journal of the American Ceramic Society,* vol. 52, pp. 443-446, 1969.

[155] M. Stewart, M. G. C. and, and D. A. Hall, Ferroelectric Hysteresis Measurement & Analysis, 1999.

[156] S. P. Thompson, J. E. Parker, J. Potter, T. P. Hill, A. Birt, T. M. Cobb, F. Yuan, and C. C. Tang, Beamline I11 at Diamond: A new instrument for high resolution powder diffraction, *Review of Scientific Instruments,* vol. 80, p. 075107, 2009.

[157] R. Garg, B. N. Rao, A. Senyshyn, P. S. R. Krishna, and R. Ranjan, Lead-free piezoelectric system $(Na_{0.5}Bi_{0.5})TiO_3$-$BaTiO_3$: Equilibrium structures and irreversible structural transformations driven by electric field and mechanical impact, *Physical Review B,* vol. 88, 2013.

[158] Diffrac plus TOPAS v. 3.0 (Manual), Karlsruhe2006.

[159] J. E. Daniels, Determination of directionally dependent structural and microstructural information using high-energy X-ray diffraction, *Journal of Applied Crystallography,* vol. 41, pp. 1109-1114, 2008.

[160] A. P. Hammersley, S. O. Svensson, M. Hanfland, A. N. Fitch, and D. Hausermann, *High Pressure Res.,* vol. 14, 1996.

[161] A. A. Coelho and R. W. Cheary. (1996). *Xfit*. Available: http://www.ccp14.ac.uk/

[162] S. Sayyed, S. A. Acharya, P. Kautkar, and V. Sathe, Structural and dielectric anomalies near the MPB region of $Na_{0.5}Bi_{0.5}TiO_3$-$SrTiO_3$ solid solution, *RSC Advances,* vol. 5, pp. 50644-50654, 2015.

[163] A. Hussain, A. Maqbool, R. A. Malik, M. H. Kim, T. K. Song, and W. J. Kim, Structural and electromechanical properties of $Na_{0.5}Bi_{0.5}TiO_3$ ceramics produced by different synthesis routes, presented at the IOP Conference Series: Materials Science and Engineering, 2016.

[164] T. A. Skidmore, T. Stevenson, T. P. Comyn, and S. J. Milne, phase Development during Mixed-Oxide Processing of a $[Na_{0.5}K_{0.5}NbO_3]_{1-x}$-$[LiTaO_3]_x$ powder, *Key Engineering Materials,* vol. 368-372, pp. 1886-1889, 2008.

[165] Y. Zhen and J. F. Li, Normal Sintering of (K,Na)NbO_3 - Based Ceramics: Influence of Sintering Temperature on Densification, Microstructure, and Electrical Properties, *Journal of the American Ceramic Society,* vol. 89, pp. 3669-3675, 2006.

[166] K. Parmar and N. S. Negi, Tailoring structural and electrical properties of A-site non-stoichiometric $Na_{0.5}Bi_{0.5}TiO_3$ ceramic at different sintering temperature, *Advances in Applied Ceramics,* pp. 1-10, 2016.

[167] S. Swain, Synthesize and Characterizations of SrBi2Ta2O9 Modified NBT-BT and NBT-KNN Ferroelectric Ceramics near Morphotropic Phase Boundary, PhD Thesis, National Institute of Technology Rourkela, 2015.

[168] J. Zhao, M. Cao, Z. Wang, Q. Xu, L. Zhang, Z. Yao, H. Hao, and H. Liu, Enhancement of energy-storage properties of $K_{0.5}Na_{0.5}NbO_3$ modified $Na_{0.5}Bi_{0.5}TiO_3$–$K_{0.5}Bi_{0.5}TiO_3$ lead-free ceramics, *Journal of Materials Science: Materials in Electronics,* vol. 27, pp. 466-473, 2016.

[169] H. Wang, R. Zuo, Y. Liu, and J. Fu, Densification behavior, microstructure, and electrical properties of sol–gel-derived niobium-doped (Bi0.5Na0.5)0.94Ba0.06TiO3 ceramics,

Journal of Materials Science, vol. 45, pp. 3677-3682, 2010.

[170] G. Viola, R. Mkinnon, V. Koval, A. Adomkevicius, S. Dunn, and H. Yan, Lithium-Induced Phase Transitions in Lead-Free $Bi_{0.5}Na_{0.5}TiO_3$Based Ceramics, *The Journal of Physical Chemistry C,* vol. 118, pp. 8564-8570, 2014.

[171] Y. Ehara, N. Novak, S. Yasui, M. Itoh, and K. G. Webber, Electric-field-temperature phase diagram of Mn-doped $Bi_{0.5}(Na_{0.9}K_{0.1})_{0.5}TiO_3$ ceramics, *Applied Physics Letters,* vol. 107, p. 262903, 2015.

[172] W. P. Cao, W. L. Li, Y. Feng, D. Xu, W. Wang, Y. F. Hou, T. D. Zhang, and W. D. Fei, Enhanced depolarization temperature in 0.90NBT–0.05KBT–0.05BT ceramics induced by BT nanowires, *Journal of Physics and Chemistry of Solids,* vol. 78, pp. 41-45, 2015.

[173] J. Zhang, Z. Pan, F.-F. Guo, W.-C. Liu, H. Ning, Y. B. Chen, M.-H. Lu, B. Yang, J. Chen, S.-T. Zhang, X. Xing, J. Rödel, W. Cao, and Y.-F. Chen, Semiconductor/relaxor 0–3 type composites without thermal depolarization in $Bi_{0.5}Na_{0.5}TiO_3$-based lead-free piezoceramics, *Nature Communications,* vol. 6, p. 6615, 2015.

[174] K. H. Härdtl, Electrical and mechanical losses in ferroelectric ceramics, *Ceramics International,* vol. 8, pp. 121-127, 1982.

[175] G. Borchhardt, J. von Cieminski, and G. Schmidt, Aging of Strontium Barium Niobate and PLZT ceramic, *Physica Status Solidi (a),* vol. 59, pp. 749-754, 1980.

[176] T. R. Shrout, W. Huebner, C. A. Randall, and A. D. Hilton, Aging mechanisms in $Pb(Mg_{1/3}Nb_{2/3})O_3$-based relaxor ferroelectrics, *Ferroelectrics,* vol. 93, pp. 361-372, 1989/05/01 1989.

[177] W. A. Schulze, J. V. Biggers, and L. E. Cross, Aging of Dielectric Dispersion in PLZT Relaxor Ceramics, *Journal of the American Ceramic Society,* vol. 61, pp. 46-49, 1978.

[178] E. Sapper, R. Dittmer, D. Damjanovic, E. Erdem, D. J. Keeble, W. Jo, T. Granzow, and J. Rödel, Aging in the relaxor and ferroelectric state of Fe-doped $(1-x)(Bi_{1/2}Na_{1/2})TiO_3$-$xBaTiO_3$ piezoelectric ceramics, *Journal of Applied Physics,* vol. 116, p. 104102, 2014.

[179] Q. Yao, F. Wang, F. Xu, C. M. Leung, T. Wang, Y. Tang, X. Ye, Y. Xie, D. Sun, and W. Shi, Electric Field-Induced Giant Strain and Photoluminescence-Enhancement Effect in Rare-Earth Modified Lead-Free Piezoelectric Ceramics, *ACS Applied Materials & Interfaces,* vol. 7, pp. 5066-5075, 2015.

[180] F. Wang, M. Xu, Y. Tang, T. Wang, W. Shi, and C. M. Leung, Large Strain Response in the Ternary $Bi_{0.5}Na_{0.5}TiO_3$–$BaTiO_3$–$SrTiO_3$ Solid Solutions, *Journal of the American Ceramic Society,* vol. 95, pp. 1955-1959, 2012.

[181] E. Sapper, S. Schaab, W. Jo, T. Granzow, and J. Rödel, Influence of electric fields on the depolarization temperature of Mn-doped $(1-x)Bi_{1/2}Na_{1/2}TiO_3$-$xBaTiO_3$, *Journal of Applied Physics,* vol. 111, p. 014105, 2012.

[182] R. Garg, B. Narayana Rao, A. Senyshyn, and R. Ranjan, Long ranged structural modulation in the pre-morphotropic phase boundary cubic-like state of the lead-free piezoelectric $Na_{1/2}Bi_{1/2}TiO_3$-x%$BaTiO_3$, *Journal of Applied Physics,* vol. 114, p. 234102, 2013.

[183] R. D. Shannon, Revised Effective Ionic Radii and Systematic Studies of Interatomic Distances in Halides and Chapcogenides, *Acta Crystollographica Section A,* vol. A32, p. 751, 1976.

[184] H. D. Megaw and C. N. W. Darlington, Geometrical and structural relations in the

rhombohedral perovskites, *Acta Crystallogr. Sec. A,* vol. 31, pp. 161-173, 1975.

[185] J. L. Jones, E. B. Slamovich, and K. J. Bowman, Domain texture distributions in tetragonal lead zirconate titanate by x-ray and neutron diffraction, *Journal of Applied Physics,* vol. 97, p. 034113, 2005.

[186] D. A. Hall, A. Steuwer, B. Cherdhirunkorn, T. Mori, and P. J. Withers, Analysis of elastic strain and crystallographic texture in poled rhombohedral PZT ceramics, *Acta Materialia,* vol. 54, pp. 3075-3083, 2006.

[187] L. Daniel, D. A. Hall, J. Koruza, K. G. Webber, A. King, and P. J. Withers, Revisiting the blocking force test on ferroelectric ceramics using high energy x-ray diffraction, *Journal of Applied Physics,* vol. 117, p. 174104, 2015.

[188] D. A. Hall, A. Steuwer, B. Cherdhirunkorn, T. Mori, and P. J. Withers, A high energy synchrotron x-ray study of crystallographic texture and lattice strain in soft lead zirconate titanate ceramics, *Journal of Applied Physics,* vol. 96, p. 4245, 2004.

[189] A. J. Royles, A. J. Bell, J. E. Daniels, S. J. Milne, and T. P. Comyn, Observation of a time-dependent structural phase transition in potassium sodium bismuth titanate, *Applied Physics Letters,* vol. 98, p. 182904, 2011.

[190] V. Pal, R. K. Dwivedi, and O. P. Thakur, Dielectric and Ferroelectric Properties of Lead-Free Ceramic System, *Advances in Materials Science and Engineering,* vol. 2013, p. 7, 2013.

[191] B.-J. Chu, D.-R. Chen, G.-R. Li, and Q.-R. Yin, Electrical properties of $Na_{1/2}Bi_{1/2}TiO_3$–$BaTiO_3$ ceramics, *Journal of the European Ceramic Society,* vol. 22, pp. 2115-2121, 2002.

[192] K. Wang, A. Hussain, W. Jo, J. Rödel, and D. D. Viehland, Temperature-Dependent Properties of $(Bi_{1/2}Na_{1/2})TiO_3$-$(Bi_{1/2}K_{1/2})TiO_3$-$SrTiO_3$ Lead-Free Piezoceramics, *Journal of the American Ceramic Society,* vol. 95, pp. 2241-2247, 2012.

[193] I. Levin, I. M. Reaney, E. M. Anton, W. Jo, J. Rödel, J. Pokorny, L. A. Schmitt, H. J. Kleebe, M. Hinterstein, and J. L. Jones, Local structure, pseudosymmetry, and phase transitions in $Na_{1/2}Bi_{1/2}TiO_3$–$K_{1/2}Bi_{1/2}TiO_3$ ceramics, *Physical Review B,* vol. 87, 2013.

[194] F. H. Schader, Z. Wang, M. Hinterstein, J. E. Daniels, and K. G. Webber, Stress-modulated relaxor-to-ferroelectric transition in lead-free $(Na_{1/2}Bi_{1/2})TiO_3$–$BaTiO_3$ ferroelectrics, *Physical Review B,* vol. 93, 2016.

11 Appendix

11.1 Full pattern refinement profiles

11.1.1 Poled NBT-0.01KN

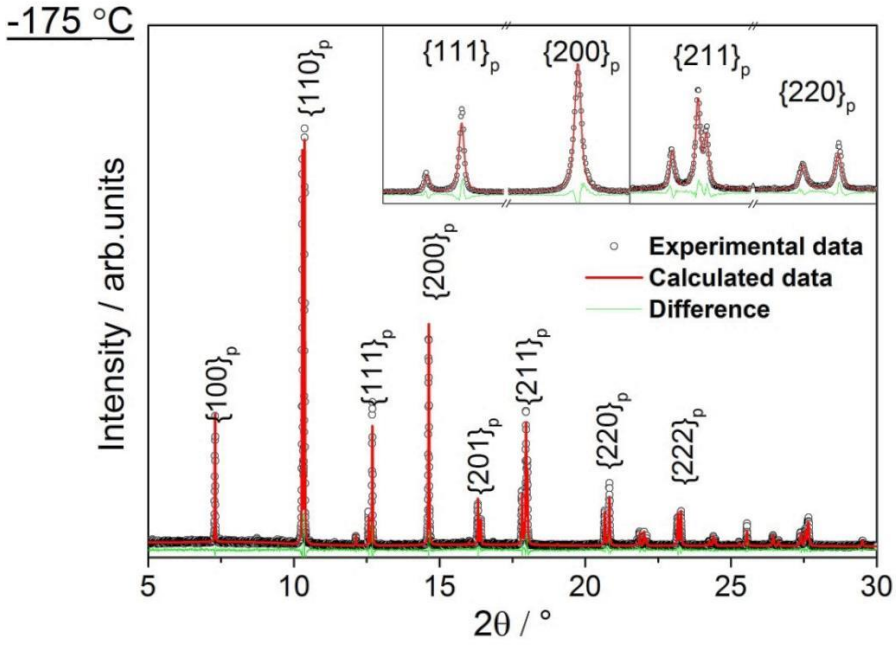

Figure 11.1 The SXPD full patterns refinement for poled NBT-0.01KN powder at -175 ºC.

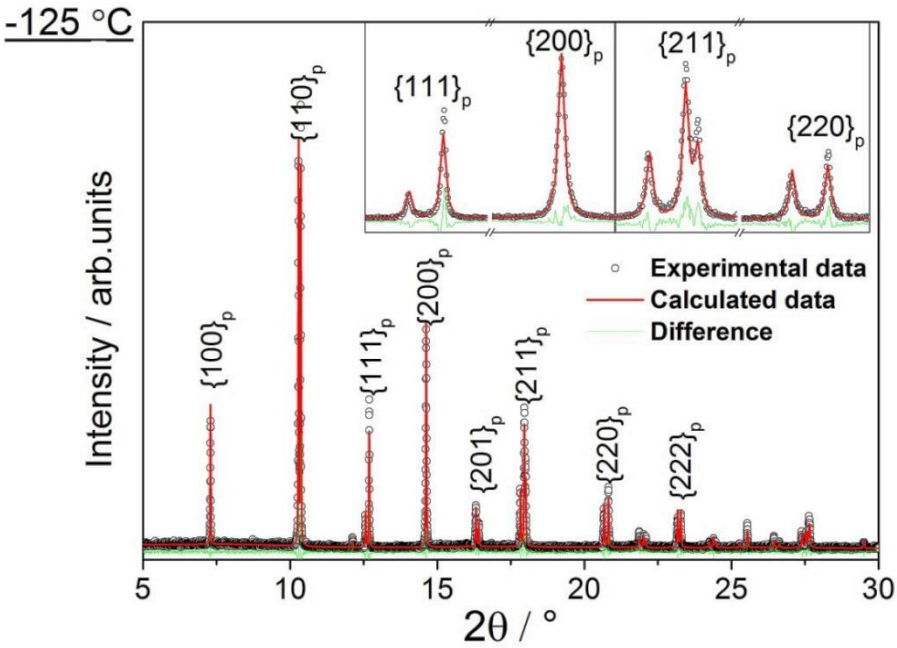

Figure 11.2 The SXPD full patterns refinement for poled NBT-0.01KN powder at -125 ºC.

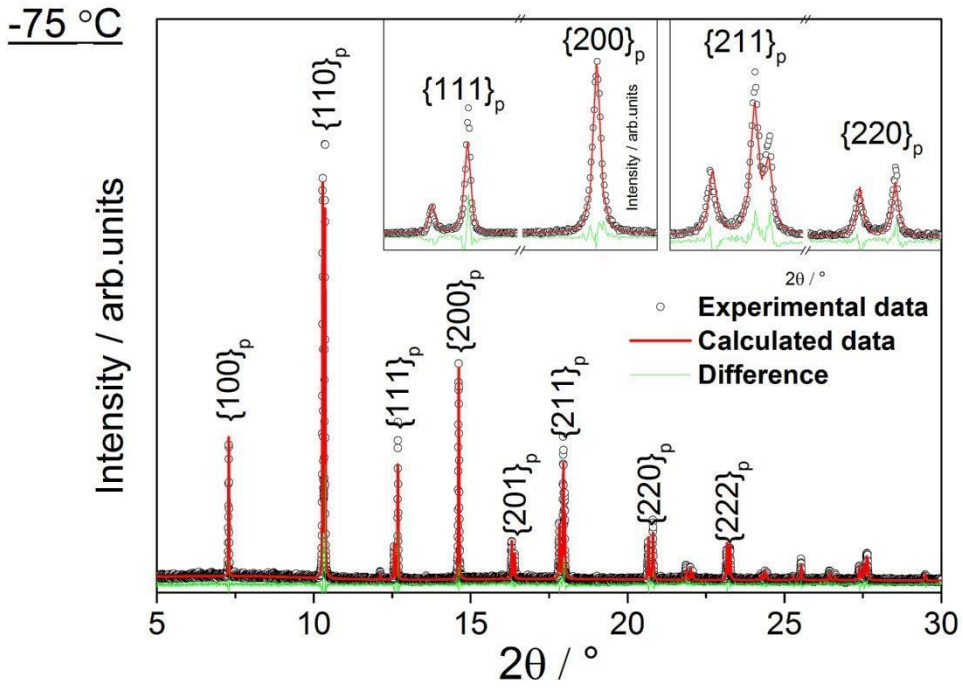

Figure 11.3 The SXPD full patterns refinement for poled NBT-0.01KN powder at -75 ºC.

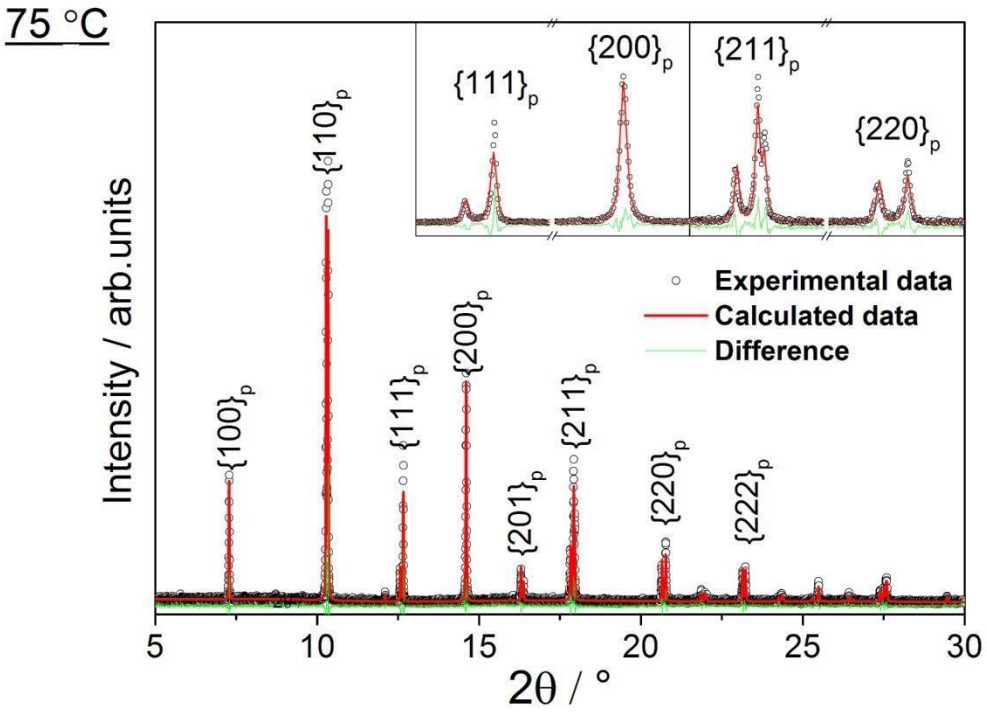

Figure 11.4 The SXPD full patterns refinement for poled NBT-0.01KN powder at 75 ºC.

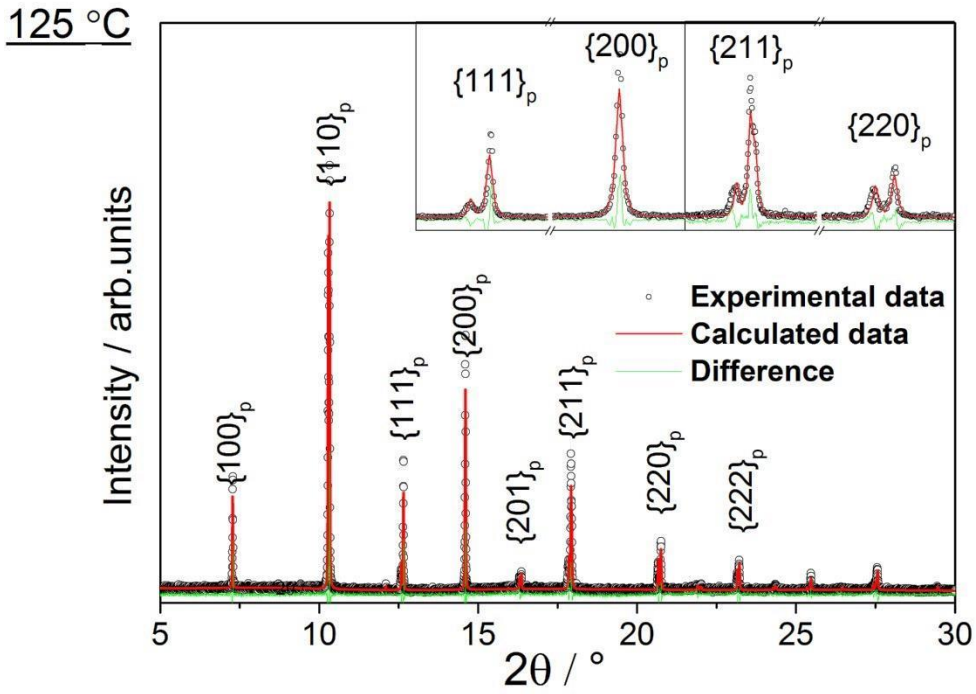

Figure 11.5 The SXPD full patterns refinement for poled NBT-0.01KN powder at 125 ºC.

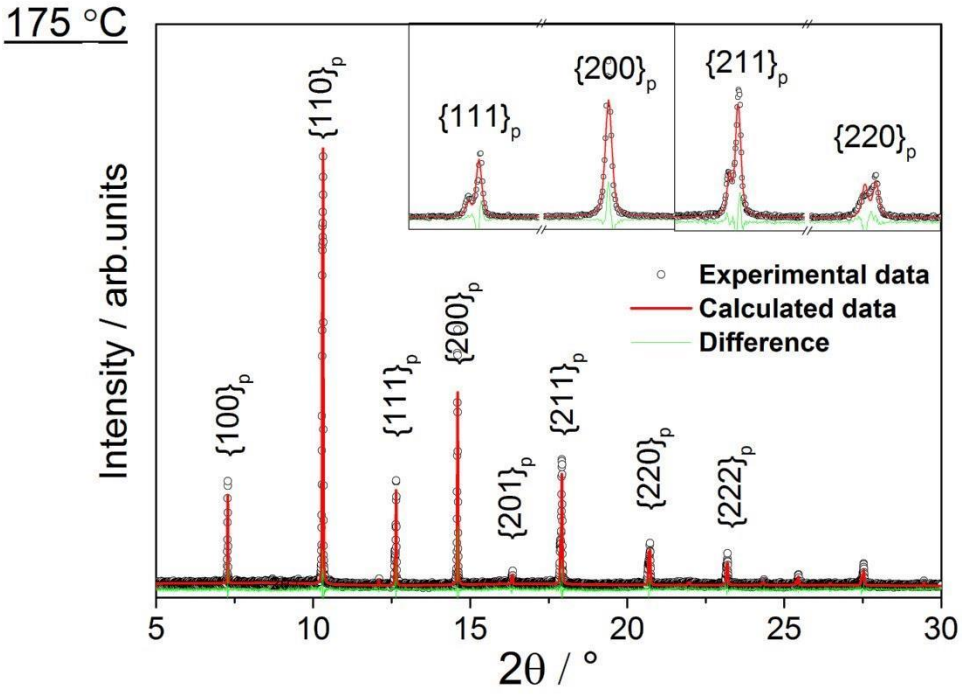

Figure 11.6 The SXPD full patterns refinement for poled NBT-0.01KN powder at 175 ºC.

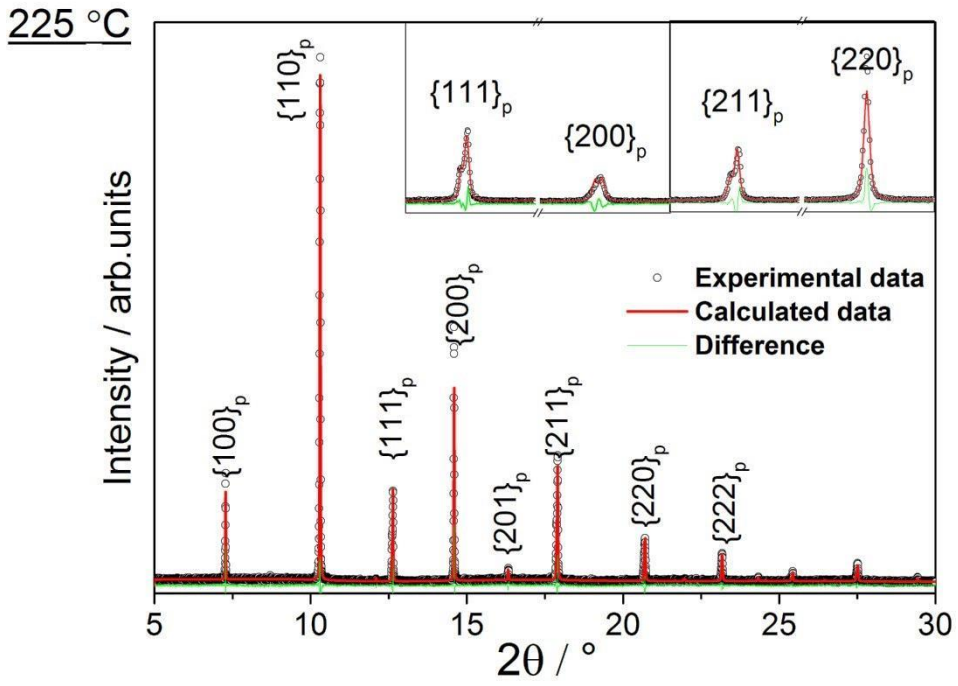

Figure 11.7 The SXPD full patterns refinement for poled NBT-0.01KN powder at 225 ºC.

11.1.2 Unpoled NBT-0.01KN

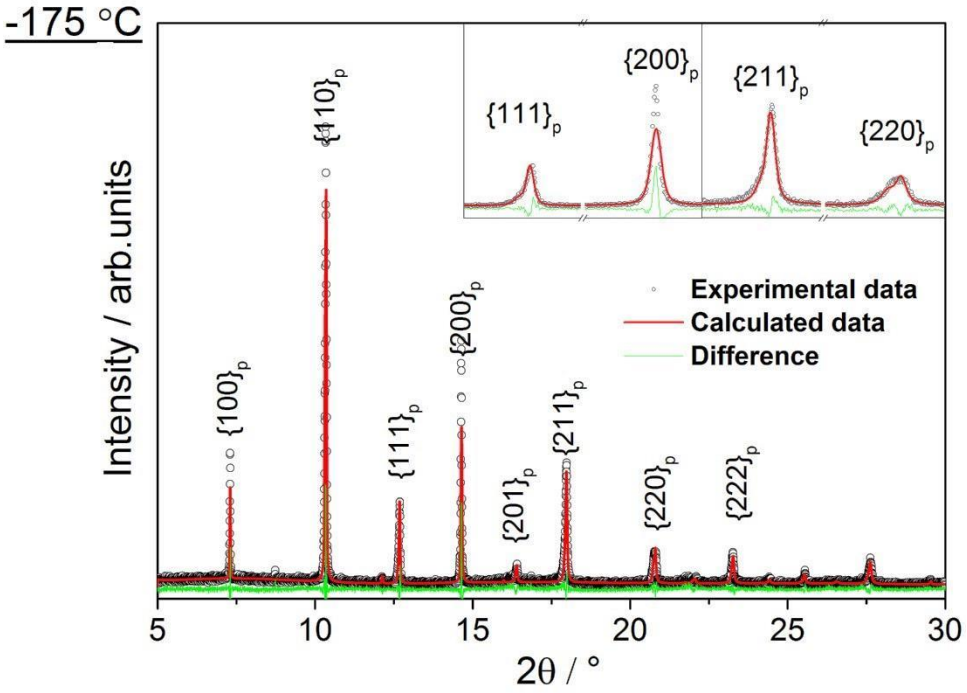

Figure 11.8 The SXPD full patterns refinement for unpoled NBT-0.01KN powder at -175 ºC.

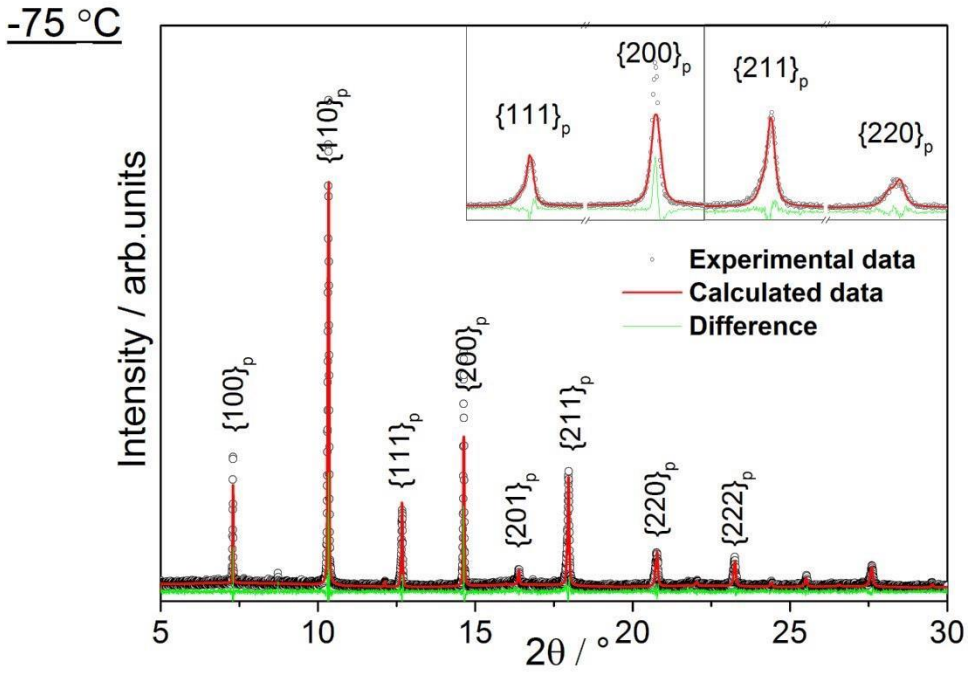

Figure 11.9 The SXPD full patterns refinement for unpoled NBT-0.01KN powder at -75 ºC.

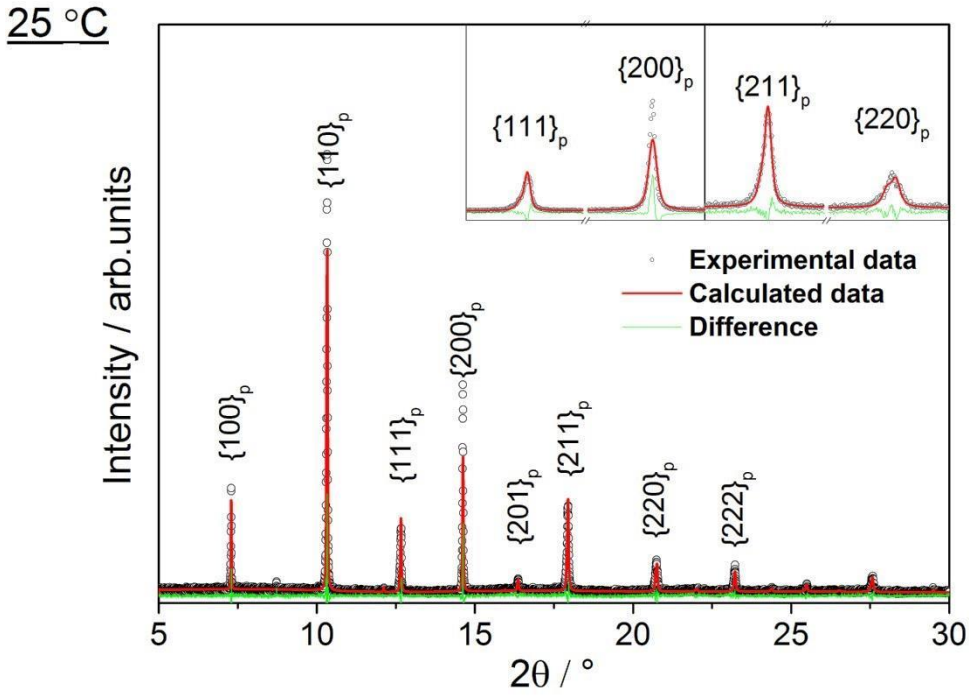

Figure 11.10 The SXPD full patterns refinement for unpoled NBT-0.01KN powder at 25 ºC.

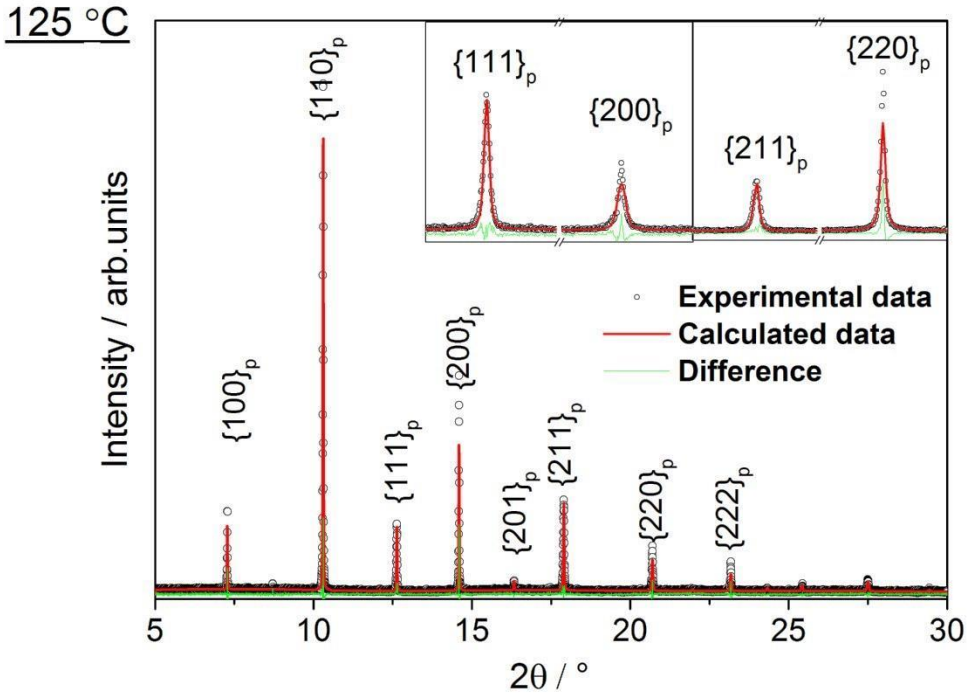

Figure 11.11 The SXPD full patterns refinement for unpoled NBT-0.01KN powder at 125 ºC.

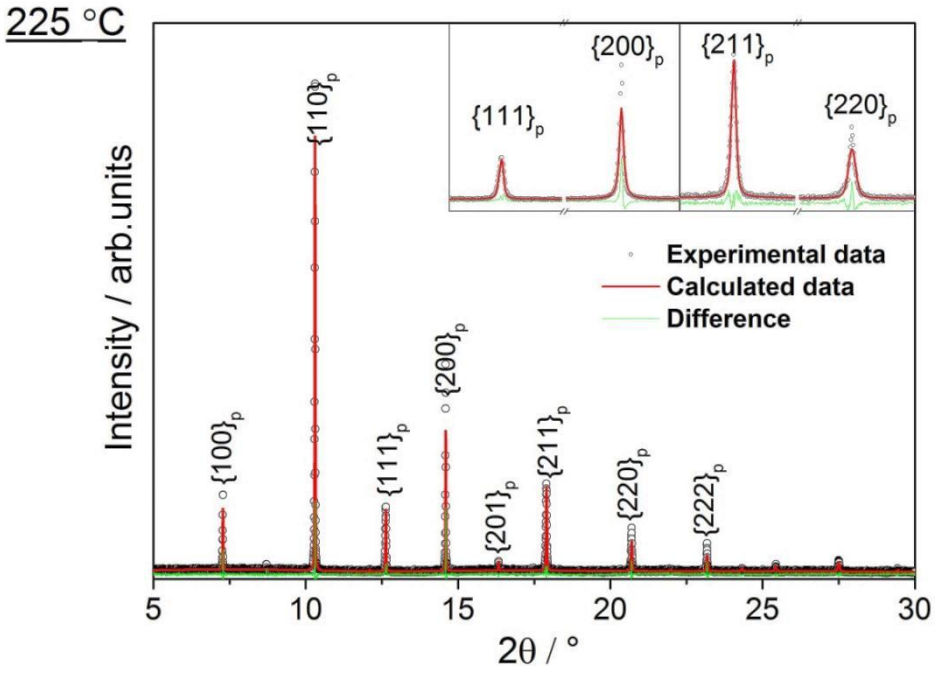

Figure 11.12 The SXPD full patterns refinement for unpoled NBT-0.01KN powder at 225 ºC.

11.1.3 Poled NBT-0.03KN

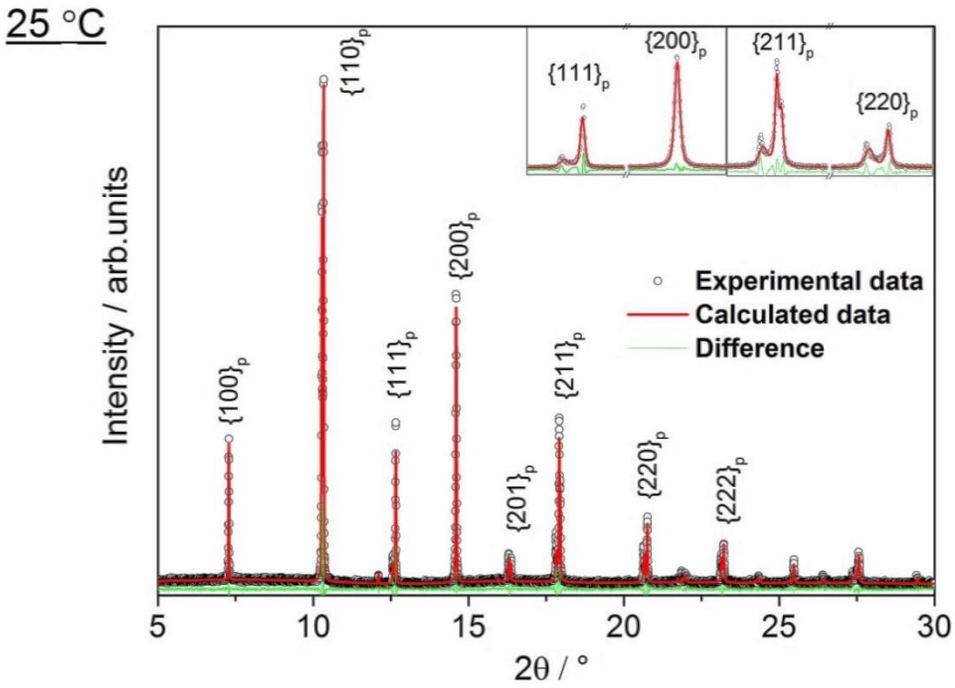

Figure 11.13 The SXPD full patterns refinement for poled NBT-0.03KN powder at 25 ºC.

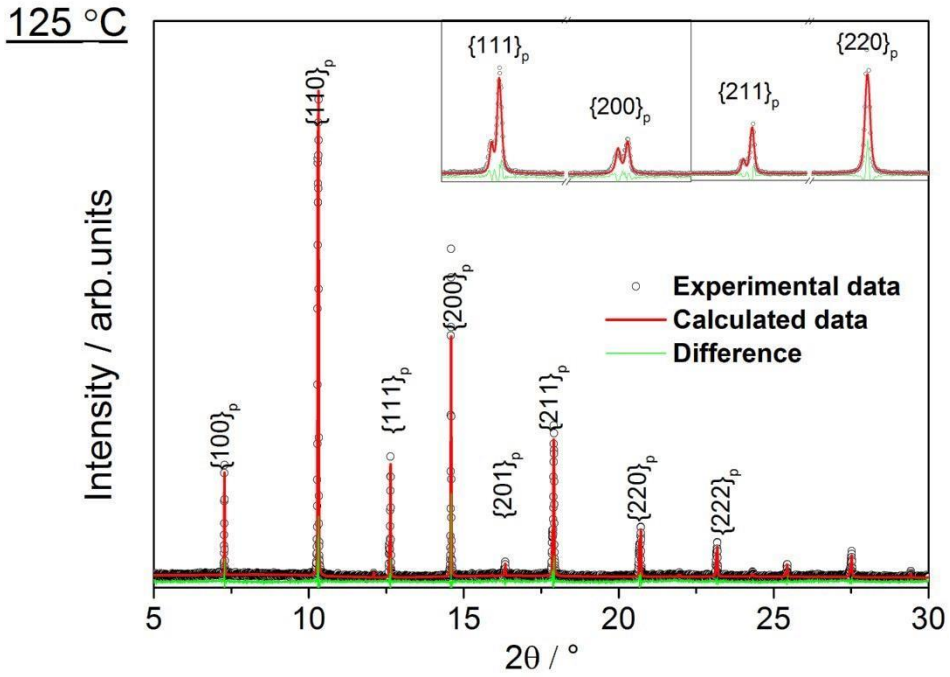

Figure 11.14 The SXPD full patterns refinement for poled NBT-0.03KN powder at 125 ºC.

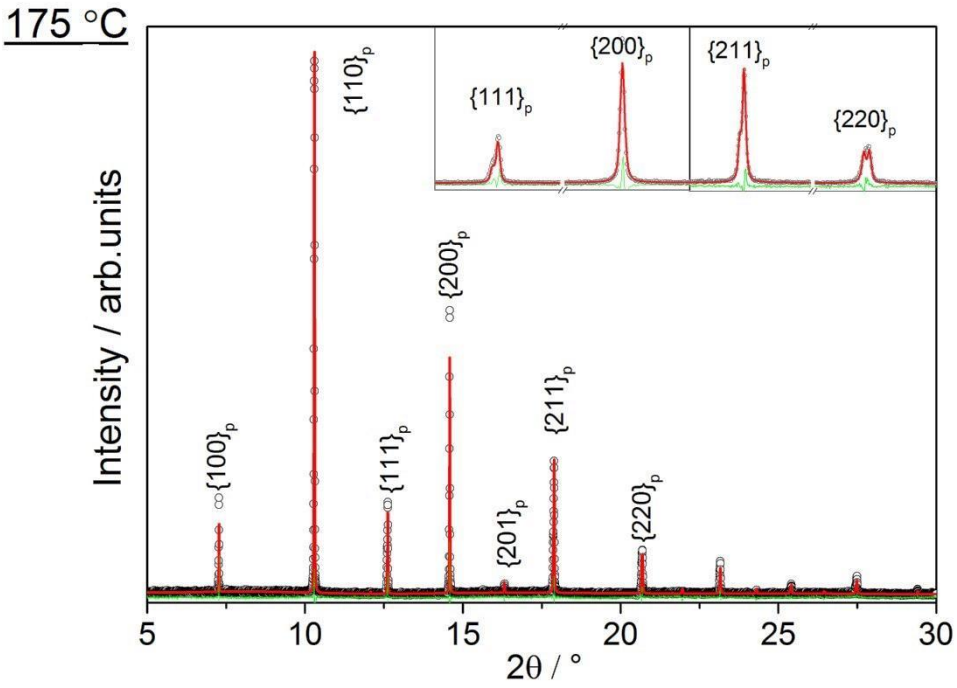

Figure 11.15 The SXPD full patterns refinement for poled NBT-0.03KN powder at 175 ºC.

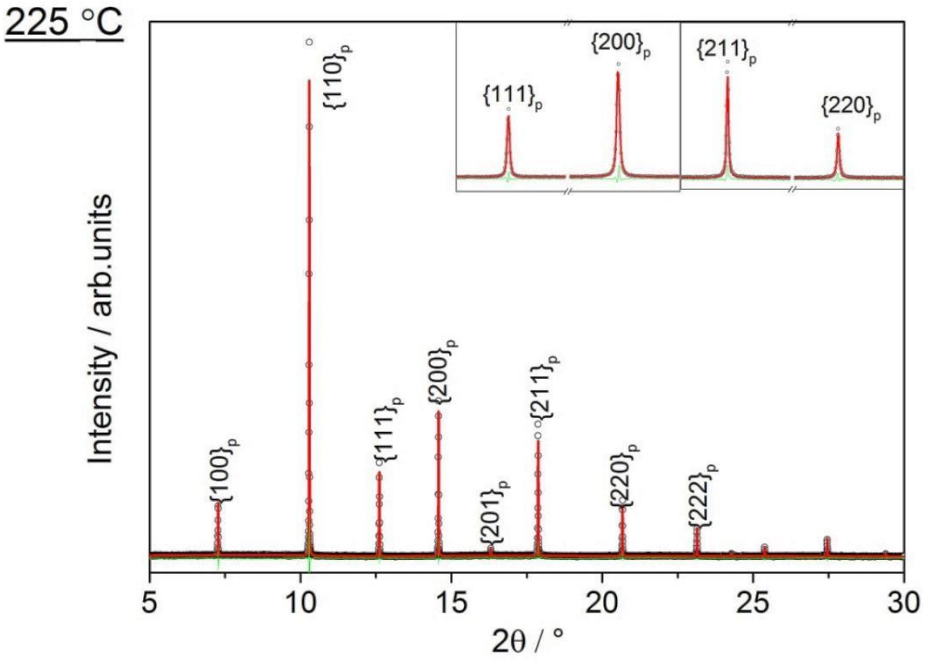

Figure 11.16 The SXPD full patterns refinement for poled NBT-0.03KN powder at 225 ºC.

11.1.4 Poled NBT-0.05KN

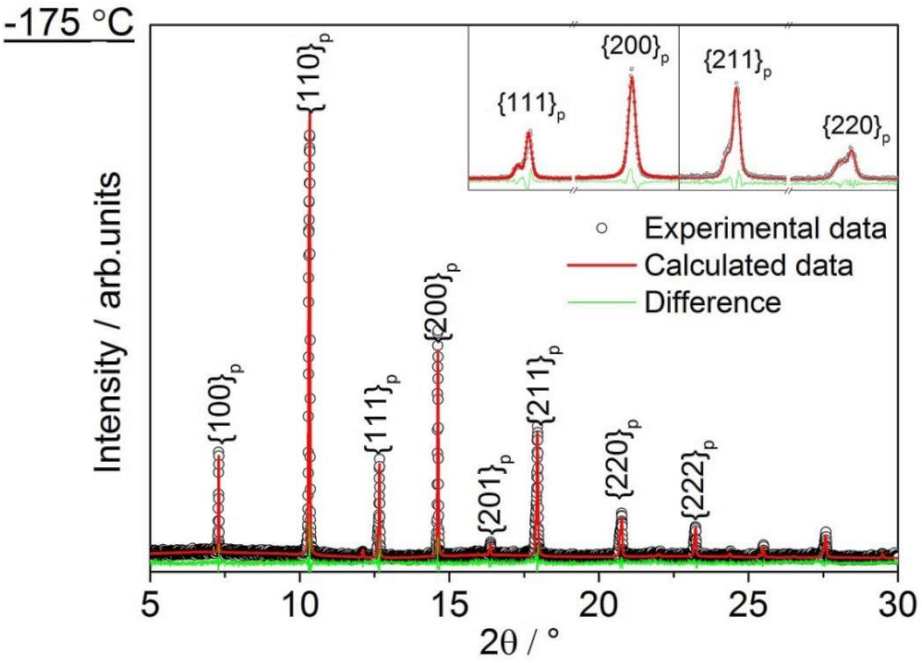

Figure 11.17 The SXPD full patterns refinement for poled NBT-0.05KN powder at -175 ºC.

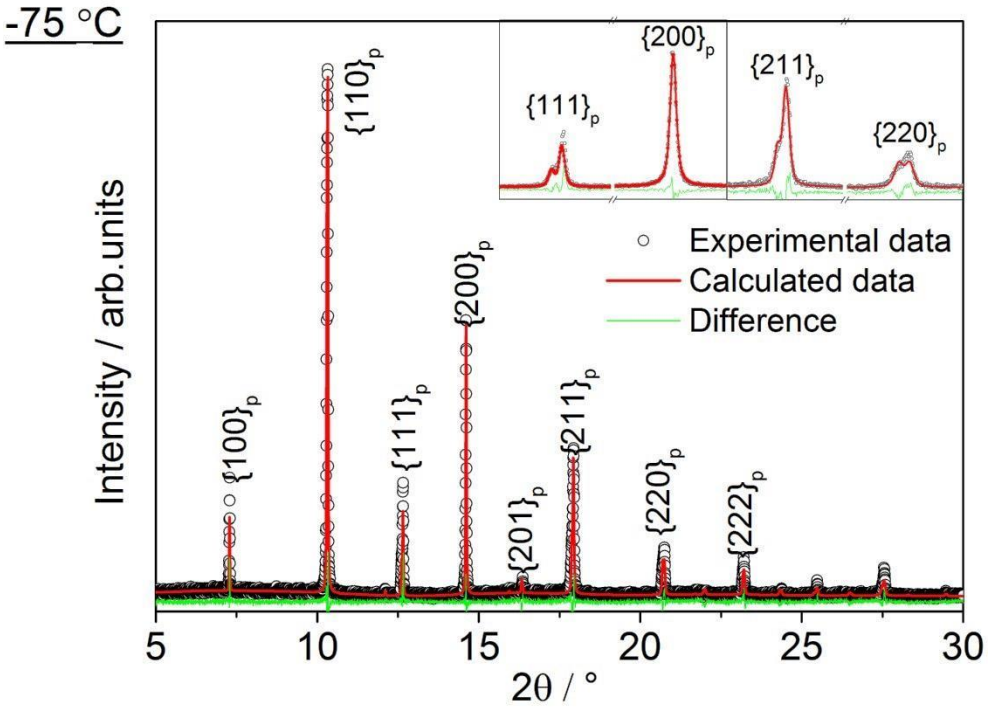

Figure 11.18 The SXPD full patterns refinement for poled NBT-0.05KN powder at -75 ºC.

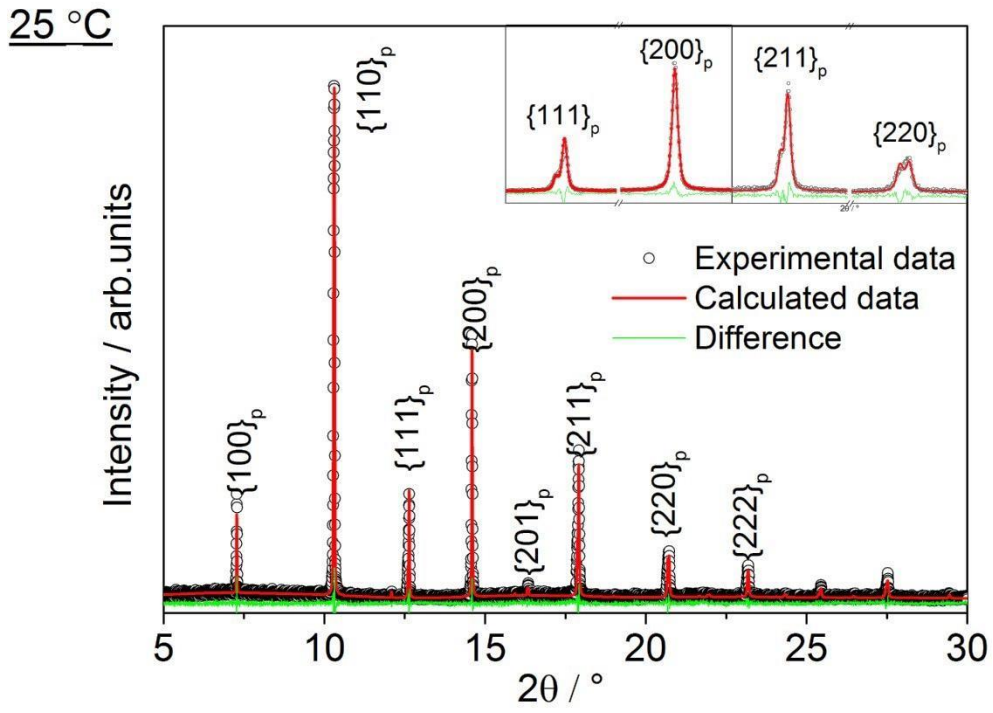

Figure 11.19 The SXPD full patterns refinement for poled NBT-0.05KN powder at 25 ºC.

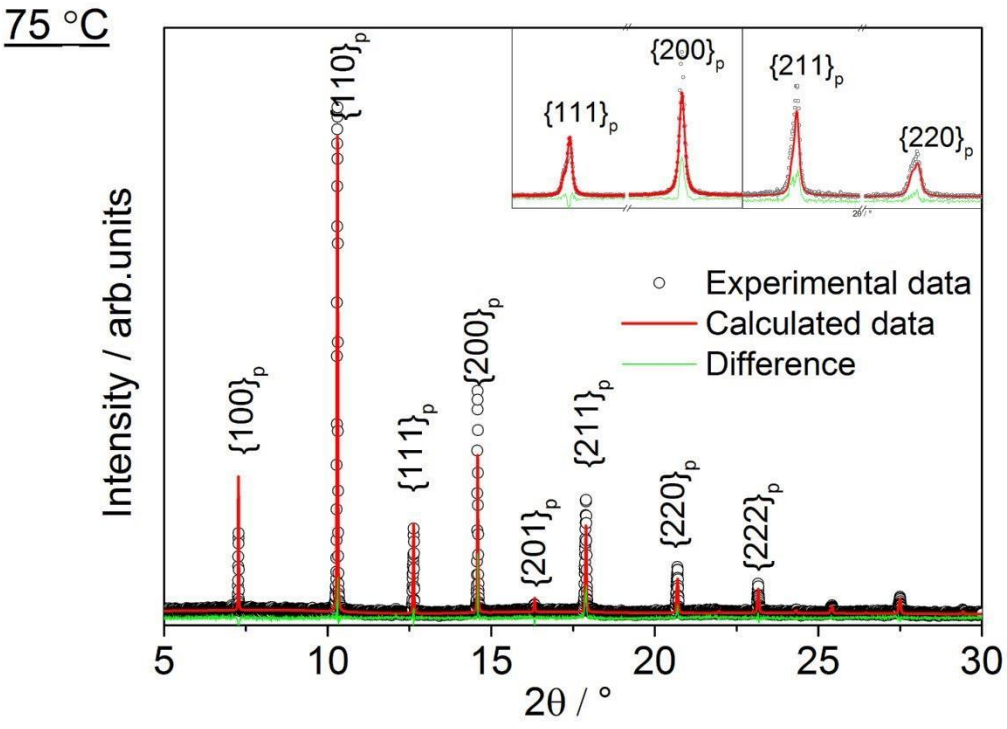

Figure 11.20 The SXPD full patterns refinement for poled NBT-0.05KN powder at 75 ºC.

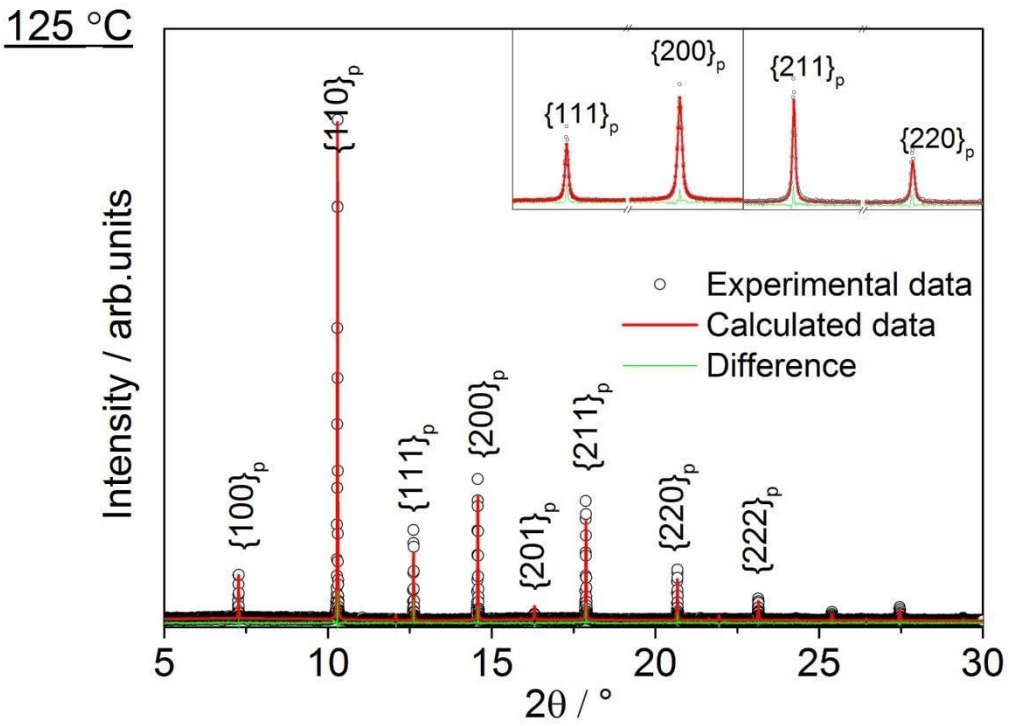

Figure 11.21 The SXPD full patterns refinement for poled NBT-0.05KN powder at 130 ºC.

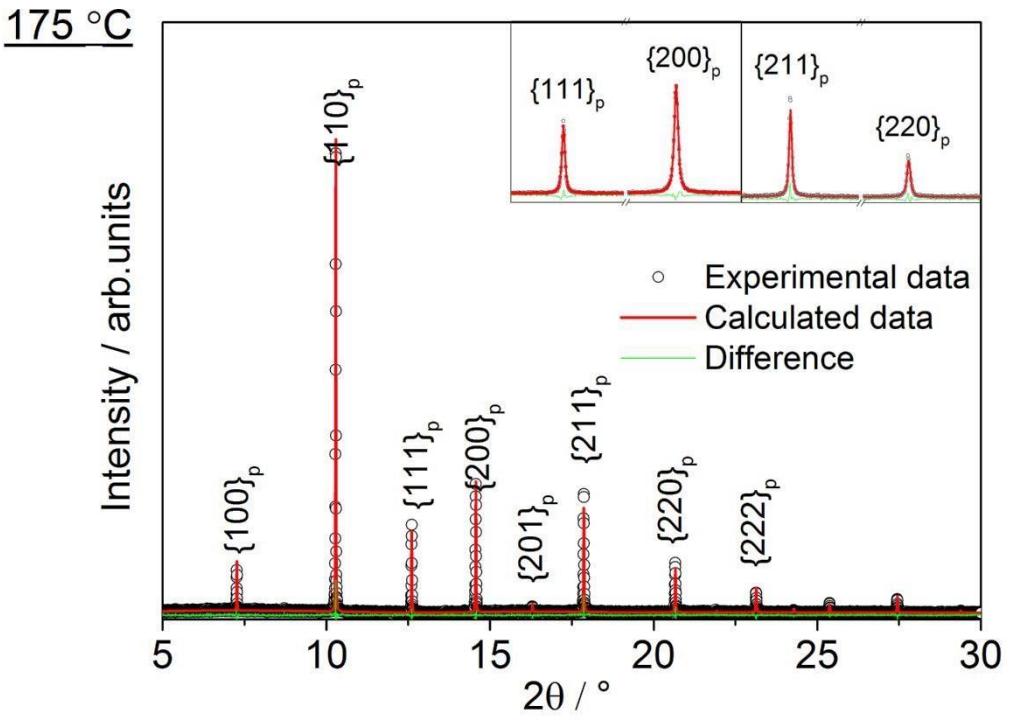

Figure 11.22 The SXPD full patterns refinement for poled NBT-0.05KN powder at 175 ºC.

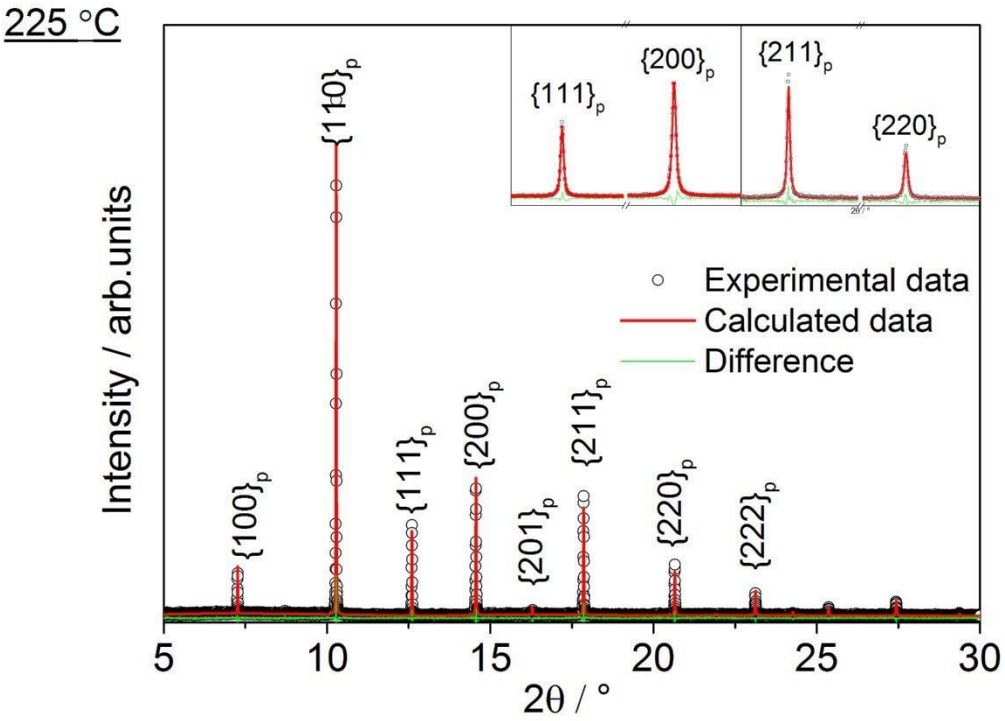

Figure 11.23 The SXPD full patterns refinement for poled NBT-0.05KN powder at 225 ºC.

11.1.5 Poled NBT-0.09KN

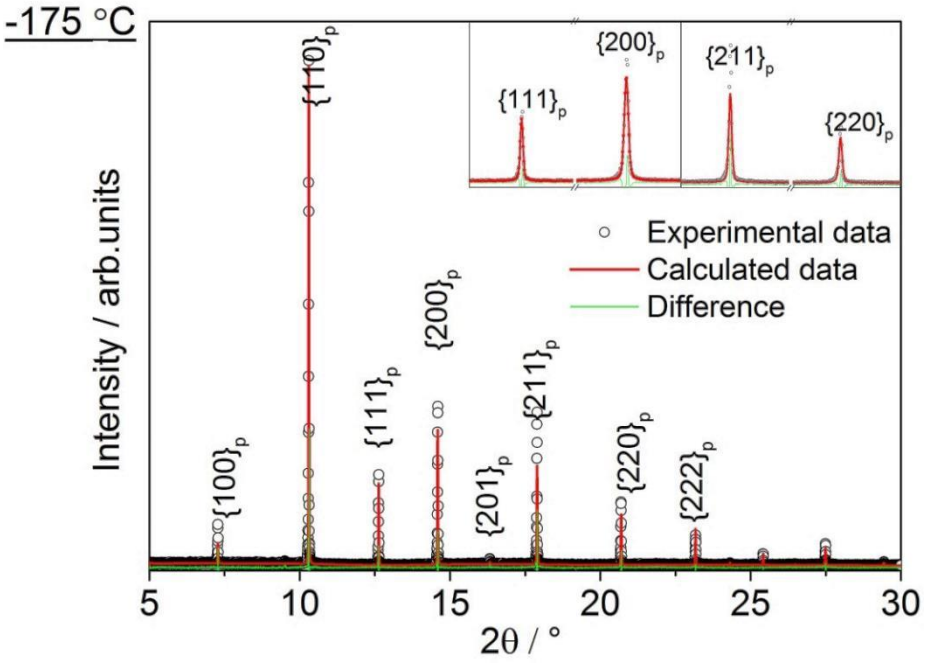

Figure 11.24 The SXPD full patterns refinement for poled NBT-0.09KN powder at -175 ºC.

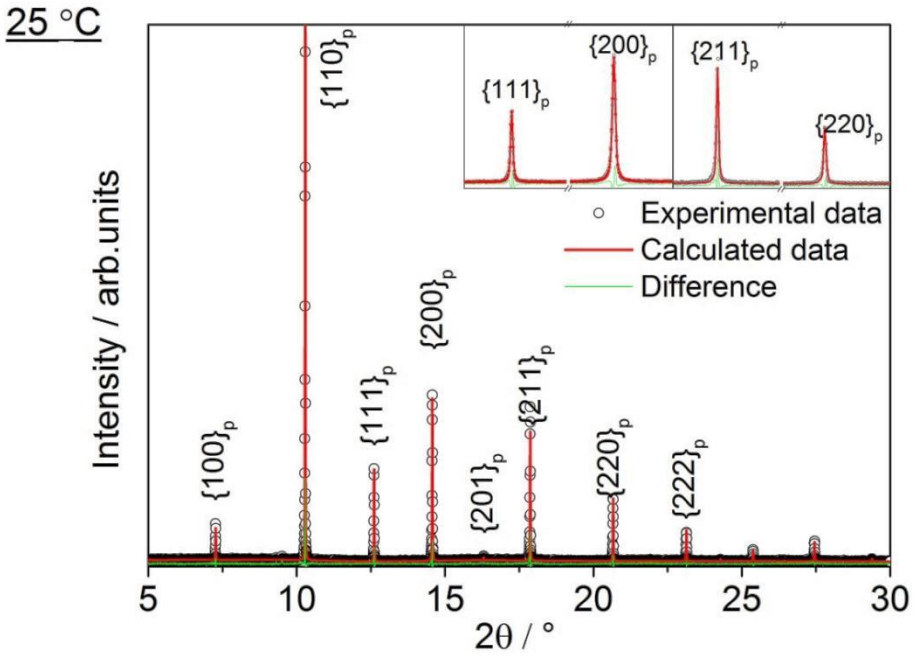

Figure 11.25 The SXPD full patterns refinement for poled NBT-0.09KN powder at 25 ºC.

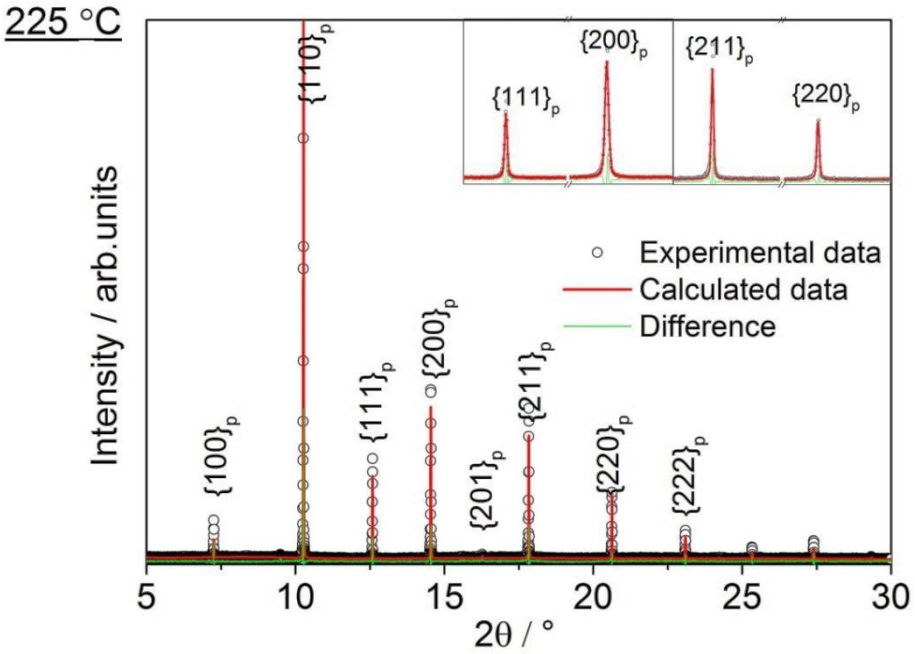

Figure 11.26 The SXPD full patterns refinement for poled NBT-0.09KN powder at 225 ºC.

11.2 Rietveld refinement parameters

11.2.1 Poled NBT-0.01KN

Temp/ºC	lattice parameter a / Å	lattice parameter c / Å	GOF	Rwp
-175	5.47349(18)	13.5612(5)	1.15	13.26
-125	5.47351(4)	13.55570(13)	1.15	18.89
-75	5.47612(4)	13.55529(14)	1.14	19.13
-25	5.47910(4)	13.55484(13)	1.14	18.58
25	5.48441(19)	13.5596(5)	1.67	11.56
75	5.4877(2)	13.5551(6)	1.08	19.23
125	5.48947(5)	13.52258(17)	1.16	20.9
175	5.4974(3)	13.5100(7)	1.05	19.54
225	5.50159(19)	13.5054(5)	1.10	14.79

11.2.2 Unpoled NBT-0.01KN

Temp/ºC	lattice parameter a / Å	lattice parameter c / Å	GOF	Rwp
-175	5.4799(6)	13.4780(14)	1.23	20.01
-125	5.4823(8)	13.4795(5)	1.18	18.84
-75	5.4845(2)	13.4801(7)	1.21	17.64
-25	5.4871(10)	13.4803(11)	1.09	16.69
25	5.4893(4)	13.4805(12)	1.08	16.94
75	5.4933(9)	13.4871(7)	1.11	18.89
125	5.4961(3)	13.4909(7)	1.07	18.01
175	5.5005(8)	13.4935(5)	1.16	17.96
225	5.5033(2)	13.4950(6)	1.07	18.37

11.2.3 Poled NBT-0.03KN

Temp/ºC	lattice parameter a / Å	lattice parameter c / Å	GOF	Rwp
25	5.4906(2)	13.5489(6)	1.15	14.64
125	5.5018(2)	13.5182(6)	1.07	16.14
175	5.5069(3)	13.5131(6)	1.06	16.77
225	5.51386(11)	13.5030(4)	1.13	13.14

11.2.4 Poled NBT-0.05KN

Temp/ºC	lattice parameter a / Å	lattice parameter c / Å	GOF	Rwp
-175	5.4881(5)	13.5002(11)	1.05	15.32
-75	5.4913(3)	13.5015(8)	1.05	17.27
25	5.4984(4)	13.5104(11)	1.02	17.55
75	5.5048(3)	13.5119(7)	1.17	18.78
125	5.51310(17)	13.5044(7)	1.06	16.37

175	3.90005(6)	3.90005(6)	1	15.64
225	3.90178(6)	3.90178(6)	1.02	15.16

11.2.5 Poled NBT-0.09KN

Temp/ºC	lattice parameter a / Å	lattice parameter c / Å	GOF	Rwp
-175	3.89472(12)	3.89472(12)	1.65	17.465
25	3.90014(10)	3.90014(10)	1.54	16.24
225	3.90739(12)	3.90739(12)	1.58	17.42

12 Attended conferences

1. Oral presentation "In-situ electric field study in $Na_{0.5}Bi_{0.5}TiO_3$-$KNbO_3$ ceramics" was given in ISAF 2016 conference, Darmstadt, Germany.

2. Oral presentation "Phase switching behaviour in lead-free piezoelectric ceramics" was given in Piezo 2015 conference, Maribor, Slovenia.

3. Oral presentation "Phase switching behaviour in $Na_{0.5}Bi_{0.5}TiO_3$-$KNbO_3$ piezoelectric ceramics" was given in UK Ferroelectric 2015, NPL, UK.

4. Poster "Field-induced phase transformation and crystallographic texture analysis in $Na_{0.5}Bi_{0.5}TiO_3$-$NaNbO_3$ ceramics" was exhibited in ISAF 2016 conference, Darmstadt, Germany.